Nicolaus Copernicus University in Toruń
Faculty of Physics, Astronomy and Informatics
Department of Atomic, Molecular and Optical Physics

Ultra-stable optical cavities in KL FAMO for metrology and fundamental physics

Mateusz Narożnik

Dissertation submitted in partial fulfilment
of the requirements for the degree of

Doctor of Physics

Thesis supervised by dr hab. Michał Zawada, prof. NCU, and dr Marcin Bober
Department of Atomic, Molecular and Optical Physics
Institute of Physics, Nicolaus Copernicus University in Toruń

Toruń 2024

Acknowledgments/Podziękowania

Pragnę podziękować mojemu promotorowi, dr hab. Michałowi Zawadzie, prof. UMK, za umożliwienie mi pracy w Krajowym Laboratorium Fizyki Atomowej, Molekularnej i Optycznej, za celne uwagi oraz za współpracę, zaufanie i poświęcony czas.

Dziękuję również mojemu promotorowi pomocniczemu, dr Marcinowi Bobrowi, za wprowadzenie mnie do świata ultrastabilnych wnęk, za ultraprecyzyjne pory obiadowe i rozmowy nie tylko o fizyce.

Chciałbym również podziękować całemu zespołowi FAMO -2, Marcinowi i Linkowi, Adamowi i Januszowi, Sławkowi, Piotrowi oraz Jakubowi za wspólne rozmowy i czas spędzony w Cafe FAMO. In this place, I also want to thank my PhD companions, Omid and Domagoj. I hope life is good for both of you :).

Dziękuję za wsparcie i każde dobre słowo w ciągu studiów doktoratu moim Rodzicom, Braciom i ich Rodzinom. Dziękuję również osobom, które zrodziły we mnie zainteresowanie matematyką, fizyką i astronomią: Cioci Danusi, Cioci Teresie, Panu Krzysztofowi Sądejowi i Panu Tomaszowi Kacikowi.

Na koniec najważniejsze. Dziękuję mojej żonie Marysi, która towarzyszy mi od początku mojej drogi z doktoratem. Za wsparcie, motywację, wysłuchiwanie moich smętów, wyrozumiałość i dobre obiadki. Za wiarę we mnie. Rozumiesz?!

The research presented in this dissertation was supported and partially financed by the *A next-generation worldwide quantum sensor network with optical atomic clocks project* (TEAM/2017-4/42) within the TEAM IV Programme of the Foundation for Polish Science co-financed by the European Union under the European Regional Development Fund. This project has received funding from the EMPIR Programme co-financed by the Participating States and from the European Union's Horizon 2020 Research and Innovation Programme (EMPIR 20FUN08 NEXTLASERS). This project has received funding from the National Science Centre in the project *Cavity-Enhanced Quantum Optical Clocks* (Quantera Q-Clocks 2017/25/Z/ST2/03021). The project was performed at the National Laboratory FAMO (KL FAMO) in Toruń, Poland, and were supported by a subsidy from the Polish Ministry of Science and Higher Education.

FNP
Foundation for Polish Science

European Funds
Smart Growth

European Union
European Regional
Development Fund

EMPIR
EURAMET
The EMPIR initiative is co-funded by the European Union's Horizon 2020 research and innovation programme and the EMPIR Participating States

FAMO

NATIONAL SCIENCE CENTRE
POLAND

Contents

1. Introduction

Nobel Prize laureate Arthur Shawlow once stated, "Never measure anything but frequency!". This principle is indeed correct, as frequency is by far the most accurately measured physical quantity [1]. By locking the frequency of the free-running laser to an external rigid Fabry-Pérot interferometer [2], so-called ultra-stable cavity, one can benefit from the cavity's length stability and obtain remarkable fractional frequency noise levels below 10^{-16} in the mHz to Hz range [3–5]. As an indispensable element of the most precise measuring systems, an optical cavity, used along with an optical atomic clock play a significant role in various fundamental physics tests. These include searching for dark matter using the global network of optical atomic clocks [6, 7], tests of the Lorentz invariance violation on Earth [8–10] as well as in the outer space [11], setting constraints on the quantum fluctuations amplitude [9, 12], detecting gravitational waves [13–15], searching for exotic beyond the standard model (SM) particles [15, 16], potential SM violation with ultra-narrow atomic transitions [17], and as a frequency reference for Very Long Baseline Interferometry (VLBI) observations [18]. Currently, modern advanced technologies such as precision radar-ranging systems [19] and deep-space navigation [20] also require ultra-stable optical resonators. Moreover, an upcoming redefinition of a second will be based on the optical narrow atomic transition where atoms are interrogated by a laser locked to the ultra-stable cavity [21–24].

Over the years, significant efforts have been made to improve the performance of ultra-stable cavities, including changing and optimizing the resonator's geometry, choosing less dissipative/noisy materials, lowering and stabilizing the residing temperature [25–30]. Furthermore, successfully mitigating technical noises allowed to reach the fundamental thermal limit in the mHz-Hz frequency range [3], where the overall cavity performance is limited by the internal material properties of the resonator's components. Currently, state-of-the-art table-top resonators and km-scale interferometers are limited by thermal processes in the μm-thick layers of highly reflective Bragg coatings [31, 32]. Even though many attempts have been made to reduce mechanical losses for existing SiO_2/Ta_2O_5, such as annealing [33, 34], doping [32, 35] or exploring new dielectric materials Al_2O_3 [36] and GeO_2 [37], none have significantly improved their dissipation factor (mechanical losses). Recently, $Al_{0.92}Ga_{0.08}As/GaAs$ crystalline coatings has demonstrated a promising tenfold improvement in room temperature [38], but cryogenic performance in 124 K, 16 K, and 4 K does not confirm the expected loss angle value [4, 5]. Another promising project involves using low-noise microstructured mirror coatings [39, 40] - however, despite optimistic predictions of the mechanical loss values, they still show relatively low finesse $\mathcal{F} = 12000$ for ultra-stable cavity performance and too much scattering for use in gravitational wave interferometers [41].

As mentioned above, cavities are generally made of low-noise materials that exhibit exceptionally low thermal expansion coefficient α (CTE). Therefore, one can categorize optical resonators based on their operational temperature: where zero-crossing temperature T_0 of the CTE (defined as $\alpha(T_0) = 0$) are at room temperature (materials like Zerodur [42] and ultra-low expansion (ULE) glass [43]) or way below 0 °C in a cryogenically cooled environment, like single-crystal silicon with two zero-crossing points at $\sim$123-124 K and $\sim$16-17 K [44]. Although sapphire has no zero-crossing points, its CTE is extremely low at 4 K as well [45, 46]. Hence, the current trend in minimizing thermal noise in state-of-the-art cavities focuses on lowering the operating temperature, where the CTE tends towards zero as it approaches 0 K [44]. At the moment, the best cavities operate at temperatures of 4 K, 16 K, and 124 K [4, 5]. The current status for the lowest operational temperatures of the continuously used ultra-stable single-crystal silicon (SCS) cavity is 1.7 K [47] and 4 K [4, 5, 30]. Further temperature reduction to sub-kelvin levels (even down to 20 mK) is underway [48]. However, improving the resonator's performance may introduce new technical challenges related to heat extraction from the cavity's mirrors. [48].

This dissertation mainly focuses on designing room-temperature ultra-stable cavities equipped with thermal shields and vacuum housing to detect high-frequency gravitational waves and low-frequency space-time fluctuations. Moreover, theoretical calculations were performed to enhance the cavity's sensitivity for the mentioned fundamental physics research. The thesis is structured as follows:

- Chapter 2 presents the basic introduction of the Fabry-Pérot resonator working scheme along with the Gaussian beam's properties and behaviour. Next, the idea of laser frequency locking, mainly Pound-Drever-Hall (PDH), will be presented. The last important subsection is dedicated to frequency stability characterization, covering typical quantities used to describe noise, such as Allan deviation $\sigma_y(\tau)$, modified Allan deviation mod $\sigma_y(\tau)$, power spectral density (PSD) $S_x(f)$, and the relation between them.

- Chapter 3 shows the stability constraints of ultra-stable cavities, focusing mainly on the cavity's thermal noises, i.e. Brownian, thermoelastic and thermo-optic. Additionally, single-crystal silicon and coatings mechanical losses are collected to calculate the possible uncertainty of thermal noise evaluation using the fluctuation-dissipation theorem (FDT). The next subsection introduces the idea of using convex-concave mirrors, including several examples of reducing thermal noises while maintaining optically stable. Additionally, one subsection presents the issues emerging in the cryogenic and extreme cryogenic (subkelvin) conditions. The final section focuses on using a NEXCERA spacer as a promising material for achieving the lowest long-term frequency drift for the room temperature cavities. It also introduces using fused silica (FS) and SCS substrates instead of ULE to reduce Brownian thermal noises.

- Chapter 4 provides the complete design of the room temperature, 30 cm long ULE cavity, and vacuum chamber design. Next, the room's acoustic characteristics were measured using speakers to identify and mitigate resonance modes of the room. In the same room, seismic noises were measured using a millihertz seismometer. The chapter also introduces the concept of the transfer function (TF) and measurements of the disturbed beatnote signal between the strontium clock transition (698 nm) laser, optical frequency comb (OFC) and the strontium cooling laser (689 nm).

- Chapter 5 proposes using an ultra-stable optical cavity as a resonant gravitational wave detector. Firstly, it presents the theoretical background of gravitational waves and the current status of potential gravitational radiation detectors and sources. Then, the chapter demonstrates the working scheme of the detector, highlighting possible limitations given by thermal noises and various potential sources. The final section of the chapter discusses the current significant experimental constraints and considerations for this design and proposal.

- Chapter 6 describes using an ultra-stable cavity system as a quantum fluctuation detector. I use the best available ultra-stable cavities' data to set more stringent constraints on the quantum fluctuation amplitude.

- Conclusions is an overview of the main results of this work, including potential future implementation of the designed ultra-stable room-temperature cavity.

2. Optical resonator and stability

2.1. Fabry-Pérot interferometer

The Fabry-Pérot resonator was developed at the end of the 19th century [49]. Since then, it has demonstrated its indispensable role in numerous research fields from fundamental physics to modern technology applications. In the following section, we will briefly introduce the essential properties and characteristics of the Fabry-Pérot operational principle, which will be used throughout the rest of this thesis.

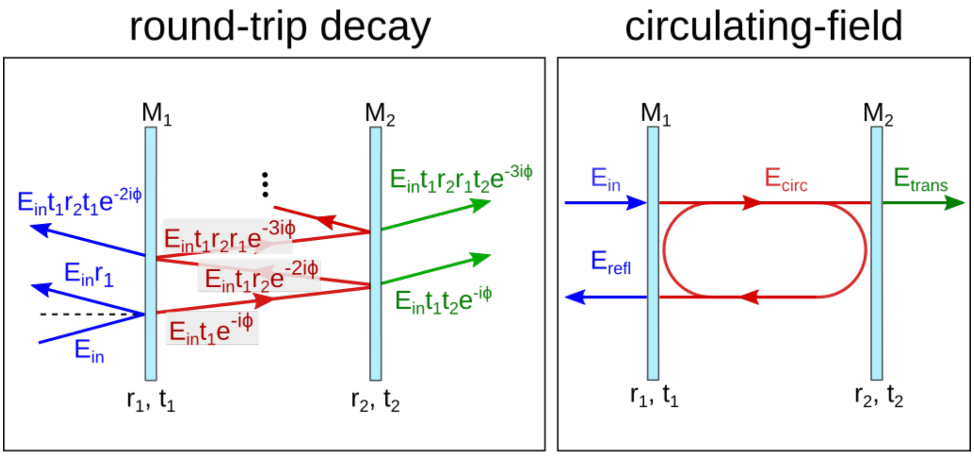

Figure 2.1: Simplified schemes of the Fabry-Pérot plane-parallel resonator illuminated by the electromagnetic wave with the E_{in} complex amplitude. Blue, red, and green arrows indicate reflected, gained/circulating and transmitted light, respectively. The round-trip decay (left) and circulating-field (right) present two alternative approaches to describe the resonator's static response.

Assume that light with the complex amplitude E_{in} of a plane wave is incident on the surface of the left mirror M_1 from outside the Fabry-Pérot interferometer (see Fig. 2.2). Together with the second mirror M_2 they form plane-parallel plates separated by a distance L, simulating the simplest form of a Fabry-Pérot resonator. Fig. 2.1 illustrates two possible methods to calculate the amplitude of reflected E_{ref}, circulating E_{circ} and transmitted E_{trans} cavity light. First concept, often referred to as round-trip decay (as shown in Fig. 2.1), focuses on studying the infinite number of reflections and transmissions inside the resonator (for more details, see [50–52]). The factor $e^{-i\phi}$ (red arrows

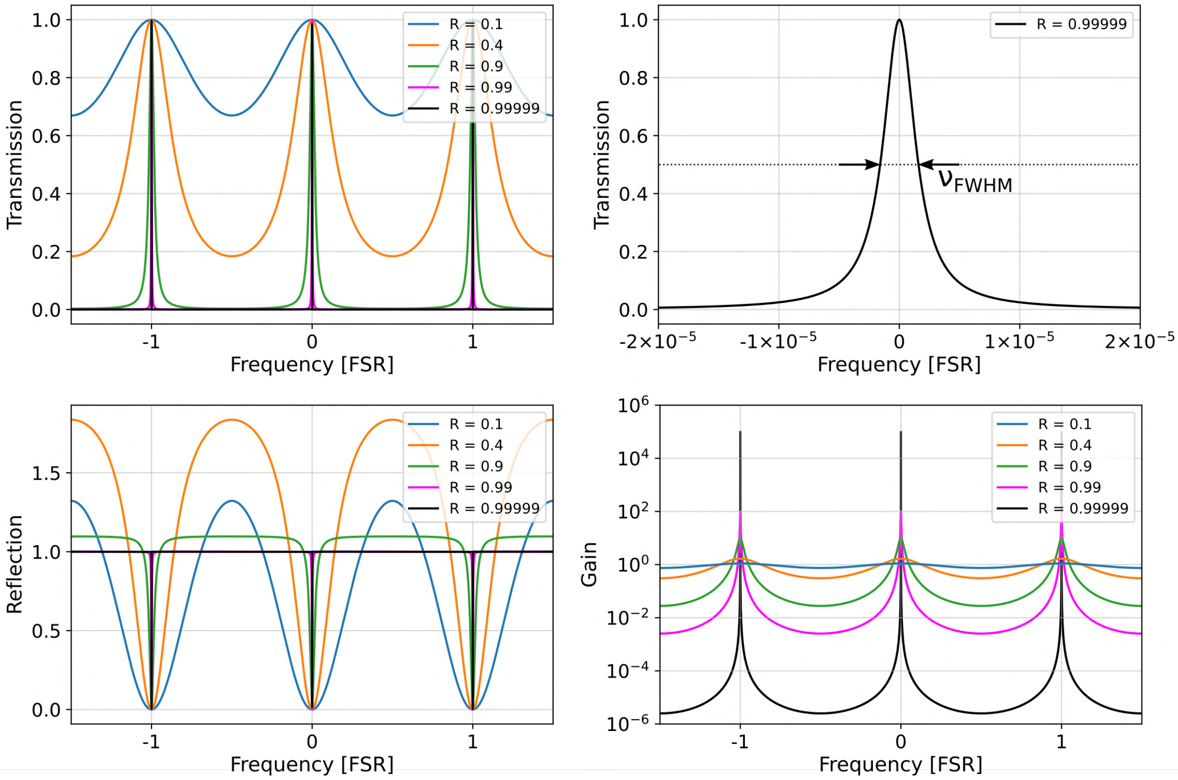

Figure 2.2: **(Top left)** Transmission $\mathcal{T}$ of the Fabry-Pérot resonator for five exemplary reflectances R in the function of free-spectral range (FSR). The highest presented value, $R = 0.99999$, shows typical performance for state-of-the-art coatings materials used in ultra-stable cavities. **(Top right)** An individual mode shape for $R = 0.99999$ with the full-width at half maximum ν_{FWHM}. In addition, reflection $\mathcal{R}$ **(bottom left)** and gain $\mathcal{G}$ **(bottom right)** for the same parameters are presented for the comparison.

in Fig. 2.1) represents phase shift between each consecutive waves, built up within the resonator length L. The phase coefficient is defined as $\phi = kL$, where $k = 2\pi/\lambda$ is the wavenumber of the E_{in} and λ is the wavelength. We will derive the final formulas by summing the amplitudes of the electric field inside the resonator, reflected and transmitted. An alternative method employs the circulating-field technique, assuming constant intensity, so-called steady state. In this approach, E_{circ} is defined as the interference between light transmitted through M_1 and the round-trip light that moves forward (into M_2), undergoing two reflections and phase shifts [53]. Regardless of the used approach, we will obtain the same results for the following amplitude coefficients

$$\begin{aligned}
E_{ref} &= E_{in} r_1 - E_{in} \frac{t_1^2 r_2 e^{-2i\phi}}{1 - r_1 r_2 e^{-2i\phi}}, \\
E_{circ} &= E_{in} \frac{t_1 e^{-i\phi}}{1 - r_1 r_2 e^{-2i\phi}}, \\
E_{trans} &= E_{in} \frac{t_1 t_2 e^{-i\phi}}{1 - r_1 r_2 e^{-2i\phi}},
\end{aligned} \tag{2.1}$$

where the $r_{1,2}$, $t_{1,2}$ are the amplitude reflection and transmission coefficients for the mirror 1 and 2. The practical physical meaning is obtained by each amplitude squared. Hence, the reflectance and transmittance are given by the following expressions $R_{1,2} = r_{1,2}^2$ and $T_{1,2} = t_{1,2}^2$. This analysis assumes lossless mirrors, which simplifies the general formula from $R + T + Losses = 1$ to $R + T = 1$. The final formulas for the intensity of the reflected $\mathcal{R}$ (reflection), circulating $\mathcal{G}$ (gain) and transmitted $\mathcal{T}$ (transmission) light are derived relative to the incident light intensity I_{in} in the following way:

$$\begin{aligned}
\mathcal{R} &\equiv \frac{I_{refl}}{I_{in}} = \frac{|E_{refl}|^2}{|E_{in}|^2} = \frac{(\sqrt{R_1} - \sqrt{R_2})^2 + 4\sqrt{R_1 R_2}\sin^2(\phi)}{(1 - \sqrt{R_1 R_2})^2 + 4\sqrt{R_1 R_2}\sin^2(\phi)}, \\
\mathcal{G} &\equiv \frac{I_{circ}}{I_{in}} = \frac{|E_{circ}|^2}{|E_{in}|^2} = \frac{1 - R_1}{(1 - \sqrt{R_1 R_2})^2 + 4\sqrt{R_1 R_2}\sin^2(\phi)}, \\
\mathcal{T} &\equiv \frac{I_{trans}}{I_{in}} = \frac{|E_{trans}|^2}{|E_{in}|^2} = \frac{(1 - R_1)(1 - R_2)}{(1 - \sqrt{R_1 R_2})^2 + 4\sqrt{R_1 R_2}\sin^2(\phi)}.
\end{aligned} \tag{2.2}$$

According to Eq. 2.2 the maximum transmission and gain, along with minimum reflection (it indicates the positive interference), require fulfilling the condition $\sin\phi = 0$, i.e. $\phi = m\pi$ where $m \in \mathbb{Z}$. This criterion in the frequency unit is formulated such that half the wavelength must be an integer multiple m of the distance between the mirrors, expressed as $L = m\lambda/2n$, where n is a refractive index. Therefore, for light, where $c = \nu\lambda$ (with c representing the speed of light, ν the light frequency, and λ the wavelength), an important quantity is known as the free spectral range (FSR) of the cavity

$$\nu_{FSR} = \frac{c}{2nL}, \tag{2.3}$$

which is the frequency distance between two consecutive maxima, and $l\nu_{FSR}$ for $l \in \mathbb{Z}$ gives a discrete set of possible longitudinal resonant frequencies. Fig. 2.2 presents the transmission, reflection and gain for the Fabry-Pérot resonator for five exemplary reflectances (assuming equal reflectance on both mirrors $R_1 = R_2 = R$) in the function of free-spectral range (FSR), calculated using Eq. 2.2. In Fig. 2.2 (top right), individual mode shape is shown with the full width at half maximum ν_{FWHM}, which may be found by finding the width of the transmission.

$$\nu_{FWHM} = \frac{c}{2\pi nL}\frac{1 - R}{\sqrt{R}}. \tag{2.4}$$

An essential parameter characterizing the resonator is the so-called finesse, which is the ratio of free-spectral range ν_{FSR} to the linewidth ν_{FWHM}

$$\mathcal{F} \equiv \frac{\nu_{FSR}}{\nu_{FWHM}} = \pi \frac{\sqrt{R}}{1-R}. \tag{2.5}$$

According to Fig. 2.2, the highest presented value of the reflectance $R = 0.99999$ indicates a linewidth that is ≈ 314000 (finesse value equivalent to $R = 0.99999$) times smaller than FSR. This performance is typical performance for state-of-the-art coating materials used in ultra-stable cavities. Using the definition of finesse (Eq. 2.5) and Eq. 2.2 the transmission is often presented in the following form

$$\mathcal{T} = \frac{1}{1+\left(\frac{2\mathcal{F}}{\pi}\right)^2 \sin^2(\phi)}. \tag{2.6}$$

More in-depth analysis can be found in the following textbooks [50–53] and a review paper [54].

2.1.1. Optical stability

The cavity's length and the curvature of its mirrors must ensure the condition of a self-consistent laser beam. This fundamental condition may be presented in the language of geometrical optics. Analysis with the paraxial approximation allows us to follow the ray trace with effectively small angles (so $\sin(\theta) \approx \theta$). The light path in the stable cavity condition is ultimately replicated. Therefore, technically speaking, we will check if the beam will remain within the cavity and reproduce itself after n-round trips. A common practice in geometric optics involves the use of linear transformations through the ray transfer matrix (often referred to as the ABCD matrix) [52, 53]:

$$\begin{bmatrix} A & B \\ C & D \end{bmatrix} \begin{bmatrix} x \\ \theta \end{bmatrix} = \lambda \begin{bmatrix} x \\ \theta \end{bmatrix}, \tag{2.7}$$

where A, B, C, D are the elements that characterize the final state of the light's round trip between the mirrors, transforming the initial beam's distance from the optical axis x and the beam's slope θ. The right-hand side of the equation represents the eigenvalue λ and the vector comprising x and θ. After deriving the expressions and considering n-round-trips, the final stability condition for the matrix elements simplifies to

$$0 \leq \frac{A+D+2}{4} \leq 1. \tag{2.8}$$

The final formula, that involves essential cavity parameters, i.e. the length of the cavity L and the mirrors' radii of curvature R_{m1} and R_{m2} is as follows:

$$0 \leq \left(1 - \frac{L}{R_{m1}}\right)\left(1 - \frac{L}{R_{m2}}\right) \leq 1, \tag{2.9}$$

where it is often stated that $g_{1,2} = 1 - L/R_{m1,m2}$, which finally gives [55]

$$0 \leq g_1 g_2 \leq 1. \tag{2.10}$$

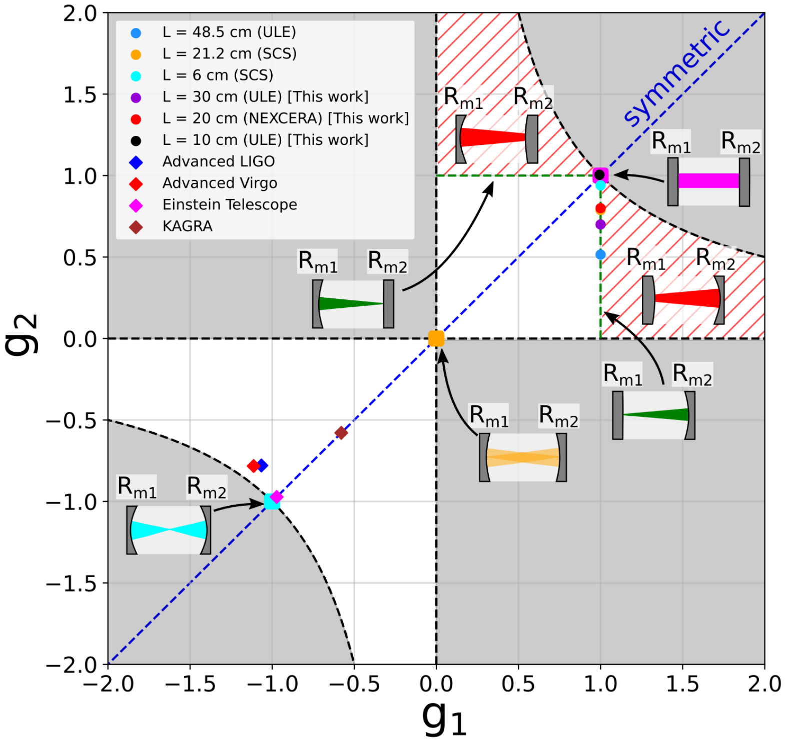

Figure 2.3: Stability diagram for the proposed ultra-stable cavities in this thesis ($L = 10$ cm, $L = 20$ cm and $L = 30$ cm) and examples of existing ones [56–58], as well as large-scale gravitational wave interferometers such as Advanced LIGO [59], Advanced Virgo [60], KAGRA [61], and future planned Einstein Telescope [62]. The grey-shaded area shows the optically unstable regions. Additionally, the convex-concave configuration region is hatched with the red lines and schematically drawn, together with plane-parallel (magenta square), confocal i.e. $R_{m1} = R_{m2} = L$ (orange square), symmetric i.e. $R_{m1} = R_{m2} = L/2$ (cyan square), and plano-concave configurations (green dashed lines).

The condition presented in Eq. 2.10 is essential for the beam to maintain a finite size after n-round trips. If this condition is not satisfied, the light may diverge from the optical axis and leave the resonator. The common practice is visualising stable (white area) and unstable regions (shaded area) on the plot (see Fig. 2.3). While this analysis is relatively simple, it is crucial in designing cavities. The stability factor $g_1 g_2$, when approaching 0 or 1, gets more sensitive (closer to unstable region) to any cavity's length or mirrors' radii of curvature change.

In Fig. 2.3, the configurations such as parallel mirrors (where $R_{m1} = R_{m2} = \infty$), can quickly become unstable, similar to concentric ($R_{m1} = R_{m2} = L/2$) and confocal (R_{m1}

$= R_{m2} =$ L) configurations. The points on the stability diagram for the investigated ultra-stable cavities, with the plano-concave ($L = 10$ cm, $L = 20$ cm and $L = 30$ cm) and convex-concave mirror configurations, are presented. Additionally, the diagram includes examples of the best existing table-top optical cavity systems [4, 56, 57], as well as large-scale gravitational wave interferometers such as Advanced LIGO [59], Advanced Virgo [60], KAGRA [61], and the future planned Einstein Telescope [62].

2.2. Gaussian beam and transverse electromagnetic modes (TEMs)

Apart from the longitudinal modes in the resonator, denoted as $l\nu_{FSR}$, the transversal modes play an essential role in the cavity's frequency analysis. These transversal electromagnetic modes (TEM) can be derived starting from the classical Helmholtz wave equation for the electric field $\vec{E}$ [53, 63]

$$\nabla^2\vec{E} + k^2\vec{E} = 0. \tag{2.11}$$

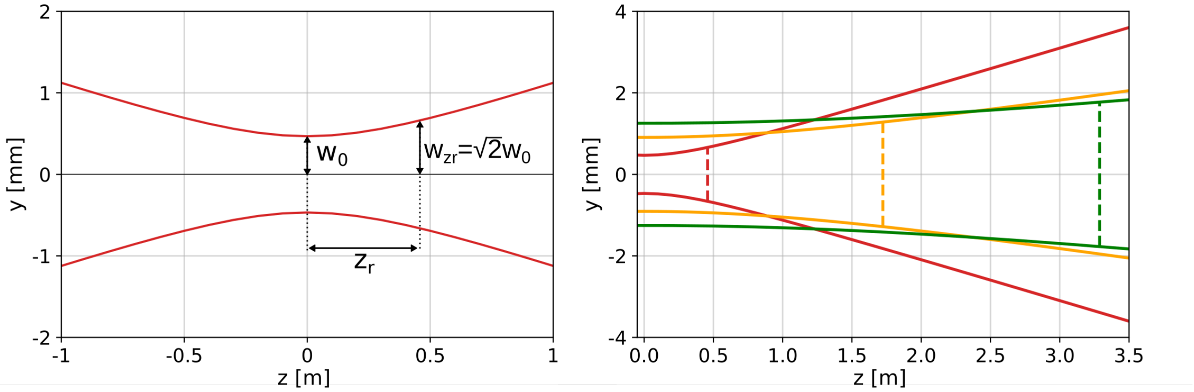

Figure 2.4: **(Left)** Exemplary Gaussian beam with the denoted typical beam characteristics, i.e. waist w_0 and the beam size in the Rayleigh range w_{zr} for the 1.5 μm wavelength. **(Right)** Three Gaussian beams with different waist (at $z = 0$) showing the diverse divergence and the beam size at Rayleigh range (dashed lines).

One can solve this partial differential equation by reasonably assuming the slowly varying envelope approximation for the beam [53, 63], i.e., the transverse beam variation is significantly smaller compared to the electromagnetic wave's wavelength, $\lambda = 2\pi/k$, in the z-direction (the direction of the Poynting vector). Therefore, we can substitute $E(x, y, z) = a(x, y, z)e^{-ikz}$ to obtain the so-called paraxial Helmholtz equation. This leads to the derivation of the final form of the wave equation [63]

$$\left(\frac{\partial^2}{\partial x^2} + \frac{\partial^2}{\partial y^2} - 2k\frac{\partial}{\partial z}\right)a(x, y, z) = 0. \tag{2.12}$$

By applying an appropriate ansatz, we can derive the general solution of the Eq.2.12. This general solution describes the spatial configuration and comprises the entire set of solutions known as transverse-electromagnetic modes TEM_{mn} (for $m, n \in 0, 1, 2, \ldots$).

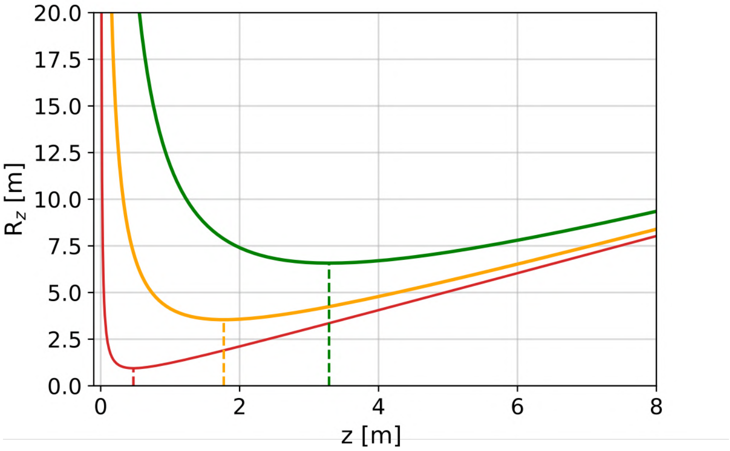

Figure 2.5: The evolution of the Gaussian beam wavefront curvature radius $R_z(z)$ for the beams plotted in Fig. 2.4. Coloured dashed lines illustrate the Rayleigh range value, where the wavefront curvature radius is the smallest. The wavelength of all beams is 1.5 μm, with waist radii of 474 μm, 920 μm, and 1.284 mm for the red, orange, and green solid lines, respectively.

The evolution of the Gaussian beam wavefront curvature radius $R_z(z)$ for the beams is plotted in Fig. 2.4. Coloured dashed lines illustrate the Rayleigh range value, where the wavefront curvature radius is the smallest. The wavelength of all beams is 1.5 μm, with waist radii w_0 of 474 μm, 920 μm, and 1.284 mm for the red, orange, and green solid lines, respectively.

The solution for the complex wave amplitude is as follows

$$E_{mn}(x, y, z) = E_0 \frac{w_0}{w(z)} H_m\left(\frac{\sqrt{2}x}{w(z)}\right) H_n\left(\frac{\sqrt{2}y}{w(z)}\right) \exp\left(-\frac{x^2+y^2}{w^2(z)}\right) \tag{2.13}$$

$$\exp\left(-i\frac{k(x^2+y^2)}{2R(z)} ikz + \zeta(z)\right), \tag{2.14}$$

where H_m and H_n are the Hermite polynomials. The w_z represents the radius of the beam, defined as $1/\text{e}^2$ of the maximum beam intensity[1] and $R_z(z)$ is the wavefront curvature radius:

$$w(z) = w_0\sqrt{1 + (z/z_r)^2} \quad \text{and} \quad R_z(z) = z\left[1 + \left(\frac{z_r}{z}\right)^2\right] \tag{2.15}$$

---

[1] This corresponds to approximately 0.135 of the maximum intensity, in contrast to 0.5 in the Full Width at Half Maximum (FWHM) definition. The relationship is given by $w_z = \text{FWHM(z)}/\sqrt{2\ln(2)}$

where z_r is the Rayleigh range ($z_r \equiv \pi w_0^2/\lambda$), the distance at which the beam's cross-sectional area is doubled (equivalently, $w_z = \sqrt{2} w_0$) and up to this point, the beam is considered to be "focused" [63].

The beam waist w_0 and wavelength λ determine the spatial evolution of the Gaussian beam. Beyond Rayleigh range z_r, the beam's divergence increases linearly, and the wave-front radius of curvature increases (see Fig. 2.5). As can be clearly seen from Fig. 2.4, a smaller waist results in greater divergence, which can be quantitatively expressed by the divergence angle $\theta = \lambda/(\pi w_0)$.

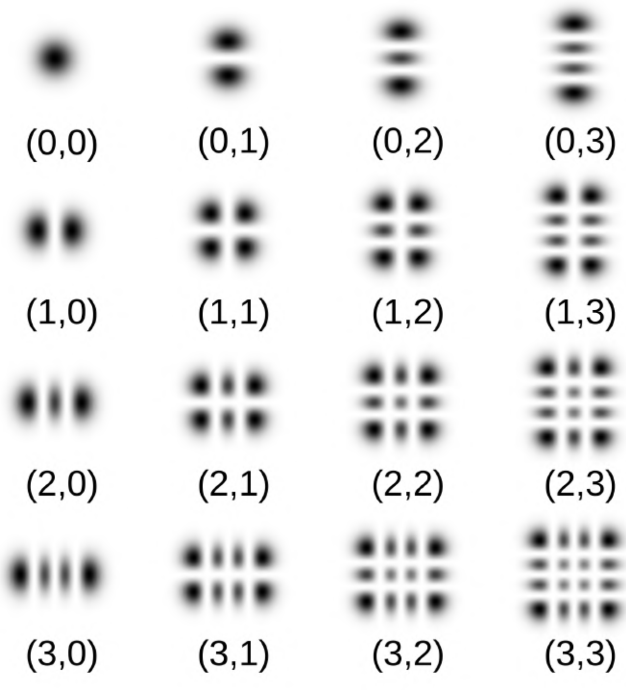

Figure 2.6: The light intensity distribution in the plane transverse to the optical axis. They are characterised by solutions of the paraxial Helmholtz equation in terms of Hermite-Gauss polynomials from fundamental TEM_{00} to TEM_{33}.

The last quantity from Eq. 2.14 is the Gouy phase shift, which arises because the Gaussian beam experiences spatial transversal confinement [64]; that is, it undergoes focusing at some point, which induces a phase shift in comparison to the ideal e^{-ikz} planar wave [2]. Thus, the expression for the phase shift, becomes $e^{ikz+\zeta}$, where ζ represents the Gouy phase shift

---

[2] Any spatial transversal confinement introduces spreading effect in transverse momentum, according to the uncertainty principle $\Delta k_x \Delta x \leq$ const. This confinement leads to a shift in the expectation value of the momentum associated with the phase.

$$\zeta(z) = \arctan(z/z_r). \tag{2.16}$$

For the higher order modes (where $m, n > 0$), they experience a Gouy phase shift given by $\phi(z)_{mn} = (m+n+1)\zeta(z)$, which results in the following frequency shift

$$\nu_{mn} = \frac{\phi_{m,n}(z)}{2\pi}\nu_{FSR} = (m+n+1)\frac{\zeta(z)}{2\pi}\frac{c}{2L}. \tag{2.17}$$

We are particularly interested in the phase change along the resonator length, where the phase evolves as $\phi(z_2 - z_1) = kL - (n+m+1)[\zeta(z_2) - \zeta(z_1)]$, where $z_{1,2}$ denotes the position of the mirrors and $\zeta(z_2) - \zeta(z_1) = \arccos(\pm\sqrt{g_1 g_2})$ [53]. Therefore, taking into account the longitudinal modes as well, the final frequency shift for higher-order modes can be calculated by [53]

$$\nu_{lnm} = \nu_{FSR}\left[l + (m+n+1)\frac{\arccos(\pm\sqrt{g_1 g_2})}{\pi}\right]. \tag{2.18}$$

Fig. 2.6 illustrates the intensity pattern of a set of Hermite-Gauss modes. The first one, TEM_{00} is commonly called fundamental Gaussian mode and represents the desired signal in the cavity. The remaining modes are often considered parasitic and unexpected.

The intensity of the Gaussian beam in the plane $r = \sqrt{x^2 + y^2}$ transverse to the optical axis z, according to the definition $I(r, z) = |E_{00}(r, z)|^2$, follows a specific profile

$$I(r, z) \equiv \frac{2P}{\pi w^2(z)} \exp\left(\frac{-2r^2}{w^2(z)}\right), \tag{2.19}$$

where P denotes the beam power.

2.3. Laser frequency narrowing and locking

A laser consists of three main elements: an external pump source, an active laser medium, and an optical resonator. The precision of controlling parameters of these three elements, such as temperature, voltage, current, mirror position, etc., limits the frequency stability of the so-called free-running laser. Therefore, to improve the laser frequency stability by the orders of magnitude, one must use an additional external Fabry-Pérot cavity, which can be isolated and controlled much more effectively than the laser itself. This process is commonly referred to as laser frequency locking and allows transfering of the stability of the well-controlled external Fabry-Pérot cavity to the laser.

An ultra-stable cavity mode linewidth is determined by the finesse and the cavity length. For the $\mathcal{F} = 300000$ and a length of 30 cm mode width is 1.666 kHz. The linewidth of the state-of-the-art stabilized laser is already below 10 mHz [3] or 16 mHz [65], compared to the kHz level of the resonator's line FWHM. This effect is achieved by the locking and stabilization techniques, such as Pound-Drever-Hall [2, 66] (see Fig. 2.7).

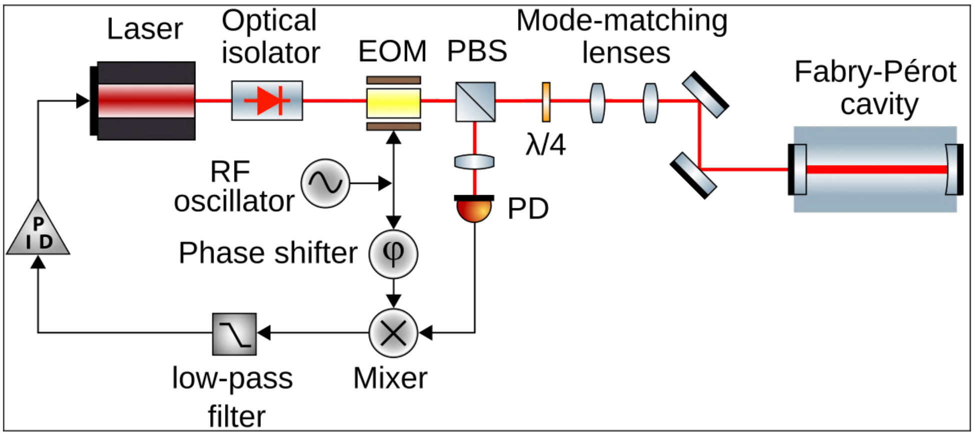

Figure 2.7: The scheme includes all essential elements for implementing the Pound-Drever-Hall locking method [2]. An EOM is an electro-optic modulator, PD is a photodiode, PBS is the polarizing beam splitter, and $\lambda/4$ is a quarter-wave plate. To avoid circular polarisation, one of the optical components can be substituted i.e. a quarter-wave plate can be replaced by a Faraday rotator. This adjustment is particularly relevant for birefringent materials, such as crystalline coatings. The diagram was created using the free svg library [67].

Fig. 2.7 illustrates the typical configuration for ultra-stable cavity frequency locking using PDH technique (see [2] for details). This method's core principle is the interference between the sidebands generated $\nu \pm \nu_{\text{mod}}$ by the electro-optic modulator (EOM) and the carrier light ν. The carrier exhibits a phase shift upon any disturbance in the cavity. If the light is perfectly coupled to the cavity, no reflection of the carrier occurs, and no beat-note signal is detected on the photodiode (PD). If a signal is detected, it is mixed with the RF oscillator signal and passed through a low-pass filter to the PID, which generates the corrections to the frequency from the error signal.

The PDH error signal ϵ, which determines the quality of the lock (how narrow it would be) near resonance, may be written as [2]

$$\epsilon = D\delta f = -\frac{8\sqrt{P_c P_s}}{\nu_{FWHM}}\delta f = -\frac{16L\mathcal{F}\sqrt{P_c P_s}}{c}\delta f, \tag{2.20}$$

where D is known as the discriminant signal slope (linear around the resonant carrier), determining the error signal magnitude and, therefore, the quality of the lock. Then, P_c and P_s are the power in the carrier and sideband of the phase-modulated incident beam, and δf is the frequency noise around the resonance. From Eq. 2.20, we see that increasing the finesse $\mathcal{F}$ and beam power P_c, P_s increases the error signal and the sensitivity Nevertheless, it has a drawback in increasing the intracavity power, which heats the mirror's surface and increases the thermal noises. Hence, the overall cavity performance may not be improved. The math behind PDH technique and Eq. 2.20 is introduced in [2]. More detailed information about the most common locking schemes and comparisons can be found in the comprehensive review paper [68].

2.4. Frequency instability characterization

The remarkable stability level of the optical Fabry-Pérot resonator is obtained through precise stabilization of the cavity's distance $L_0 = L$ between the reflective surfaces. Any fluctuation in the cavity's length changes the wavelength that can fit into it, and therefore, the cavity mode resonance frequency ν_0, according to the following formula

$$\frac{\Delta\nu(t)}{\nu_0} = \frac{\Delta L(t)}{L_0}. \tag{2.21}$$

The instantaneous frequency fluctuation may be expressed as

$$\Delta\nu(t) = \nu(t) - \nu_0 \equiv \frac{1}{2\pi}\frac{d\phi(t)}{dt}, \tag{2.22}$$

where $\phi(t)$ represents the phase deviation in the oscillator signal $\sin[2\pi\nu_0 t + \phi(t)]$.

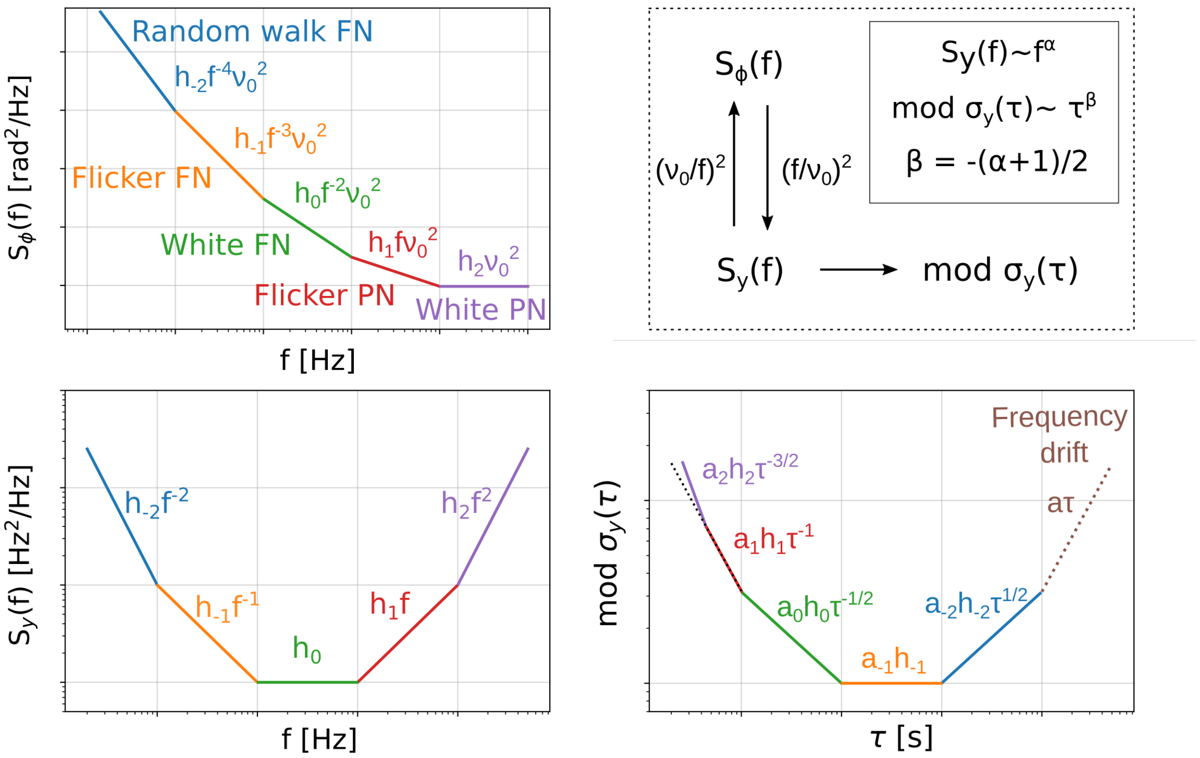

Figure 2.8: The characteristics of typical noises in the oscillator are illustrated in the form of power spectral density of the phase **(top left)** and fractional frequency **(bottom left)**, along with modified Allan deviation **(bottom right)**. Additionally, the power-law relationship between all these quantities are presented **(top right)**. All curves are schematically drawn in the log-log plots. Colours between plots indicate the same noise type, with PN and FN denoting phase noise and frequency noise, respectively. The black dotted line on the modified Allan deviation plot shows the τ^{-1} line for Allan deviation, which does not discriminate these noises. The constant a_α is necessary for recalculating from power spectral density to modified Allan deviation for each noise separately. White FN is often referred to as random walk PN.

Moreover, we can define an important dimensionless quantity (already expressed in Eq. 2.21), namely fractional frequency fluctuation $y(t)$, which quantifies the stability of the oscillator by comparing the deviations in frequency $\Delta\nu(t)$ to the nominal frequency ν_0 over a specified time interval

$$y(t) = \frac{\Delta\nu(t)}{\nu_0} = \frac{1}{2\pi\nu_0}\frac{d\phi(t)}{dt} \tag{2.23}$$

and the phase equivalent as a normalized phase fluctuation $x(t) = \phi(t)/(2\pi\nu_0)$, where $y(t) = dx(t)/dt$.

A classical statistical tool for data analysis is known as variance

$$\sigma_s^2 = \Big\langle (y - \langle y \rangle^2) \Big\rangle = \frac{1}{N-1}\sum_{i=1}^{N}(y_i - \langle y \rangle)^2, \tag{2.24}$$

where $\langle \dots \rangle$ indicates the expected value [3]. However, classical variance σ_s^2 and standard deviation σ_s have a flaw that limits its applicability in the analysis of time and frequency measurements; specifically, it diverges with an increasing number of samples for certain types of noise, such as flicker frequency noise (see Fig. 6 in [69]). To overcome these limitations, a new tool known as Allan variance (AVAR) $\sigma_y(\tau)$ was developed [4]. Unlike the classical variance, which is calculated based on the difference between each signal and the ensemble average, AVAR takes a different approach. In this method, the variance is calculated based on the difference between consecutive mean frequencies

$$\sigma_y^2(\tau) = \frac{1}{2}\Big\langle (\bar{y}_{i+1} - \bar{y}_i)^2 \Big\rangle = \frac{1}{2\tau^2}\Big\langle (x_{i+2} - 2x_{i+1} + x_i)^2 \Big\rangle, \tag{2.25}$$

where $\bar{y}_i = (x_{i+1} - x_i)/\tau$ is the i-th frequency deviation during time τ. For the N number of samples, the AVAR is expressed as [70]

$$\sigma_y^2(\tau) = \frac{1}{2(N-1)}\sum_{i=1}^{N-1}(\bar{y}_{i+1} - \bar{y}_i)^2 = \frac{1}{2(N-2)\tau^2}\sum_{i=1}^{N-2}(x_{i+2} - 2x_{i+1} + x_i)^2. \tag{2.26}$$

The Allan variance and deviation (ADEV) as well as overlapping ADEV [5] are excellent tools for quickly examining the dominating noise source in a system. Figure 2.8 illustrates the characteristic slopes of each of the noises, allowing for almost complete knowledge of its performance and limitations in measured time and frequency ranges by a glance at power spectral density (PSD) of the phase $S_\phi(f)$ and fractional length $S_y(f)$ deviations,

---

[3] For N equally probable samples, $\langle y \rangle = \frac{1}{N}\sum_{i=1}^{N} y_i$.

[4] It is a specific case of M-sample variance, $\sigma^2(M, T, \tau)$, with zero-dead (thus T=τ) and $M = 2$, denoted as $\sigma_y^2(2, \tau, \tau)$, or simply $\sigma_y(\tau)$.

[5] A practical and commonly used alternative to classical ADEV offers better confidence compared to ADEV because it uses more data (a larger N) to derive final values. Hence, the confidence is improved, as indicated by $\pm\sigma_y(\tau)/\sqrt{N}$.

and modified AVAR mod$\sigma_y(\tau)$. Nevertheless, ADEV has limitations, e.g. fast oscillation sources, i.e., high-frequency signals, are visible as one $\sigma_y \approx \tau^{-1}$ flicker noise, wherein both flicker τ^{-1} and white $\tau^{3/2}$ phase noise (PN) are present. AVAR does not discriminate between flicker and white PN (dotted line in Figure 2.8). To overcome this limitation, modified Allan variance was introduced [71] as

$$mod\ \sigma_y^2(\tau) = \frac{1}{2}\left\langle \left(\frac{1}{n}\sum_{i=1}^{N} \bar{y}_{i+n} - \bar{y}_i \right)^2 \right\rangle, \tag{2.27}$$

and for N-samples

$$mod\ \sigma_y^2(\tau) = \frac{1}{2n^4(N-3n+1)} \sum_{j=1}^{N-3n+1} \left[\sum_{i=j}^{j+n-1} \left(\sum_{k=i}^{i+n-1} \bar{y}_{k+n} - \bar{y}_k \right) \right]^2. \tag{2.28}$$

Another helpful quantity implemented rather for short-term performance analysis (high-frequency analysis) than for long-term (as in ADEV) is the power spectral density (PSD), $S_x(f)$, defined as the Fourier Transform of the autocorrelation function of a signal [50]. In practice, integration over the selected bandwidth will provide the amount of signal's power accumulated in this range, where integration from $-\infty$ to $+\infty$ results in the total power. Furthermore, according to Parseval's theorem, which connects the time domain with the frequency domain, the root mean square (RMS) of the displacement x within the $[f_1; f_2]$ frequency range can be determined as

$$x_{RMS}^2 = \int_{f_1}^{f_2} S_x(f)df. \tag{2.29}$$

It is worth mentioning that the PSD of the length $S_L(f)$, frequency $S_\nu(f)$, phase $S_\phi(f)$ and normalized phase $4\pi\nu_0^2 S_\phi(f)$, and the fractional PSD $S_y(f)$ are connected as follows

$$S_y(f) = \frac{S_\nu(f)}{\nu_0^2} = \frac{S_L(f)}{L_0^2} = \frac{f^2}{\nu_o^2}S_\phi(f). \tag{2.30}$$

Time domain AVAR and frequency domain PSD are related and can be converted but not exactly reciprocally. We may obtain a general formula for converting frequency domain (PSD) to time domain (AVAR and mod AVAR) [50, 72]:

$$\sigma_y^2(\tau) = 2\int_0^\infty S_y(f)\frac{\sin^4(\pi f\tau)}{(\pi f\tau)^2}df, \tag{2.31}$$

$$mod\ \sigma_y^2(\tau) = 2\int_0^\infty S_y(f)\frac{\sin^6(\pi f\tau)}{(\pi fn\tau)^2\sin^2(\pi f\tau_0)}df. \tag{2.32}$$

The opposite conversion, i.e., from AVAR to PSD, does not yield a unique solution as expected and required. Many PSDs, hence many integrals in Eq. 2.31 as well as in Eq. 2.32, would have the same Allan variances. Therefore, we may distinguish between the

Table 2.1: Relations between fractional power spectral density (PSD) $S_y(f)$, Allan variance $\sigma_y^2(\tau)$, and modified Allan variance (mod AVAR) mod $\sigma_y^2(\tau)$ for individual power-law noise types with amplitude of h_α for $\alpha = \{-2, -1, 0, 1, 2\}$. The cutoff frequency f_h is essential in avoiding divergence (infinite results) in Eq. 2.31. The modified Allan variance resolves this issue. All calculation taken from [73, 74].

Type of noise	$\mathrm{S}_y(\mathrm{f})$	$\sigma_y^2(\tau)$	mod $\sigma_y^2(\tau)$
Random walk FN	$h_{-2}f^{-2}$	$\frac{2\pi^2}{3}h_{-2}\tau$	$\frac{11}{20}\pi^2 h_{-2}\tau$
Flicker FN	$h_{-1}f^{-1}$	$2\ln(2)\ h_{-1}$	$\frac{27}{20}\ln(2)h_{-1}$
White FN	h_0	$0.5\ h_0\tau^{-1}$	$0.25h_0\tau^{-1}$
Flicker PN	$h_1 f^1$	$\frac{1.038+3\ln(2\pi f_h\tau)}{4\pi^2}h_1\tau^{-2}$	$\frac{3\ln(256/27)}{8\pi^2}h_1\tau^{-2}$
White PN	$h_2 f^2$	$\frac{3f_h}{4\pi^2}h_2\tau^{-2}$	$\frac{3}{8\pi^2}h_2\tau^{-3}$

noises and their slopes and recalculate them individually, according to the Tab. 2.1 and by using the superposition[6] of each individual noises in the case of fractional PSD with the amplitude of h_α

$$S_y(f) = \sum_{\alpha=-2}^{2} h_\alpha f^\alpha. \tag{2.33}$$

Further discussion on the transfer function, filters and precise derivations of Eq. 2.31 and 2.32 is provided in textbooks [50, 69, 74] and overview papers [72, 73, 75, 76].

2.5. Ultra-stable cavity for the metrology and fundamental physics

Ultra-stable optical resonators are essential in ongoing state-of-the-art scientific projects and future ones. Their performance guarantees the performance of today's best measurement apparatus, therefore, much effort has been taken to improve cavities performance. Figure 2.9 illustrates the timewise improvement of ultra-stable cavity performance in terms of Allan deviation at 1 s.

To analyze the performance of an individual optical resonator, one must introduce another optical signal (reference) for interference. In the case of beat-note frequency between two oscillator signals (σ_A and σ_B) with uncorrelated noises, the output is essentially the sum of their Allan variances

$$\sigma_{AB}^2(\tau) = \sigma_A^2(\tau) + \sigma_B^2(\tau). \tag{2.34}$$

Therefore, to roughly estimate the performance of individual resonator A, resonator B must be significantly less noisy, as the overall noise is the sum of both. To explicitly detect the individual resonator instability, at least three resonators are necessary. The

---

[6] It is worth to notice that for white FN *mod* $\sigma_y^2(\tau) = 0.5\sigma_y^2(\tau)$, for flicker PN *mod* $\sigma_y^2(\tau) = 0.67\sigma_y^2(\tau)$ and for random walk FN *mod* $\sigma_y^2(\tau) = 0.82\sigma_y^2(\tau)$.

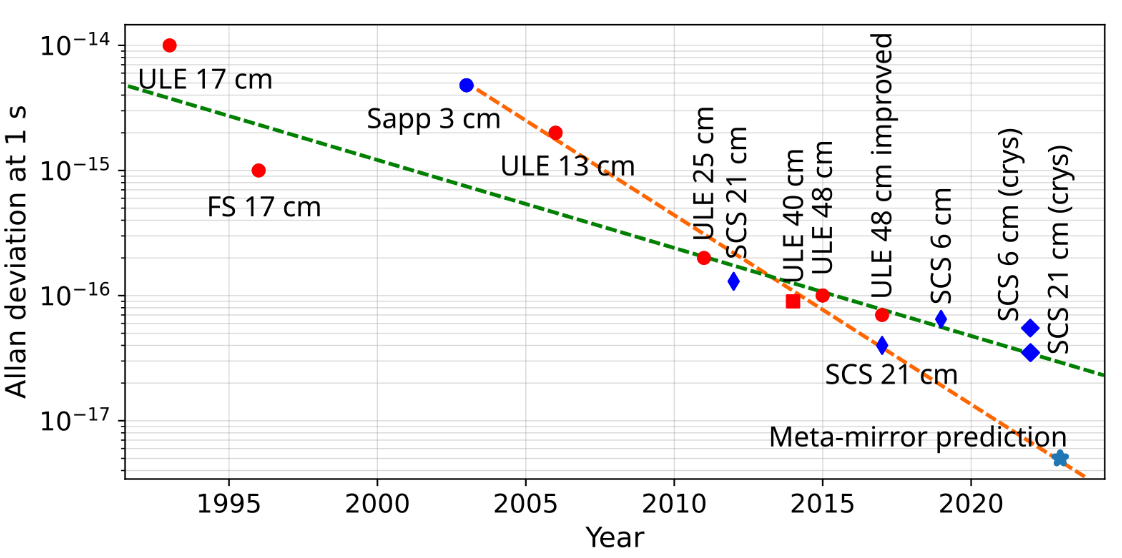

Figure 2.9: Measured stability of the state-of-the-art Fabry-Pérot resonators through the years in terms of as an Allan deviation. Each point description shows the spacer's length and its material. Marker shape and colour depict the resonator's spacer geometry (cylindrical, cuboid, double-cone) and residing temperature (red - room temperature, blue - cryogenic temperature), respectively. Additionally, thicker double-cone for SCS means crystalline mirror coatings (crys), and blue star means the predicted performance of meta-mirror-based resonators. Two possible improvement rates were fitted with orange and green lines to extrapolate the instability for future resonators. Data taken from: ULE 17 cm [77], FS 17 cm [78], Sapp 3 cm [8], ULE 13 cm [79], ULE 25 cm [28], SCS 21 cm [28], ULE 40 cm [30], ULE 48 cm [29] and ULE 48 cm improved [3], SCS 21 cm [3], SCS 6 cm [31], SCS 6 cm (crys) and SCS 21 cm (crys) [4, 5], and meta-mirrors prediction [39, 40]

method known as the three-cornered hat involves the recording of signals from three pairs of resonators [4, 80] as follows

$$\begin{aligned} \sigma^2_{AB}(\tau) &= \sigma^2_A(\tau) + \sigma^2_B(\tau) & & & S_{AB}(f) &= S_A(f) + S_B(f) \\ \sigma^2_{BC}(\tau) &= \sigma^2_B(\tau) + \sigma^2_C(\tau) & &\text{and} & S_{BC}(f) &= S_B(f) + S_C(f) \\ \sigma^2_{AC}(\tau) &= \sigma^2_A(\tau) + \sigma^2_C(\tau) & & & S_{AC}(f) &= S_A(f) + S_C(f) \end{aligned} \tag{2.35}$$

Thus, simple mathematics allows for the derivation of individual Allan variances

$$\sigma^2_A(f) = \frac{1}{2}\left[\sigma^2_{AB}(f) + \sigma^2_{AC}(f) - \sigma^2_{BC}(f)\right] \tag{2.36}$$

$$\sigma^2_B(f) = \frac{1}{2}\left[\sigma^2_{AB}(f) + \sigma^2_{BC}(f) - \sigma^2_{AC}(f)\right] \tag{2.37}$$

$$\sigma^2_C(f) = \frac{1}{2}\left[\sigma^2_{AC}(f) + \sigma^2_{BC}(f) - \sigma^2_{AB}(f)\right] \tag{2.38}$$

In general, the three-cornered hat method, depicted in Eq. 2.38, is not always applicable because apparatus noises are not necessarily uncorrelated. Therefore, the analysis must involve correlation factors. Different approaches to addressing the system's correlation issue are worth mentioning [81–83].

3. Ultra-stable cavity thermal noise limitations

Noises in optical interferometers can generally be divided into two categories. The first category includes inherent fundamental noises that limit optical readout related to the quantum nature of light and statistical thermal fluctuations. Efforts to overcome these challenges have involved quantum-enhanced methods (such as light-squeezed states [84]), laser beam shaping [85, 86] and sizing (part of this work), and the generation of higher-order Gaussian modes [87]. The second noise category comprises non-fundamental noises such as seismic vibrations, vacuum level fluctuations, temperature instability, PDH locking precision and residual amplitude modulation (RAM), the influence of parasitic etalons, etc. These can often be effectively mitigated through careful engineering and design of the apparatus, including isolation systems, optics, vacuum, and electronics [25, 27, 50, 88].

This chapter will mainly focus on fundamental limitations affecting cavity performance rather than on ambient and technical noises. Moreover, it will cover thermal noise theory, present the current techniques for calculating thermal noise, and address the challenges associated with the material constants values and their uncertainties. All these play an essential role in estimating the ultra-stable cavity performance. Therefore, understanding the above-mentioned factors is crucial in designing the optical resonators and enhancing their sensitivity.

3.1. Cavity components and their general properties

For an optical resonator to be ultra-stable, it must comprise the best materials in several aspects. Firstly, the material should possess rigidity to mitigate sensitivity to acceleration fluctuations, described by a specific stiffness, the ratio of Young's modulus E to the density ρ. The second essential property is insensitivity to temperature fluctuations, i.e., a small coefficient of thermal expansion (CTE) that influences length change due to any temperature fluctuation, which always exists in real-case experiments. In Fig. 3.1, I plot the most common materials used for ultra-stable cavities. The best materials for ultra-stable cavity construction are located in the upper left corner, where stiffness is high and CTE is low. Additionally, Fig. 3.1 shows typical materials used for the vacuum chamber and all other necessary components, such as the cavity support structure.

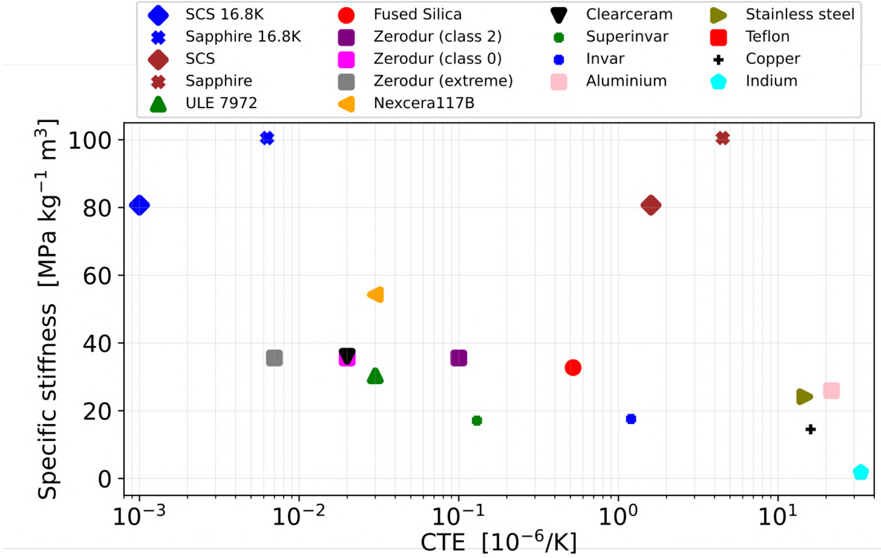

Figure 3.1: The graph shows the specific stiffness versus coefficient of thermal expansion (CTE) for commonly used materials in ultra-stable cavities and ultra-high vacuum conditions. A higher specific stiffness reduces susceptibility to external acceleration and lower Brownian thermal noise. Lower CTE results in easier temperature control and stability. The CTE values are provided at room temperature unless labelled differently, i.e. sapphire and SCS in 16.8 K.

In this work, a ULE spacer is used with a fused silica substrate and ULE compensation rings, Super Invar, and Teflon for the cavity support structure, a specific aluminium alloy for the vacuum chamber, and indium for the vacuum sealing as a gasket instead of a commonly used copper gaskets. Moreover, the best materials have a crystal (SCS and sapphire) or a glassy-ceramic-like structure (ULE, fused silica, Zerodur). Fig. 3.1 illustrates all values for room temperature, except for sapphire and SCS, which is presented at ∼17 K, where they exhibit an order of magnitude better CTE. Furthermore, as plotted in Fig. 3.2, the CTE decreases when approaching 0 K. Consequently, the coefficient of thermal expansion becomes flatter and smaller, and zero-crossing is not needed anymore. For example, SCS shows $\alpha_{SCS} = 4.6 \times 10^{-13}/\mathrm{K}$ at 1.6 K [44], while at 16.4 K, $\alpha_{SCS} = 9.2 \times 10^{-8}/\mathrm{K}$ [89] (see [90] for the current comparison of the SCS α measurements). In Fig. 3.2, we observe the evolution of the most commonly used materials for ultra-stable optical references. Not all exhibit zero-crossing far from 0 K, such as sapphire. In temperature stabilization, the zero-crossing point is crucial; however, the rate at which the CTE changes, represented by the function's slope, is also significant (bottom image in Fig. 3.2). This indicates how a slight shift in temperature will affect the CTE and the length change by that, e.g., SCS at its first zero-crossing at 124.2 K has a function two orders of magnitude steeper (more sensitive) than at its second zero-crossing at 16.8 K [44].

The imperfect temperature stabilization leads to fluctuations in the cavity length and, consequently, to frequency shifts. The fractional length change is

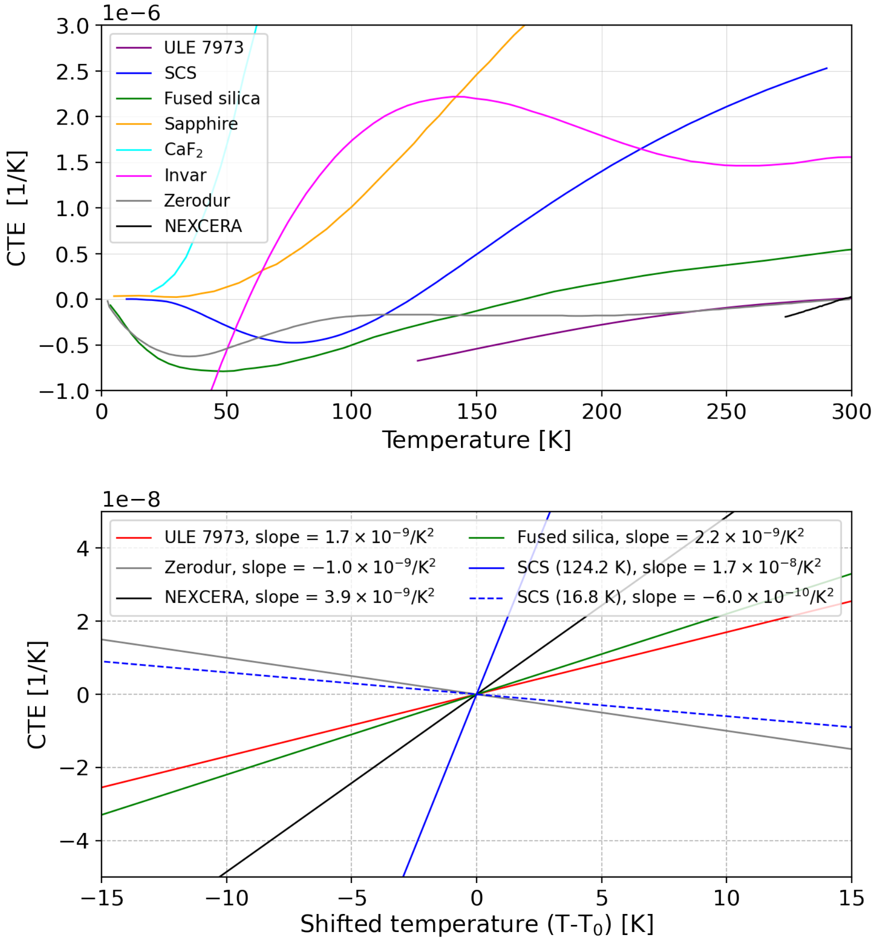

Figure 3.2: **(Top)** Coefficient of thermal expansion (CTE) in the function of temperature for the most common cavity materials: ULE 7973 [43] single-crystal silicon (SCS) [90], fused silica [91], sapphire [45], calcium fluoride (CaF_2) [45], invar [92], Zerodur [93, 94], Nexcera [95, 96]. **(Bottom)** Zoomed slope of the CTE for the shifted zero-crossing temperature $T-T_0$, except for the fused silica (FS) whose slope is shown in room temperature but it has $T_0 \sim 170$ K. ULE, Zerodur, Nexcera have T_0 in room temperature and SCS has it in 124.2 K and 16.8 K.

$$\frac{\Delta L}{L} = \alpha(T)\Delta T + \frac{1}{2}\alpha'(T)\Delta T^2 + \mathcal{O}(\Delta T^3), \tag{3.1}$$

where $\alpha'(T) = d\alpha(T)/dT$, and ΔT is a slight temperature fluctuation that may be caused by imprecision in temperature control. To understand the necessary degree of temperature stabilization, consider a scenario where the zero-crossing point, i.e where $\alpha(T = T_0) = 0$), and the slope for ULE is $\alpha'_{ULE}(T) = 1.7 \times 10^{-9}/\mathrm{K}^2$, according to Fig. 3.2. To achieve fractional frequency instability of 10^{-17}, the temperature must be stabilized to 0.1 mK.

3.2. Thermal noise theory

3.2.1. Introduction to the thermal noise theory and the cavity spacer thermal fluctuation

The values of physical parameters in a thermodynamic system at equilibrium do not possess an exact value. When existing in an environment with a non-zero temperature, the system exhibits statistical spontaneous fluctuations caused by the random movement of its molecules. It was first derived quantitatively by Einstein that mean square displacement $< x^2 >$ is related to the fundamental Boltzman constant k_b, temperature T, time t and the particle mobility in the fluid B by a formula $< x^2 >= 2k_bBTt$. Later on, a more general solution of a so-called Brownian motion was described using Newton's equations with a velocity-like dumping force $f\dot{x}$, and it is often referred to as the Langevin equation [97]:

$$m_{mol}\ddot{x} + \lambda\dot{x} = F_{Brownian} \ , \tag{3.2}$$

where m_{mol}, λ, $F_{Brownian}$ are the molecular mass, damping coefficient and Brownian random force, respectively. By applying Hooke's law to the Eq. 3.2, we obtain the complete expression for a driven dumped harmonic oscillator. The above-mentioned description is correct in the context of viscous regime systems when the drag force is non-negligible. In the actual experimental setup, the system operates under ultra-high vacuum (UHV) conditions, which makes the external velocity damping approach not suitable here. Therefore, the internal displacement damping, which is not velocity-proportional, is considered the only dissipative factor for a certain material.

According to Hooke's law, force F is proportional to the product of displacement x and the spring constant k. Nevertheless, this description is only applicable to a perfectly elastic material. In a real-case scenario, there is a non-zero phase delay $\phi(f)$ between the acting harmonic force F and the system response x:

$$F = -kx[1 + i\phi(f)] \ . \tag{3.3}$$

It means that in an anelastic body exhibiting phase shift, phase delay $\phi(f)$ corresponds to the energy dissipation. This is an aprroximation of the $F = -kx[1 + i\tan\phi(f)]$, under the ϕ <<1 condition, where $\tan\phi \approx \phi$. We will consider only materials where the highest ϕ is on the order of 10^{-4}. Therefore, we obtain a harmonic oscillator equation with the general Hookes law (Eq. 3.3) internal dumping

$$m\ddot{x} + kx(1 + i\phi(f)) = F \ . \tag{3.4}$$

where m is the mass of an oscillator. The $\phi(f)$, known as "mechanical loss angle" or just "loss angle" is reciprocally used with the quality factor $Q(f)$. By definition, Q-factor denotes how much of the energy stored in an oscillator E_{stored} is lost/dissipated during one full oscillatory cycle E_{diss} :

$$Q(f) = \frac{1}{\phi(f)} = 2\pi \frac{E_{stored}}{E_{diss}}. \tag{3.5}$$

An additional theorem will be introduced to provide a full description of the thermal influence on length measurement. So-called Fluctuation-Dissipation Theorem [98, 99] shows the relation between measured length fluctuation represented by power spectral density $S_x(f)$ and the dissipation represented by the right-hand side of the following equation:

$$S_x(f) = \frac{4k_BT}{(2\pi f)^2} Re[Y(f)], \tag{3.6}$$

where Re$[Y(f)]$ indicates the real part of the admittance, which describes the velocity response v to the force F applied on a body. It is often referred to as a conductance $G(f) = Re[Y(f)] \equiv v(f)/F(f)$. For a better intuitive understanding of Eq. 3.6, one may consider an oscillating force $F\cos(2\pi ft)$ acting on the oscillator with resonance frequency f_0. For the $f < f_0$ displacement x is in phase with force F and shifted by $\pi/2$ (in quadrature) with velocity v. In the case of $f > f_0$, displacement is in antiphase force (so-called antiresonance), and the velocity is in quadrature. In both of these cases $Re[Y(f)] = 0$, which implies that dissipative process is the only solution to have a non-zero conductance.

Solving the Eq. 3.4 and switching from time domain to the Fourier domain i.e. substitute $x(t)$ into the $x(\omega)e^{iwt}$ and $\dot{x} = i\omega x$ we have

$$F(\omega) = i\omega m\dot{x} + k\dot{x}\Big(\frac{1}{i\omega} + \frac{\phi}{\omega}\Big) . \tag{3.7}$$

Therefore, the admittance is equal

$$Y(\omega) = \frac{k\omega\phi + i\omega(m\omega^2 + k)}{\phi^2k^2 + (k - m\omega^2)^2} . \tag{3.8}$$

Taking the real part from Eq. 3.8 and putting it into Eq. 3.6 we receive [97]

$$S_x(\omega) = \frac{4k_BT}{\omega^2} \frac{k\omega\phi}{\phi^2k^2 + (k - m\omega^2)^2} , \tag{3.9}$$

and by substituting $k = \omega_0^2 m$ and $\omega = 2\pi f$, we receive the final formula for the thermal noise of a solid body with mass m (such as cavity's spacer), loss angle $\phi(f)$ and resonance frequency f_0:

$$S_x(f) = \frac{4k_BT}{(2\pi)^2} \frac{\phi(f)}{m} \frac{f_0^2}{f} \frac{1}{\phi(f)^2f^4 + (f_0^2 - f^2)^2} . \tag{3.10}$$

In general, any system with continuous mass distribution possesses more than one characteristic frequency, namely $f_1, f_2, f_3, ...$, known as overtones. Nevertheless, for our application, we will use only fundamental mode f_0. A simple analytical approximation presents the position of the n_r-th resonance

$$f_n = \frac{1}{2L}\sqrt{\frac{E}{\rho}}(n_r + 1), \tag{3.11}$$

where L, E, and ρ are spacer length, Young modulus and density, respectively. By using the formula for the resonance with $n_r = 0$ and the formula for the Brownian noise (Eq. 3.10) with the constants provided in Tab. 3.1, we obtain Figure 3.3 (bottom).

Table 3.1: Spacer material constants, such as Young modulus E, density ρ, Poisson's coefficient σ, and the loss angle ϕ used for the calculations of the spacer Brownian thermal noise.

Material	E [Gpa]	ρ [kg/m^3]	σ	ϕ [10^{-8}]
Zerodur [42, 100]	90.3	2530	0.24	3.2×10^4 (293 K)
ULE [43, 100]	67.6	2210	0.17	1.6×10^3 (293 K)
Sapphire [101, 102]	400	3980	0.29	20 (293 K) / 0.4 (4 K)
SCS (111) [103, 104]	188	2329	0.26	1 (124 K) / 0.2 (4 K)

Apart from the general representation of thermal noise by the Eq. 3.10, it is worth considering three characteristic frequency ranges. First and most commonly use is low frequency approximation ($f << f_0$), which shows a distinctive $1/f$ behaviour in the PSD plot (top of Fig.3.3):

$$S_x(f) = \frac{4k_BT}{2\pi}\frac{\phi}{fk} \ . \tag{3.12}$$

Taking a linear elastic bahaviour with Hooke's law $F = kL$ and the definition of Young modulus E we obtain $E = kL/[\pi(R^2 - r^2)]$, where $\pi(R^2 - r^2)$ is the spacer crosssection area [38, 105]:

$$S_x(f) = \frac{2k_BT}{\pi^2 f}\frac{\phi}{E}\frac{L}{(R^2 - r^2)}, \tag{3.13}$$

The maximum values of the thermal fluctuations are achieved at the resonance frequency $f = f_0$:

$$S_{x,res}(f) = \frac{4k_BT}{(2\pi^3)^3}\frac{1}{m\phi}\frac{1}{f_0^3}, \tag{3.14}$$

Above the resonance frequency we observe fast f^{-5} decline in the noise (Fig. 3.3):

$$S_x(f) = \frac{4k_BT}{(2\pi)^3}\frac{\phi(f)}{m}\frac{1}{f^5}, \tag{3.15}$$

According to Eq., 3.6, thermal noise reduction is achievable by adjusting and controlling external parameters, such as ambient temperature, and the internal material properties, including mass m, and most importantly, the loss angle ϕ. Numerous studies were performed to discover materials with improved internal properties, particularly concerning the loss angle [38, 39, 41].

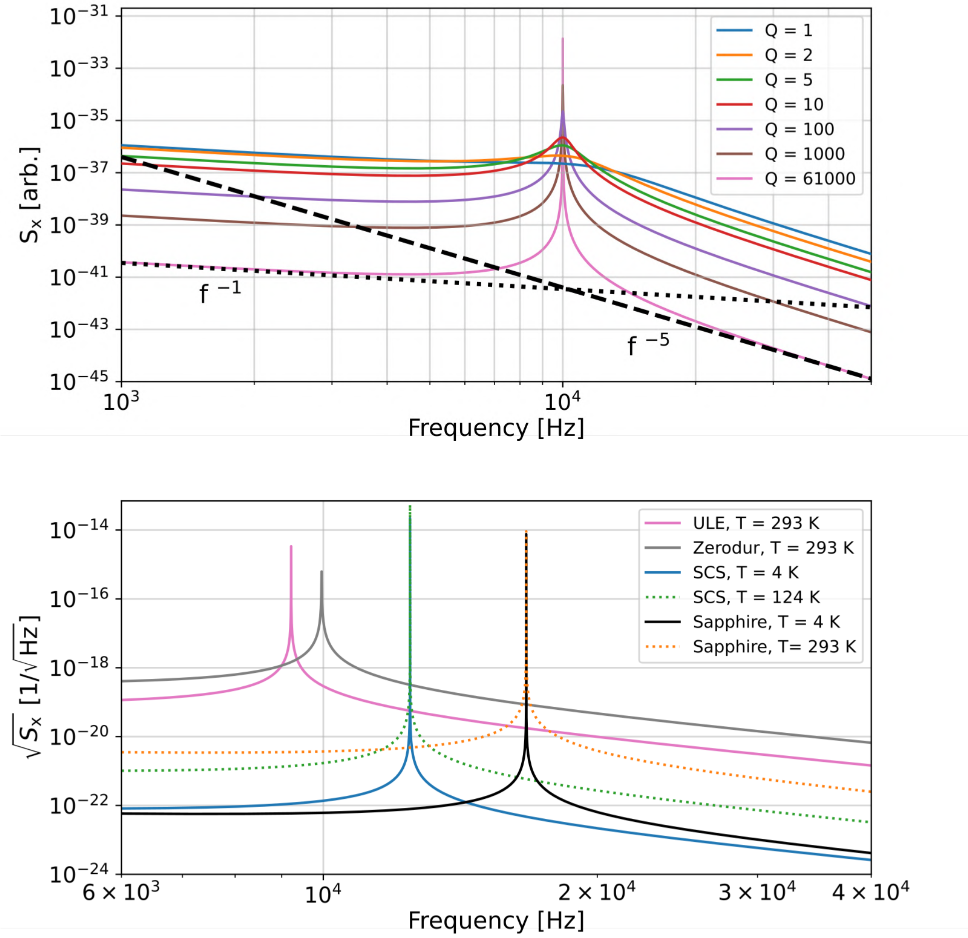

Figure 3.3: **(Top)** Power spectral density $S_x(f)$ of the Brownian thermal noise for spacers with the same resonance frequency, different quality factors Q, along with the fitted f^{-1} (below resonance) and f^{-5} (above resonance) curve. The value $Q = 6.1 \times 10^4$ corresponds to the quality factor of a ULE. **(Bottom)** Fractional amplitude spectral density $\sqrt{S_x(f)}$ for the 30 cm long spacer for commonly used materials and temperatures.

At first, FDT description may seem contradictory with the equipartition theorem, which states that each degree of freedom contains $1/2k_bT$ of energy. Taking an ideal spring with the energy $1/2kx^2$, we have the root mean square (RMS) of a displacement x as

$$x_{RMS} = \sqrt{\frac{k_B T}{k}} = \sqrt{\frac{k_B T}{4\pi^2 f_0 m}}. \tag{3.16}$$

Therefore, for the 30 cm long ULE spacer residing in a room temperature T=293 K, with $f_0 = 9218$ Hz and $m = 5.5$ kg we get $x_{RMS} \sim 2 \times 10^{-15}$ m. According to Eq. 2.29 x_{RMS} is the integral of PSD signal over the chosen spectra. Therefore, by reducing the loss angle, more energy is effectively stored in the resonance peak, and less is distributed in the rest of the signal. The effect is clearly observed in the top of Fig. 3.3), where different values of the quality factor $(1/\phi)$ for the same resonance frequency are plotted. An area under each curve is the same and equal x^2_{RMS}.

Two important components remain to complete the total Brownian thermal noise description of the cavity: substrates and reflective coatings. Unlike the spacer, which we can treat as a spring with single constant k, where all forces and dissipations are distributed homogenously, mirrors made of substrates and coatings need to be treated in a different manner [106–112].

3.2.2. Brownian noise of the substrates and reflective coatings

Ultra-stable cavity mirrors are typically composed of multilayer coatings on a substrate [3, 31, 38]. However, a recently developed promising solution involves the use of so-called "meta-mirrors", which reduce thermal noise by at least an order of magnitude compared to Bragg coatings. Unfortunately, "meta-mirrors" have still insufficiently low finesse ($\mathcal{F} = 12000$ at max) for ultra-stable laser applications [39, 41].

All cavity components are optically contacted, forming a rigid body. This is in contrast to gravitational wave detectors, that use mirrors suspended on wires, allowing for a "free-falling" configuration [113]. By removing the spacer, we effectively obtain a Fabry-Pérot cavity similar to one of the LIGO interferometer arms. As a result, the Brownian thermal noise theory which will be applied here was primarily developed for the purpose of gravitational wave detection [97, 107, 109, 114].

To calculate thermal noises, I will use the so-called Levin's direct approach, which was developed by studying the mirror's amplitude response to oscillatory Gaussian-distributed varying pressure $p(\vec{r}, t)$ [109, 110]

$$p(\vec{r}, t) = F(t)f(\vec{r}) = F_0 \cos(2\pi f t)\frac{1}{\pi r^2}e^{-r^2/w^2}, \tag{3.17}$$

where w is beam spot radius on the mirror. The thermal noise for the time-averaged dissipated power W_{diss} under an oscillating force with amplitude F_0 is given by [109]

$$S_x(f) = \frac{2k_bT}{(\pi f)^2}\frac{W_{diss}}{F_0^2}. \tag{3.18}$$

Moreover, a useful relationship can be introduced as $W_{diss} = 2\pi f \phi U_0$, where U_0 represents the maximum elastic energy resulting from material deformation induced by the pressure $p(\vec{r}, t)$, as depicted in Eq. 3.17. The value of U_0 could be determined using either analytical expressions or, if necessary, numerically through finite-element analysis.

Skipping precise derivations and focusing on the final Brownian thermal noise formula for the substrate (sb), we obtain PSD for the half-infinite approximation i.e. when the mirror's diameter R and thickness h is much greater than beam radius w [109, 110] :

$$S_{x,sb}(f) = \frac{4k_bT}{f}\frac{1-\sigma_{sb}^2}{2\pi^{3/2}}\frac{\phi_{sb}}{E_{sb}}\frac{1}{w}, \tag{3.19}$$

where σ_{sb} indicates the Poisson's ratio.

Apart from the substrates, the second and the most dominant component of the mirror's thermal noise for ultra-stable cavities [31], as well as for LIGO-like interferometers [115], is μm layer of reflective coatings (ct). The thermal fluctuation PSD for the coatings was evaluated using different approaches ([109] and [108, 111, 112]). In this analysis, the thin layer of coating is treated as a structure with the same elastic properties as bulk substrate but with a different dissipation due to the distinction in loss angle value ($\phi_{ct} \neq \phi_{sb}$). The final formula is as follows:

$$S_{x,ct}(f) = \frac{4k_BT}{\pi^2 f}\frac{\phi_{ct}}{E_{sb}}\frac{d_{ct}}{w^2}(1+\sigma_{sb})(1-2\sigma_{sb}). \tag{3.20}$$

where d_{ct} is the coatings' thickness.

Further studies show the results for a more realistic scenario involving different coatings and substrates with differing elastic properties, such as Young's modulus E and Poisson's ratio σ. Assuming the isotropic loss angle value ($\phi_\perp = \phi_\parallel$) [114], we obtain the following:

$$S_{x,ct}(f) = \frac{4k_BT}{\pi^2 f}\frac{\phi_{ct}}{E_{sb}}\frac{d_{ct}}{w^2}\frac{E_{ct}^2(1+\sigma_{sb})^2(1-2\sigma_{sb}^2)+E_{sb}^2(1+\sigma_{ct})^2(1-2\sigma_{ct}^2)}{2E_{sb}E_{ct}(1-\sigma_{ct}^2)(1-\sigma_{sb}^2)}. \tag{3.21}$$

The numerical value of the PSD in Eq. 3.20 (equal elastic properties) is overestimated when compared to equation 3.21 (different elastic properties) by 3% and 8% for fused-silica (FS) substrates with dielectric coatings and crystalline coatings, respectively. Material constant from Tab. 3.2 were used for the calculation. Alternating layers of the silicon dioxide (SiO_2) and tantalum pentoxide (Ta_2O_5), commonly referred to as dielectric SiO_2/Ta_2O_5, along with gallium arsenide (GaAs) and aluminium-alloyed gallium arsenide ($Al_{0.92}Ga_{0.08}As$), commonly referred to as crystalline AlGaAs/GaAs, are two the best and most widely used coating materials [36, 38, 116].

Studies show that the material parameters, such as the loss angle and Young's modulus, can vary from sample to sample [36]. These variations depend on the material itself, its size, manufacturing technique, structural irregularities, impurities etc. Despite the known range of loss angle and Young modulus values, the most definitive way to quantify it is to measure each sample individually (see discussion in Chapter 3.2.5).

Adjusting external (environmental) or internal cavity setup parameters can reduce the mirror's thermal noise. Therefore, finding materials with higher Young's modulus E, lower loss angle ϕ, and appropriate Poisson's ratio is desirable, but we do not have control

Table 3.2: The substrates and coatings material constant i.e. loss angle ϕ, Young modulus E and Poisson ratio σ. All of the values were taken for a room temperature (293 K), except for the loss angle for SCS (100) substrates (124 K). FS loss angle is presented for the two extreme values [100, 117]. Indeces diel. and crys. refers to the SiO_2/Ta_2O_5 and $GaAs/Al_{0.92}Ga_{0.08}As$ coating materials, respectively.

Parameter	Value
ϕ_{ct} (diel.[100]/ crys.[38])	4×10^{-4} / 2.5×10^{-5}
ϕ_{sb} (FS [100, 117, 118] / SCS [104])	$(1 - 0.1) \times 10^{-6}$/ 1×10^{-8}
E_{ct} (diel. [36] / crys.[119])	91 GPa / 100 GPa
E_{sb} (FS [120] / SCS [103])	73 GPa / 188 GPa
σ_{ct} (diel [36]/ crys [119])	0.20 / 0.32
σ_{sb} (FS [120] / SCS [103])	0.16 / 0.28

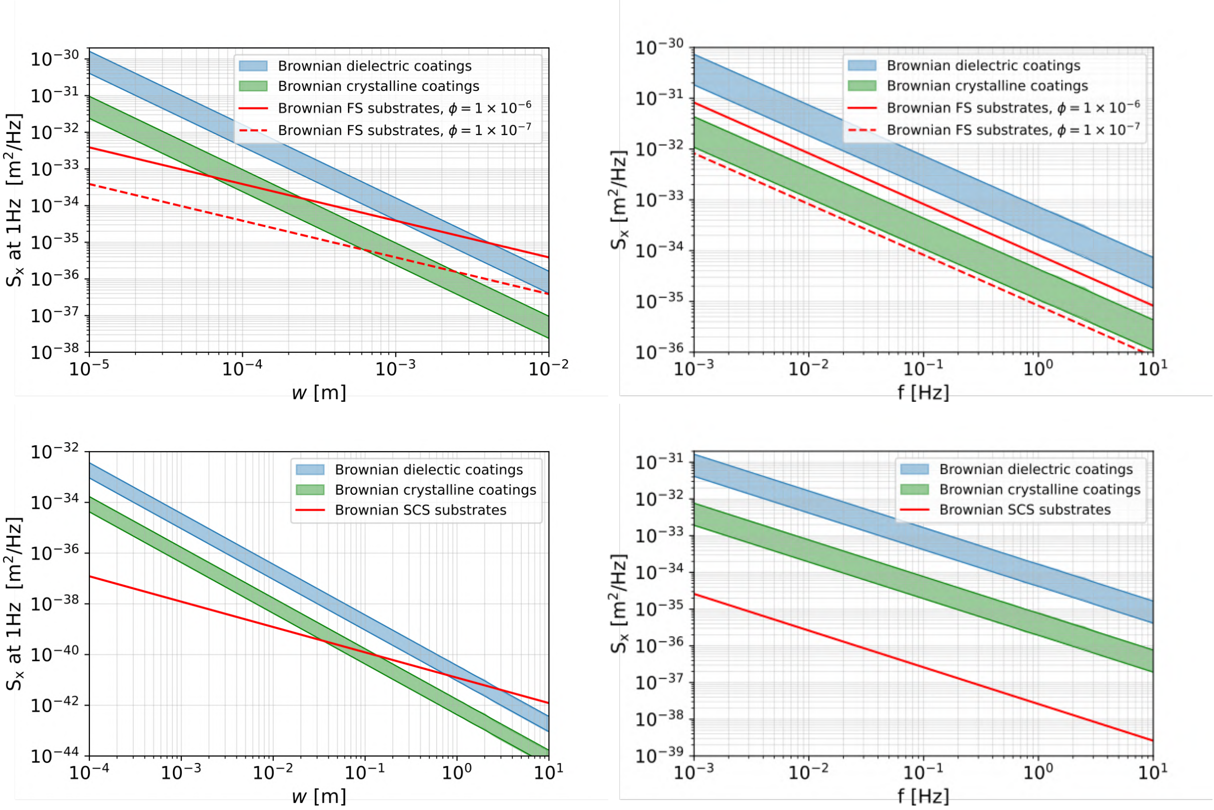

Figure 3.4: **(Top)** PSD (S_x) of the Brownian thermal noise in the function of beam spot radius on the mirror w (left) and frequency for a given $w = 470$ μm (right) for the crystalline and dielectric coatings with typical thickness $d_{ct} \in [3; 12]$ μm, and the fused-silica substrates in 293 K, for two loss angle values. **(Bottom)** The same studies are shown for SCS substrates in 124 K for loss angle value presented in Tab. 3.2.

over this. Alternatively, what is doable but challenging is reducing the thermal noise by employing a cryostat (minimizing temperature T) or increasing the beam spot radius w

by controlling the cavity length and the mirror's radius of curvature (ROC). Generally, the larger the spot size is, the smaller the noise is. From Eq. 3.19 and 3.20, different sensitivities to spot size appear, where $S_{x,sb} \sim 1/w$ and $S_{x,sb} \sim 1/w^2$. These differences can be intuitively described by the coatings' closeness to the fluctuating surface, resulting in a larger effect and surface damping in contrary to bulk dumping in substrate [109]. However, increasing the spot size remains effective up to a certain value. Fig. 3.4 illustrates $S_x(f = 1$ Hz) for two commonly used substrate materials (FS in 293 K and SCS in 124 K) and coatings (dielectric and crystalline) as a function of spot size. Furthermore, it is observed that for $w = 470$ μm, which is a spot size on the flat mirror for 30 cm long spacer with plano-concave configuration with ROC = 1 m, room temperature FS substrates dominate as the source of noise for the 12 μm thick crystalline coatings, for the substrates loss angle $\phi_{sb} = 1 \times 10^{-6}$ [100].

3.2.3. Thermoelastic substrate noise

Statistical fluctuations of a volume V (volume fluctuation variance $< (\Delta V)^2 > \sim T$ [121]) and corresponding mechanical losses are responsible for the Brownian fluctuations, described in Chapter 3.2.1 and 3.2.2. Nevertheless, it does not cover the whole picture of the thermal noise budget. From thermodynamic principles, we know that the total variance of temperature fluctuations within a volume V can be described by the following formula [121, 122]:

$$< \delta T^2 > = \frac{k_B T^2}{\rho C V}, \tag{3.22}$$

where k_B, ρ, and C correspond to Boltzmann constant, material density and heat capacity, respectively.

In an ideal theoretical situation, temperature and volume fluctuations are uncorrelated $< \delta T \delta V > = 0$. Therefore, any temperature variations should not influence the length change. However, in real case scenarios, the coefficient of thermal expansion CTE for cavity purposes is often small ($< 10^{-6}$/K, see Fig. 3.1) but non-negligible

$$\alpha \equiv \frac{1}{L}\frac{\partial L}{\partial T}. \tag{3.23}$$

With this relation, any temperature fluctuations are coupled to the length variations and create so-called thermoelastic noise, which, together with the Brownian noises, fundamentally limits the cavity's performance [122]. Inhomogenous temperature distribution creates gradients which induce heat flow and increase the entropy S. All of this leads to thermal dissipation processes, often named thermoelastic damping:

$$W_{diss} = \left\langle T\frac{dS}{dt} \right\rangle = \left\langle \int \frac{\kappa}{T} (\nabla \delta T)^2 d^3 r \right\rangle. \tag{3.24}$$

where κ is thermal conductivity.

Again, by using the FDT and deriving the exact formula for W_{diss}, the final equation for substrate thermoelastic noise is presented in [123]

$$S^{TE}_{x,sb}(f) = \frac{4k_B T^2}{\sqrt{\pi}} \frac{\alpha^2_{sb}(1+\sigma_{sb})^2 w}{\kappa_{sb}} J(f/f_T), \tag{3.25}$$

$$J(f/f_T) = \left(\frac{2}{\pi^3}\right)^{1/2} \int_0^\infty du \int_{-\infty}^{\infty} dv \frac{u^3 e^{-u^2/2}}{(u^2+v^2)[(u^2+v^2)^2 + (f/f_T)^2]}, \tag{3.26}$$

$$f_T = \frac{\kappa_{sb}}{\pi C_{sb} w^2}, \tag{3.27}$$

where κ_{sb} and C_{sb} are the substrate's thermal conductivity and heat capacity, respectively. Eq. 3.26 has two boundary solutions. The first, for the $f/f_T << 1$

$$J(f/f_T) = \frac{2}{3\sqrt{\pi f/f_T}}, \tag{3.28}$$

and the second for the $f/f_T >> 1$, which is often called the adiabatic limit:

$$J(f/f_T) = \frac{1}{(f/f_T)^2}. \tag{3.29}$$

Boundary limits for high ($f/f_T \gg 1$) and low ($f/f_T \ll 1$) frequency ratios, as derived from the full formula (Eq. 3.26), are depicted in the left panel of Fig. 3.5. The right panel of Fig. 3.5 illustrates the thermoelastic noise of FS and ULE substrates with 1 m and 10.2 m ROCs, respectively. Generally, the contribution of thermoelastic noise from substrates is highly dependent on the coefficient of thermal expansion, denoted as $S^{TE}_x \sim \alpha^2$. Therefore, thermoelastic noise from ULE substrates is significantly lower than from FS substrates (as shown in the right panel of Fig. 3.5). Nevertheless, FS substrates are used due to their mechanical loss properties, which are at least an order of magnitude better than ULE.

The same temperature fluctuations are the source of another noise associated with temperature dependence on the refractive coefficient n, defined as the coefficient of thermorefraction (CTR), $\beta = \frac{\partial n}{\partial T}$. Fluctuation of CTR leads to additional light phase fluctuations within the coatings and substrates. While this effect is negligible for substrates where light passes through only once, it becomes significant for coatings where both thermorefractive and thermoelastic noise must be considered [109, 124]. However, these types of noise, collectively called thermo-optic noise, can be treated coherently [125–127] and can be suppressed through careful coatings design and coherent cancellation of these effects [116]. The final formula for coatings thermo-optic noise is [116, 127]

$$S^{TO}_{x,ct}(f) = S_T \Gamma_{tc} \Big(\alpha_{ct} d_{ct} - \beta_{ct}\lambda - \alpha_{sb} d_{ct} C_{ct}/C_{sb}\Big)^2, \tag{3.30}$$

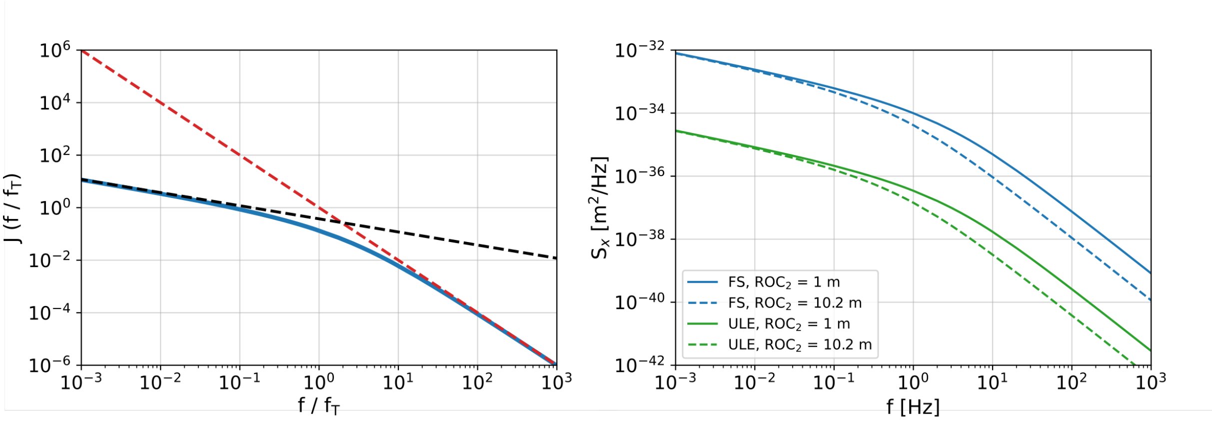

Figure 3.5: **(Left)** Frequency f/f_T dependence of the substrates thermoelastic noise represented by three possible scenarios: full formula $J(f/f_T)$ in Eq. 3.26 (solid blue line), black dashed line scenario where $f/f_T << 1$ (Eq. 3.28) and red dashed line for $f/f_T >> 1$, so-called an adiabatic limit (Eq. 3.29). **(Right)** Substrates thermoelastic noise frequency dependence for ULE and FS substrates at 293 K presented with a plano-concave configuration with two possible curvatures for the second mirror, denoted as ROC_2. The spacer length is set to 0.3 m.

where Γ_{tc} is the thick coatings correction [127], α_{ct} and α_{sb} coatings and substrate CTE, d_{ct} is coating total thickness, β_{ct} is coatings CTR, λ is the laser wavelength, C_{ct} and C_{sb} are the coatings and substrates heat capacities. S_T is defined as

$$S_T(f) = \frac{2\sqrt{2}k_B T^2}{\pi \kappa_{sb} w} M(f/f_T), \tag{3.31}$$

where

$$M(f/f_T) = \int_0^\infty du \, \mathrm{Re}\left[\frac{u e^{-u^2/2}}{(u^2 - i f/f_T)^{1/2}}\right]. \tag{3.32}$$

For the $f/f_T << 1$

$$M(f/f_T) = \sqrt{\frac{\pi}{2}}, \tag{3.33}$$

and for the $f/f_T >> 1$ (adiabatic limit) :

$$M(f/f_T) = \frac{1}{\sqrt{2f/f_T}}. \tag{3.34}$$

Fig. 3.6 (left panel) illustrates the low frequency and high, i.e. adiabatic approximations compared to the exact formula in Eq. 3.32. The right panel shows the PSD of the thermo-optic coatings noises for FS substrates and crystalline coatings with two different radii of curvature (ROCs). Nevertheless, as presented in [116], coherent reduction of this noise is possible within a chosen frequency range. It is also important to note that both coatings' thermo-optic and substrates' thermoelastic noises depend on temperature as T^2, and the Brownian noise as T. Therefore, while coatings' thermo-optic noise

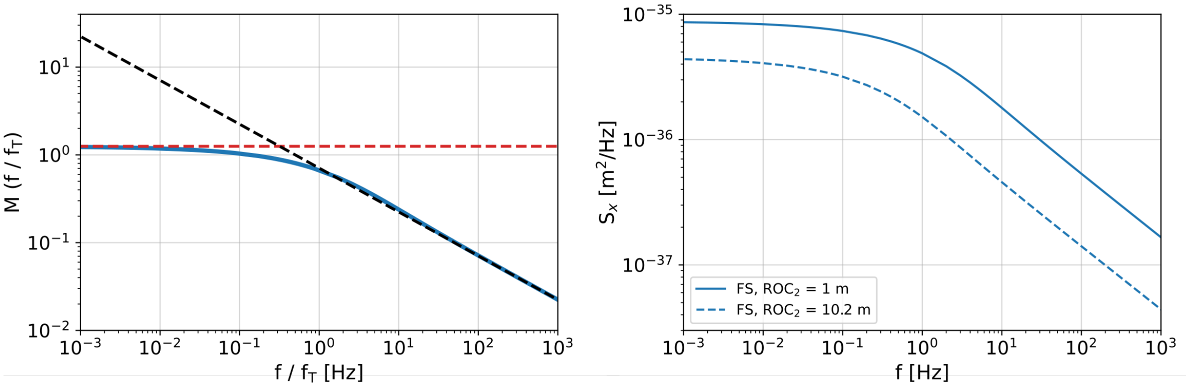

Figure 3.6: **(Left)** Frequency f/f_T dependence of the coatings thermo-optic noise represented by three possible scenarios: full formula $M(f/f_T)$ in Eq. 3.32 (solid blue line), black dashed line scenario where $f/f_T << 1$ (Eq. 3.33) and red dashed line for $f/f_T >> 1$, so-called an adiabatic limit (Eq. 3.34). **(Right)** Crystalline coatings thermo-optic noise frequency dependence for FS substrates at 293 K presented with a plano-concave configuration with two possible curvatures for the second mirror, denoted as ROC$_2$. The spacer length is set to 0.3 m.

and substrates' thermoelastic noise are issues at room temperature, they are significantly mitigated in cryogenic conditions.

3.2.4. Thermal noise floor for the room-temperature cavities

Overall cavity performance is calculated as a sum of the PSDs of cavity components. In this work, noises such as spacer thermoelastic [116, 128] or photothermal (coatings and substrates noise induced by the laser beam heating effect) [129] are ignored because of their negligible influence on the thermal noise budget. An overview of the cavity of these noises is given in [126]. Therefore, the final thermal noise of the cavity is given by

$$S_x(f) = S^{Br}_{x,sp}(f) + 2S^{Br}_{x,sb}(f) + 2S^{Br}_{x,ct}(f) + 2S^{TE}_{x,sb}(f) + 2S^{TO}_{x,ct}(f). \tag{3.35}$$

Fig. 3.7 and 3.8 shows the performance of the ULE spacer 30 cm long, with FS substrates and crystalline coatings. Furthermore, Fig. 3.7 shows the difference in plano-concave mirror configuration between the ROC = 1 m and ROC = 10.2 m. Coatings' thermo-optic noise is calculated without structural optimization, which would reduce the influence of noise within the chosen frequency range [116]. For a 30 cm long cavity designed in this work, thermoelastic noise will be the dominant noise from 0.1 Hz to 1 Hz. At higher frequencies, coatings' thermo-optic noise will be the predominant noise due to the lack of coherent noise cancellation in this design. Therefore, unlike typical situations where the thermal noise floor is mainly limited by Brownian noise from coatings, thermo-optic noises from substrates and coatings dominate.

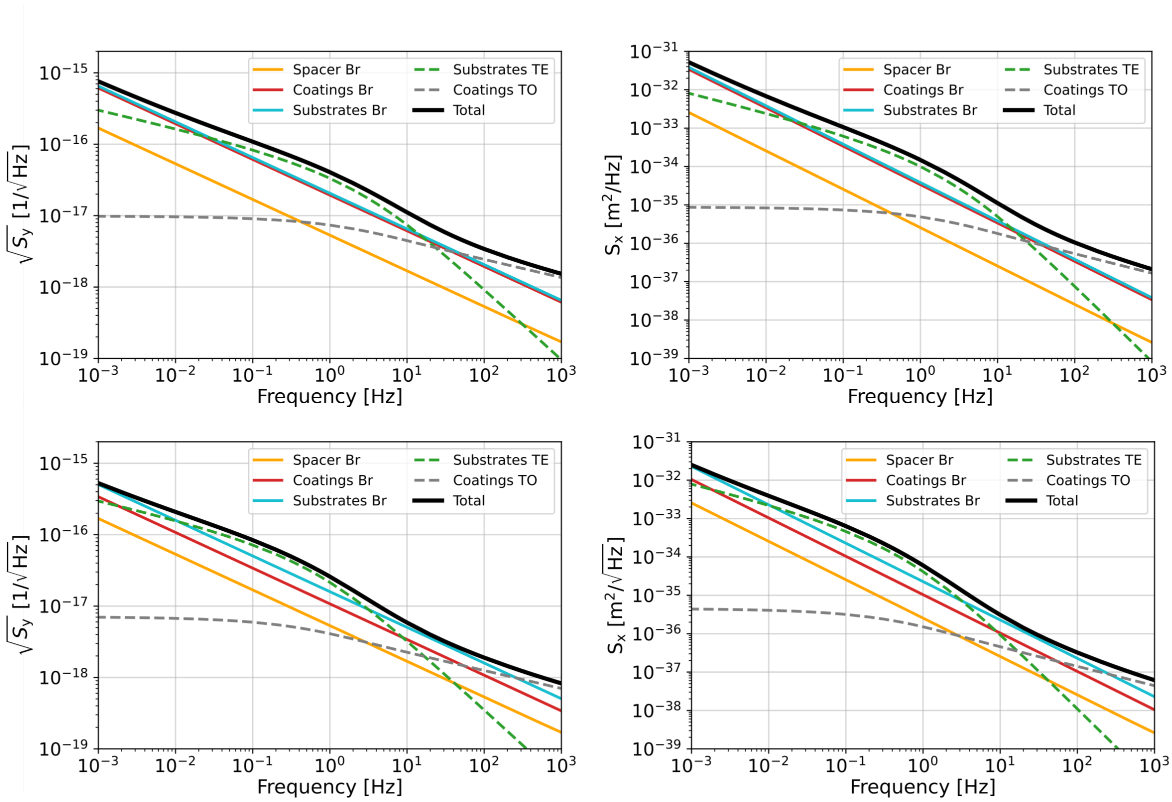

Figure 3.7: **(Top)** Fractional amplitude spectral density $\sqrt{S_y(f)}$ (Left) and power spectral density $S_x(f)$ of the Brownian, thermoelastic and thermo-optic noises of the cavity components. The cavity spacer is 30 cm long ULE, and the substrates and coatings are FS and crystalline, respectively. Mirrors plano-concave configuration with ROC $= 1$ m. **(Bottom)** The same as in top figures but with ROC $= 10.2$ m.

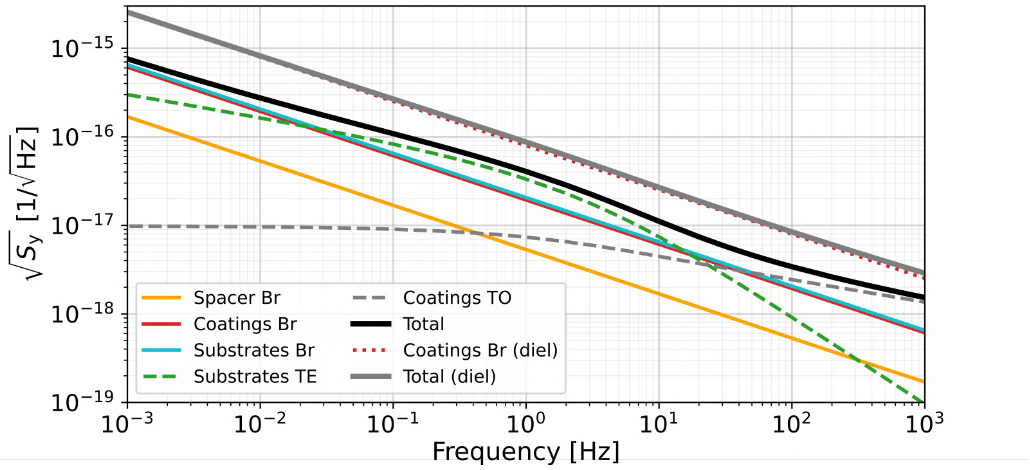

Figure 3.8: Fractional amplitude spectral density $\sqrt{S_y(f)}$ for the cavity designed in this work (black line), i.e. 30 cm long ULE, plano-concave mirrors configuration (ROC = 1 m) with crystalline coatings. For the comparison, Brownian noise from dielectric coatings and the total noise of the cavity with dielectric coatings are shown (grey line).

3.2.5. Loss angle temperature and frequency dependence

Loss angle, along with Young's modulus, are two fundamental internal parameters in the thermal noise budget for state-of-the-art cavity experiments. Therefore, much effort is put into finding material with the best thermo-mechanical and thermo-elastic properties [34, 36, 38, 39]. Due to the temperature dependence of thermal noise, where $S_x^{Br} \sim T$ and $S_x^{TE} \sim T^2$, cavity operating temperatures are often reduced using cryostats, even down to the single kelvins (sapphire [8] and SCS [30]).

Fig. 3.9 (top) illustrates the temperature dependence of the loss angle for commonly used Fabry-Pérot cavity materials. As we see, the temperature decrease is not always helpful, as in the case of FS, where ϕ increases as T decreases. Generally, when lowering the temperature, materials such as sapphire or single-crystal silicon (SCS) exhibit a significant reduction in mechanical loss. Moreover, the loss angle for thin structures, such as coatings, is much larger than for bulk materials like substrates and spacers. In Fig. 3.9, the loss angle for coatings is at least three orders of magnitude higher than that for substrates and spacer materials. Furthermore, accurately simulating and predicting the loss angle is challenging, and measurement remains the definitive method for checking the loss angle value.

The reported values for dielectric multilayer coatings vary and depend on factors such as material composition, doping, and heat treatment (annealing) processes. The loss angles for unannealed silica is $(0.5 \pm 0.3) \times 10^{-4}$, and for tantala, $(4.4 \pm 0.2) \times 10^{-4}$, with the final loss angle for the multilayer coating at approximately 2.7×10^{-4} at room temperature [33]. Tantala, the dominant component, often has its loss angle reduced to

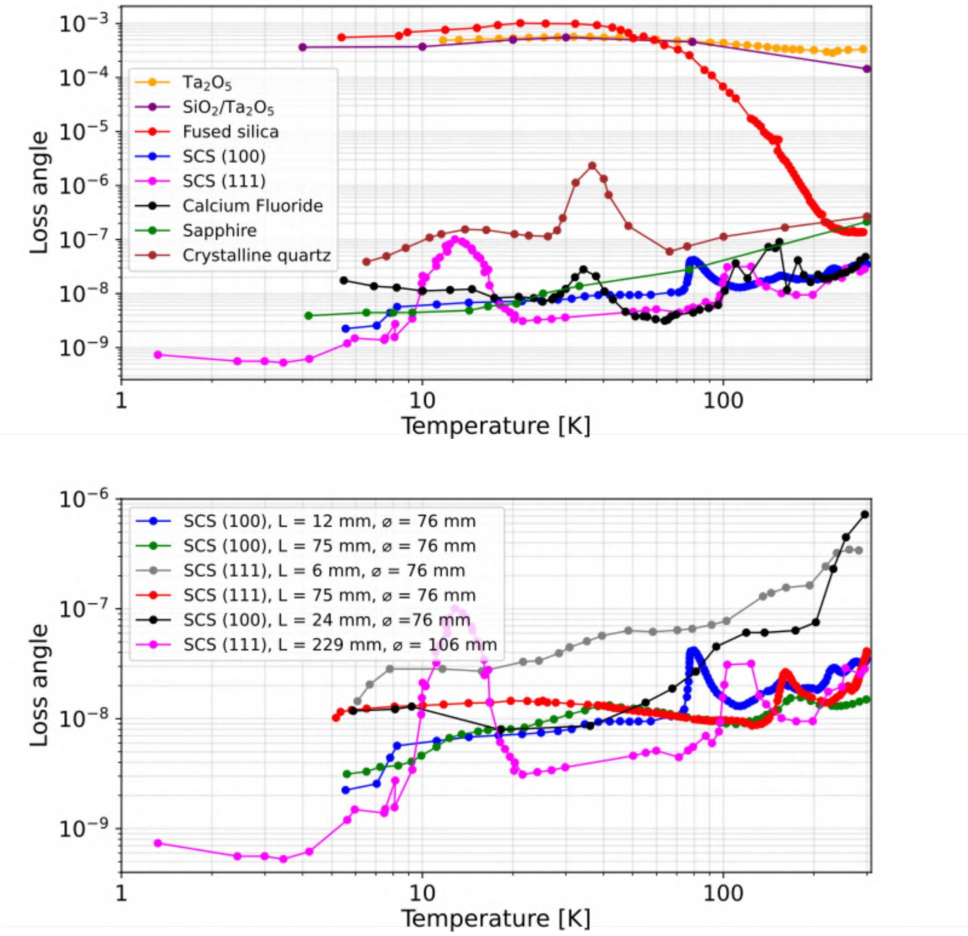

Figure 3.9: **(Top)** Loss angle vs temperature for the most common dielectric coatings materials Ta_2O_5 (1 kHz, 0.5 μm thickness) [34], multilayer SiO_2/Ta_2O_5 (1.1 kHz, 4.8 μm thickness) [130]), as well as substate and spacer materials, such as fused silica (17,2 kHz, 76.2 mm in diameter and 12 mm thick) [117], SCS (100) (SCS, 14.9 kHz, 76.2 mm diameter and a thickness of 12 mm. (100)) [104], SCS (111) (diameter 10.6 cm, length 22.9 cm, mass 4.9 kg (111), 19.5 kHz) [131], Calcium Fluoride CaF_2 (17,2 kHz, 76.2 mm in diameter and 12 mm thick, f = 41302 Hz, (100)) [132], sapphire (68 kHz, sapphire cylinder of 100 mm in diameter and 60 mm in length [102], crystalline quartz (substrates/disc diameter 76 mm thickness 24 mm, 19,4 do 19.8 kHz) [133]. **(Bottom)** Loss angle vs temperature for different samples of single-crystal silicon for two crystal axes [104, 131, 133].

2×10^{-4} at 292 K through doping with titanium oxide (TiO_2) and annealing [34, 35]. Moreover, there may be frequency and thermal dependencies in the loss angles. However, measurements show very little frequency f dependence for silica, $(1.0 \pm 0.2) \times 10^{-4} + f(1.1 \pm 0.5) \times 10^{-9}$, and for tantala, $(3.8 \pm 0.2) \times 10^{-4} + f(1.8 \pm 0.5) \times 10^{-9}$ in the 2-6 kHz and 10-72 kHz frequency ranges, respectively [36]. Since coatings are a significant factor in the cavity's thermal noise budget, indirect measurements of the loss angle were conducted by evaluating the overall noise budget in cavities within the mHz-Hz range. Data from cavities residing at 124 K, 16 K, and 4 K demonstrate the loss angle for dielectric coatings SiO_2/Ta_2O_5 as $(5.6 \pm 0.9) \times 10^{-4} \times f^{-0.05\pm0.01}$, $(3.2 \pm 0.3) \times 10^{-4} \times f^{-0.11\pm0.02}$, $(2.4 \pm 0.3) \times 10^{-4} \times f^{0.06\pm0.02}$, respectively [31]. All mentioned measurements indicate a very weak frequency and temperature dependence of the loss angle for thin coating layers.

3.2.6. Other source of noises and limitation

Any measurement system that relies on optical laser readout is subject to the fundamental quantum limitation known as the standard quantum limit (SQL). The inherently quantum nature of photons leads to fluctuations in their apparent number, N, which follows a Poisson distribution. Consequently, the photon counting statistics vary around an average with a variance given by $\langle \delta N^2 \rangle = \langle N \rangle$. A photodiode measures the power, expressed as $P = \langle N \rangle \hbar \omega t$. These photon counting statistics, often called shot-noise, limits the experimental setup [2]:

$$S_{x,shot} = \frac{2\pi\hbar c}{64} \frac{\lambda}{\mathcal{F}^2 P_{inc}}, \tag{3.36}$$

where $\hbar$ is the reduced Planck constant, λ is the wavelength of light, and P_{inc} is the power of light injected into the cavity. Fig. 3.10 illustrates how the value of shot noise changes with increasing injected power. Nevertheless, the shot noise limit can be reduced by the so-called light squeezing [134, 135].

The second noise induced by photon number fluctuation is radiation pressure noise. When the photon flux varies statistically over time, the pressure exerted on the mirror also changes, causing the mirror's position to shift. Variations in photon number mean variations in photon momentum, which effectively alters the mirror's position. This phenomenon is known as back-action. This type of noise is significant for experiments with suspended optics, such as LIGO, but it is negligible for optically contacted mirrors, such as ultra-stable cavities [136].

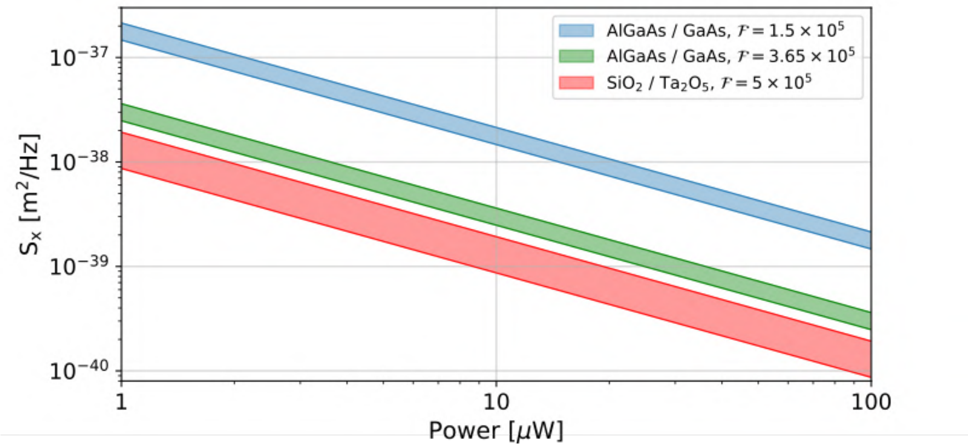

Figure 3.10: PSD of the shot noise S_x^{SN} as a function of the power injected into the cavity. Crystalline mirrors (AlGaAs/GaAs) are shown for two values of finesse: 150000 and the maximum reported finesse of $\mathcal{F} = 365000$ for the coatings used in the cavity [4]. This analysis considers the range of typically used laser wavelengths (1064 nm, 1550 nm), where the coatings' central transmission spans from 900 nm to 2 μm. For dielectric coatings made of SiO_2/Ta_2O_5, the laser wavelengths are also typically in the range from 698 nm to 1550 nm, and for a finesse of $\mathcal{F} = 500000$ [3, 56].

3.3. Thermal noise reduction

3.3.1. Mirror's convex-concave configuration for thermal noise reduction

Based on the fluctuation-dissipation theorem, Brownian thermal noise depends on temperature T, mechanical loss ϕ, and the laser beam spot radius w on the coating's surface $S_{x,ct}^{Br} \sim \phi T/w^2$. To increase sensitivity, one can look for substrates and coatings with a lower ϕ or lower the operational temperature (as demonstrated with SCS and sapphire cavities [12, 30]). We propose an alternative method for reducing thermal noise by increasing the beam spot on mirrors using a convex-concave mirror configuration. We demonstrate the feasibility and advantages of using a cavity with a radius of curvature ranging from 20 m to -25 m for 10 cm and 30 cm long cavity spacers. This approach significantly reduces both the coatings' and substrate's thermal noises as well as thermoelastic and thermo-optic noises, compared to the usual ROCs and plano-concave design. Fig. 3.11 shows the conceptual scheme of placing the convex-concave configuration in comparison to the typical plano-concave with respect to the Gaussian beam and its wavefront curvature. In Fig. 3.11, the increase in the beam spot size on the mirror is visible. Unlike plano-concave or concave-concave configuration waist is placed outside the cavity.

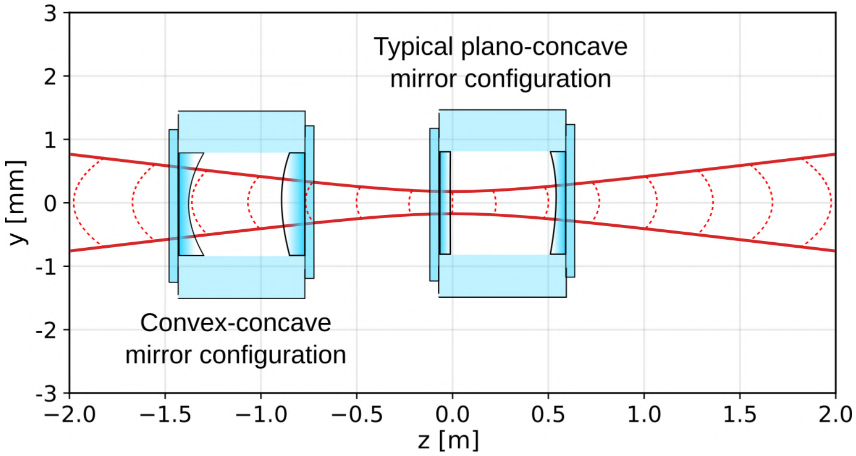

Figure 3.11: Conceptual scheme illustrating the Gaussian beams and their wavefront curvatures (dashed lines), with a typical plano-concave setup and proposed convex-concave mirror configuration.

3.3.2. Optical stability near-unstable convex-concave configuration

The reduction of thermal noises by increasing the mirror's laser beam spot size has already been proposed for use in future gravitational wave detection [137] in the form of a near-unstable solution using a plano-concave cavity. In this work, we propose a convex-concave design for the cavity mirrors to increase the beam spot size further. The following analyses will be based on the optical stability described in Sec. 2.1.1.

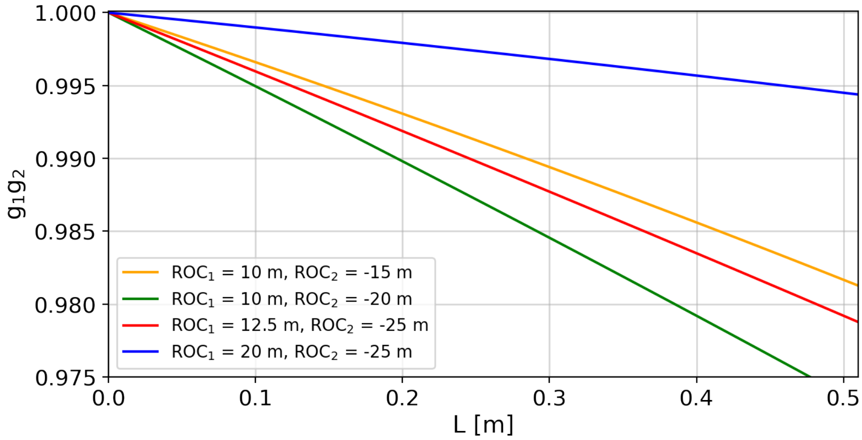

Figure 3.12: Stability factor g_1g_2 as a function of the spacer length for four configurations of mirror curvature.

For a convex-concave configuration to achieve the same spot size as a plano-concave setup, less extreme mirror curvatures are needed. For a 30 cm long cavity with $\mathrm{ROC}_1 =$ 10 m and $\mathrm{ROC}_2 = -15$ m, we can obtain beam sizes on the mirrors of $w_1 = 1.211$ mm and $w_2 = 1.181$ mm, with $g_1g_2 = 0.9894$. To achieve similar spot sizes with a plano-concave configuration, $\mathrm{ROC}_1 = \infty$, and $\mathrm{ROC}_2 = -28$ m are needed, and $g_1g_2 =$

0.9892. Furthermore, to achieve a comparable spot size with a convex-concave setup using $\mathrm{ROC}_1 = 20$ m and $\mathrm{ROC}_2 = -25$ m with $g_1g_2 = 0.9946$, a plano-concave setup would need $\mathrm{ROC}_1 = \infty$ and $\mathrm{ROC}_2 = 50$ m, results in slightly more stable optical condition with $g_1g_2 = 0.9940$.

Fig. 3.12 illustrates how the stability factor g_1g_2 varies with changes in the spacer's length for four specified configurations of the mirror's curvature. It is observed that increasing the length for $\mathrm{ROC}_1 = 10$ m, and $\mathrm{ROC}_2 = -20$ m, is most beneficial in terms of enhancing stability among the presented cases. However, an increase in length may also increase sensitivity to external vibrations. Fig. 3.13 shows stability maps for three spacer lengths: 0.1 m, 0.3 m, and 0.5 m, with markers denoting the chosen ROC, also presented in Fig. 3.12. These maps and calculations of the beam spot on the mirrors indicate whether increasing the ROC is beneficial for cavity overall stability.

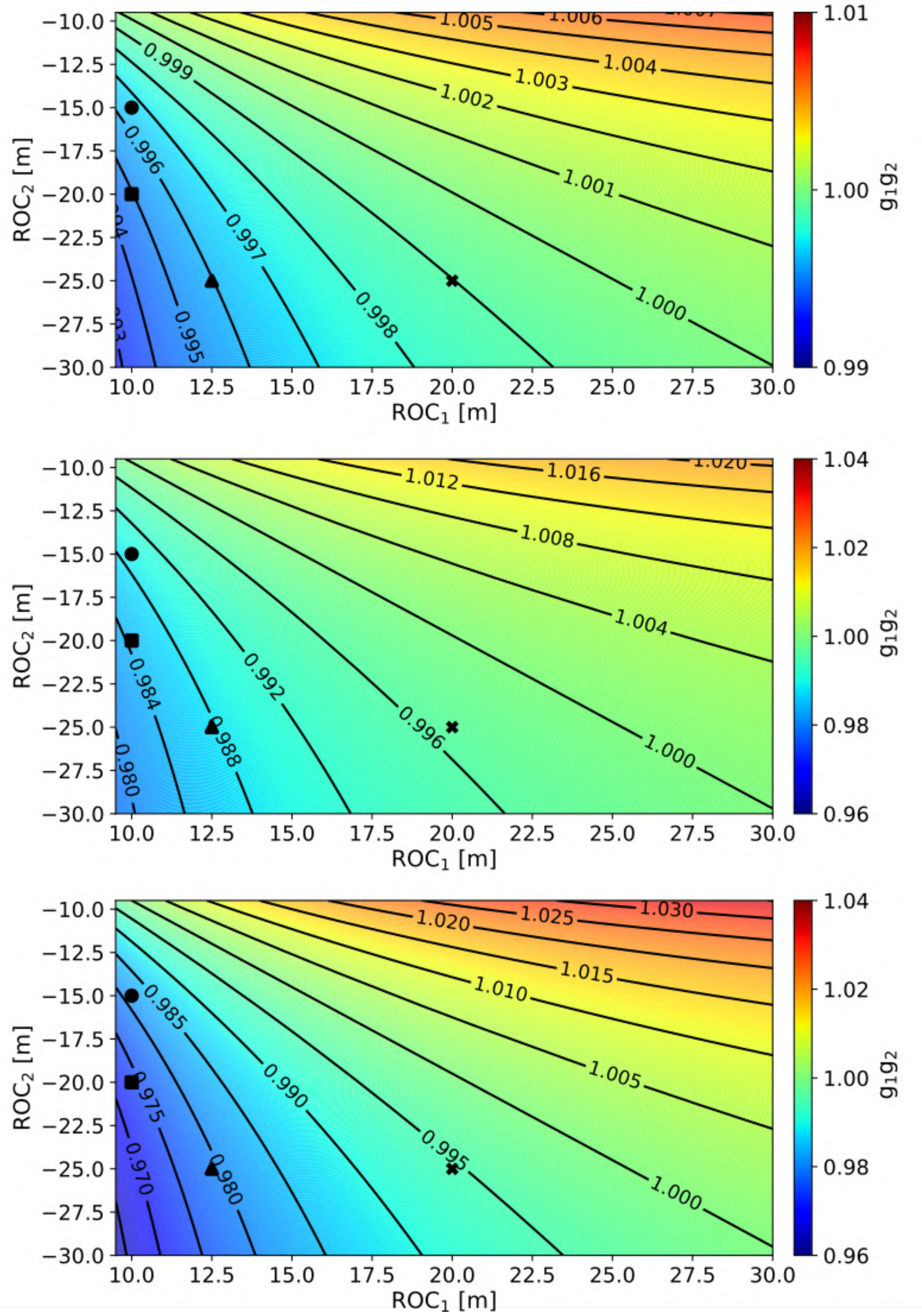

Figure 3.13: Stability maps for the near-unstable convex-concave mirrors' cavity configuration. Four possible ROCs pairs are marked by black points for 0.1 m (Top), 0.3 m (Middle) and 0.5 m (Bottom) long spacer.

3.3.3. Coatings and substrates thermal noise reduction

Brownian thermal noise from coatings and substrates is the dominant noise source in an ultra-stable cavity, both at room and cryogenic temperatures. Tab. 3.3 illustrates the numerical improvement in the PSD of the coatings $S_{y,ct}$ and substrates $S_{y,sb}$ in the concave-convex ROC compared to the typical configuration $S_{y,ct}^{(\infty,1)}$ and $S_{y,sb}^{(\infty,1)}$. We observe an order of magnitude improvement between $S_{y,sb}^{(20,-25)}$ and $S_{y,sb}^{(\infty,1)}$. Additionally, Fig. 3.14 depicts the mode-matched mirror positions for a given radius of curvature for four configurations. In all cases, the beam waist is at a distance of 0.

Table 3.3: Several configurations of the ROCs for the 30 cm long cavity, including plano-concave, concave-concave and convex-concave mirrors. The mirror's curvature and spacer's length determine the fundamental optical stability parameter g_1g_2, along with laser beam spot size on the mirror w_1, w_2, which determines the thermal noise floor. Thermal noise of the coatings (ct) and substrates (sb) is depicted as a ratio between the $\mathrm{R}_{m1} = \infty$, $\mathrm{R}_{m2} = 1$ m and the particular setup to show the effect of the beam size enhancement on the fundamental thermal noise.

R_{m1}, R_{m2} [m]	$\mathrm{g_1g_2}$	w_1, w_2 [mm]	$\mathrm{S}_{y,ct}^{(R_{m1},R_{m2})}/\mathrm{S}_{y,ct}^{(\infty,1)}$	$\mathrm{S}_{y,sb}^{(R_{m1},R_{m2})}/\mathrm{S}_{x,sb}^{(\infty,1)}$
∞, 1	0.7000	0.474, 0.567	1.0	1.0
∞, 5.0	0.9400	0.764, 0.787	0.440	0.666
∞, 10.2	0.9705	0.920, 0.934	0.308	0.557
10.2, 10.2	0.9421	0.782, 0.782	0.433	0.660
10, -15	0.9894	1.211, 1.181	0.185	0.432
10, -20	0.9845	1.100, 1.076	0.223	0.475
12.5, -25	0.9877	1.163, 1.142	0.199	0.448
20, -25	0.9968	1.627, 1.605	0.101	0.320

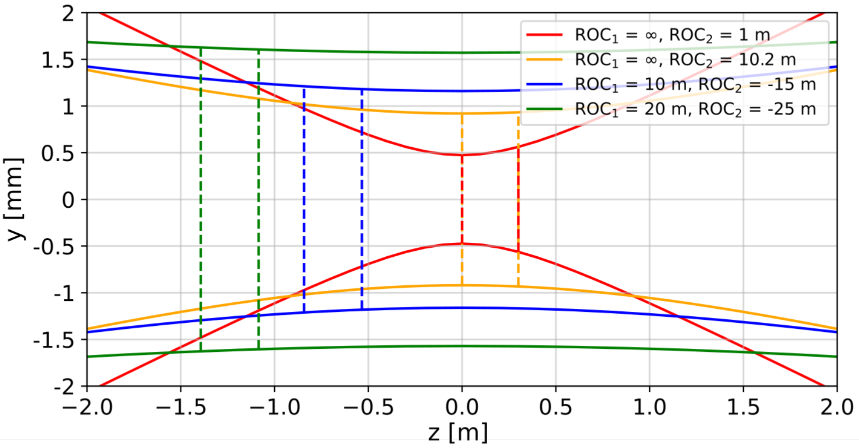

Figure 3.14: Mode-matched Gaussian beams together with the four investigated stable and near-stable configurations of the spacer length and mirrors' ROC. The dashed line indicates the location of the cavity mirrors.

3.4. Design of NEXCERA room-temperature cavity

The main motivation of this section is to design a long-term stable optical reference that operates effectively at room temperature. The long-term stability of any reference oscillator is an important property necessary for metrology and precise measurement purposes, e.g. radial velocity observation of the Earth-like exoplanets demands instability of 10^{-16} per year [1]. Common spacer materials used for room-temperature ultra-stable cavities include amorphous materials like titania-silicate glass known as ULE, silica dioxide known as fused silica, and glass-ceramic structures such as Zerodur, which primarily consist of lithium aluminium silicon oxide.

NEXCERA [96, 138], a relatively new ceramic material composed of magnesium-aluminium silicon oxide, has demonstrated promising long-term stability, significantly reducing the effects of long-term drift [95]. This drift effect arises from ageing processes, where the amorphous structure tends to crystallize over time, altering its physical size. Consequently, the measured frequency as the distance between the mirrors changes. Tab. 3.4 presents the typical drift rates for both long (1/yr) and short-term (1/s) stability for the most common spacer materials.

Table 3.4: Drift rate $(1/L)\delta\dot{L}$ for the most common materials for the ultra-stable optical resonator spacers. The rate is given on two characteristic timescales, 1/s and 1/yr. Zerodur, ULE and NEXCERA are the glass and ceramic structures that operate at room temperature, whereas the crystalline SCS and sapphire reside in a cryogenic environment.

Material	Linear drift rate [10^{-17}/s]	Linear drift rate [10^{-9}/yr]
Zerodur	304.8 [139], 697.6 [140]	96.12 [139], 22.00 [140]
ULE	4.572 [139], 8.157 [95], 20.41 [141]	1.442 [139], 2.572 [95], 6.437 [141]
NEXCERA N117B	1.738 [95]	0.548 [95]
NEXCERA N118C	54.97 [142]	17.34 [142]
SCS	-0.0247 [143], -0.0970 [144]	-0.008 [143], -0.031 [144]
Sapphire	-0.064 [145]	-0.020 [145]

Crystalline materials in cryogenic conditions, such as SCS and sapphire, exhibit significantly lower drift rates—two to three orders of magnitude lower— than amorphous structures at room temperature (see Tab. 3.4). In theory, SCS and sapphire should not demonstrate this behaviour because of the already settled crystalline structure. Moreover, the crystalline spacers extend as the glass-like materials shrink over time. According to Tab. 3.4, the drift rate varies significantly even for the same material. This variation may depend on the measurement duration (time averaging), changing environmental conditions, and the specific glass sample. Additionally, ageing processes slow down in time,

---

[1] Assuming typical radial velocity of a star induced by the planet on the level of 30 cm/s.

and instead of constant frequency drift [146], they follow a stretched exponential function [147]. A decreasing drift rate in the spacer over time means an enhancement with age, suggesting the use of an "older" piece of material. Regardless of material ageing, the change in applied laser input power can also affect the mirror coatings and substrates, resulting in an additionally induced effect of the resonance frequency drift [144].

According to Tab. 3.4, the smallest frequency drifts are reported for Zerodur at 2 Hz/s [139], ULE at 23 mHz/s [95], NEXCERA N117B at 4.9 mHz/s [95], and among crystalline materials, SCS shows the best performance at -48 μHz/s [143]. Nevertheless, it is important to mention that another type of NEXCERA, i.e. N118C, exhibits a more significant thermal drift than ULE glass (as indicated in Tab. 3.4).

3.4.1. Thermal noise for NEXCERA

While the long-term performance of NEXCERA cavities is promising, one critical material parameter that determines the fundamental limitations of the cavity is still officially unknown, i.e. mechanical loss angle ϕ. Although there are no published results of the NEXCERA's loss angle, preliminary measurements were recently performed at Technische Universität Braunschweig by Nico Wagner. Three sets of 50 mm discs with 0.5 mm thickness and surface roughness defined as Ra ≤ 5 nm [2] of NEXCERA117B were supplied to Braunschweig (by Nicolaus Copernicus University) and measurement of the loss angle was performed there at room temperature using gentle nodal suspension method [148]. Measured loss angle for the four frequencies, from approximately 3 kHz to 21 kHz, is from 1.89×10^{-5} to 3.06×10^{-5}, respectively. For the comparison, the loss angle of ULE is 1.7×10^{-5} and Zerodur is 3.2×10^{-4}.

No NEXCERA-based cavity has yet achieved thermal noise floor performance, so the real limitations are unknown. Generally, the Brownian effect of the spacer is much smaller than that of the substrates and coatings due to its bulk body properties. Fig. 3.15 illustrates the thermal Brownian and thermoelastic noise contributions for various substrate and coating configurations. The NEXCERA N117B spacer noise, depicted as the blue-shaded area, is calculated for the loss angles ranging from 1.89×10^{-5} to 3.06×10^{-5}. NEXCERA worse loss angle gives almost the same Brownian noise as ULE spacer (purple solid line in Fig. 3.15). All NEXCERA cavities, whose performance was published [95, 142, 149], are supplied with ULE substrates due to ULE transparency for the laser light and similar thermal properties, such a comparable CTE. However, ULE exhibits a loss angle that is at least an order of magnitude larger, resulting in increased Brownian noise. As illustrated in Fig. 3.15 (left), Brownian noise from the ULE substrates would be the dominant component, suggesting the replacement of ULE substrates with fused silica, as

---

[2] Ra is a commonly presented quantity defining the quality of surface, and it is the arithmetic average of profile height deviations from the average value over the measured line.

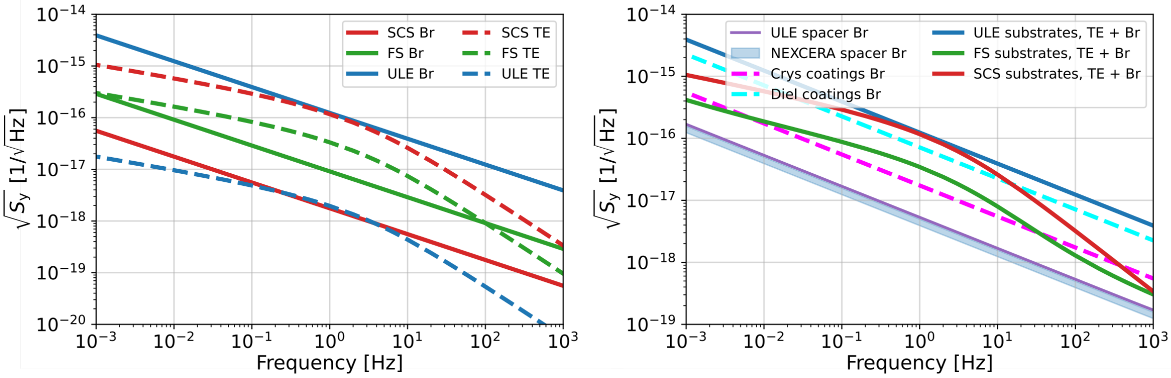

Figure 3.15: **(Left)** Brownian (Br) and thermoelastic (TE) noises shown as fractional amplitude spectral density $\sqrt{S_y(f)}$ for the three types of the substrates: ULE, FS and SCS. **(Right)** Brownian noise of dielectric and crystalline coatings, along with noise generated by NEXCERA N117B spacer for a loss angle ranging from 1.89×10^{-5} to 3.06×10^{-5}. The sum of substrate thermoelastic (TE) and Brownian (Br) noises is also included. ULE and NEXCERA spacer are 30 cm long, and the mirrors are plano-concave with ROC of 1 m.

it is commonly applied for ULE spacer cavity as well as in this work. This replacement significantly reduces the Brownian noise from the substrates, which is a limiting factor in the case of ULE (as shown in the upper right of Fig. 3.15). Nevertheless, this exchange requires additional attention to the zero-crossing point due to different CTEs. Hence, an analysis similar to Lagero et al. [150] is necessary for determining the effective CTE of NEXCERA-FS cavity and adjusting this value with NEXCERA compensation rings. This will be covered in the following section. Using FS substrates will reduce overall thermal noise, and using SCS substrates will reduce thermal noise except for the 0.1 - 10 Hz because of high thermoelastic noise in this range. Fig. 3.15 (right panel) demonstrates that replacing the ULE spacer with NEXCERA does not affect the noise budget negatively. Additionally, Fig. 3.15 shows the combined Brownian and thermoelastic noises for substrates. The results presented in Fig. 3.15 suggest replacing ULE substrates with SCS or FS.

Fig. 3.16 illustrates the noise budget for the 30 cm long NEXCERA cavity at 293 K, with plano-concave mirrors (ROC = 1 m). The left panel shows how changing substrates from ULE to FS or SCS will improve the overall thermal noise. Coatings' thermo-optic noise is ignored here because of its negligible influence on dielectric and optimized crystalline coatings. The best upgrade of ULE substrates seems to be the FS substrate with crystalline constraints, which has much smaller TE noise than SCS (because of the small CTE at room temperature). The right panel of Fig. 3.16 depicts an effect of increasing the ROC from 1 m (solid line) to 10.2 m (dotted line). The bigger ROC with FS substrate and crystalline coating will allow to reach the level $\sim 2.48 \times 10^{-17}$ $1/\sqrt{\text{Hz}}$ instability at 1 Hz. If the loss angle for NEXCERA is greater than $\sim 10^{-3}$ at 1 Hz (which is highly

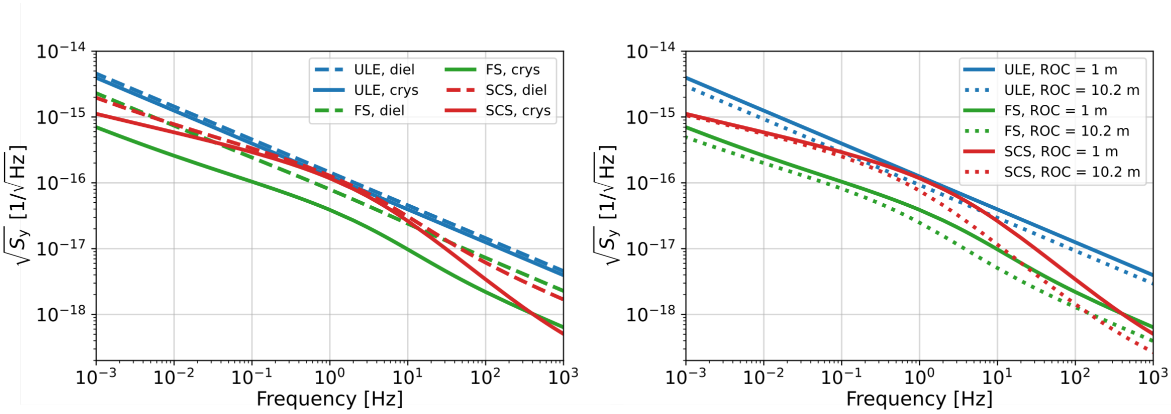

Figure 3.16: **(Left)** Total fractional amplitude spectral density $\sqrt{S_y(f)}$ for the cavity with NEXCERA spacer, three possible substrates, and dielectric or crystalline coatings, for plano-concave mirrors configuration with ROC = 1 m and 30 cm long spacer. **(Right)** Total $\sqrt{S_y(f)}$ of a NEXCERA spacer cavity for three possible substrates materials with crystalline coatings and two ROC (1 m and 10.2 m) of plano-concave configuration.

unlikely with 1.89×10^{-5} for ∼3 kHz), the FS substrates will generate less noise than the spacer. Then, it might be beneficial to consider using SCS substrates. However, SCS has a higher CTE than FS at room temperature, which increases the thermoelastic noise and could shift the zero-crossing temperature of the entire cavity to even lower values. This topic will be discussed and explained in the following section.

Additionally, NEXCERA demonstrates superior thermal conductivity at room temperature with values of 3.7 $\mathrm{Wm^{-1}K^{-1}}$ for N113B, 4.2 $\mathrm{Wm^{-1}K^{-1}}$ for N117B, and 4.5 $\mathrm{Wm^{-1}K^{-1}}$ for N118C [96], compared to ULE which has a thermal conductivity of 1.3 $\mathrm{Wm^{-1}K^{-1}}$ [151]. Therefore, NEXCERA offers a more homogeneous temperature distribution and better dynamic stress behaviour under temperature changes than ULE.

3.4.2. Zero-crossing calculation

Room temperature cavities are commonly made of two different materials. Combining materials with different CTE (spacer and substrates) results in a shift of the designed spacer zero-crossing at room temperature. The first experimental evidence of this was observed with a sapphire spacer and FS substrates at cryogenic temperatures, which shifted the zero-crossing point and modified the shape of the effective CTE by adjusting the substrate thickness [152]. In-room temperature setups, ULE spacer with FS substrates are the standard configuration [29, 153–155]. NEXCERA and ULE show very similar CTE curves and closely aligned zero-crossing points (see the left panel of Fig. 3.17). Therefore, no significant zero-crossing deviation is expected. However, because of possible significant improvement in the noise contribution by substrate, I will demonstrate that the change of the substrate material will influence the zero-crossing point. Eq. 3.1 describes how the temperature fluctuation influences the cavity length with identical spacer and substrate

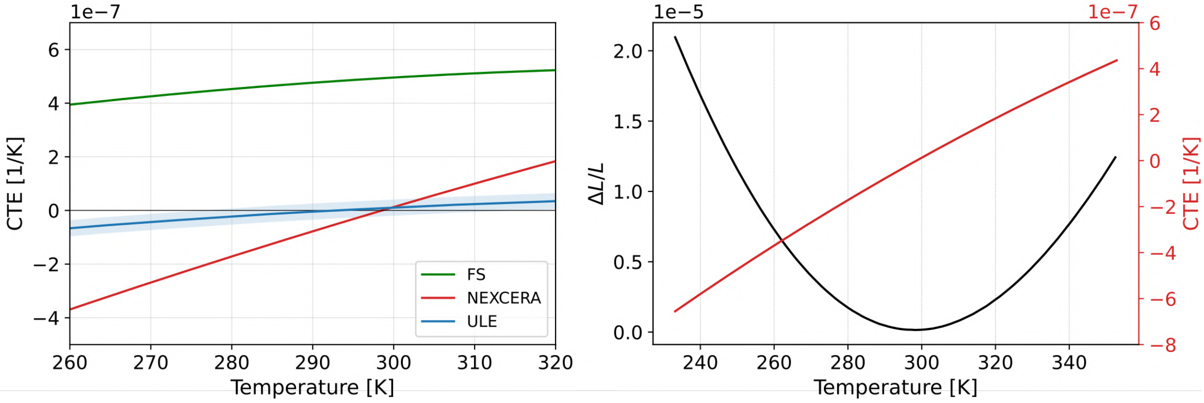

Figure 3.17: **(Left)** The CTE for considered materials (except for SCS) in the vicinity of room temperature. The CTE of ULE, including the manufacturer's uncertainty, and FS, are taken directly from [43] and [156], respectively. **(Right)** The CTE for NEXCERA (red line) was derived from the thermal expansion ratio $\Delta L/L$ [96] (as a derivative), depicted as the black line.

materials. For configurations involving two different materials, the CTE must be replaced with the effective CTE [27]

$$\alpha_{eff}(T) = \alpha_{sp}(T) + 2\delta\frac{R}{L}[\alpha_{sb}(T) - \alpha_{sp}(T)], \tag{3.37}$$

where the $\alpha_{sp}(T)$ and $\alpha_{sb}(T)$ represent the CTE of the spacer and substrate, R is the substrate radius, L is the spacer length and δ is the coupling coefficient. This coupling coefficient depends on the geometry, sizes and materials of the substrates and spacer. In [27] δ value was simulated by FEM.

In this work, I show how the coupling coefficient will change the zero-crossing temperature for the NEXCERA spacer and ULE, FS, or SCS substrates for one, arbitrarily assumed, value of δ. Further studies involving the FEM simulation would be necessary in the case of a particular design.

Fig. 3.18 demonstrates how the composition of two materials in the spacer-substrate setup (solid lines) shifts the zero-crossing point compared to a single material composition (dashed lines), assuming coupling coefficient $\delta = 0.49$, which is similar to the value determined by FEM simulations [27] for ULE and FS. According to Fig. 3.18 and [27], FS substrates optically contacted to the ULE spacer cause a shift of $\sim$20 K. Additionally, the substrate geometry and the coupling coefficient manipulation can be fine-tuned by adding a so-called ULE compensation ring, introduced in [27], and commonly used in ULE-FS cavities (also in [27]). By manipulating the compensation ring sizes, one may effectively reduce the FS-induced zero-crossing shift.

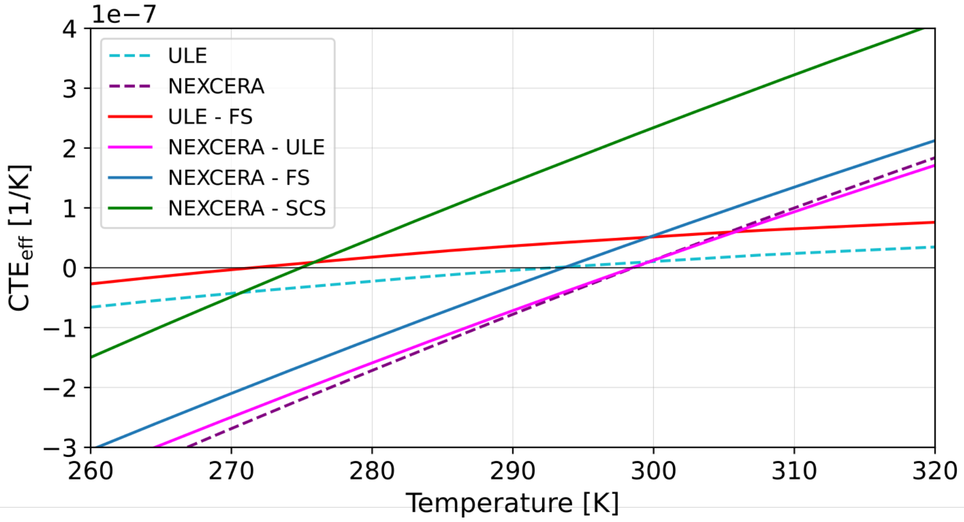

Figure 3.18: Effective zero-crossing temperature for various compositions of spacer-substrate configurations, e.g., ULE-FS denotes a ULE spacer with FS substrates. Calculations were performed for a 30 cm long spacer, a 2.54 cm substrate radius, and a coupling coefficient $\delta = 0.49$.

4. Cavity and cavity enclosure design

The previous chapter describes the fundamental limitations of cavity stability. Nevertheless, many aspects must be addressed carefully to reach the $< 10^{-16}$ fractional frequency instability. In the current chapter, I will show the process of designing optical resonators to become ultra-stable, i.e., reaching fundamental thermal noise floors in practice.

Initially, one must choose the cavity's temperature to determine the spacer's material. Three materials are commonly used for the room temperature setup, where zero-crossing points are between 5 °C and 35 °C: ULE [43, 151], Zerodur [42], and ceramic material known as NEXCERA [96]. Currently, ULE replaced Zerodur due to its superior quality factor. Each material has a characteristic behaviour of CTE (see Fig. 3.2) with zero-crossing temperature. Zero-crossing may vary from piece to piece of the same material. The goal is to find this point and precisely stabilize the temperature.

This chapter will provide the complete design of the vacuum chamber, thermal shields and 30 cm-long ULE room temperature cavity. In addition, the vibrational analysis study will be presented. Due to significant delays (over one year) in the delivery of the vacuum system, work to complete the assembly of the cavity setup is still ongoing.

Fig. 4.1 illustrates the cavity setup and a significant part of the room, i.e., the building and separate foundations. The idea was to decouple the cavity from the building vibrations with a separate foundation. Therefore, the cavity will rest on the separate foundation, then on the post made from various materials (such as concrete, lead, granite, MDF) intended to dissipate and scatter low-frequency vibrations. Then, an active antivibration platform will rest on a separate foundation and post. On top of that, the vacuum chamber with the ultra-stable cavity will be placed, which is presented in more detail at the bottom of Fig. 4.1. A cross-section of the zoomed vacuum chamber reveals the part in-vacuum elements. Besides the vacuum chamber, three additional layers of chambers are presented. In Fig. 4.1, they are called shields because of their purpose. The first layer (orange chamber) will rest on three Peltier elements. The other two (red and grey) and the Super Invar support rest on the glass balls. Finally, the ultra-stable 30 cm long ULE cavity is positioned on the four elastic Viton balls.

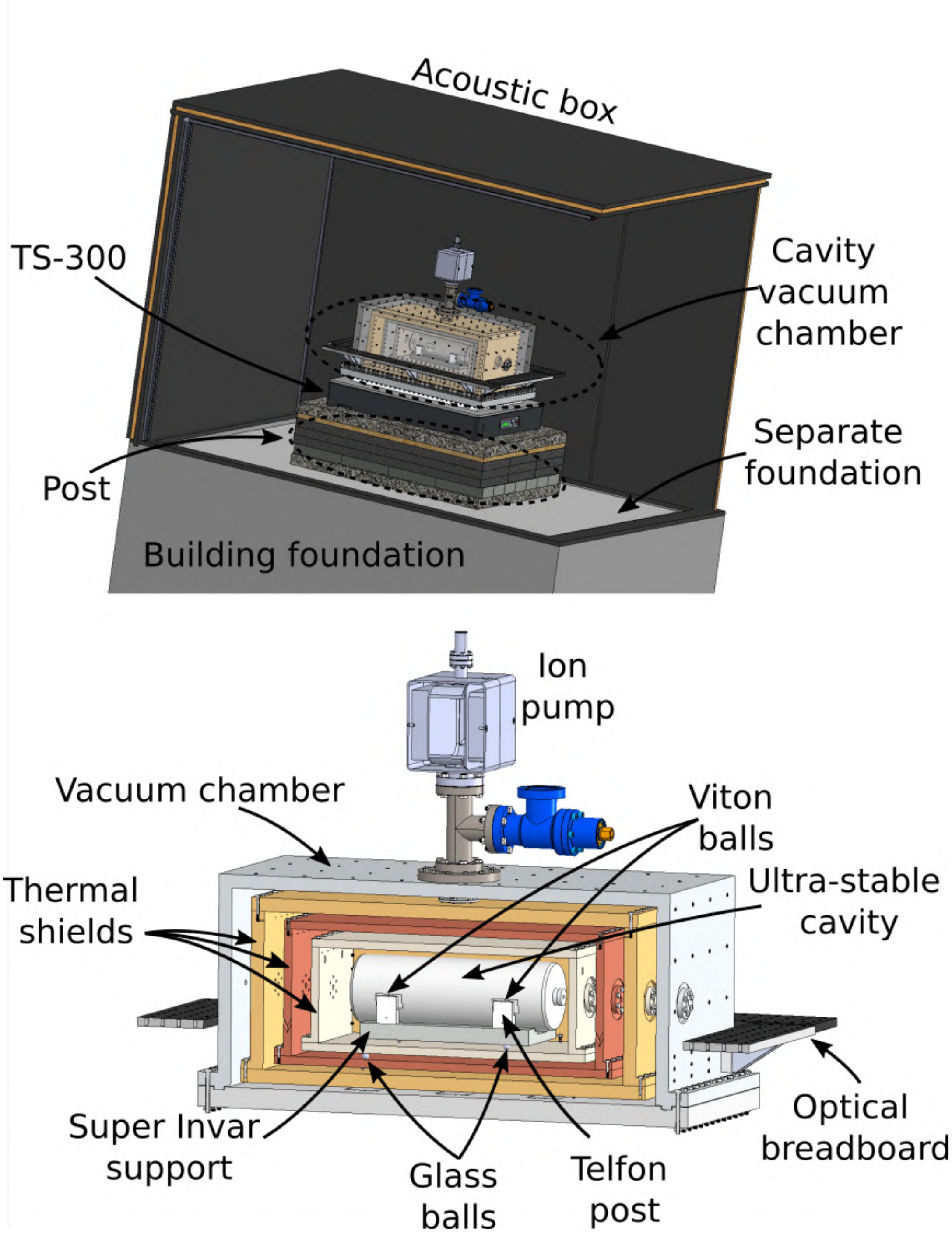

Figure 4.1: **(Top)** 3D scheme of the essential elements of the ultra-stable cavity setup, with the part of the building foundation and foundation separated from the building. Additionally, a post is made of various materials (lead, concrete, granite) and an active anti-vibrational platform TS-300. All is closed in an acoustic box. **(Bottom)** Cross-section of the ultra-stable cavity vacuum setup, thermal shields, Super Invar support, Teflon post, and Viton and glass balls. Different colours are used only to distinguish layers. All thermal shields are made from specific aluminium alloy.

4.1. Ultra-stable cavity spacer geometry

Different approaches have been made to design the cavity's most massive element, i.e., the spacer. Choosing a bigger length L results in better fractional stability ($S_y(f) = S_x(f)/L^2$), but with the potential drawbacks of greater susceptibility to vibration and significantly larger cavity price, along with increased vacuum chamber volume and mass. Furthermore, the cavity's alignment (vertical or horizontal) and the spacer's shape need to be selected. Fig. 4.2 illustrates the typical spacer geometries in state-of-the-art optical resonators. Each has its benefits and drawbacks. We decided to use a cylindrical ULE spacer (top right in Fig. 4.2).

Fig. 4.2 shows the cavities without their support structures. In the actual setup, horizontal cavities rest on four elastic Viton balls, which are usually positioned on four Teflon posts. In contrast, vertical cavities (top left in Fig. 4.2) are supported at three points by a rigid post structure made of materials such as PEEK [58].

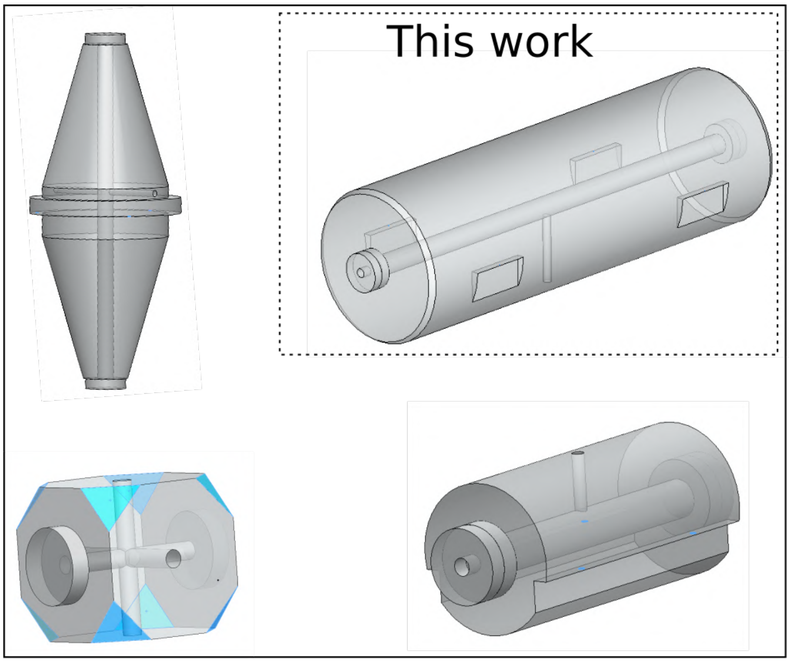

Figure 4.2: CAD drawings of the typical geometries of state-of-the-art optical resonators include the double-cone **(top left)** [3], cylindrical with the cut support pads **(top right)** [29, 153], and commercial solutions i.e. cube shape [157, 158] and notched cavity [158]. Scale is not maintained.

4.2. Vibration-insensitive design of the cavity geometry

Vibration are one of the biggest limitations for the many precise experiments. For instance, the performance of the long-range "free-falling" interferometers, even after multistage pendulum isolation (so-called super attenuators) is limited below 10 Hz [88]. However, the background acceleration noises' level depends on the apparatus location [159]. In the case of table-top ultra-stable cavities with rigid spacers, careful design of its geometry may considerably decouple the cavity from the Earth's movements and other vibration sources [25, 26]. Over the years, several cavity spacer geometries and support structures were tested [25, 26, 157, 158].

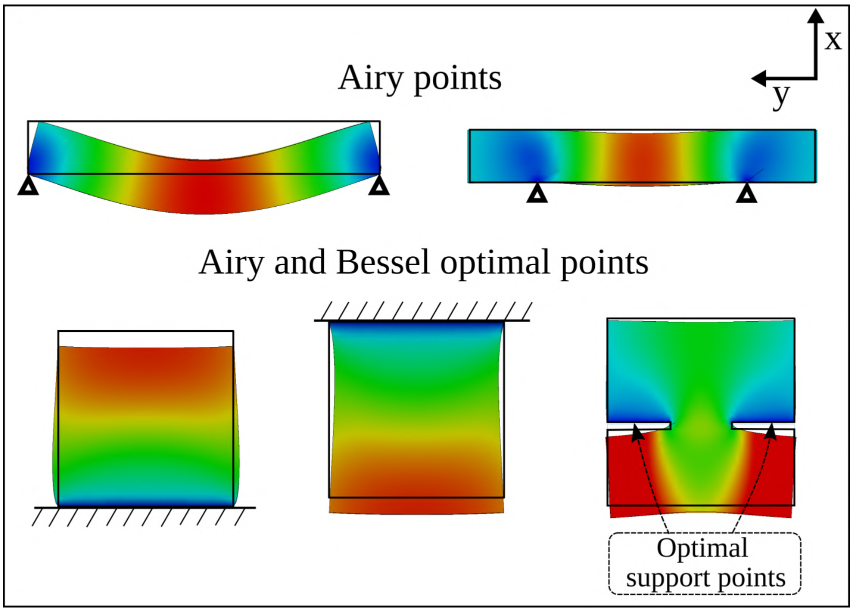

Figure 4.3: **(Top)** Finite element method simulation showing exaggerated displacement along y-axis of the body experiencing acceleration for the non-optimal support point position (Left) and Airy points (Right). **(Bottom)** By finding the optimal support points, the body will not extend in size along the optical axis dimension (Bessel points), and the edges will remain parallel (Airy points), resulting in a highly suppressed cavity susceptibility to external disturbances.

Fig. 4.3 illustrates the two effects that affect the cavity shape in the presence of acceleration. In this simple 2D model, the black line represents the original shape without gravity, and the colours indicate the displacement amplitude along y-axis. In the case of a cavity, Bessel points refer to the support points where the spacer will not extend along the optical axis (the length remains unchanged), whereas Airy points denote the support positions at which the mirrors remain parallel. Finding a proper position for the support points that minimizes both of these effects is the main goal of the cavity geometry design.

4.2.1. FEM simulation of the optimal support points position

Due to the sophisticated geometry of the spacer, I use FEM (Finite Element Method) simulations made in Solidworks software, to find the optimal support points under $9.81\ \mathrm{m/s^2}$ acceleration. Optimal support for a mirror involves simultaneously finding both Bessel points (no length change) and Airy points (mirror ends remain parallel), which reduces cavity acceleration sensitivity [29, 160].

Fig. 4.4 shows a quarter of the cavity used for the FEM simulation, along with the characteristic dimensions. Here, Δx, Δy, and Δz represent the distances from the optical axis, the centre of the cavity, and the edge of the spacer to the support point, respectively. These three dimensions and the support diameter are four crucial parameters I will adjust to find the optimal solution. In the simulation, I benefit from the symmetry in the xy-plane and xz-plane from the centre of the cavity and use a quarter of the cavity. Fig. 4.5 shows the cavity scheme along with the meshing used for the FEM simulations. A curvature-based mesh was implemented with varying mesh sizes: the mirror's inner surface at 0.05 mm, the support position at 0.02 mm, and the rest of the cavity at 1 mm. The support pad dimensions, as depicted in Fig. 4.5, was set to 40 mm to provide sufficient space for manoeuvring and the width was set to 5 mm.

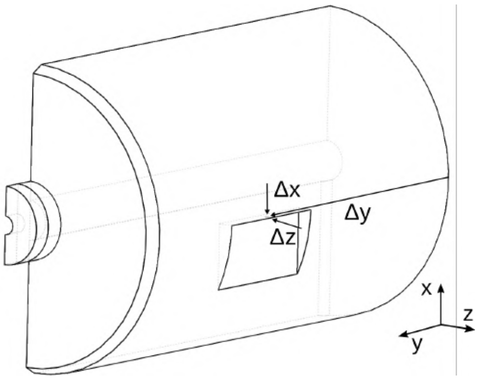

Figure 4.4: Scheme of the quarter of the cavity with characteristic dimensions Δx, Δy, Δz used in the FEM simulation.

Fig. 4.6 illustrates the results of the FEM simulations of the cavity. The top left plot shows the mirror's tilt due to gravitational acceleration. The length extension due to gravity and support points is close to zero, compared to the designed cavity length L. We can observe that with the pivotal point at $x = 0$ and $y = 0$ (the mirror's centre is unchanged), the tilt of the mirrors changes on the scale of $\Delta L/L = 10^{-9}$. Therefore, the optimal support location is between simulated values of $\Delta y = 87$ mm and $\Delta y = 92$ mm. The effect of mirror's parallelism is determined by identifying the sign change in the mirror's tilt, as presented in Fig. 4.6 (Top right). The linear fit identifies the optimal point at 88.82 mm. The Airy support points are given by $L/\sqrt{3}$ relation, which results in $\Delta y = 86.60$ mm. Therefore, the difference is only ∼2 mm. It may shift slightly (∼ 1-2 mm) on both sides if Δx were significantly different.

Fig. 4.6 (Bottom left) illustrates the effect of changes in the contact surface diameter between the Viton ball and the spacer pads, denoted as d_{support}. For a given Δx and a position in the zy-plane ($\Delta z = 2$ mm and $\Delta y = 86.82$ mm) I simulated the change in the cavity's fractional length as a function of support diameter. The results show that a larger d_{support} increases the length of the cavity both in the optical axis and 1 mm above it. Specifically, between $d_{\text{support}} = 1.5$ mm and $d_{\text{support}} = 2$ mm, the fractional

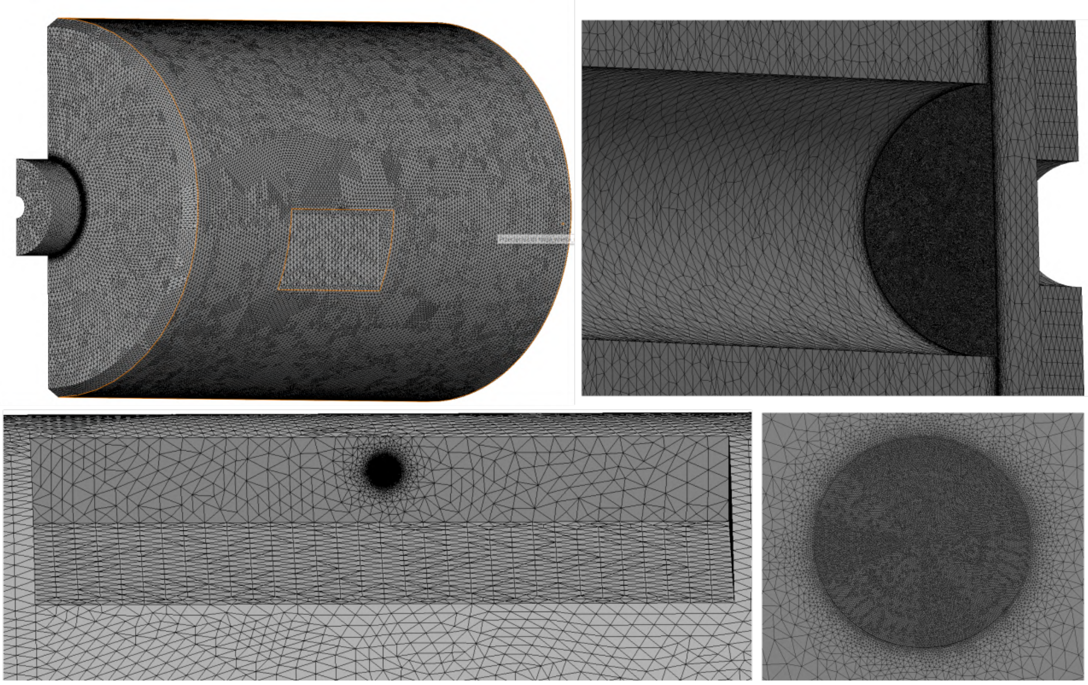

Figure 4.5: Picture of the meshed quarter **(Top left)** of the cavity, together with crucial elements i.e., mirror inner surface **(Top right)**, support pad **(Bottom left)**, and zoomed support area **(Bottom right)**.

length changes by 10^{-10}. Thus, we can theoretically manoeuvre to find the optimal Airy position by choosing different Viton balls (sizes and hardness). We can shift the fractional cavity length by fixing an optimal Δy and changing Δz, as shown in the bottom right of Fig. 4.6. From the analysis performed in this section, we observe that the optimal support points depend on numerous parameters, making practical implementation challenging. Nevertheless, the results of the simulations presented in Fig. 4.6 demonstrate the available space for adjustment.

After completing the design of the cavity, we ordered the spacer and substrates from Optrovision and the coatings from Thorlabs Crystalline Solutions. Fig. 4.7 illustrates a photograph of the designed ultra-stable ULE cavity, along with the corresponding FEM simulation of displacement in the y-direction at the optimal support points.

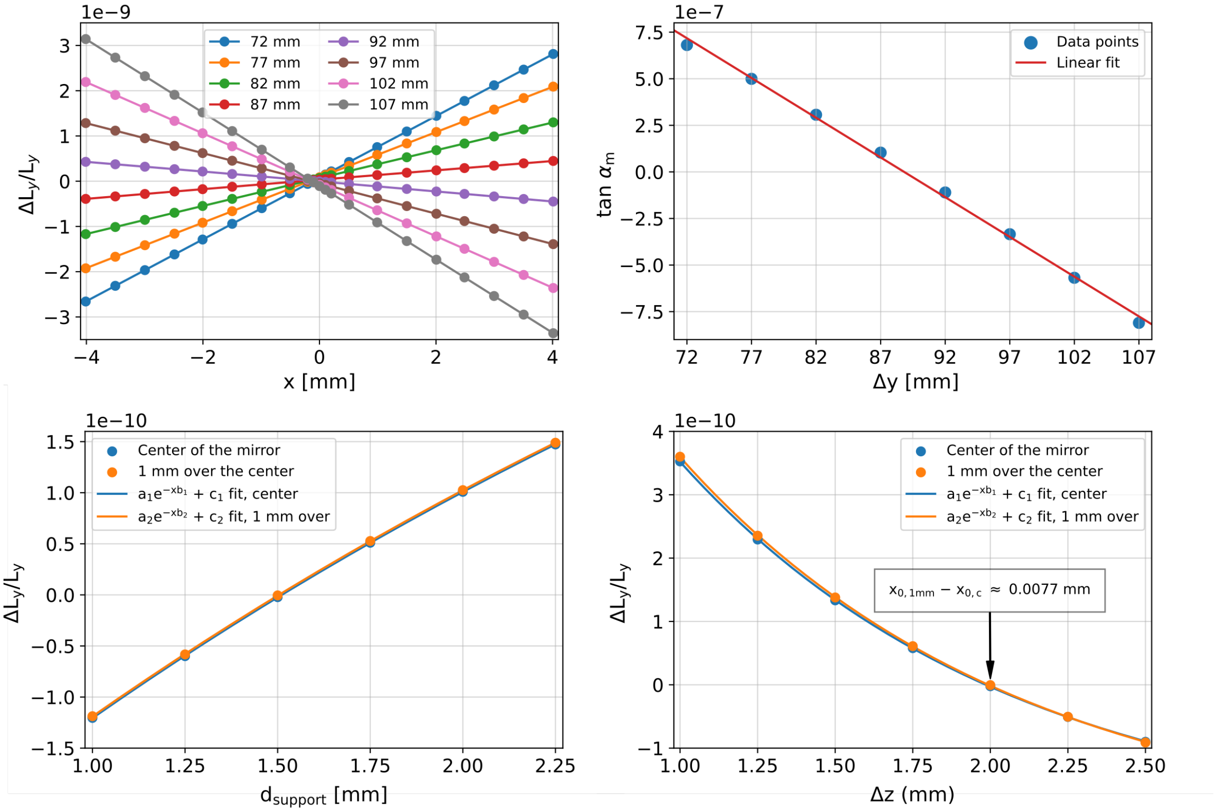

Figure 4.6: **(Top left)** Fractional displacement of the mirrors in the y-direction under the Earth acceleration. The support diameter d_{support} was set to 1.5 mm and $\Delta z = 2$ mm. **(Top right)** An angle of the mirrors tilt for the different δy distance. Data is taken from the top left figure. Fit shows the optimal Airy point where the mirrors are parallel in $\Delta y = 88.82$ mm. **(Bottom left)** Fractional displacement of the mirror's centre (blue line) and 1 mm over the optical axis (orange line) in the function of changing support points diameter and **(Bottom right)** distance from the edge of the pad in the z-direction in the Earth acceleration ($\mathrm{g} = 9.81\ \mathrm{ms}^{-2}$).

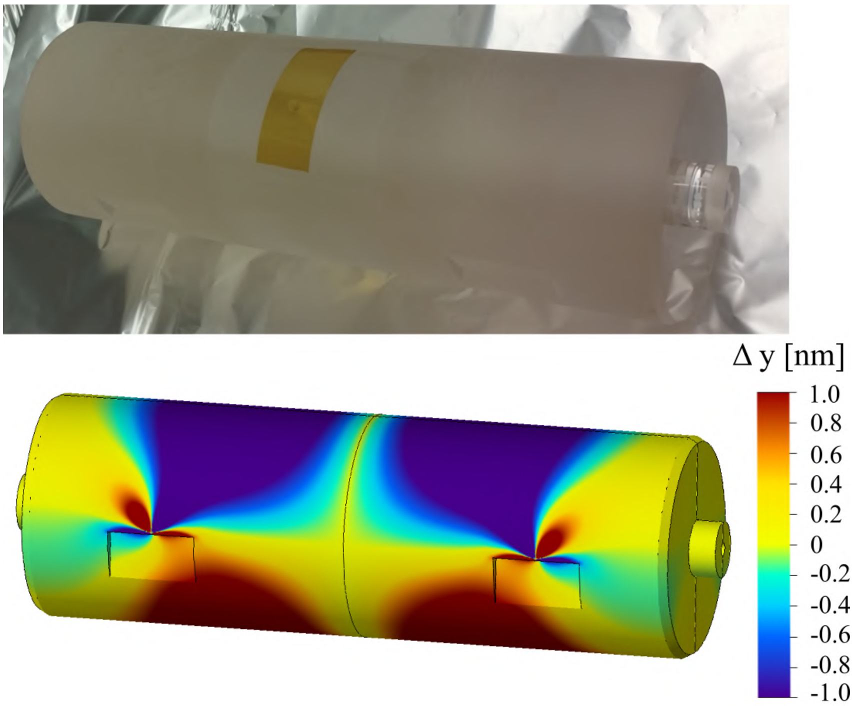

Figure 4.7: Photo of our 30 cm long ULE cavity with fused silica substrates and ULE compensation rings, along with its finite element method simulation in 1 g.

4.2.2. Cavity support structuture

In the actual design, the cavity will rest on four elastic Viton balls positioned on Teflon posts and laid into a structure made of Super Invar. It is crucial for this structure to have a similarly low coefficient of thermal expansion at room temperature to prevent structural tensions. According to Fig. 3.1, the CTE of Super Invar is only approximately three times larger than that of ULE, and for Teflon, it is about five times larger.

Fig. 4.8 top left shows five possible Viton balls, ranging from a diameter of 1/8" to 3/8" and with hardnesses from 70A to 90A on the Shore scale. A glass ball will be used between the Super Invar support and the first thermal shield. The top right of the Fig. 4.8 illustrates the support structure without the cavity resting on it, and the bottom left with the cavity. The aluminium cavity was machined to have the same size and mass as the ULE equivalent to observe the effect of ball squeezing and to refine the process of safely positioning the cavity.

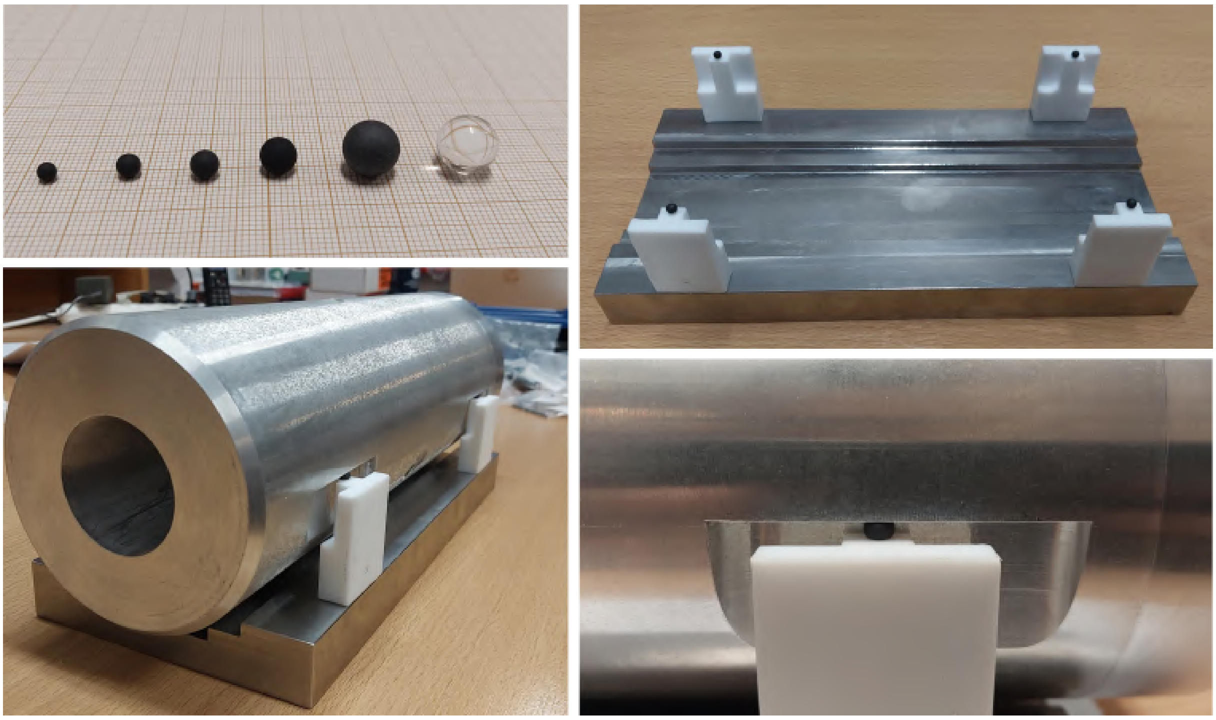

Figure 4.8: Mass and size equivalent aluminium model of the ULE cavity together with super-invar support structure, teflon posts and various possibles size of viton balls and glass ball, which will divide super-invar and first aluminium thermal shield.

4.2.3. External half-rings for the support points correction

As presented in the previous section, support points are sensitive to changes in almost all parameters, from the positioning in the support pads and support area diameter to the manufacturing precision of the spacer itself. Also, simulations involving cavities with Viton balls may differ from those simplified with a fixed area performed in this work. Moreover, precise positioning of cavity support balls may be challenging in practice.

Therefore, it is helpful to have a backup plan to adjust the optimal point, e.g., by applying an external load to the cavity. I performed a simulation with additional external Teflon half-rings, which effectively reshapes the mirror's tilt and the distance between mirrors. Fig. 4.9 illustrates how the shape of the mirror, for $\Delta z = 1$ mm, $d_{\text{support}} = 1.75$ mm, and $\Delta z = 92$ mm (blue line), is adjusted and reshaped by an additional external Teflon half-ring for $\Delta z = 92.45$ mm (orange line). The proper positioning of the external mass half-ring on the spacer allows the shift of the optimal support point without moving the cavity.

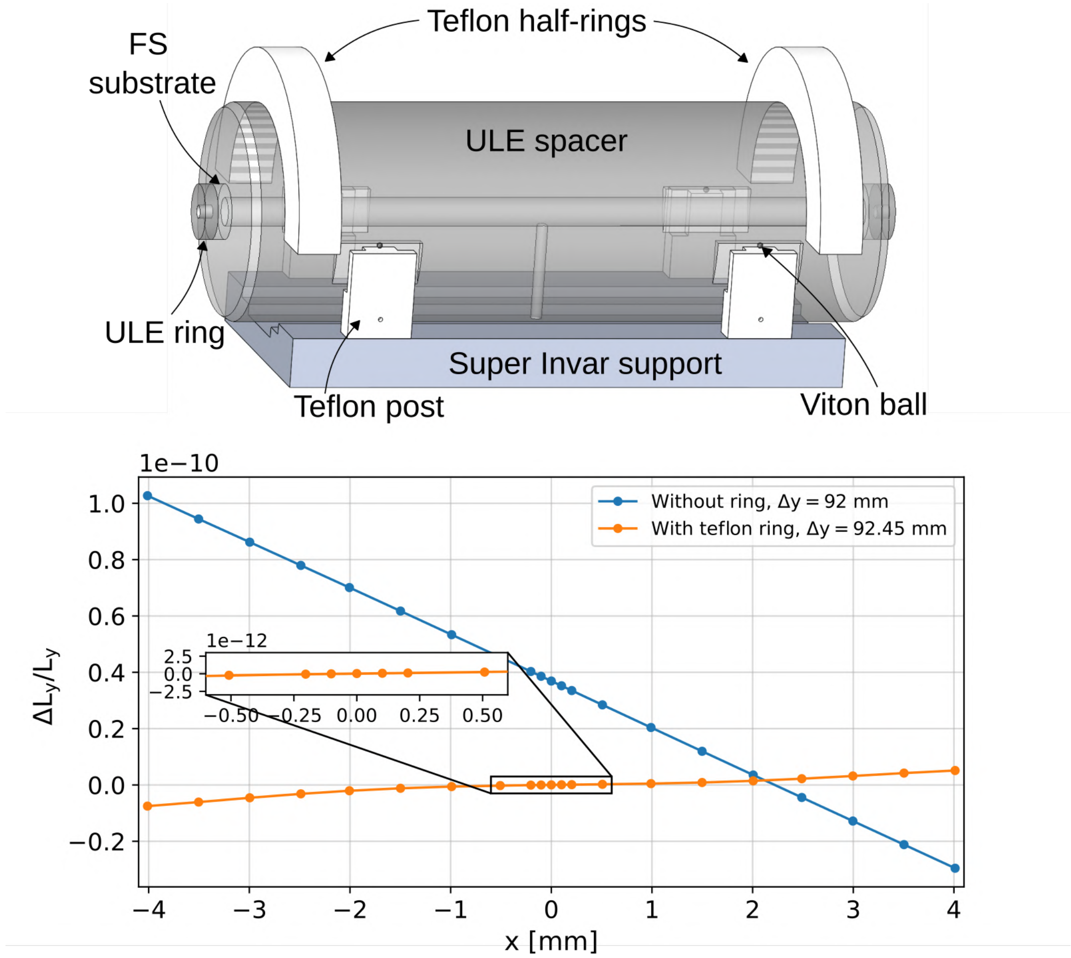

Figure 4.9: **(Top)** The 3D model of a ULE cavity support structure with the Teflon half-rings on the top of a spacer for the mirror shape adjustment. **(Bottom)** The effect of shifting the Airy point with the external Teflon half-ring placed on the top of the cavity.

4.3. Mitigation of acoustic and seismic noise

4.3.1. Acoustic insulation

Despite the ultra-stable cavity residing in an ultra-high vacuum (UHV) of $\sim 10^{-9}$ mbar, acoustic noise will influence elements outside the vacuum and create noise. The presence of acoustic noises in the system may introduce significant limitations, especially for higher frequencies (kHz) proposed for gravitational wave detection. Therefore, several steps were taken to mitigate these noises, beginning with the measurement of the resonance frequencies of the cavity room (the room where the cavity will be situated). These were measured by inducing a sinusoidal signal from speakers in the 20 - 500 Hz range and detecting the response with accelerometers inside the active anti-vibrational platform Table Stable TS-300, where the cavity will be situated. In addition to internal passive isolation, the TS-300 offers an active stabilization mechanism. Knowing the resonant frequencies allows the design of passive isolation for the most significant frequencies.

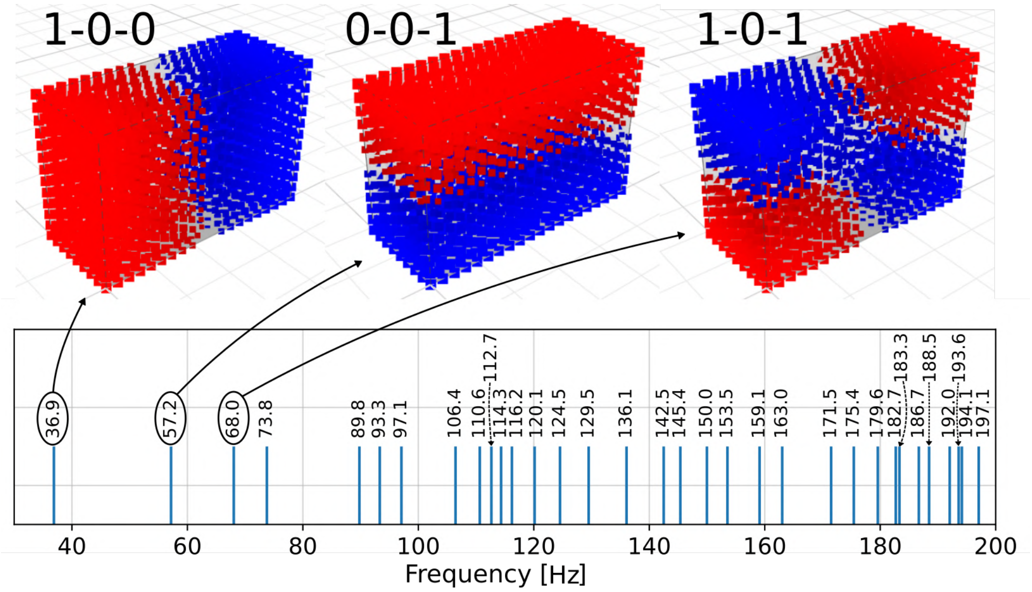

Figure 4.10: The diagram shows the calculated resonance modes for the cavity room using Eq. 4.1, for modes up to $n_{rx,\ ry,\ rz} = 3$. The room dimensions are $L_{rx} = 4.65$ m, $L_{ry} = 1.91$ m, and $L_{rz} = 3.0$ m. Additionally, the diagram illustrates the shapes of the three lowest frequency modes at maximum pressure, depicted in red and blue for better visualization. These mode shapes were calculated using [161].

An approximate formula for the speed of sound as a function of temperature is given by $v_s(T) \approx 332 + 0.6T$, where T is the temperature in degrees Celsius. Using this, along with the formula

$$f = \frac{v_s}{2}\sqrt{\left(\frac{n_{rx}}{L_{rx}}\right)^2 + \left(\frac{n_{ry}}{L_{ry}}\right)^2 + \left(\frac{n_{rz}}{L_{rz}}\right)^2}, \tag{4.1}$$

one can calculate the room resonances, where the $n_{rx,\ ry,\ rz}$ are the modes number $(1, 2, 3, ...)$ and L_{rx}, L_{ry}, L_{rz} are the length 4.65 m, width 1.91 m and height 3.00 m, respectively. Fig. 4.10 illustrates the resonance modes up to $n_{rx,\ ry,\ rz} = 3$ for the cavity room and the shape of the three lowest frequency modes. These calculations were performed to initially check the resonance values. At higher frequencies (above 300 Hz), the resonances become denser and harder to separate, which is in good agreement with the measurements (see the top panel in Fig. 4.11). In Fig. 4.11, five calculated resonances are shown (dashed light blue lines) to demonstrate the agreement of the calculations with the measurements. These resonances are located at 93.3 Hz, 120.1 Hz, 142.5 Hz, 171.6 Hz, and 194.1 Hz.

During the measurements, resonances were induced by speakers positioned outside the room, transmitting through a closed door. To prevent any resonance generation, we aim to create an "echo-free" (soundproof) room by isolating it from external noise sources (e.g., door isolation) and by installing acoustic foams, absorbers, diffusers, and bass traps in the room's interior. The sound absorption coefficient (SAC), defined as the ratio of sound energy absorbed by a material E_{abs} to all incident energy E_{inc}, is given by $\alpha(f) = E_{abs}/E_{inc}$. SAC strongly depends on material properties such as density, porosity, and irregularities. Furthermore, the SAC of any absorber depends on the sound wavelength; thus, larger wavelengths require larger or longer absorbers. For walls made of painted concrete, α ranges from 0.01 to 0.1, depending on the frequency. The sound absorption coefficient α_s for the acoustics foams and absorbers varies from 0.6 at 125 Hz to 0.85 at 250 Hz, and increases for higher frequencies, approaching 1. The active stabilization for the TS-300 operates within the 0.7-200 Hz range, while passive methods are more effective for higher frequencies. Fig. 4.12 illustrates the effect of the room's soundproofing. Measurements were performed with and without active stabilization of the TS-300. The results presented in Fig. 4.11 show that active stabilization significantly reduces noise amplitude.

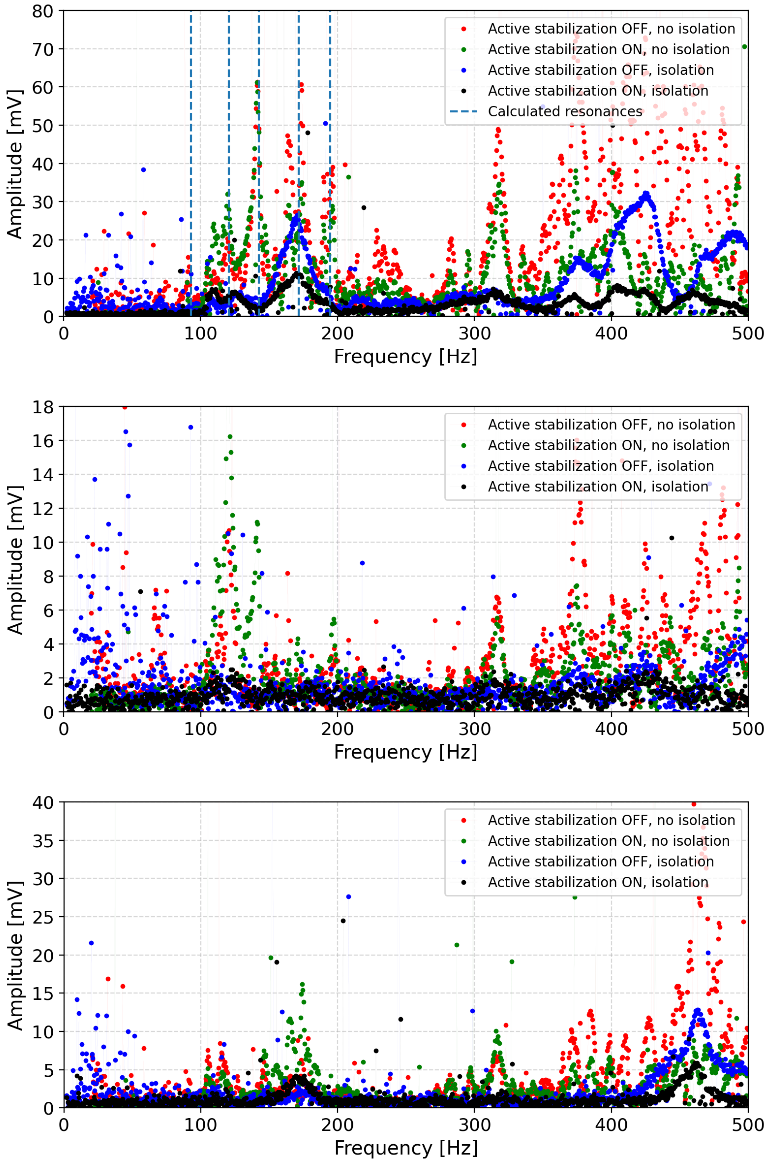

Figure 4.11: Results of the room acoustic resonance measurements using TS-300 internal accelerometers for the vertical direction L_{rz} with five exemplary calculated resonances at 93.3 Hz, 120.1 Hz, 142.5 Hz, 171.6 Hz, and 194.1 Hz **(Top)**, longer horizontal direction L_{rx} **(Middle)**, and shorter horizontal direction L_{ry} **(Bottom)**. After measurements (depicted as "no isolation"), proper acoustic isolation foams were positioned in the room to attenuate the acoustic resonances. Black dots indicate isolation installed with the active anti-vibrational platform mode switched on. In the end, the cavity will reside in an additional acoustic box, resulting in the suppression of resonance even further.

Figure 4.12: Cavity's room before and after acoustic insulation. The black-taped rectangle in the right photo represents a separate foundation on which the Table Stable TS-300 rests during the measurements.

4.3.2. Seismic insulation

Apart from high-frequency acoustic noise, there is low-frequency vibration of the ground, known as seismic noise, which limits both table-top cavities and long-range LIGO interferometers. Because actively isolating the setup in the mHz-Hz frequency range is very challenging, we design and construct passive isolations in the form of separate foundation and the post made of various density materials. As presented in Fig. 4.12 (black area surrounded by black-yellow tape), the cavity will be placed on a separate foundation to decouple the cavity from building movements and disturbances. Additionally, the cavity room is located below the ground surface, which should reduce environmental noises induced by human activity. Furthermore, posts of various density materials (lead, granite, concrete) were constructed to decrease the mHz-Hz noise even further. In the end, the cavity will rest on a TS-300, which actively isolates seismic noise above 0.7 Hz, with potential upgrades to the bandwidth of active isolation by integrating an external seismometer. In our case, we acquired a three-dimensional low-noise seismometer, Guralp 3T-360, which shows self-noise levels as low as 4×10^{-8} m/s^2 in the range of 360 s (2.8 mHz) to 50 Hz, and even better 1×10^{-9} m/s^2 in the range of 0.003 Hz to 3 Hz. Additionally, three one-dimensional 731A/P31 Wilcoxon accelerometers with a bandwidth of 0.05 Hz – 450 Hz will be attached to the exterior of the vacuum chamber for higher frequency corrections.

To assess the impact of the separate foundation and general background noise in the location of the cavity, we invited Janusz Mirek and Lukasz Rudzinski from IGF PAN. They performed measurements using three GeoSIG VE-53-BB (bandwidth 8s-160Hz) seismometers and Nanometrics TCPH (bandwidth 120s-108Hz) under normal operational conditions in the laboratory, including activities such as walking, door opening, and talking. Fig. 4.13 illustrates the cavity room during the measurements. GeoSIG seismometers were positioned at three locations: the building foundation, separate foundations, and a post, for comparative analysis. The detailed results of the seismic measurements in the form of Probabilistic Power Spectral Density (PPSD) are presented in Fig. 4.14 and Fig. 4.15. Seismometers located on the post show slight mitigation of the seismic signal at low frequencies, i.e. below 1 Hz, which was the goal of this design. However, there is a signal amplification at frequencies from 30 to 80 Hz. This won't be a problem because, using TS-300, we can actively mitigate 30-80 Hz. Therefore, the post and the separate foundation reduce the seismic signal to around 0.1 Hz and below, but the effect is not significant. As it is shown in Fig. 4.14 the noise level is lower than the New High Noise Model (NHNM) [159], except in the 1-10 Hz range.

Additionally, Fig. 4.15 compares the signals from two Nanometrics (bottom figures) and Geosig (top figures), demonstrating the PPSD of the acceleration. According to the Nanometrics data shown in Fig. 4.15, for 5 - 20% of the time, the signal is weaker than the NHNM, particularly at lower frequencies, which are crucial for our applications and more challenging to mitigate and cancel.

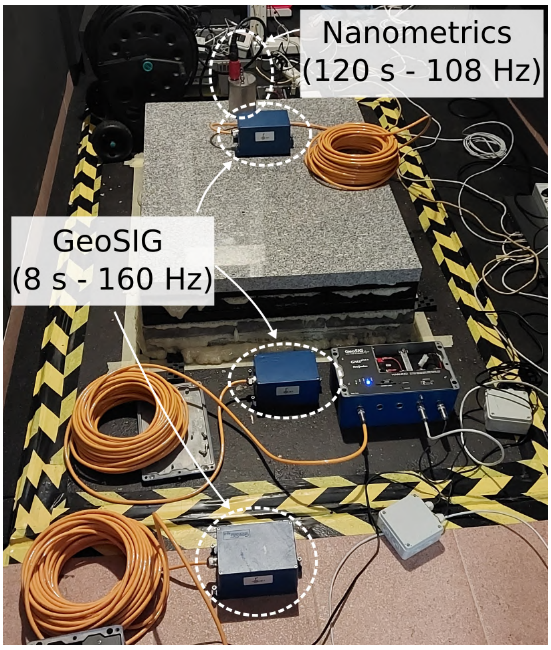

Figure 4.13: Photos taken while measuring the seismic noise in the cavity room. Detectors are highlighted in white ovals. GeoSIGs are positioned in three locations for comparative analysis: on the main building foundation, the separate foundation, and the post built on the separate foundation. Additionally, a low-frequency Nanometrics detector is placed on the post.

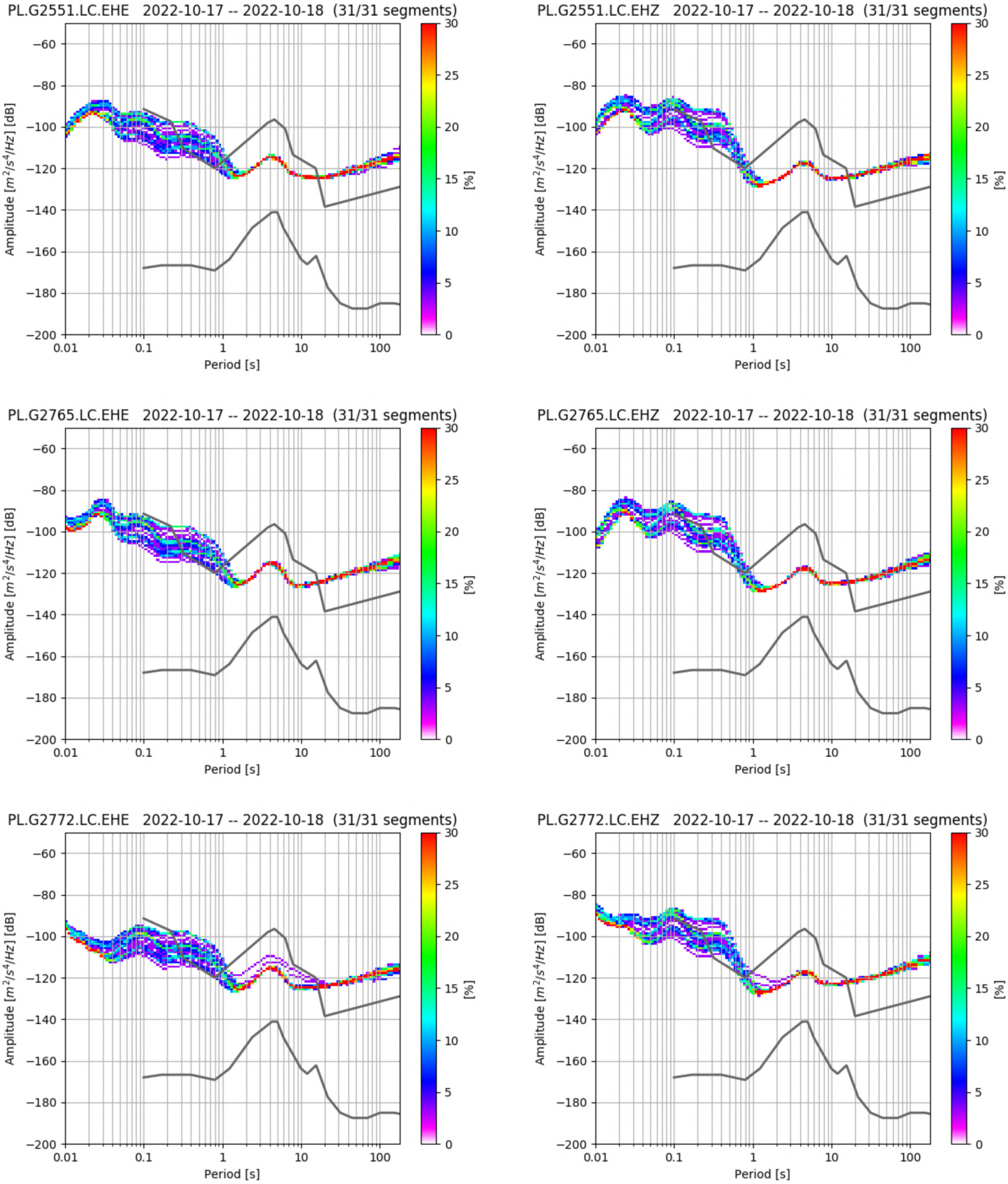

Figure 4.14: Probabilistic power spectral density of the seismic measurements for the **(Top)** post, **(Middle)** separate foundation, **(Bottom)** building foundation for the GeoSIG VE-53-BB. The left column depicts the horizontal direction, and the right column is vertical. Janusz Mirek and Łukasz Rudziński from IGF PAN, Warsaw, recorded and analysed data presented in these figures.

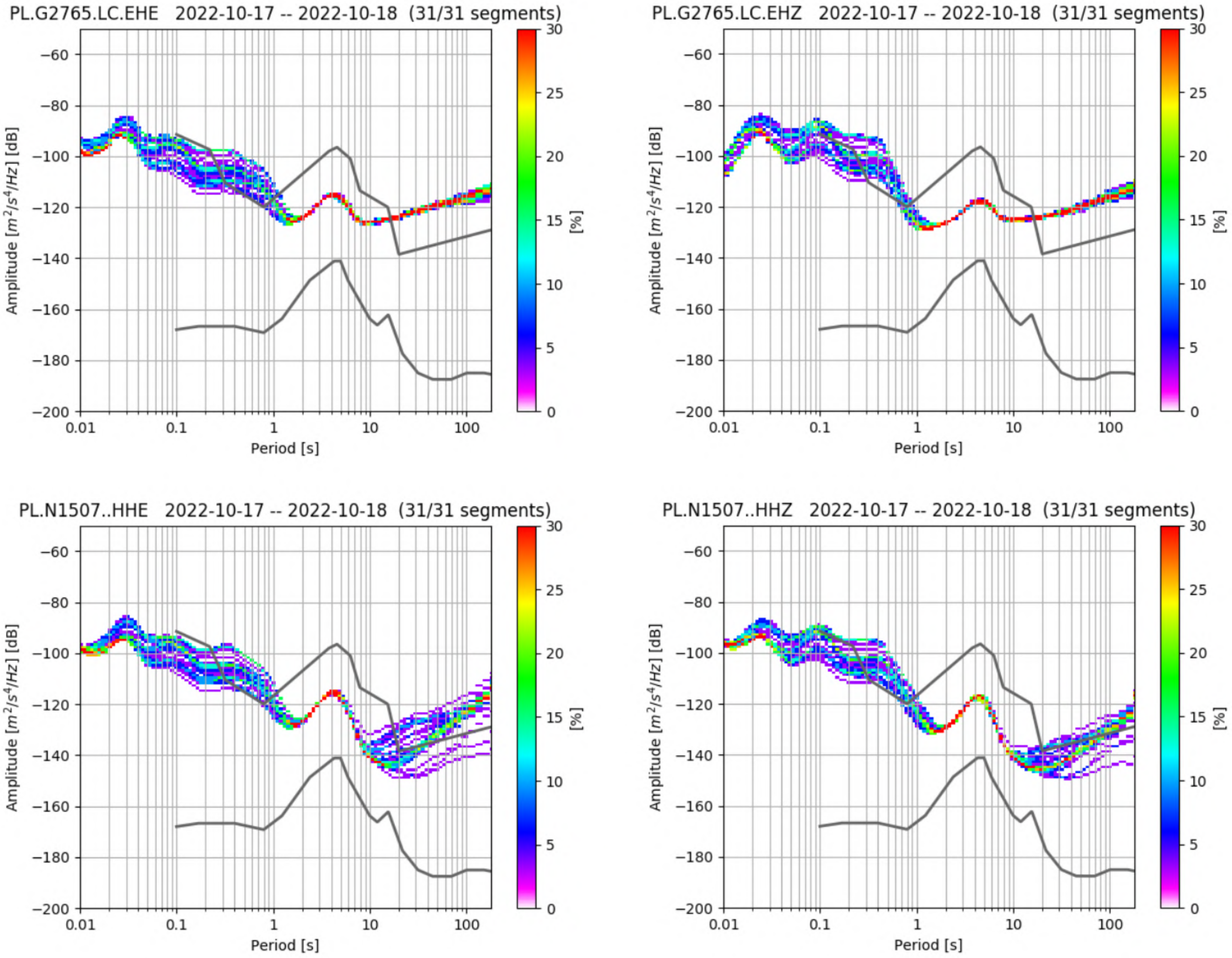

Figure 4.15: Probabilistic power spectral density of the seismic measurements for the post for the **(Top)** GeoSIG VE-53-BB and Nanometrics TCPH **(Bottom)**. The left column depicts the horizontal direction and the right vertical direction. Janusz Mirek and Łukasz Rudziński from IGF PAN, Warsaw, recorded and analysed data presented in these figures.

4.3.3. Transfer function measurements using 689 nm and 698 cavities

Measurements discussed in this subsection were performed on two existing 10 cm ULE cavities, not on the 30 cm ULE cavity that is designed in this work. We analyzed the cavity's frequency response to vibrations to understand its dynamic response to external perturbations, which is essential for optimizing feed-forward techniques. By introducing disturbances to the 698 nm ultra-stable cavity, we measured how specific frequencies and amplitudes of perturbation impact the laser frequency. The quantitative relationship of the variation in laser frequency induced by external perturbations is referred to as the transfer function (TF). The method for measuring the transfer function is illustrated in Fig. 4.16 (Top), as a block scheme. A periodic sinusoidal disturbance between 0.1-500 Hz was applied to the 698 nm cavity breadboard using a modified Visaton BG 20 speaker, with a 3D-printed post attached to its membrane, which was fixed to the cavity breadboard. An accelerometer monitored the speaker's output to measure breadboard movements as a signal amplitude for a given frequency.

To measure the TF of the setup, an unperturbed reference is necessary. As the two lasers' frequency differs by about 9 nm, an optical frequency comb is required to transfer the stability between them. In the experiment the 698 nm laser, was narrowed and stabilized to a cavity. The repetition rate of an optical frequency comb was stabilize to the 698 nm cavity too, while 689 nm laser was locked to the unperturbed cavity. Additionally, 689 nm light was beat noted with the nearest teeth of the comb. In this way, the stability of two cavities with different wavelengths was transferred through the comb. Mechanical modulation of the 698 nm cavity broadens the beat note signal, as observed on a spectrum analyzer (see Fig. 4.17), indicating the vibration's impact on cavity frequency.

Fig. 4.18 shows the speaker with the 3D-printed post (left panel), the speaker positioned below the cavity breadboard during measurement along with the sinusoidal signal recorded by an accelerometer (top right panel), and a spectrum analyzer displaying the detected frequency beatnote in the comb room (bottom right panel). The vibration effect of the speaker was measured by the broadening of the beatnote compared with the one without oscillation. In the middle panel of Fig. 4.17), three exemplary beatnote signals are shown: one without oscillation and two with oscillations at 0.3 Hz and 3 Hz. The final TF is presented in the bottom panel of Fig. 4.17. Fig. 4.17 shows that the largest shift in laser frequency occurs up to 100 Hz, with two maxima at 170 Hz and 250 Hz at higher frequencies. The ultra-stable cavity is almost insensitive to vibrations exceeding 300 Hz. As the TF distribution exhibits non-trivial behaviour, such as linear growth, decrease, or a constant shift (see bottom of Fig. 4.17), it must be digitally programmed into a DDS. The correction signal is then sent directly to an AOM for the final frequency adjustment (as presented at the bottom of Fig. 4.16).

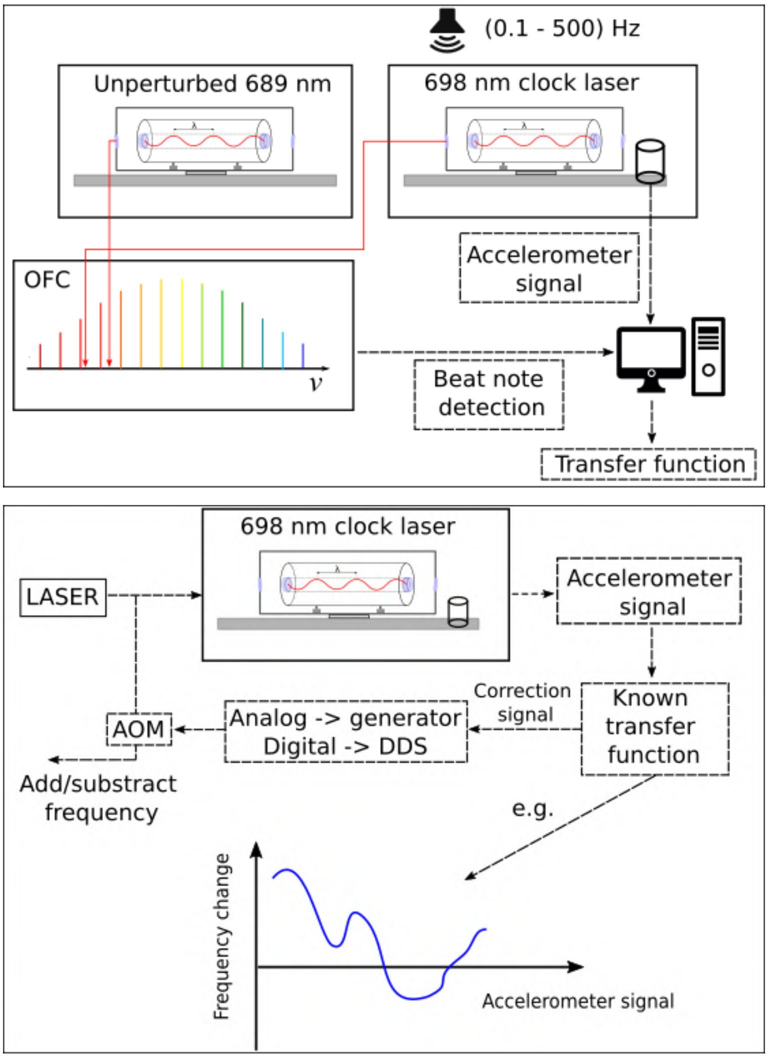

Figure 4.16: **(Top)** Block scheme of the transfer function measurements. The measurements are performed by optically locking a 698 nm clock laser with a 698 nm laser via an optical frequency comb. Induced vibrations by the modified speaker are observed with an accelerometer and beat note with a spectrum analyzer to create the transfer function. **(Bottom)** Schematic diagram illustrating a potential application of the transfer function to the ultra-stable cavity system by sending an analog or digital signal to the AOM, which corrects the frequency.

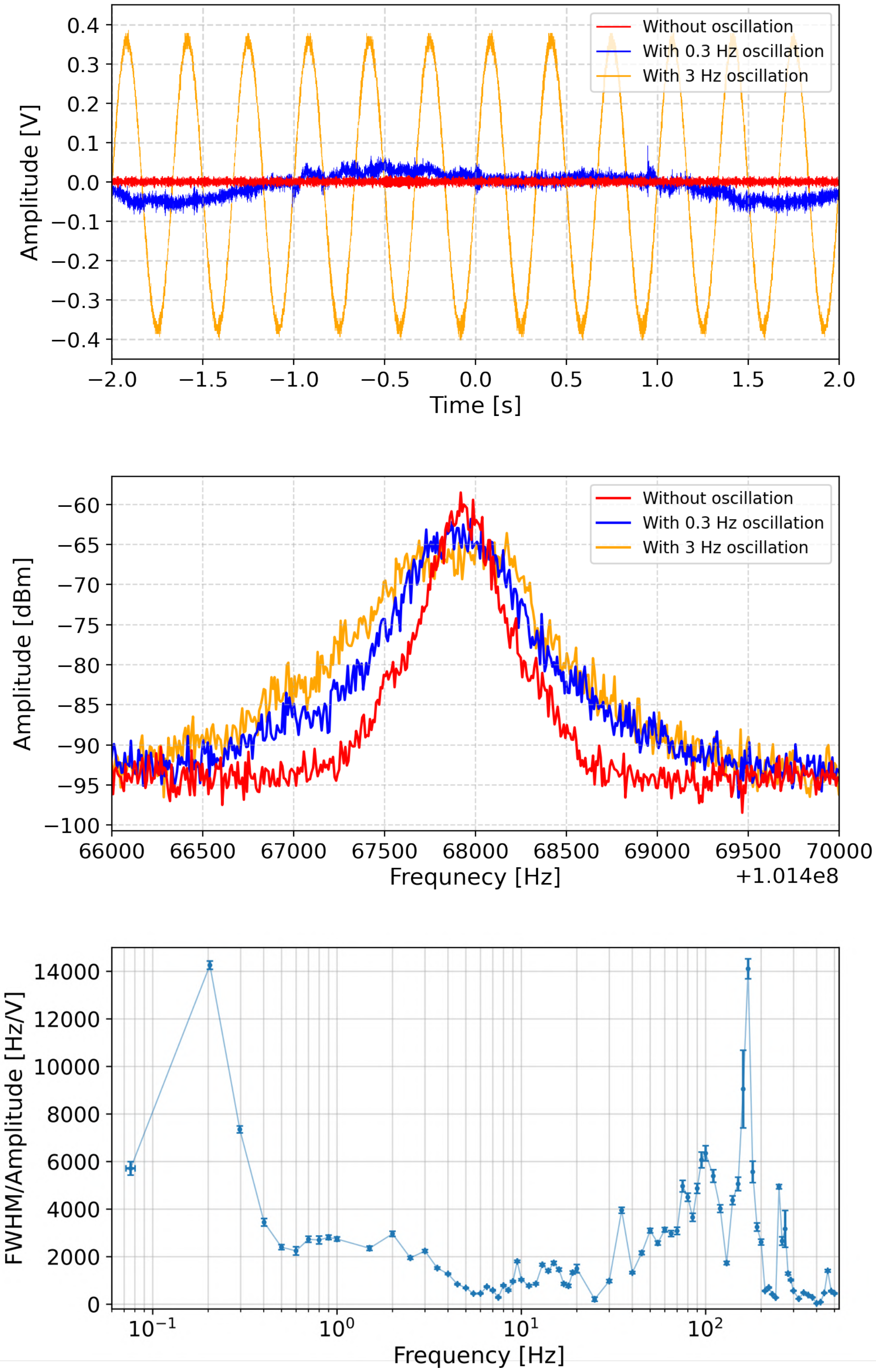

Figure 4.17: **(Top)** Two exemplary sinusoidal signals from the accelerometer located on the cavity's breadboard, together with the background signal (without oscillation). **(Middle)** The influence of corresponding 0.3 Hz and 3 Hz vibrations on the 689 nm laser beatnote broadening. **(Bottom)** The results of transfer function measurements as a ratio of disturbed FWHM beat frequency [Hz] to accelerometer signal amplitude [V] in the range of 0.1 - 500 Hz.

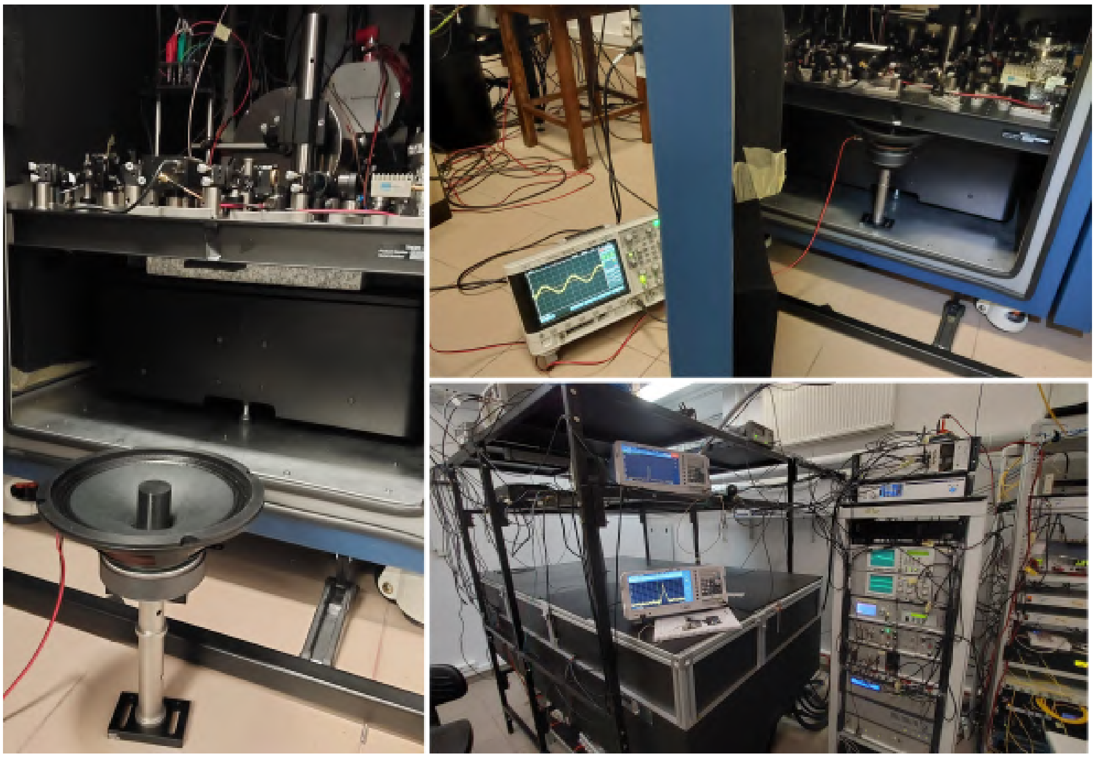

Figure 4.18: **(Left)** Photo of a 3D-printed post glued to the speaker's membrane, which served as a vibration generator, alongside an opened acoustic box of the 698 nm ultra-stable cavity. **(Top right)** Photo of the ongoing measurements where the speaker is placed below the breadboard of the cavity. The oscilloscope shows a sinusoidal signal recorded by an accelerometer placed on the breadboard. **(Bottom right)** Photo of the spectrum analyzer displaying the detected frequency beatnote in the comb room.

4.4. Vacuum chamber and thermal shields

4.4.1. Vacuum chambeer design

The performance of any apparatus using light for measurement purposes may also be constrained by the vacuum level within the hosting chamber. The fluctuating number of molecules along the light trajectory affects the optical path length L_{optical} due to the variation of the optical refractive index n, and it is connected with the physical cavity length by $L_{\text{optical}} = nL$. The refractive index as a function of temperature T and pressure p is described by the corrected Edlen equation [162, 163].

$$n - 1 = \frac{p(n-1)_s}{96095.43} \frac{[1 + 10^{-8}(0.601 - 0.00972T)p]}{1 + 0.0036610T}, \tag{4.2}$$

$$(n-1)_s = 3 \times 10^{-8} \Big[8342.54 + \frac{2406147}{130 - 1/\lambda^2} + \frac{15998}{38.9 - 1/\lambda^2} \Big], \tag{4.3}$$

where λ is the laser wavelength equals 1.55 μm. According to Eq. 4.2, the refractive index in $T = 293$ K is

$$n - 1 \approx (2.43 \times 10^{-9}/\text{Pa})p. \tag{4.4}$$

This gives a connection between the fractional frequency instability and pressure variation Δp

$$\frac{\Delta \nu}{\nu_0} = \Delta n \approx (2.43 \times 10^{-9}/\text{Pa})\Delta p. \tag{4.5}$$

To achieve the calculated theoretical thermal limit of 4.83×10^{-17} at one second, one must provide a pressure fluctuation of $< 1.98 \times 10^{-8}$ Pa. Therefore, the cavity must reside in the ultra-high vacuum (UHV). Fig. 4.19 illustrates the cavity vacuum chamber with the most important elements to preserve the required vacuum level. The optical elements necessary for mode-matching, PDH, etc., will be on the optical breadboard surrounding the vacuum chamber. The entire chamber is made of aluminium, which exhibits high thermal conductivity, allowing for isotropic temperature distribution. Additionally, the top part of the vacuum chamber is made from a single piece of aluminium, which provides better thermal isotropy and decreases the probability of leakage compared to a chamber made of individual walls. The top left panel in Fig. 4.19 shows a 3D view of the pumping elements of the vacuum system. Since the chamber is made of aluminium, an adapter to CF is necessary. The adapter to CF will be connected to the chamber using an indium seal. The rest of the elements are typically connected via a tee fitting, a valve for turbo pumping, and a 20 l/s ion pump, which will maintain the vacuum during the experiment. The bottom left panel of Fig. 4.19 shows how the glass windows structure will look. The surface of the viewports is tilted to prevent unwanted etalons, as seen in the bottom left panel in Fig. 4.19. The bottom right panel of Fig. 4.19 shows the connection scheme between the top and bottom parts of the chamber with an indium wire.

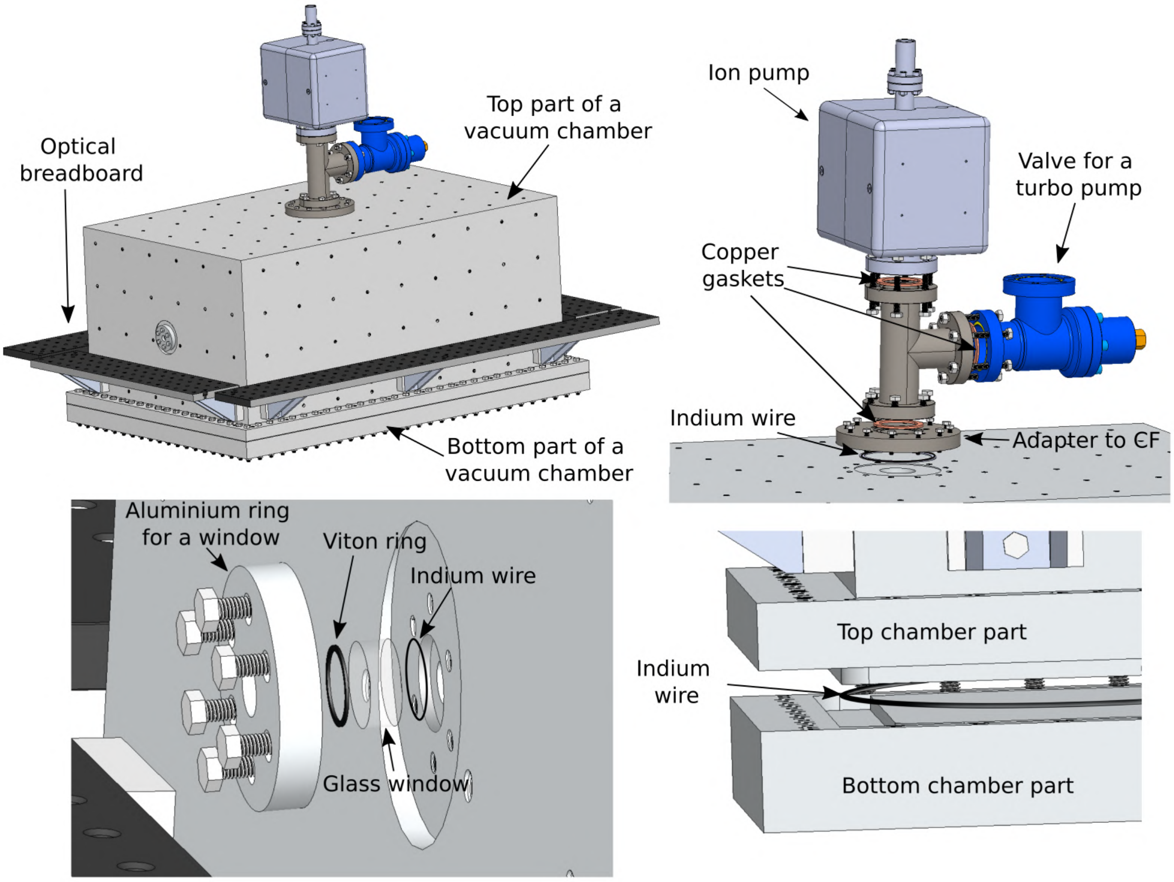

Figure 4.19: 3D model of the vacuum chamber setup with an exploded view of the crucial elements necessary to achieve and sustain an ultra-high vacuum.

4.5. Thermal shields

There are three main types of heat transfer: conduction, convection, and radiation [164]. In the case of an ultra-stable cavity, radiation is a major source of heat transfer. To decrease the amplitude and rate of heat transfer, i.e. temperature changes, the cavity is additionally enclosed within three chambers (see Fig. 4.20). The first chamber, the active shield, lies on Peltier modules, which stabilize the temperature at the cavity's zero-crossing point. The other two inner chambers, in Fig. 4.20 called as passive shields, lie on glass balls. The two passive shields are designed to extend the timescale of temperature fluctuations. The whole setup achieves a time constant of > 10 days [165]. As ultra-high vacuum (UHV) guarantees a negligible effect of convection, conduction is significantly reduced by using glass balls between each shield layer, which provides a small contact surface and low thermal conductivity $\kappa \sim 1$ W/mK. Therefore, the heat exchange is due to radiation between consecutive thermal shield layers. The radiative heat flow $\dot{q}_{\mathrm{rad}}$ from the surfaces area A is described by the Stefan-Boltzmann law $\dot{q}_{\mathrm{rad}} = \sigma_{\mathrm{SB}}\epsilon A T^4$, where σ_{SB} and ϵ are the Stefan-Boltzmann constant and emissivity, respectively. In the case of the radiative heat flow between two equal and parallel surfaces with temperatures T_1 and T_2 ($T_2 > T_1$), and emissivities ϵ_1 and ϵ_2, it is described as [164]

$$\dot{q}_{rad} = \frac{\sigma_{SB} A (T_2^4 - T_1^4)}{1/\epsilon_1 + 1/\epsilon_2 - 1}. \tag{4.6}$$

For more sophisticated cases, such as different geometries, calculating the so-called view factor between those surfaces is required [166]. Eq. 4.6 indicates that emissivity must be minimised. Usually, to achieve high reflectivity (low emissivity), people use superinsulation foil, golden-coating or high-quality surface polishing. In this work, the thermal shields and vacuum chamber were manufactured and polished to below Ra 0.3 and 0.5, respectively. Moreover, to preserve isotropic temperature distribution, the vacuum chamber and thermal shields are made of aluminium alloy PA-13/AW-5083, which exhibits a high thermal conductivity of 117 W/mK. For comparison, stainless steel, a commonly used material for UHV, has a thermal conductivity of 15 W/mK.

Fig. 4.20 illustrates the scheme of the vacuum housing along with thermal shields and the electrical analogy to a low-pass RC filter. The right panel shows a schematic of the behaviour of a sinusoidal temperature fluctuation on the active shield and the subsequent passive shields.

Fig. 4.21 presents the 3D design of the cavity thermal shields and the ultra-stable cavity with invar-teflon support structure. Fig. 4.22 illustrates the top and side views of the ultra-stable cavity's support structure and thermal shields. The Peltier modules, shown in the bottom panel of Fig. 4.22, adjust the temperature of the internal layers to match the zero-crossing temperature. To manage the heating or cooling of the Peltier modules, we will install several resistance thermometers Pt1000 at various points, such

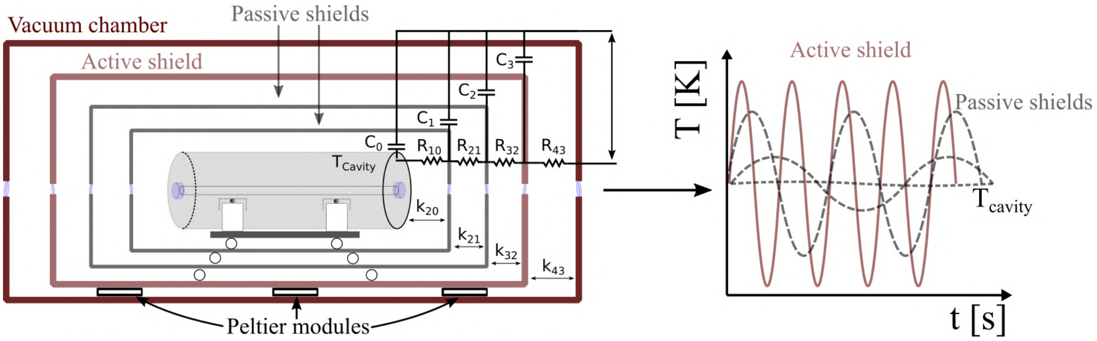

Figure 4.20: **(Left)** Sketch of the cavity's vacuum housing and thermal shields, illustrating how the thermal shielding functions as a low-pass filter for temperature fluctuations. **(Right)** Schematic behaviour of an exemplary sinusoidal temperature fluctuation on an active shield, followed by its attenuation through subsequent passive shields.

as near the panels and on the top part of the last shield (orange layer). By monitoring the actual temperature with Pt1000, we can precisely stabilize the thermal shield to the zero-crossing temperature by controlling the Peltier modules current.

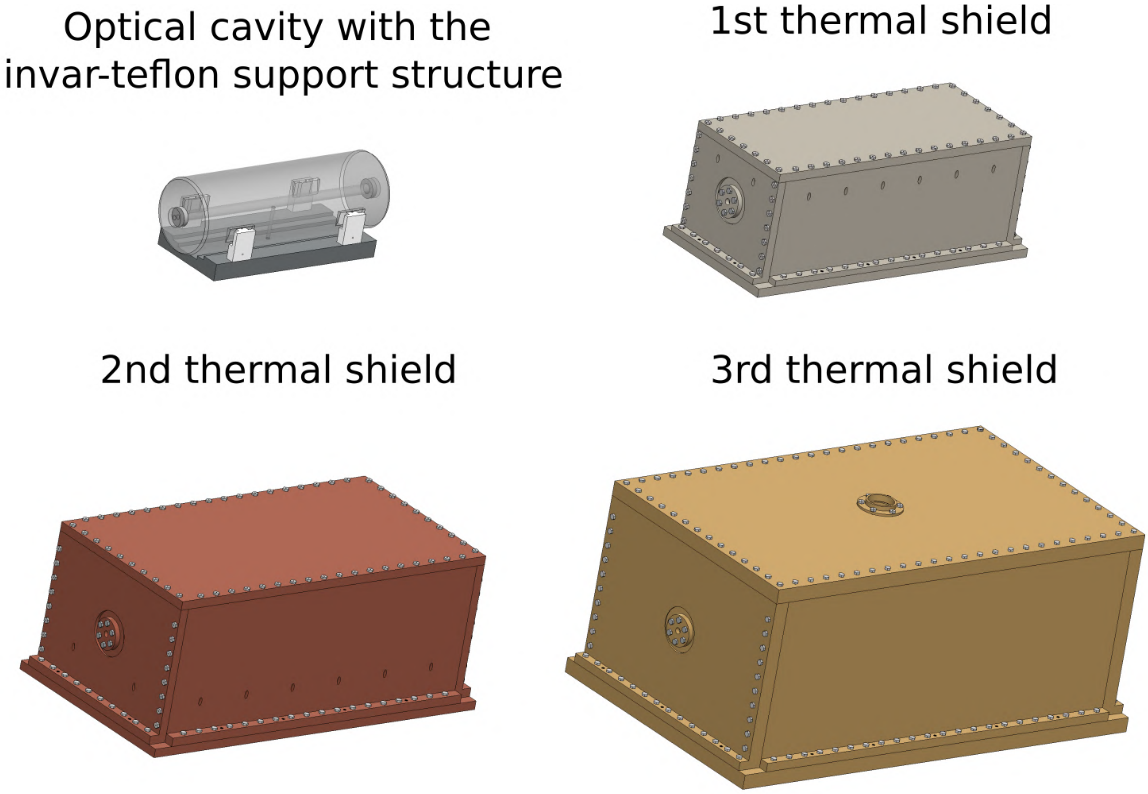

Figure 4.21: 3D design of the cavity, support structure, and consecutive thermal shields. All the shields are made from aluminium. Different colours are used only to distinguish layers.

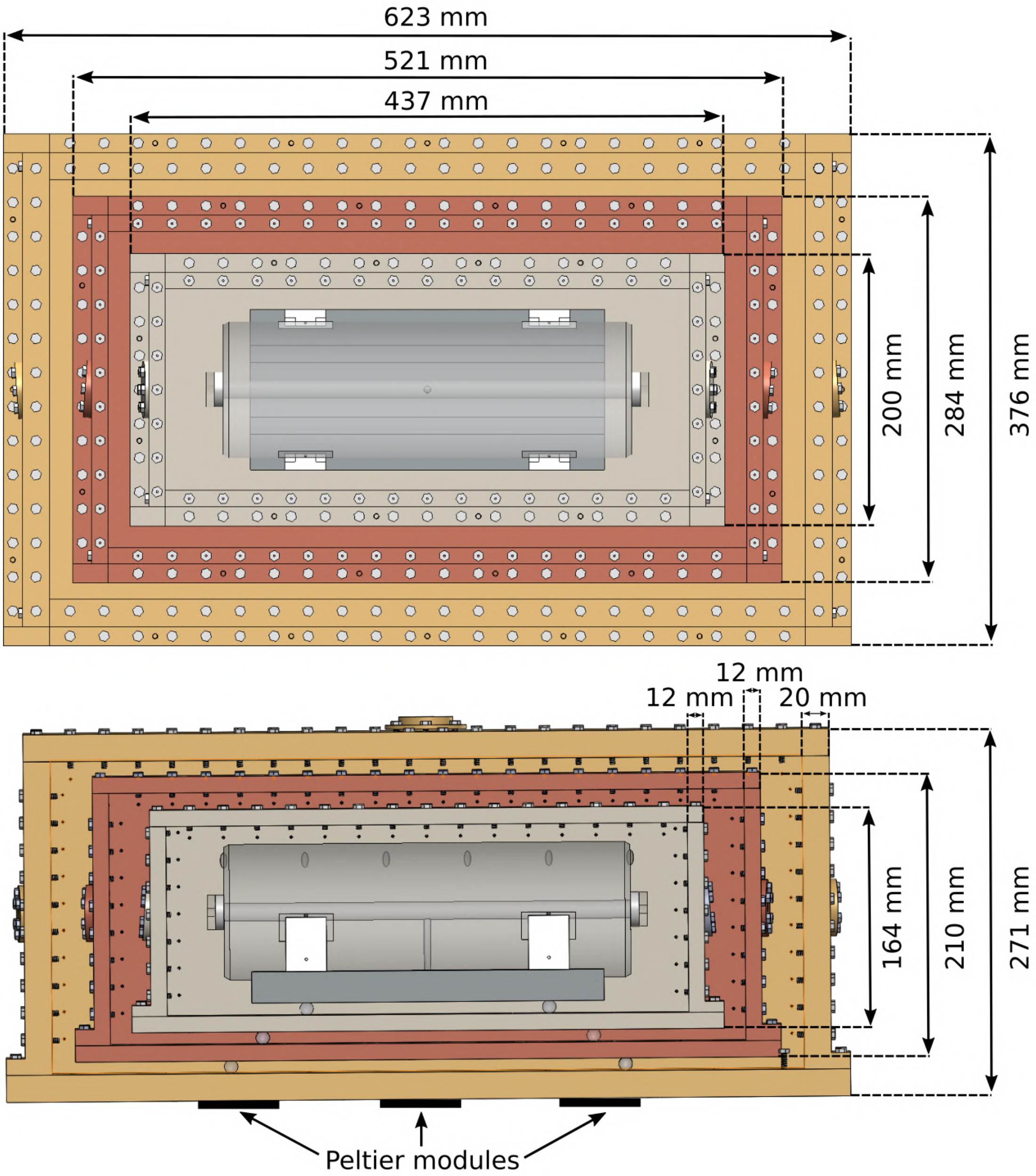

Figure 4.22: Top and side views of the 3D design of the cavity support structure and consecutive thermal shields. All of the shields are made from aluminium. The colours in the illustrations are used only for layer distinction

5. Ultra-stable optical cavities for gravitational waves detection

5.1. Theoretical introduction to the wave equation in general relativity

The General Theory of Relativity (GR) can be expressed through two fundamental postulates: the equivalence of the local gravitational field and non-inertial reference frames, and the invariance of physical laws under coordinate system transformations, known as general covariance. Formulas that follow these postulates are collectively expressed in Einstein's field equation (EFE), which describe how the distribution of mass and energy on the right-hand side of the equation influences the geometry of space-time on the left-hand side [113]

$$R_{\mu\nu} - \frac{1}{2} R g_{\mu\nu} = \frac{8\pi G}{c^4} T_{\mu\nu}, \tag{5.1}$$

where $R_{\mu\nu}$ is the Ricci tensor (m^{-2}), R is the scalar curvature (m^{-2}), $g_{\mu\nu}$ is the metric tensor (dimensionless), G is the gravitational constant ($\mathrm{m}^3\mathrm{kg}^{-1}\mathrm{s}^{-2}$), c is the speed of light (ms^{-1}), and $T_{\mu\nu}$ is the energy-momentum tensor (Jm^{-3}).

The complexity of the metric tensor makes the EFE solution challenging. Therefore, soon after Einstein created the principle of GR in 1916 [167], he derived a linearised field equation [168]. The so-called weak-field approximation states that the complete and complex form of metric tensor $g_{\mu\nu}$ can be simplified to the sum of Minkowski flat space-time tensor $\eta_{\mu\nu}$ and small linear perturbation $h_{\mu\nu}$. This simplification reduces the hyperbolic-elliptic partial differential equations of GR to the linear system. Moreover, an appropriate selection of the gauge helps to solve the problem in a simple analytical form of

$$\Box h_{\mu\nu} = -\frac{16\pi G}{c^4} T_{\mu\nu}, \tag{5.2}$$

where $\Box = \partial^\mu \partial_\mu = 1/c^2 \partial_t^2 - \partial_x^2 - \partial_y^2 - \partial_z^2$ depicts the d'Alembert operator.

Eq. 5.2 has a typical form of the wave equation ($\Box$ Potential = source) as in electrodynamics, where $\Box A^\nu = -\mu_0 J^\nu$. Applying the so-called Newtonian limit, we can prove the physical meaning of $h_{\mu\nu}$ as a gravitational potential V, more specifically $h_{00} \sim 2V/c^2$. The final step interests us as observers and involves finding a solution outside the source, i.e., in a vacuum, where $T_{\mu\nu} = 0$. By solving $\Box h_{\mu\nu} = 0$ with the so-called transverse-traceless gauge condition, we obtain the solution with only two degrees of freedom (known as plus h_+ and cross h_x polarisations). The amplitude of GW can be expressed as

$$h_{\mu\nu} = \frac{2G}{c^4}\frac{\ddot{I}_{\mu\nu}}{d}, \tag{5.3}$$

where $I_{\mu\nu}$ is quadrupole moment of the GW source and d is the distance to the observer. The constant part of Eq. 5.3 is equal $2G/c^4 \approx 10^{-44}$ s^2 kg $^{-1}$ m $^{-1}$. Therefore, the part characterising the source must be big, even for astrophysical objects.

According to Eq. 5.3, at least a quadrupole moment is required for the emission of gravitational radiation. The monopole moment represents the mass-energy of the isolated system, and it cannot change due to the conservation law of mass-energy[1]. Variations in the gravitational dipole moment are also forbidden due to the conservation of momentum within the system. Therefore, the first nonzero second derivative of time in the multipole expansion corresponds to the quadrupole moment. Hence, GW is emitted only by dynamic and non-axially symmetric massive objects. Step-by-step derivation of the formulas from this chapter is presented in textbook [113].

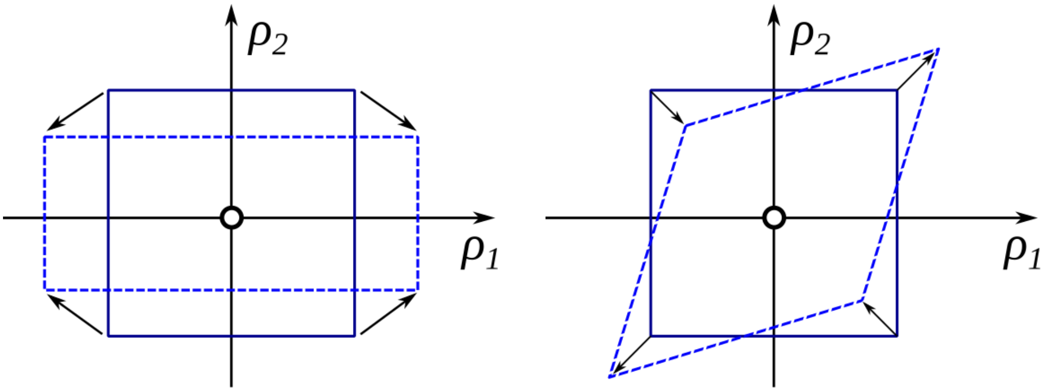

Figure 5.1: Behaviour of the test mass frame under the gravitational wave propagating in z direction, for pure plus h_+ **(Left)** and cross h_x **(Right)** polarisations. However, within the framework of metric theories, there exists an extensive group of alternative theories to tensor gravity theory, which predicts up to six polarisations [169–171].

The behaviour of gravitational waves (GW) is illustrated in Fig. 5.1. It shows that the distances in the x and y directions change simultaneously, with the x direction decreasing while the y direction increases by the same amount. This behaviour is akin to the ordinary tidal effect and can be demonstrated through a comparative analysis of classical tidal acceleration and the Newtonian limit of EFE. Hence, if L_{GW} represents the length of the original unperturbed frame, propagating gravitational waves induce a total change in both directions, resulting in $2\Delta L_{GW}$. This change is referred to as GW strain and it is denoted simply as strain

---

[1] This is analogous to electromagnetism, where the total charge cannot vary, and thus monopolar radiation does not exist. Variations of the dipole moment are necessary for the electromagnetic radiation.

$$h = \frac{\Delta L_{GW}}{L_{GW}}. \tag{5.4}$$

To have some understanding of the magnitude of the strain which we aim to observe, one considers two neutron stars (NS) with the lowest allowed NS mass, $M = 1.17\ \mathrm{M}_{\odot}$ [172] separated by a distance of $r_d = 500$ km on their orbits. Additionally, they are situated $d = 20$ Mpc away from the Earth observer, encompassing the entire Local Supercluster. In such a scenario, the detected strain amplitude is on the order of [173]

$$h \approx \frac{2G}{c^4}\frac{2GM^2}{dr_d} = 3.86 \times 10^{-23}. \tag{5.5}$$

Therefore, the required level of precision is equivalent to measuring the distance to the nearest star (α Proxima Centauri) with an accuracy of approximately 9×10^{-8} m, which is comparable to the size of a molecule or the wavelength of extreme ultraviolet light.

5.2. Introduction to the gravitational waves sources and detection methods

Gravitational radiation has a continuous spectrum limited around 10^{-19} Hz from below by the age of the Universe. Its frequency is strictly connected to the characteristic size and dynamics of the individual stars (so-called burst sources) or binary system (inspirals and mergers), such that GW frequency depends on double the orbital frequency $f_{GW} = 2f_{orb}$. The binary systems are expected to be the main source of GW emission, which is already confirmed by the observations [174, 175].

Kepler's law connects the orbital period to the objects' masses when classically treating this binary system. This connection allows us to introduce a reasonable approximation of the maximum emitted frequency by the binary without full relativistic description, known as the innermost stable circular orbit frequency. This frequency is strictly connected to the movement of the binary system components around the centre of mass, such that the gravitational wave frequency is equal [113]

$$f_{ISCO} = \frac{c^3}{6^{3/2}\pi G}\frac{1}{M_{sum}} \approx 4397\Big(\frac{M_{\odot}}{M_{sum}}\Big)\mathrm{Hz}. \tag{5.6}$$

According to 5.6, the maximum frequency of the binary system is determined by their masses $M_{sum} = m_1 + m_2$. Hence, a detector bandwidth is appropriately designed for the desired astrophysical objects. The following important and widely used quantity is a chirp mass [13]

$$\mathcal{M} = \frac{(m_1 m_2)^{3/5}}{(m_1+m_2)^{1/5}} = \frac{c^3}{G}\Big(\frac{5}{96}\pi^{-8/3}f^{-11/3}\dot{f}\Big)^{3/5}, \tag{5.7}$$

where f depicts wave frequency and $\dot{f}$ its evolution. According to the Eq. 5.7, knowledge about f and $\dot{f}$, by looking at the waveform signal (Fig. 5.2), is enough to derive a lower

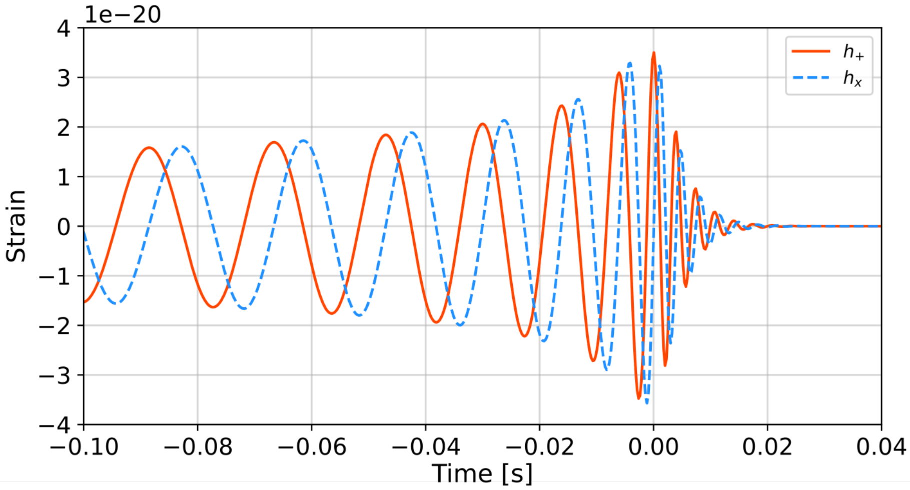

Figure 5.2: Time evolution of a typical strain signal for both plus h$_+$ and cross h$_x$ polarizations for the two black holes merger. The distance from the observer was set at 20 Mpc, and the black hole's masses were 30$_\odot$ each. Figure plotted using PyCBC package [176].

bound for the binary system mass. To summarize, Eqs. 5.5, 5.6, 5.7 define the most fundamental properties of gravitational wave sources and gravitational radiation.

5.2.1. Gravitational wave sources

Gravitational radiation sources may be distinguished by three primary parameters: maximum characteristic strain frequency f_{max} (ultra-low frequencies $<$ nHz, low nHz$-\mu$Hz, average μHz$-$Hz, high Hz$-$kHz, and ultra high $>$ kHz), dynamics of the emission process itself (inspiral, burst and continuous) and the origin of the gravitational radiation sources (stochastic, astrophysical or cosmological). In this section, I will share a general view of the GW sources based on the emitted maximum strain frequency. According to Fig. 5.3 the lowest frequency (except for stochastic background which probably covers whole spectrum up to 10^{-19}) is generated by supermassive black holes mergers (SMBH - SMBH) [202], because of their high masses exceeding 10^6M$_\odot$. The most probable act of emission happens during a collision of galaxies, which have SMBHs in their centres [210].

The second significant range consists of μHz$-$Hz waves covering astrophysical objects, such as compact binaries (white dwarf (WD) binaries, AM CVn and Ultra-compact X-ray binaries) [205, 211], extreme mass ratio inspirals (EMRI) which happen when a compact object, e.g. WD, NS or black hole (BH) is falling into the SMBH [203, 212], and extreme mass ratio bursts (EMRB) when lower massive component of a binary has high eccentric orbit, and consequently it burst GW during each pericenter passage [204]. The last average frequency sources are the intermediate massive black holes mergers (IMBH-IMBH), which is supposed to be the natural link in the transition phase between BH and SMBH. The simulations [213] and observations [214] indicate that the global clusters and dwarf galaxies

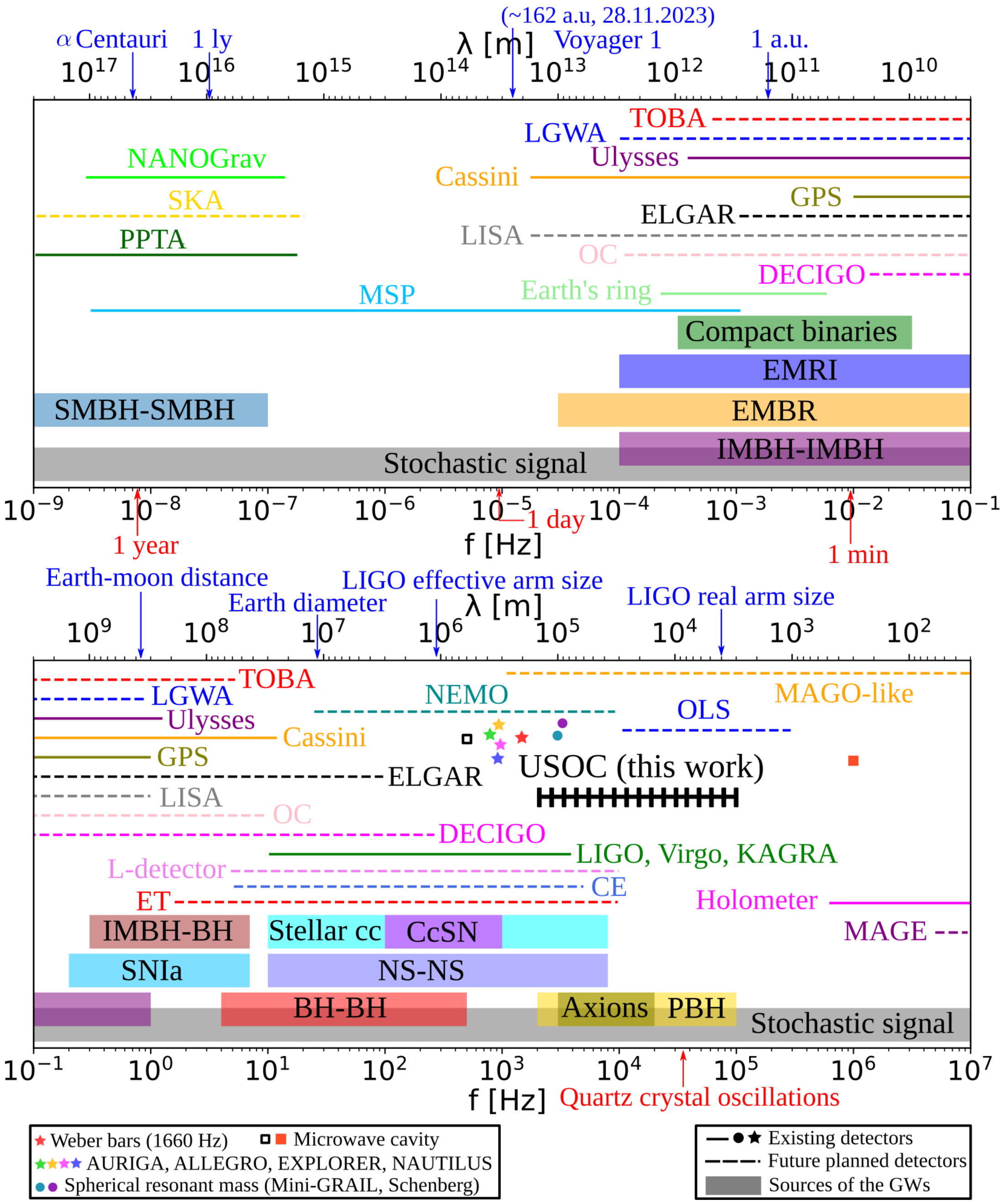

Figure 5.3: The top and bottom graphics illustrate the current status of the existing and proposed detectors with possible GW sources, plotted in the function of the GW frequency (lower x-axis) and wavelength (upper x-axis). Blue arrows show the characteristic objects and their distances compared to the GW wavelength. Detectors: TOBA [177], LGWA [178], Earth normal modes [179], GPS [180], Cassini and ULYSSES [181], LISA [182], OC [14], MSPs [183], SKA [184], NANOGrav [185], DECIGO [186], ELGAR [187], NEMO [188], OLC [189], ET [190], LIGO Livingston and Virgo o3 [191], GEO [192], KAGRA [192], resonant detectors: Auriga [193], Allegro [194], Explorer [194], Nautilus [194], Schenberg Antenna [195], Mini-Grail [196], MAGE [197], Holometer [198], MAGO-like [199], L-detector [200], CE [201]. GW sources: SMBH-SMBH [202], EMRI [203], EMRB [204], compact binaries [205], IMBH-IMBH [202], IMBH-BH [206], SNIa [202], stellar cc [207], NS-NS [208], BH-BH [202], axions and PBH were calculated using equations from [113, 209].

should be the IMBHs' main habitat. However, their existence wasn't confirmed until the LIGO-Virgo detection in 2019 [215]

The next characteristic area lies in-between average and high frequencies zone (Fig. 5.3) and is populated by intermediate-mass black hole (IMBH)-black hole (BH) mergers [206] and type Ia supernova (SNIa) bursts since it is predicted that their explosions are highly asymmetric [2].

The last interesting astrophysical range covers frequencies detected by existing ground-based detectors such as LIGO, Virgo, KAGRA, and phenomena like two black hole mergers (BH BH) [13], neutron star mergers (NS-NS) [217] and stellar core-collapse [216]. In general, GW with frequencies higher than 8-10 kHz is expected to be dominated by non-classical sources, such as primordial black holes (PBH) [218, 219] or axion-based gravitational waves [220, 221]. GW sources beyond the standard model are predicted to exist in high-frequency range, i.e. above 10 kHz. These objects are particularly interesting for the proposed Ultra-Stable Optical Cavity (USOC) gravitational wave detector.

5.2.2. Gravitational wave detectors

Thanks to the theoretical proofs of the detectability of gravitational waves [222, 223], people began developing tools to observe them. The first serious attempt was made by Joseph Weber in his description of the detector based on the antenna reciprocal relationship of quadrupole mass detector [224]. The so-called Weber bars working principle is based on acoustic resonance phenomena in large aluminium cylinders triggered by the propagation of GW. Despite Weber reporting several detections at the 1660 Hz resonance [225], nobody repeated these results, and almost certainly, the detector's sensitivity (at the level of 10^{-16}) was too low for successful detection. While direct detection was highly improbable, indirect observation showed promising results. Thanks to the Arecibo radio telescope, people observed the orbital period decay of a pulsar (the Hulse-Taylor pulsar [226]) in a binary system with other neutron stars. The characteristic shape of the pulsar's period decline agrees with the predictions of general relativity for energy losses through the gravitational radiation emission, as observed from 1981 to 2012 [226, 227]. It was the first experimental proof of the GW's existence.

This discovery provided a solid support for constructing a long-baseline direct GW detector based on Michelson interferometry, following the concepts proposed by Gertsenshtein [228] and Weiss [229]. The general working scheme is quite simple. When the GW passes through the instruments, it extends one arm and shrinks another. Hence, mirrors in a "free-fall configuration"[3] will feel the additional force. The light circulating in both

---

[2] Because of the weak supernove (SN) signal only Milky Way range is detectable in near future. The rate of SNIa events in our galaxy is estimated to be 0.5 ± 0.2 events per century [216].

[3] Frequently used phrase to describe the behaviour of the interferometer mirrors in the direction of the laser beam. These quotes in the literature are used to emphasize the fact that the force between mirrors

arms would travel different distances, which results in a change of the interferometry pattern and the following light intensity on the photodiode. Theoretically, this detector should be more sensitive and broader in the spectra than the resonant analogue. In 1983, a 40 m arm-length interferometer was introduced [230], and later, a longer km-size detector was proposed [231]. Since then, LIGO and later Virgo improved their sensitivity, resulting in the first GW direct detection in 2015 [13]. To date, three observational runs have been performed by the LIGO-Virgo collaboration. Ninety events were confirmed in total, where the vast majority were BHs mergers (BH-BH), along with two black hole - neutron star mergers and two neutron - neutron stars (NS-NS) mergers [174, 175, 232]. The total mass and luminosity distance (i.e. distance from the observer calculated by measuring absolute and apparent magnitudes) of binary systems were in the range from $2.74^{+0.04}_{-0.01}$ $\mathrm{M}_{\odot}$) and 40^{+8}_{-14} Mpc (NS-NS) to 142^{+28}_{-16} $\mathrm{M}_{\odot}$ and $5.3^{+2.4}_{-2.6}$ Gpc, which was the first observational evidence of the existence of a BH with a mass of bigger than 100 $\mathrm{M}_{\odot}$, so-called intermediate-mass black hole (IMBH) [233]. The fourth observation run started in May 2023 and is scheduled for 20 months. KAGRA detector [234] officially joined this campaign.

Because the range of maximum sensitivity for LIGO-like observatories (i.e. LIGO, Virgo, KAGRA, GEO600) spans between ~ 10 Hz and several kHz, plenty of other types of detectors has been proposed to cover the rest of frequency spectrum (Fig. 5.3). Starting from the lowest frequencies in Fig. 5.3, the first detectors are radio telescopes observing the regularity of the pulsars' signal emission. Fifteen years of observational data from a set of 67 pulsars reveal statistically correlated disturbances, identified as gravitational background by NANOGrav [235]. The other three ongoing projects depicted in Fig. 5.3 are Parkes Pulsar Timing Array PPTA [183], binary MiliSecond Pulsar MSP [183] and proposed Square Kilometer Array (SKA) [184]. For the period of less than a day, space satellites and probes were involved, i.e. GPS [180], Cassini and Ulysses [181]. Moreover, big-scale detectors are planned, such as Laser Interferometer Space Antenna (LISA) [182] and DECi-hertz Interferometer Gravitational-wave Observatory (DECIGO) [186], and optical clocks [14] sensitive to the GW's induced Doppler shift. Planet scale detectors were also proposed to observe GW, namely Lunar Gravitational-Wave Antenna (LGWA) [178] and Earth's ring's [179] as a planet-size resonant object in analogy to Weber bars [224]. Another approach requires using atom interferometry like the European Laboratory for Gravitation and Atom-interferometric Research (ELGAR) [187]. The only existing room-scale experiment for mHz waves is based on modulation and up-conversion of GW frequency by using TOrsion-Bar Antenna (TOBA) [177] [4]. Detectors larger in

---

in the optical axis is so negligible that we can treat them as free-falling in this direction.

[4] It's worth mentioning that authors of the paper [177] did not address the thermal noise of the substrates and coatings of the mirrors, which should have significantly decreased the sensitivity comparing to the reported values.

size and, therefore, more sensitive than LIGO are proposed in the range from Hz to kHz. These include the Neutron Star Extreme Matter Observatory (NEMO) [188], the L-detector [200], the Cosmic Explorer (CE) [201], and the Einstein Telescope (ET) [190]. Frequencies beyond LIGO range are filled by Optically Levitated Sensors (OLS) [189], Holometer [198] and Multi-mode Acoustic Gravitational wave Experiment (MAGE) [197]. For the frequencies beyond the spectrum shown in Fig. 5.3, gravitational radiation signal is restricted by the cosmic microwave background observations around $<10^{-15}$ Hz [236]. At the frequencies higher than 10^7 Hz plenty of detectors are proposed or already built [237–240].

In this work, we propose to use ultra-stable cavities (USOC in Fig. 5.3) as a gravitational wave resonant detector to fill the range between a typical LIGO-like interferometer and OLS. Therefore, our detector will be able to detect both astrophysical events such as neutron star mergers (NS-NS) and more exotic sources (PBH and Axions).

5.2.3. Characteristic strain, amplitude and energy density explained

Fig. 5.3 shows only typical signal frequencies and detector bandwidth frequencies without considering gravitational radiation amplitude. However, three typical amplitude-like quantities can be plotted to demonstrate the detector's performance compared to the source signal. First is characteristic strain, denoted as h_c, which is a dimensionless quantity formulated to consider the integration of the signal from the periodic, inspiralling GW sources. The major benefit of this approach is the fact that the vertical distance between the curves is directly associated with the signal-to-noise ratio (S/N) as follows [202]:

$$(S/N)^2 = \int_{-\infty}^{+\infty} \left[\frac{h_c(f)}{h_n(f)}\right]^2 d(log f), \tag{5.8}$$

where h_n indicates detector noise amplitude. On the other hand, h_c does not show the instantaneous amplitude of the gravitational wave. This aspect is properly represented by the amplitude spectral density (ASD) $\sqrt{S_h(f)}$ [unit $1/\sqrt{\text{Hz}}$]. Relation between $h_c(f)$ and $S_h(f)$ is $h_c(f) = \sqrt{S_h(f)f}$.

The last quantity is energy density ρ_{gw} defined by T_{00} component of the energy-density tensor in Eq. 5.1. Nevertheless, instead of ρ_{gw} the dimensionless GW density per logarithmic frequency interval is commonly used [241]

$$\Omega_{GW}(f) \equiv \frac{1}{\rho_c}\frac{d\rho_{gw}}{d\ln f}, \tag{5.9}$$

where ρ_c is the critical density for which the Universe has Euclidean spatial geometry. Therefore we may treat ρ_c as a normalisation factor equals $\rho_c \equiv 3c^2H_0^2/8G\pi$, where H_0 is the Hubble constant which varies from (67.4 ± 0.5) km s^{-1} Mpc^{-1} [242] to (74.03 ± 1.42) km s^{-1} Mpc^{-1} [243].

The choice of the GW amplitude representation ($h_c(f)$, $\sqrt{S_h}$, $\Omega(f)$) depends on the phenomena one want to plot. As mentioned, h_c allows us to consider signal integration and $\sqrt{S_h}$ gives the instant strain value, and it is connected to the RMS. On the other hand, dimensionless energy density is commonly used to describe stochastic GW sources when it is hard to distinguish individual source amplitude. All of the quantities are related by the formula [202]

$$\Omega(f) = \frac{2\pi^2}{3H_0^2} f^3 S_h^2(f) = \frac{2\pi^2}{3H_0^2} f^2 h_c^2(f). \tag{5.10}$$

5.3. Ultra-stable cavity as a resonant detector

According to the antenna reciprocity theorem in electromagnetism, transmitted and detected signals should be treated as identical. Based on that statement and adapting it to general relativity, Weber proposed the first generation of gravitational radiation detectors based on quadruple mass antenna [224]. Therefore, GW passing through the detector triggers the mechanical resonance of the mass antenna. Piezoelectric elements attached to the surface of the mass act as direct signal sensors. Consequently, the resonance induces a piezoelectric effect that can be detected as a current flow [225]. Weber's idea was developed through the years for the detector's different shapes and sizes [193–197] up to recent planet-scale detection proposals [178, 179]. Unfortunately, despite a superb noise reduction resulting in almost reaching a designed sensitivity, there is no undoubted evidence of GWs' events observed by a resonance detector. Recently 5.5 MHz signal was detected by an acoustic bulk detector [244]. However, the authors do not definitely claim that the observed signal is due to gravitational radiation. Nevertheless, the discussions on the feasibility of the MHz GW detection are worth mentioning [245, 246].

The detector proposed in this work, based on a table-top ultra-stable optical cavity, employs the same fundamental principle introduced by Weber but in a new fashion [15]. The idea is to use Fabry-Pérot resonators that have already been independently developed for optical atomic clocks [247] (see Fig. 2.9) without the need to create a new, specific type of detector. As a result, this project can benefit from the progress in optical frequency standards. With some adjustments (described in this chapter), it could become a gravitational wave detector while still improving and simultaneously playing a crucial role as a clock's flywheel.

5.3.1. Principle of observation and mathematical description

We propose two possible operational schemes for USOC for gravitational wave detection. The first scheme does not demand any changes to the current vacuum chamber designs and optical cavities themselves [15]. The only required difference is having two

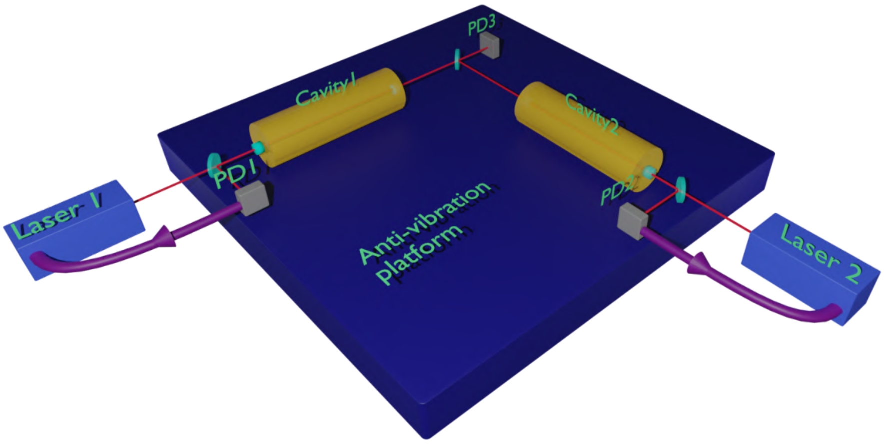

Figure 5.4: Schematic design of the ultra-stable optical cavity GW detector with the perpendicular alignment of the resonator setup for optimal signal detection. The relative length change between the cavities is observed by the frequency or phase difference between the lasers' beams stabilised to the cavities. PD means photo-diode. Picture taken from [15].

cavities instead of one because a reference is needed to detect changes in the cavity length due to GWs (Fig. 5.4). Moreover, to enhance the detection sensitivity, resonators must be aligned perpendicularly to each other, either in the horizontal (as in Fig. 5.4) or vertical plane. In this case, light, which is frequency-locked to one of the cavity modes, works as a distance discriminator. Changing the path of a photon inside the optical cavity by shrinking and extending the spacer length will move the frequency of the cavity mode according to the formula $\Delta L/L = -\Delta\nu/\nu$. With the laser frequency locked to the cavity mode frequency using the Pound-Drever-Hall technique [2], any change in the cavity's length is transferred to the frequency or the phase of the light. Any signal disturbances will be then detected on a photo-diode (PD) as a beat-note signal either with the light uncoupled from the main beams or transferred through both cavities (like in Fig. 5.4). In the former case, the light has high intensity, improving the beat-note detection signal compared to the latter case when the cavity filters the light and only small signal power is transferred for the beat-note observed on a PD (see Fig. 5.4).

In the vicinity of the GW with frequency f_{GW}, a bar-like detector with a resonant frequency f_0 can be modelled as a driven, damped harmonic oscillator [113] in the form of two masses separated by a distance L with a spring. The mass displacement x caused by a plane GW with frequency f_{GW}, flying through the spring and polarised along the spring, can be expressed using the following equation of motion

$$\ddot{x}(t) + 2\beta\dot{x}(t) + 4\pi^2 f_0^2 x(t) = F_{GW}(t), \tag{5.11}$$

where $\beta := \pi f_0 \phi$ is a damping parameter related by definition with spring mechanical loss angle ϕ, and $F_{GW} = -\frac{1}{2}hL(2\pi f_{GW})^2 \cos(2\pi f_{GW} t)$ is a GW force acting on the detecting setup.

According to Eq. 5.11, our model uses classical Newtonian force, which triggers the detector and is an approximation simplifying the entire process. This picture is justified only if the typical size of the detector is much smaller than a typical signal variation, denoted as the gravitational reduced wavelength $\lambdabar = \lambda/2\pi$. According to Eq. 3.11 and the definition of the speed of sound in the material $v_s = \sqrt{E/\rho}$, the ratio of typical lengths is the ratio of sound and light speed as follows: $L/\lambdabar = v_s/2c$. Therefore, if the speed of sound in SCS is $v_{s,\mathrm{SCS}} \approx 8791$ m/s, then $L/\lambdabar \approx 10^{-5} << 1$. Hence, the classical approximation is effective, and there is no need to use the entire relativistic picture.

A gravitational wave passing through the detector manifests as strain h, causing a mirror position x disturbance. In general, a transfer function $G(f)$ transforms the GW strain into an observable effect on the detector—in the case of USOC, this effect is the movement of mirrors. When moving from the time domain represented by $x(t)$ and $h(t)$ to the frequency domain $\tilde{x}(f)$ and $\tilde{h}(f)$, which is the natural language for this analysis, the general solution of Eq. 5.11 is [113]:

$$\tilde{x}(f) = G(f)\tilde{h}(f). \tag{5.12}$$

For the case of Eq. 5.11, we obtain the following transfer function [113]

$$G(f) = \frac{L}{2}\frac{f^2}{(f_0^2 - f^2) + iff_0\phi}. \tag{5.13}$$

The above-mentioned transfer function is perfectly valid for a system of two masses connected by a spring. Although it approximates most radially symmetrical systems, the transfer function for a solid bar differs by a small constant [113]

$$G(f) = \frac{2L}{\pi^2}\frac{f^2}{(f_0^2 - f^2) + iff_0\phi}. \tag{5.14}$$

The optimal sensitivity to GWs achievable by the system, expressed as the GW strain-equivalent power spectral density $S_h(f)$, is connected to the PSD of the noise within the system $S_x(f)$, through the following formula

$$S_h(f) = \frac{S_x(f)}{|G(f)|^2}. \tag{5.15}$$

Brownian thermal noise of the cavity spacer, which is the resonant body of the detector (Eq. 3.10), and the formula for transferring strain to the mirror's displacement (Eq. 5.14), have a similar resonant-like structure with the same value of f_0. Hence, sensitivity to strain is cancelled due to thermally-induced resonant noise, as shown in the transfer function formula (Eq. 3.10) and in Fig. 5.5 (black dotted line). Therefore, the spacer alone does not behave as a resonant detector because its sensitivity is flat over the whole spectrum without the typical resonant sensitivity peak. However, the cavity's overall performance is a sum of all elements' contribution, i.e. substrates and coatings (see Eq. 3.35). The

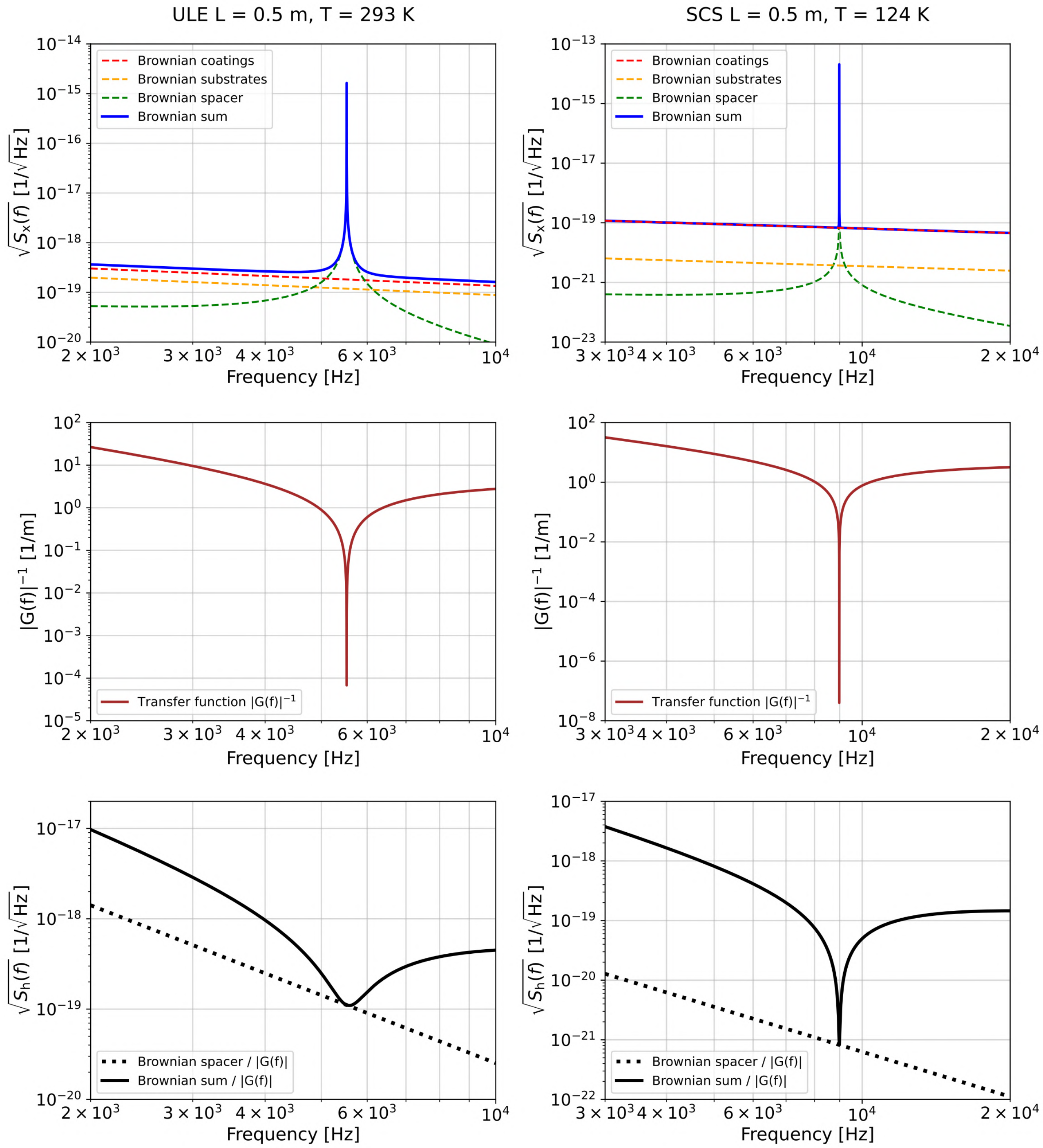

Figure 5.5: The overall Brownian thermal noise $\sqrt{S_x(f)}$ **(Top)**, inverse transfer function $|G(f)|^{-1}$ **(Middle)** and sensitivity for gravitational wave detection $\sqrt{S_h(f)}$ for the whole cavity and spacer alone **(Bottom)**. Two typical spacer materials i.e. ULE **(Left)** and SCS **(Right)** in their zero-crossing temperatures were chosen. Both cavities coatings are dielectric.

contribution of substrates and coatings increases the level of noise (decrease the sensitivity $\sqrt{S_h(f)}$) in the whole spectrum except for resonant frequency (black line in Fig. 5.5). In this scenario, the detector can be named a resonant because of the high sensitivity amplification around f_0 compared to the rest of the frequencies. Fig. 5.5 graphically explained the working scheme of the resonant mass detector. The bottom pictures depict the difference between the Brownian spacer case and overall cavity sensitivity. Therefore, the peak sensitivity is limited by the spacer's thermal properties, and the remaining noises determine the bandwidth.

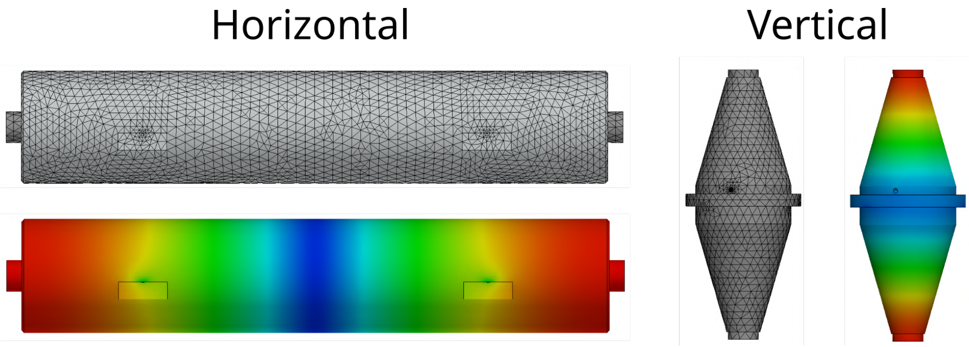

Figure 5.6: Two standard spatial configurations of an ultra-stable optical cavity used in optical atomic clock experiments, i.e. cylindrical shape spacer positioned horizontally and double-cone shape aligned vertically [3]. The picture depicts a 3 D model of the 50 cm long ULE cavity (Horizontal) and 21 cm SCS cavity (Vertical) along with the mesh used for the Finite Element Method (FEM) simulation and the results of fundamental frequency mode f_0 calculations in the optical axis direction. FEM performed in Solidworks.

In the case of USOC, the analytical resonance formula (Eq. 3.11) is not accurate in determining cavity resonance position sufficiently. Therefore, real-case adjustments were made by considering the cavity shape, Earth's gravity field, and support points (Fig. 5.6). Using material constant from Tab. 3.1, FEM simulation was performed for several existing state-of-the-art and future possible cavity set-ups. The Tab. 5.1 shows a comparison between the analytical and FEM calculations of the f_0 position. The mesh resolution is adjusted to the local radius of curvature, ranging from 1.5 mm to 7 mm. Moreover, further analysis is limited to the fundamental mode f_0, ignoring the overtones due to the ring-down limit, which is the next fundamental limitation. Ring-down limit is connected to the Fabry-Perót detector's detectable range within the frequency spectrum, which is constrained by the finite speed of light and the number of roundtrips. The finesse of the detector plays a crucial role in determining the number of photon reflections within the optical cavity before exiting, influencing the feedback to the laser frequency. A higher finesse results in an extended ring-down time for a photon in the cavity and a reduced detector bandwidth. The maximum detectable frequency of gravitational waves, denoted as f_{RD}, for a given finesse $\mathcal{F}$ is bounded by

$$f_{RD} < \frac{\pi c}{\mathcal{F} L}. \tag{5.16}$$

Fig. 5.7 shows a ring-down vs frequency plot with the fundamental acoustic resonance f_0 (dashed lines) of the 0.3 m cavities made from typical spacer's materials. Resonance is calculated analytically using Eq. 3.11, and material constants are taken from Tab. 3.1. It indicates the maximum finesse of the cavity, allowing one to observe the fundamental resonance mode while avoiding the ring-down. Quantitatively it is $\mathcal{F}_{Sapphire} = 174573$, $\mathcal{F}_{SCS} = 209799$, $\mathcal{F}_{NEXCERA} = 255885$, $\mathcal{F}_{Zerodur} = 315512$, $\mathcal{F}_{ULE} = 340818$.

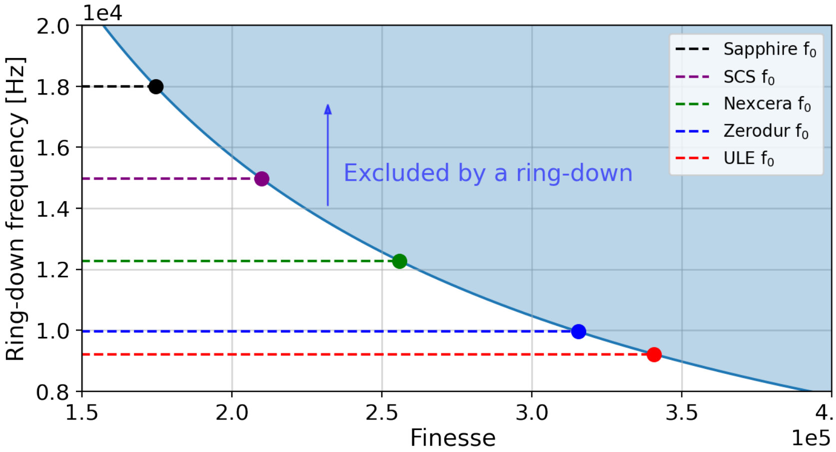

Figure 5.7: Ring-down in the function of finesse with additional fundamental mode frequencies for 0.3 m spacer made of most commonly used materials. The blue curve gives an upper limit for the maximum finesse for a given spacer material to detect fundamental f_0 mode, and the blue-shaded area is the exclude region.

According to the Tab. 5.1 values obtained analytically comparing to the FEM are in every case of material and length lower by ∼200 Hz up to ∼500 Hz. Therefore, the difference is non-negligible when talking about real-life applications, whereas in the worst-case scenario, it is a larger difference than the resonance bandwidth itself.

5.3.2. Gravitational wave sensitivity plots $\sqrt{S_h}$

An ultra-stable optical cavity GW detector can cover the sensitivity range from a single kHz to one hundred kHz. We can manipulate the resonance values with the material and spacer's length. The rest of the noises (mainly coming from coatings) are responsible for the resonance bandwidth, and their reduction is non-trivial. Additionally, the Q-factor is not perfectly known a priori for the particular material, and its experimental value often does not fit the theoretical expectations. Therefore, measurements of the Q-factor are usually required for real validation. That is why one can find in the literature different values for the particular material at a given temperature (see chapter 3.2.5). In

Table 5.1: Comparison between analytical (Eq. 3.11) and numerical (FEM) calculations of the resonance position of ULE, SCS, and sapphire cavities with cylindrical shape and different spacer lengths. The parameters for both calculation and simulation were taken from Tab. 3.1.

	Ultra-low expansion glass (ULE)					
	0.05 m	0.2 m	0.3 m	0.5 m	1 m	2 m
Analytical [Hz]	55300	13800	9220	5530	2770	1380
FEM [Hz]	55700	14100	9500	5830	2890	1540
	Single-crystal silicon (SCS)					
	0.05 m	0.2 m	0.3 m	0.5 m	1 m	2 m
Analytical [Hz]	89800	22500	15000	8990	4500	2250
FEM [Hz]	90200	22700	15300	9330	4790	2430
	Sapphire					
	0.05 m	0.2 m	0.3 m	0.5 m	1 m	2 m
Analytical [Hz]	108000	27000	18000	10800	5400	2700
FEM [Hz]	108000	27300	18400	11300	5540	2980

this section, I will show the GW sensitivity limited by the thermal noises of the USOC detectors in various configurations of length, spacer's and substrates materials and its Q-factor values, coatings materials, beam spot sizes and its heating influence (see chapter 3). A bigger spacer outer radius will also be shown and discussed (see more in chapter 3).

It is worth illustrating the current status of state-of-the-art ultra-stable cavities and their potential strain sensitivity, as is demonstrated in Fig. 5.8. Since no material breakthrough is expected under room temperature conditions, reducing the operating temperature to cryogenic is the most natural solution for improving the performance of stable resonators. Fig. 5.8 depicts the projected GW sensitivity of existing SCS cavities at 124 K, 4 K, and room temperature 48 cm long ULE cavity [3, 29], and presented in this work 30 cm ULE cavity [153]. According to Fig. 3.9, the Q-factor, which determines the thermal stability and strain sensitivity (Fig. 5.8), is significantly higher for the SCS and sapphire than in ULE, Zerodur or NEXCERA (at least 2 orders of magnitude), and increase with lowering the temperature. Therefore, SCS and sapphire are proposed to be the future ultra-stable optical cavity gravitational wave detectors (Fig. 5.9, 5.10).

In further analysis, single-crystal silicon and sapphire will be used at 4 K and at ultra-cryogenic sub-Kelvin regime to demonstrate limitations of the USOC strain sensitivity (Fig. 5.9). An ultra-cryogenic technology is already well-established, as proven by the resonant gravitational wave detector AURIGA, which reached 140 mK in 1996 [248]. SCS cavity and sapphire cavities in ∼4 K operate for at least two decades [5, 8, 30, 249]. Although sub-Kelvin cavities were not yet reported in a peer-review paper, they are

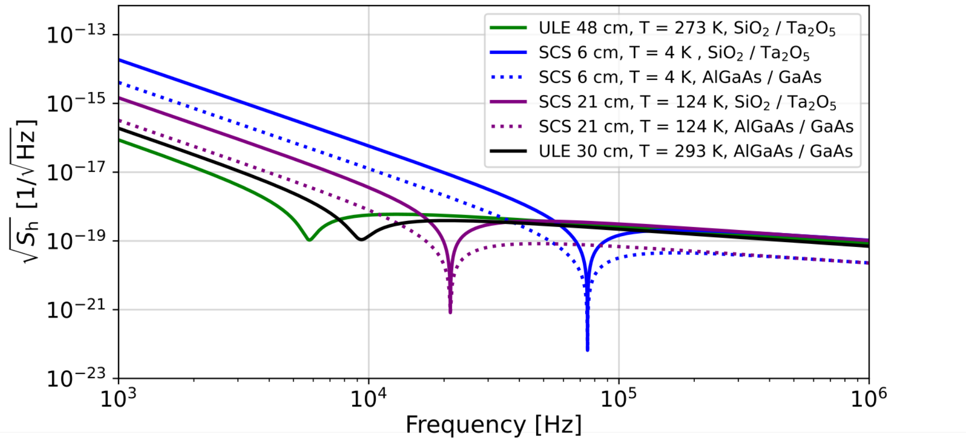

Figure 5.8: Theoretical thermal limits for the gravitational wave sensitivity shown as amplitude spectral density of the strain $\sqrt{S_h}$ for the current best ultra-stable cavities [3, 5], together with the predicted sensitivity for the 30 cm cavity designed in this work (black line) [153].

already working successfully [48]. Fig. 5.9 depicts the sensitivity difference for two values (the worst and the best) of the quality factor at 4 K. Fig. 5.9 shows the difference between 4 K and 20 mK for the best Q-factor, and finally, the predicted difference in the dielectric and crystalline coatings at 20 mK. We see that lowering temperature up to 20 mK gives an order of magnitude better sensitivity than 4 K ($\sqrt{S_h} \sim \sqrt{T}$). All material properties were assumed to be no worse than in the nearest reported temperature. However, only FS shows worse Q-factor and CTE in cryogenics than at room temperature.

Both Fig. 5.9 and Fig. 5.10 depict strain sensitivity $\sqrt{S_h}$ for the five exemplary spacer lengths ranging from 5 cm to 2 m, to show the achievable frequency span covered by USOC, which is additionally drawn in the form of dash-dotted and dotted lines representing residing temperatures of 20 mK and 4 K, respectively (Fig. 5.10). However, the 5 cm spacer is not a fundamental limitation, especially for shorter spacer lengths. There are ongoing efforts to develop very compact and portable cavities. A great example of this work is a 6.3 mm ULE spacer, with the optically contacted FS substrate of 6.5 mm thickness [154]. Due to the similar sizes of the spacer and substrates, this "mini-cavity" will have two relatively close resonance peaks: one from the spacer and the second from the substrates. The resonance peak for the spacer is at $f_{0,\mathrm{ULE}} = 438942$ Hz, and for the substrate, it is at $f_{0,\mathrm{FS}} = 443105$ Hz.

Besides selecting the cavity's component materials and surrounding conditions, one can modify the cavity geometry to enhance its sensitivity. According to the Eq. 3.14 minimum detectable strain may be further improved. Fig. 5.11 (top figure) shows the GW sensitivity dependence on the spacer radius for SCS and sapphire for 4 K and 20 mK for 1 m spacer. In previous calculations, a 5 cm outer radius was set by default for all cavity lengths. Here, we propose using a spacer with a diameter half the size of the

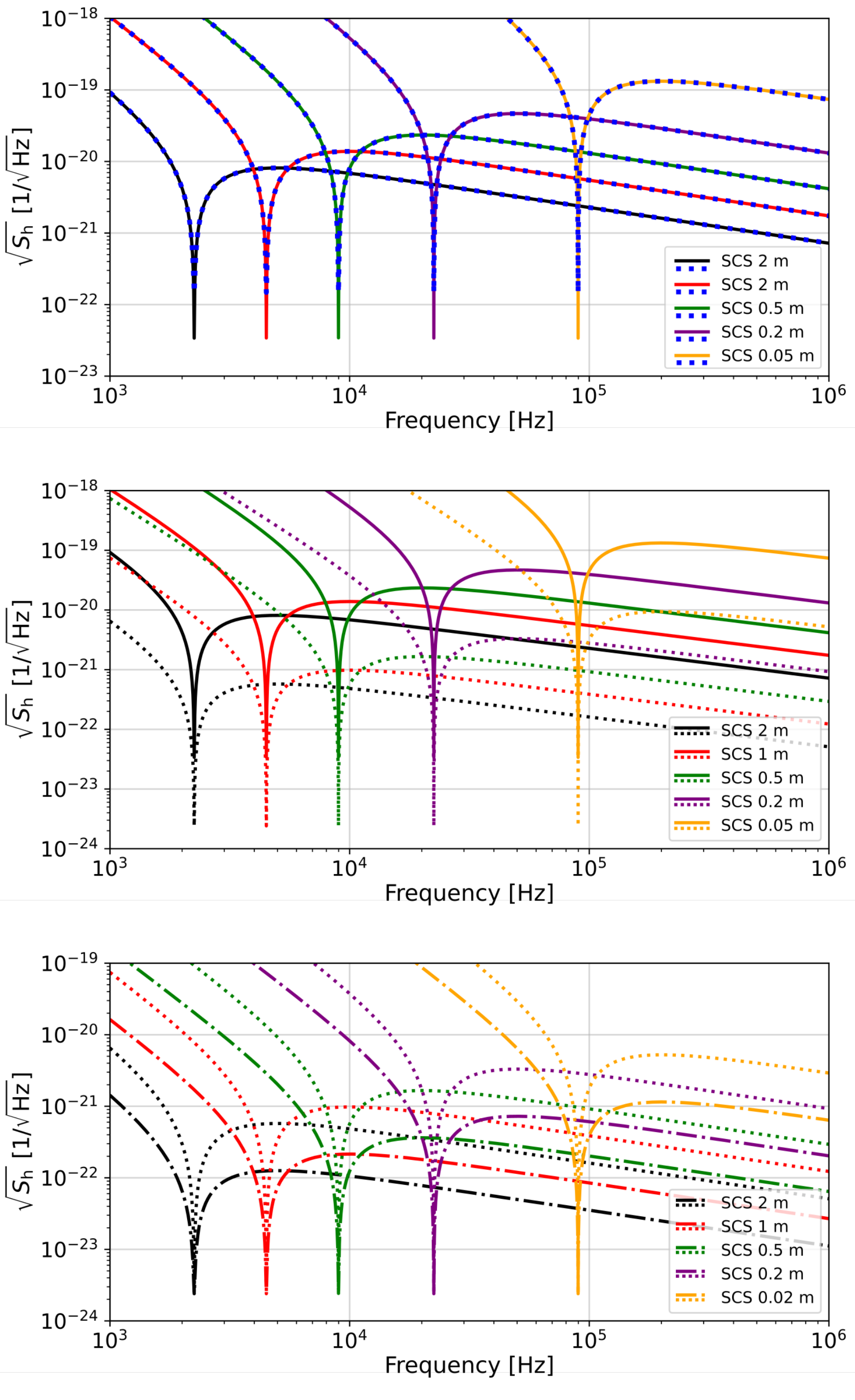

Figure 5.9: Theoretical thermal limits for the gravitational wave sensitivity shown as amplitude spectral density of the strain $\sqrt{S_h}$. The spacer's length determines the possible frequency span of the proposed USOC detector. **(Top)** SCS detector with dielectric coatings residing in 4 K with the most optimistic (solid lines) and pessimistic (blue dashed lines) values of spacer's Q-factor found in the literature (see Fig. 3.9). **(Middle)** SCS detector with dielectric coatings and the biggest spacer's Q-factor residing in 4 K (solid lines) and 0.02 K (dotted lines). **(Bottom)** SCS detector with the biggest spacer's Q-factor residing in 0.02 K with dielectric (dotted lines) and crystalline coatings (dash dotted lines).

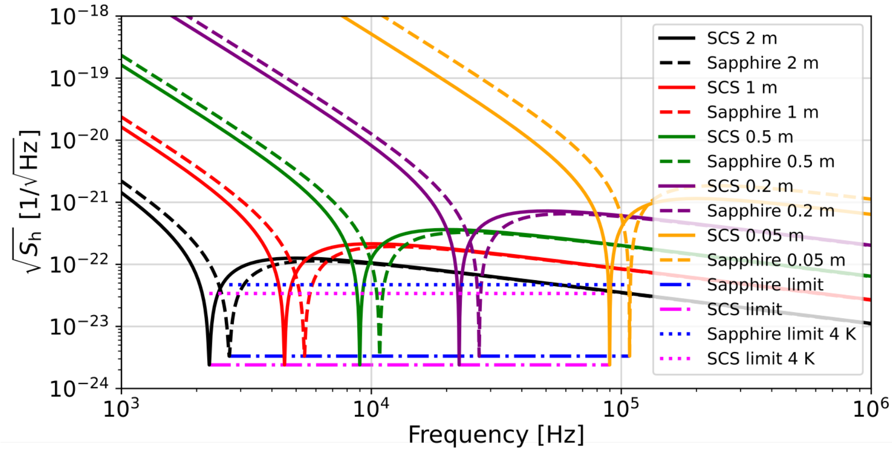

Figure 5.10: Theoretical thermal limits for the gravitational wave sensitivity shown as amplitude spectral density of the strain $\sqrt{S_h}$ for two commonly used spacer's material for ultra-cryogenic conditions (here in 20 mK). Dash-dotted and dotted lines represent thermal limits for the GW sensitivity determined by the spacer's Q factor in 20 mK and 4 K, respectively. Both cavities are supplied with crystalline coatings.

spacer's length. Even further outer radius enlarging is possible but may be unpractical because of the high spacer mass at the end (mass is proportional to the radius squared). For the SCS and sapphire 1 m spacer, the proposed method improves the sensitivity to the GW by a factor of 5 and an order of magnitude for the 2 m long cavity (Fig. 5.11). This process is profitable up to 5 cm outer radius for the 20 cm long spacer.

It was proven that the change of spacer internal and external properties improves the maximum sensitivity to the GW strain. On the other hand, the remaining noises are responsible for the detection bandwidth. Therefore, we can broaden the detectable frequency range by improving cavity substrates and coatings noises (see Fig.5.12).

Fig. 5.12 shows several scenarios for the USOC default (typical size of spacer and beam spot on the mirrors) and enhanced (larger size of spacer and beam spot on the mirrors) detector design. Two extreme SCS spacer lengths, i.e. 2 m and 5 cm in temperature of 20 mK, were chosen to show the bandwidth broadening effect. The top pictures in Fig. 5.12 shows the difference between dielectric and crystalline coatings (solid lines), together with the increased beam spot size on the mirrors (dashed lines). By default, in all calculations, mirror curvature was set to be $\text{ROC}_1 = 15$ m and $\text{ROC}_2 = 20$ m. The convex-concave configuration (here $\text{ROC}_1 = 15$ m and $\text{ROC}_2 = -20$ m) generates a significantly bigger spot size and consequently lower thermal noises (dashed lines). Quantitatively, for 2 m long spacer, the width of the resonance at 10^{-23} increases from ~ 23 Hz in dielectric to ~ 105 Hz in the crystalline coatings. Furthermore, a bigger spot size in convex-concave configuration gives the resonance width of ~ 33 Hz and ~ 154 Hz for dielectric and crystalline coatings, respectively. Increasing the beam spot benefits in

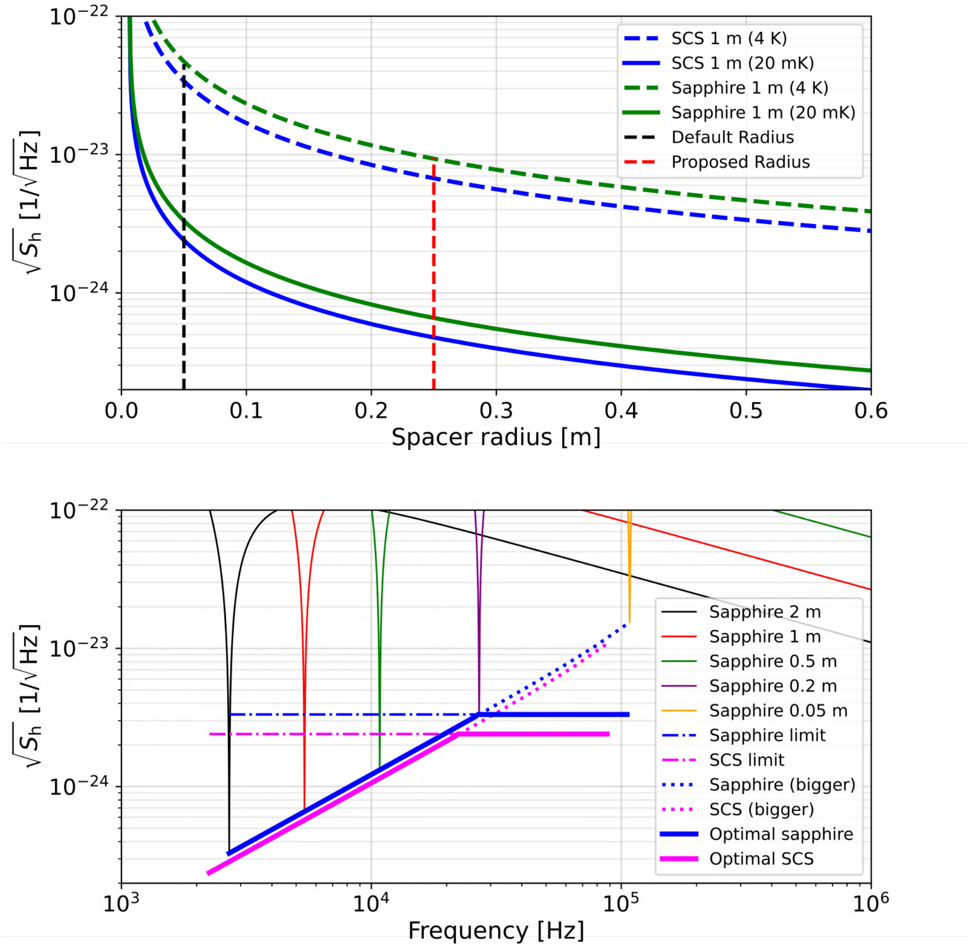

Figure 5.11: **(Top)** Strain sensitivity for spacers made of SCS and sapphire in the function of spacer radius for 1 m long cavity **(Bottom)** Limit of the strain sensitivity for the default spacer radius (dash-dotted line) for sapphire and SCS together with improved sensitivity obtained by the spacer's radius enhancement as one-fourth of the cavity length (dotted line). Sapphire (best) and SCS (best) show the best sensitivity curve (solid line). Cavities are supplied with dielectric coatings.

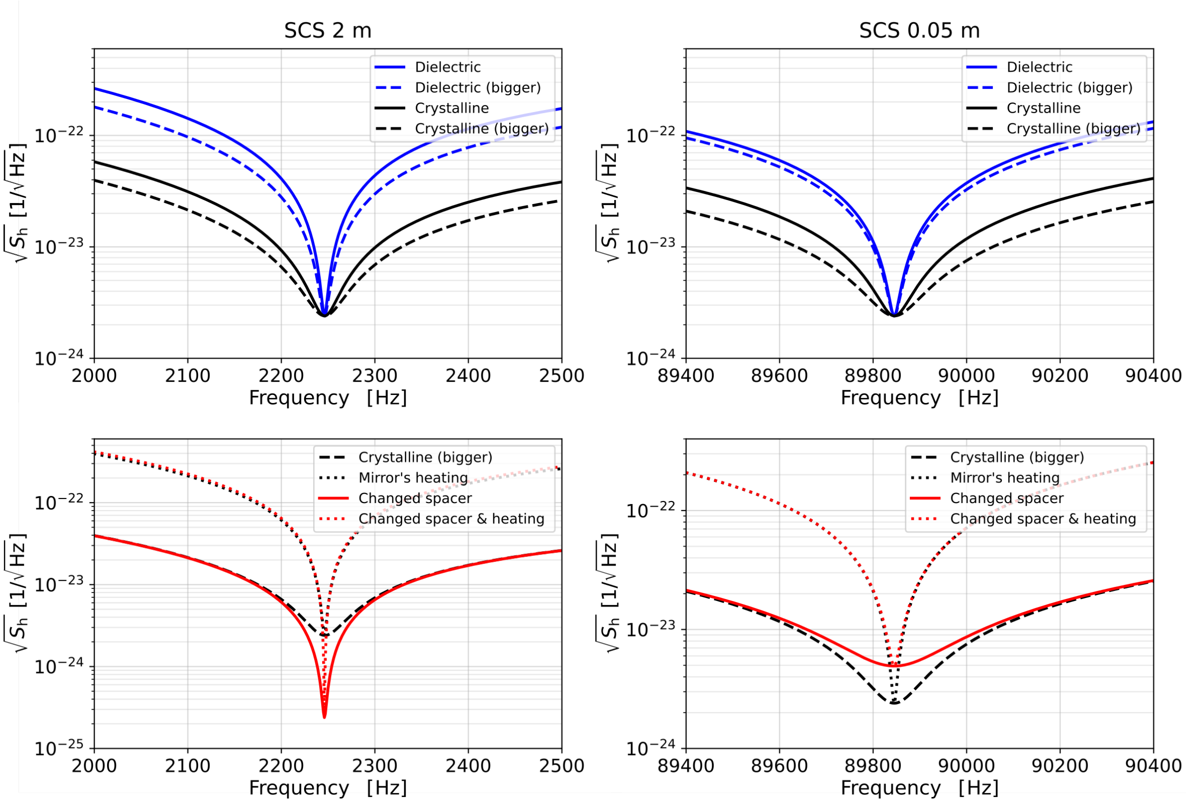

Figure 5.12: **(Top)** Strain sensitivity is limited to the resonance vicinity for 2 m and 5 cm long spacers made of SCS at 20 mK. The resonance width at a given level depends on the substrate and coating material. Dashed lines depict the bigger spot size on the mirror achieved by using convex-concave configuration, $\text{ROC}_1 = 15$ m and $\text{ROC}_2 =$ - 20 m, comparing to the same curvature radii to but with typical concave-concave configuration $\text{ROC}_1 = 15$ m and $\text{ROC}_2 = 20$ m (solid line). **(Bottom)** Strain sensitivity for the default spacer radius with a bigger spot size on the mirror (black dashed line) with the influence of the coatings heating by the laser beam (black dotted line). Effectively, the coatings and substrates temperature were set at 2 K. Additionally, red dotted and solid lines depict the strain sensitivity for the bigger spacer with and without the heating effect, respectively.

1.5 times wider detectable frequency range at 10^{-23}. For these reasons, considering the more challenging design of convex-concave mirrors is rewarding. For the higher frequencies $\sim$ 90 kHz where a 5 cm SCS spacer has a resonance, dielectric and crystalline coatings give 81 Hz and 258 Hz of width at 10^{-23}, respectively. The laser beam spot size increase results in broadening up to 92 Hz and 417 Hz, respectively.

The bottom part of Fig. 5.12 shows the influence of the mirror's heating by the laser beam (dotted line). The heat transfer from the mirrors in a sub-Kelvin temperature is ineffective because of the decreasing mirror's conductance. It results in a maximum local temperature in the laser beam spot on the mirrors. Therefore, a cooled cavity up to, e.g. 100 mK, has a nonhomogenous temperature distribution with the mirrors (coatings and substrates) at a higher temperature and a spacer in the desired conditions. By performing a simple simulation, I show that the heating for the light raises the SCS surface temperature to $\sim$1 K in a 100 mK environment. However, in Fig. 5.12 2 K heating was plotted (with 20 mK spacer) for a higher (than typically used) beam power shining on the mirror's surface. To sum up, the mirror heating effect narrowed the resonance from $\sim$ 270 Hz to $\sim$ 17 Hz in a bigger outer radius spacer for 2 m long spacer (red solid and dotted lines) and from 417 Hz to 41 Hz for a 5 cm long spacer.

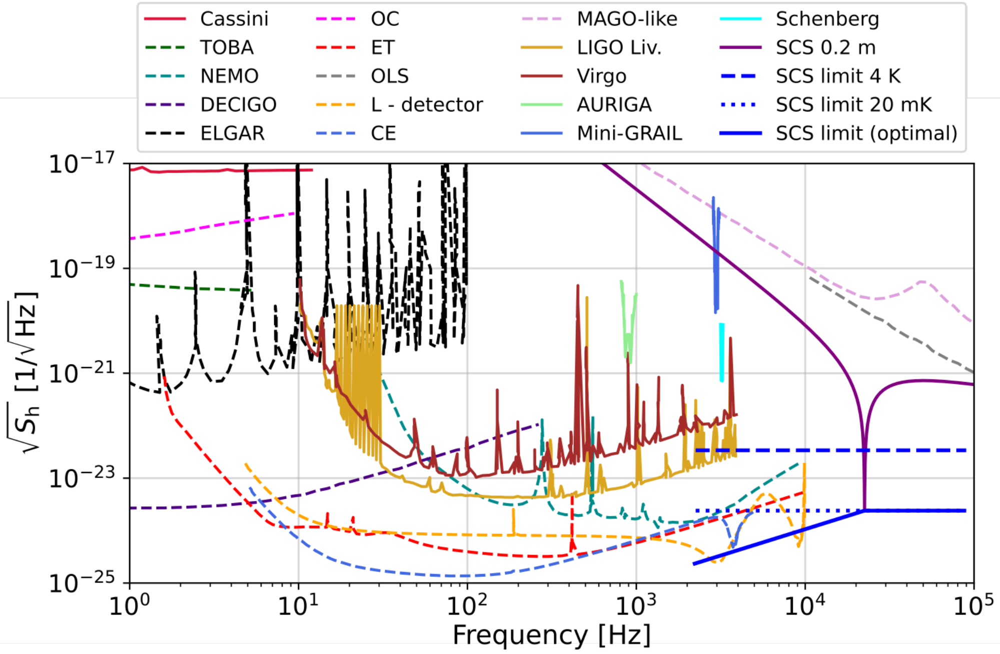

Figure 5.13: Strain sensitivity for the currently existing and future-planned detectors, together with the USOC performance limits and 4 K and 20 mK, and enhanced USOC sensitivity by the spacer size enlargement (solid blue line depicts). Moreover, one exemplary SCS curve for 0.2 m long SCS spacer with typical beam spot size and crystalline coatings. Already build detectors are Cassini [181], AURIGA [193], Mini-GRAIL [196], Schenberg Antenna [195], LIGO Livingston and Virgo o3 [191]. Future-planned detectors : TOBA [177], NEMO [188], DECIGO [186], ELGAR [187], OC [14], ET [190], OLS [189], L-detector [200], CE [201], MAGO-like [199].

Fig. 5.13 shows the GW strain sensitivity of the best existing and future-planned detectors in the 2–100 kHz frequency range. This spectra part comprises several possible astrophysical and non-astrophysical gravitational radiation sources. The strain frequency of the astrophysical GW sources is limited at the high-frequency part at the ∼10 kHz, by neutron stars' post-merger phase and stellar core collapse (Fig. 5.14). Every signal beyond these is treated as non-astrophysical (or beyond the standard model) and is suspected to be a new theoretically predicted particle and macro-object. According to Fig. 5.13, SCS in 4 K is more sensitive to high-frequency GWs than long-baseline interferometers. The blue dotted, dashed and solid lines in Fig. 5.13 show the peak sensitivity performance of the SCS USOC systems with the spacer length ranges from 2 m to 5 cm. Cavities in 4 K are already more sensitive to the high-frequency GWs than long-baseline interferometers. In addition, the USOC in 20 mK significantly improves sensitivity at 2–100 kHz range compared to the existing LIGO-like detectors and proposed OLS [189] and MAGO-like [199] detectors. Therefore, depending on the spacer's length, the USOC detector may cover both astrophysical and beyond the standard model sources, with the peak sensitivity surpassing other detectors.

5.3.3. Astrophysical sources

According to the general understanding of gravitational radiation generation, the characteristic frequency is connected to the individual object's mass [113, 250], and masses of the binary system, so-called chirp mass (see Eq. 5.7). Hence, USOC GW detector with the feasible 2-100 kHz frequency range is limited to the specific type of astrophysical gravitational radiation sources, such as collapsing stellar cores and binary neutron stars (NS) inspirals, mergers, and post-mergers (NS-NS).

Stars with masses higher than $\sim 9\ \mathrm{M}_\odot$ end their lives in rapid collapses. Theoretical prediction based on general relativistic numerical simulations [251–253] shows that the asymmetric collapsing stellar cores are typical burst gravitational waves emitters [254]. Depending on the progenitor mass and metalicity, three main remnant scenarios are possible: neutron star creation ($9 - 25\ \mathrm{M}_\odot$), black hole by fallback ($25 - 40\ \mathrm{M}_\odot$) and direct black hole generation ($> 40\ \mathrm{M}_\odot$) [255]. Both mass and metalicity, together with the progenitor spin, determine the waveform, i.e. the shape of the emitted GW. In the Fig. 5.14 (thick solid lines), three exemplary $\sqrt{S_h}$ of the CcSN within Milky Way range (30 kpc) are presented [207, 254, 256]. Despite the visible differences between models, they all have peaks around 1 kHz and typical amplitude-dropping shapes for frequencies higher than 1 kHz.

The second astrophysical objects that emit kHz GW is binary neutron stars (NS-NS) in the inspirals, mergers and post-mergers phases. All NS-NS curves presented in Fig. 5.14 are simulated by [208] using the H4 and IF equation of state (EOS) [257, 258]. Within

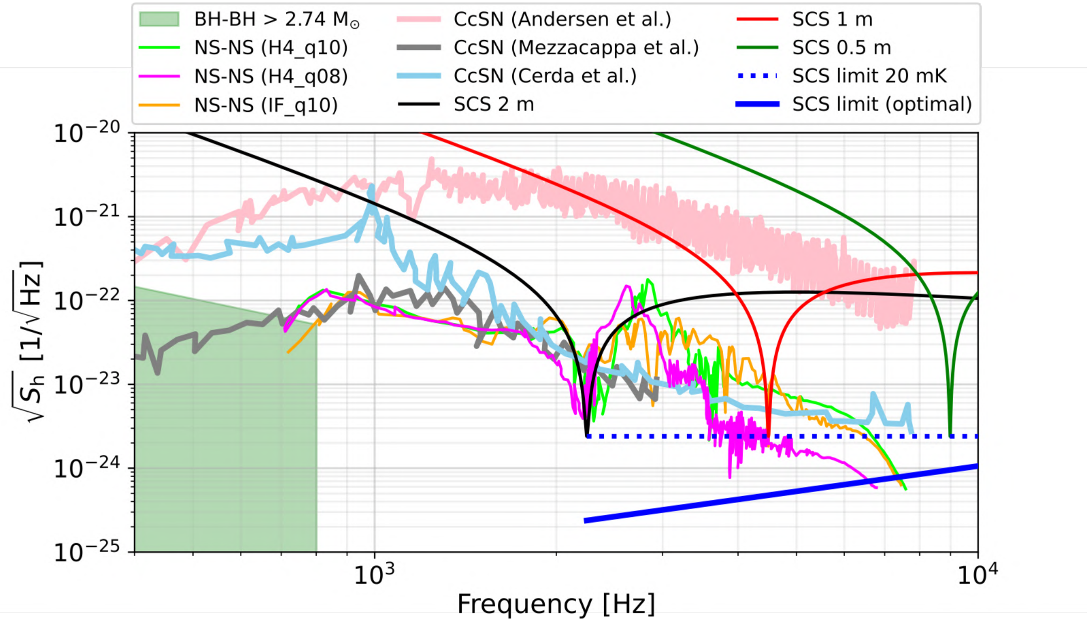

Figure 5.14: Comparison of GWs sensitivity of USOC with predicted GWs signals for the three typical astrophysical sources. Blue dotted and solid lines depict sensitivities for 0.05 - 2 m long SCS spacers in 20 mK (taken from Fig. 5.13). Additionally, three exemplary sensitivities for 2 m, 1 m, and 0.5 m long SCS spacers are presented (typical beam spot size and crystalline mirrors). The green area presents binary black holes (BH-BH) mergers in the 20 Mpc range. Singal is calculated analytically using innermost-stable circular orbit conditions for the individual black hole mass bigger than >2.74 M$_\odot$. Three exemplary models of the Core-collapse Supernova (CcSN) at the distance of 30 kpc are presented: CcSN (Anderson et al.) [256], CcSN (Mezzacappa et al.) [254], CcSN (Cerda et al.) [207]. Moreover, GW signal from three exemplary models of the neutron-stars (NS-NS) inspirals, mergers and post-mergers are plotted as a potential signal source [208].

mentioned EOS, three exemplary models are presented in Fig. 5.14 (thin solid lines) for the span of Local/Virgo Supercluster (20 Mpc). Despite the specific shape differences, the maxima land between 2-3 kHz and rapidly relax with amplitude fall. Although the tidal effects emitted during the inspiral are beyond the sensitivity frequency range, the post-mergers (signal above 1kHz) from massive neutron star remnants [259, 260] are produced by the majority of NS-NS mergers [261]. Aligning the optical cavity mechanical resonance with the peak of the GWs signal requires at least 1.5 m spacer length. Such a long spacer in cryogenics may be technically challenging but still doable. We already know that such events occur [217, 262, 263], which makes this a low-risk project.

According to the LIGO observation of neutron stars mergers, the mass of the remnant, which may be a black hole, is between 2.01 - 2.74 $\mathrm{M}_{\odot}$ [264, 265], which agrees with the theoretical prediction of Tolman-Openheimer-Volkoff limit. The upper limit was the maximum mass of each black hole in the merger from Fig. 5.13. Gravitational wave amplitude and frequency were calculated analytically for the innermost stable circular orbits (ISCO) of the BHs binaries with two exact masses >2.74 $\mathrm{M}_{\odot}$. Using the moment of inertia for the binary system and putting it into the Eq. 5.3 one can obtain

$$h = -\frac{4(\pi^2 G^5)^{1/3}}{c^4}\frac{\mu}{d}M_{sum}^{2/3} f^{2/3}\cos(2\omega t). \tag{5.17}$$

where μ is the system reduced mass $m_1 m_2/(m_1+m_2)$ and ISCO frequency is given by [113]

$$f_{ISCO} = \frac{c^3}{6^{3/2}\pi G}\frac{1}{M_{sum}} \approx 4.4\times 10^3\Big(\frac{\mathrm{M}_{\odot}}{M_{sum}}\Big)\mathrm{Hz}. \tag{5.18}$$

The mentioned signals, such as CcSn and NS-NS, allow us to observe the post-event signal. Therefore, the inspiral integration does not occur here. Nevertheless, estimated sensitivity allows us to observe the signal without second-long integration times. Another drawback is that the narrow resonance would observe only a tiny piece of the waveform evolution. To improve this, one need another cavity with a different size and correlate signals from them to reconstruct the entire signal. Nonetheless, observation is possible and worth attempting. However, detection of the sources beyond the standard model seem more promising for small, already existing USOCs.

5.3.4. Sources beyond the standard model

The studies, based on relativistic simulations, prove that the recognizable GW signal from the astrophysical objects ends at ~8 kHz (see previous chapter and Fig. 5.14). The signal is emitted in all phases of the event for NS-NS and CcSN, which maxima land at ~2-3 kHz and ~1 kHz, respectively. If any strain signal with frequencies higher than 8-10 kHz is detected, it will prove the existence of so-called beyond-the-standard model or non-astrophysical sources. The coalescences of the subsolar-mass BH binaries represent the first kind of sources. As mentioned in the previous chapter, the lowest possible BH mass is $\sim$2 $M_\odot$. There are no known mechanisms through standard stellar evolution to produce the BHs with masses below $\sim$1-2 M$\odot$ (see previous section). Detecting the BHs with the masses below that limit will indicate their primordial origin. The observations of such a binary merger are significant for verifying several important hypotheses, i.e. subsolar-mass BH potential contribution to the dark matter distribution [266–268] and verification theories on dark matter triggered formation of BHs [218, 219, 269]. Strain signals were calculated using Eq. 5.17, 5.18 for the ISCO of the equal masses binary BHs system in the Milky Way range, i.e. 30 kpc (green area in Fig. 5.15).

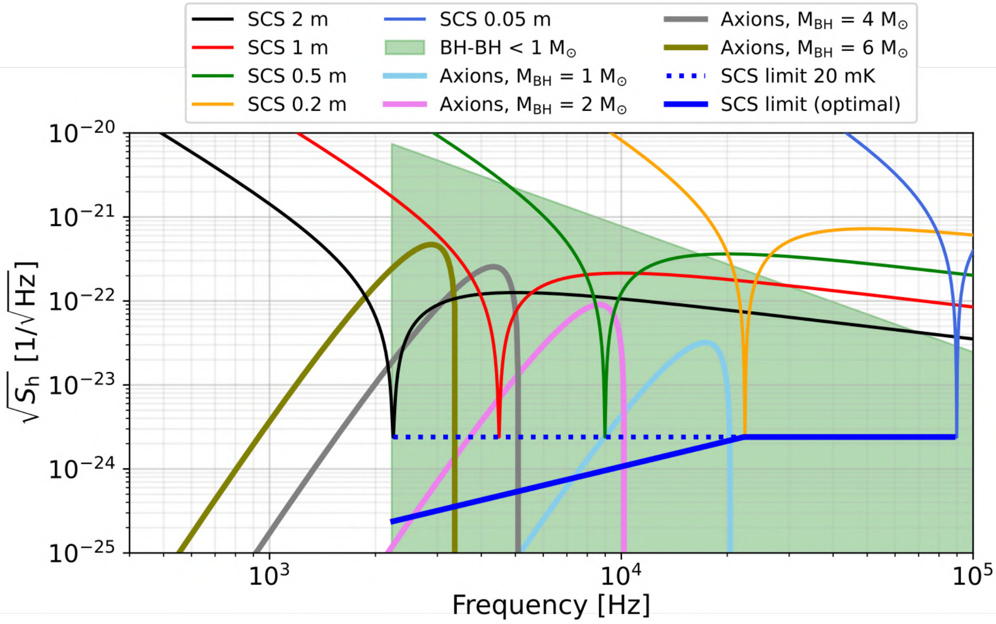

Figure 5.15: Comparison of GWs sensitivity of USOC with predicted GWs signals for two beyond the standard model sources. The green area depicts the signal emitted by the potential subsolar-mass black holes binary system for the ISCO within the Milky Way range (30 kpc). The solid blue, orange, red and brown lines present predicted signals due to GWs emitted from axions/ALPs around BHs in our galaxy within 10 kpc for one-day coherent integration time [209, 270].

The second type of sources treated as non-astrophysical are axions and ALPs (axion-like particles). In contrast with subsolar-mass BHs where the binary system emits the potentially detectable signal, the light bosonic fields such as axions may form gravitationally bound states in the black hole vicinity [271–274]. The signal frequency and amplitude depend on the particles' mass, occupation density and the distance from the black hole horizon.

Several interesting mechanisms exist for GW emission from ALPs and axion sources. These mechanisms include transitions between gravitationally bound levels, annihilation of axions/ALPs to gravitons, bosenova collapse of the axion/ALPs cloud, and superradiance, which will be the focus of this work. In this phenomenon, the number of particles increases exponentially at the cost of energy and angular momentum of the rotating black hole through superradiance [275] forming a coherent axion/ALPs bound state emitting GW [189, 209, 220, 221, 270, 276–283]. Unlike other axion and ALP sources that emit pulsed signals, these mechanisms demonstrate continuous emission, allowing for time averaging of the GW signal to increase the SNR. The potential gravitational radiation signal was calculated using the analytic approximation from [209, 270] for the values used in [189]. Fig. 5.15 depicts signal from axion/ALPs around the BHs with 1, 2, 4 and 6 $M_\odot$ initial mass and 0.9 initial spin, observed by one day (integration time). The $\sqrt{S_h}$ is calculated for the dominant level ($l = m_l = 1, n = 0$) within the 10 kHz span.

5.3.5. Gravitational background signal

The gravitational wave background (GWB) is a stochastic signal present in the entire GWs frequency spectrum. GWB may be divided into two parts according to their different origins: astrophysical GWB (AGWB) and cosmological i.e., relic GWB (RGW). The AGWB results from the superposition of many unresolved sources. The RGW can be treated as a gravitational counterpart to the cosmic microwave background (CMB, it is often called the primordial or the relic GW) and has many possible sources, e.g. cosmic strings, cosmological phase transitions, inflationary phase, and reheating of the inflation [284]. Therefore, the RGW detection will pave the way for observations of the Universe in the earliest stages (from $\sim 10^{-32}$ s) before the CMB emission [236]. Constraints for the RGW can be indirectly obtained experimentally, e.g. from observations of e^+e^- annihilation [285], QCD transition [285], abundance of elements created during Big Bang nucleosynthesis [285], and CMB temperature and polarization [236]. The above-mentioned constraints often depend on the choice between standard and alternative inflationary models [236]. Hence, observations of RGW in broad continuous spectra will provide a credible limit for RGW amplitude and validate theories of the very early evolution of the Universe.

It is typical for the stochastic signal, where the amplitude of individual GW events is hard to extract, to show the data in the form of power law energy density [236, 286]

$$\Omega(f) = \Omega_{CMB}\Big(\frac{f}{f_{CMB}}\Big)^{n_t}, \tag{5.19}$$

where $\Omega_{CMB} \equiv \Omega(f_{CMB})$ is the energy density amplitude at the pivot frequency $f_{CMB} = (c/2\pi)0.05$ Mpc^{-1} (see [287] for details). Energy density distribution also depends on the spectral index n_t, which in a single-field slow-roll inflation model [288] is connected to tensor-to-scalar ratio r_{ts} in the following way $n_t = -r_{ts}/8$. More sophisticated models which slightly deviate from power-law are well described in [285]. We will focus on standard Universe evolution with nonrelativistic matter and radiation. In that case, energy-density distribution is [236]

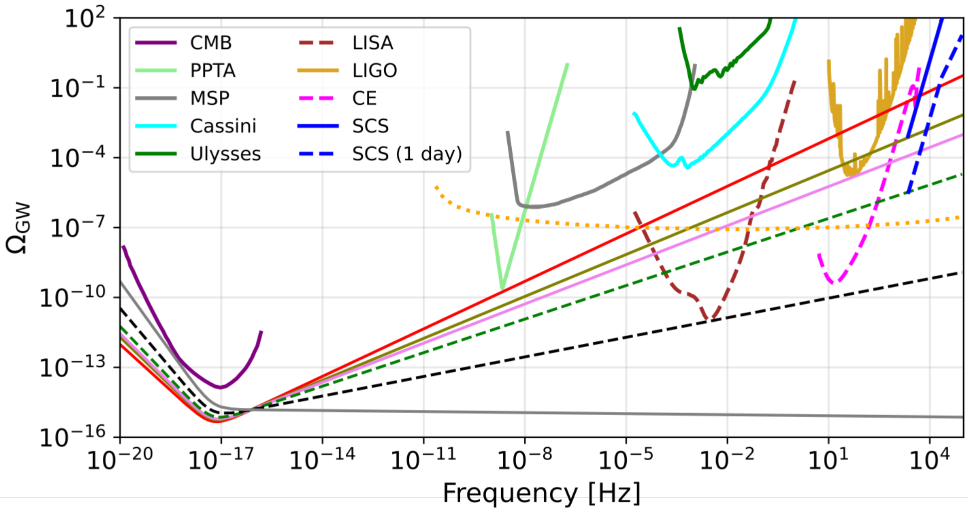

Figure 5.16: Constraints on the energy density set by the present-day (CMB [236], PPTA [183], MSP [183], Cassini [181], Ulysses [181], LIGO [174]) and future-planned detectors (LISA [182], CE [201]). Solid and dashed blue lines represent the 20 mK SCS USOC's sensitivity with a second and a day of integration time t_{int}, respectively. The orange dotted line indicates the limits set by collective indirect measurements [236]. Solid red, pink and grey lines represent the constraint on the spectral index set by current detector PPTA ($n_t < 0.68$), LIGO ($n_t < 0.56$) and CMB ($n_t = -r_{ts}/8$ for $r_{ts} = 0.12$), respectively. Solid and dashed blue lines show the constraints set by SCS USOC $t_{int} = 1$ s ($n_t < 0.6$) and SCS USOC $t_{int} = 1$ day ($n_t < 0.48$), respectively. Dashed black gives a constraint on the future-planned space-based detector LISA ($n_t < 0.28$).

$$\Omega_{RGW}(f) = \Omega_{CMB}\left(\frac{f}{f_{CMB}}\right)^{n_t}\left(\left(\frac{f_{eq}}{\sqrt{2}f}\right)^2 + \frac{16}{9}\right), \tag{5.20}$$

where f_{eq} is the frequency of the wave whose length is equal to the size of the Universe at the moment of matter-radiation equality [236].

Fig. 5.16 together with the Eq. 5.20 shows the constraints on the spectral index n_t [236] using the existing and future-planned detectors, together with USOC. We see that USOC needs at least 100 s (assuming perfect $1/\sqrt{t_{int}}$ relation) to surpass 1 s of the LIGO observations and gives a better upper limit for n_t. Moreover, one day of constant detection of USOC improves the n_t from <0.6 to < 0.48. Nevertheless, indirect observations of cosmic microwave background temperature and polarization power spectra, lensing, baryon acoustic oscillation (BAO), and big bang nucleosynthesis (BBN) still put more stringent constraints [236] on the GW energy density within the assumed model in Eq. 5.20. Therefore, a much longer observation time ∼100 days is desired to exceed the indirect limit.

5.3.6. Significant experimental constraints

While the thermal Brownian noise determines the fundamental limit of ultra-stable optical cavity stability, other non-negligible noise sources should be evaluated in an actual experimental setup. Most of the technological noise sources, like vacuum pressure fluctuations that change the index of refraction of the residual gas inside the cavity, instabilities of intracavity power that increase with the finesse of its mirrors and are converted to local heating of the cavity mirrors, and instabilities in locking techniques, e.g. due to residual amplitude modulation of the light, and instabilities of optical path in fibres used to transport light between the laser and the cavity [289] can be already mitigated to the level below Brownian thermal limit of a cavity for a certain range of frequency (see e.g. Fig. 8 in [4]). A good review of these noises, along with guidelines on how to mitigate them, can be found in [165].

Two other important sources of noise that limit the optical cavity stability are environmental perturbations: temperature fluctuations and broadband vibrations. External temperature fluctuations can be transmitted to the cavity, producing additional variations of cavity length and, thus, cavity mode frequency instability. The main mechanisms of heat transfer from the environment to the cavity placed in a vacuum are through thermal radiation by thermal conduction through the mountings of the cavity. The most effective way to filter out the temperature fluctuations is to use multiple thermal passive isolation shields of low emissivity and high thermal capacity and supporting points made from materials with very high thermal resistance (see e.g. [160]). The environmental vibrations (e.g. from cryostat pump [30]) can yield cavity deformations). The impact of these broadband noises on the cavity length can be significantly reduced by passive and active anti-vibration platforms, an acoustic isolation box, and unique shapes of cavity spacer and support that exploit symmetries [290–292]. See chapter 4 for more details and specific solutions for these issues.

Because of today's cavity operating purposes (for the optical clock [247]), the effort is focused mainly on long-term stability rather than short-term. To effectively use ultra-stable cavities for GW detection, kHz frequency noise must be mitigated by exploiting additional isolation. The mHz signal stability is also essential for signal time integration, sufficiently increasing SNR for periodic GW events. As shown in Fig. 5.17, even a substantial reduction of thermal noise will not significantly improve long-range stability without mitigating acoustic and temperature noises. Therefore, reducing the fluctuations at both high and low frequencies is indispensable for effectively detecting GW by USOC detectors.

The USOC GW detector consists of two cavities. We may reduce environmental perturbations significantly by mounting them on the single vibration isolation platform in one shared vacuum system. Because the state-of-the-art antivibrational platform does

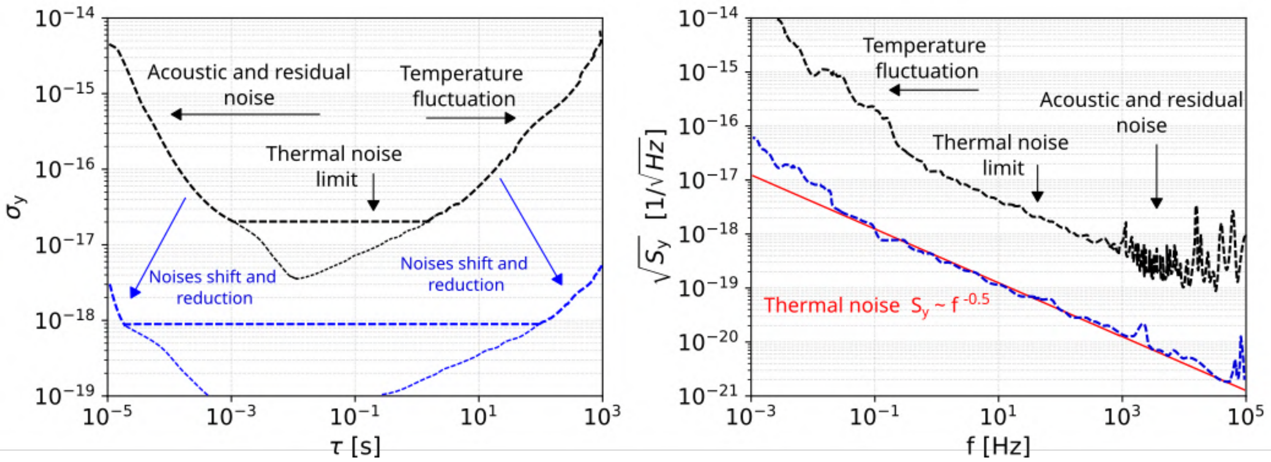

Figure 5.17: Conceptual figure of a typical cavity instability (black dashed line) and the desired future improved performance for gravitational wave detection (blue dashed line), presented in Allan deviation **(left)** and fractional amplitude spectral density plots **(right)**. In general, the main focus of cavity improvement is more on long-term instability rather than short-term. For GW detection, the goal is to observe higher frequencies, but both ranges are significant because of the signal integration time of periodic events.

not actively compensate the signal below ∼0.5 Hz, an additional low-frequency detector is needed. Today's best external seismometers placed in the chamber vicinity can measure the floor movement up to 0.03 ng at 1 Hz and 0.1 ng at 3 mHz. We can measure lasers' responses to the triggered vibrations using a seismometer and record their transfer function (TF). This TF may correct the signal and effectively give better long-term cavity stability. See details in chapter 4.3.3.

In principle, the frequencies of both cavity modes are expected to be different, and they will slowly drift with temperature changes at the level of 10^{-16}. Despite this, the coherence time between two separate lasers locked to the USOC exceeds 1 s, as demonstrated in [3]. Up to this timescale, the beat-note signal can be demodulated, detecting the phase difference between the lasers' light, corresponding to the difference in the cavities' lengths. Thus, the frequency of the GW signal can be observed directly. As mentioned in previous paragraphs, the readout can be further averaged for periodic signal detection, reaching integration times of days [3, 144].

The next crucial experimental challenge is the problem of the mirror's heating by the laser beam and its effective extraction in UHV conditions. This issue occurs mainly at cryo temperature when thermal conductivity decreases significantly. Additionally, the effect appears for the higher powers of the input beam where we want to reduce the influence of shot noise. The latest generation of crystalline coatings shows an absorption coefficient of less than 1 ppm at room temperature [293]. For 50 μW of input power, the heating at the centre of each cavity mirror is at 7.5 μW. The commercially available cryocoolers can effectively extract 1 W in temperature around 4 K and a cooling power of 80 μW at a temperature of 0.1 K (reported in 2013 [294]). Nevertheless, cavities in 20 mK were preliminary reports in [48]. Additionally, the absorption coefficient of the crystalline mirrors at low temperatures will be further reduced as the free carriers freeze out, approaching zero absorption. Further advancements in reducing shot noise can be achieved by increasing the finesse and utilizing phase-squeezed light. Further improvement in reducing shot noise can also be reached by increasing the finesse and using phase-squeezed light.

5.3.7. Design and cost considerations

According to the National Science Foundation [295], the construction cost of LIGO was approximately 1.1 billion USD, with annual operating and maintenance costs of 45 million USD. The development of the next generation of ground-based interferometers, such as Einstein Telescope [190], Cosmic Explorer [201], NEMO [188] are likely to be even more expensive. In contrast, a system comprising two cryogenic ultra-stable cavities costs around 2 million USD, emphasizing the undeniable cost advantage of table-top experiments. The new cavity system will be profitable not only for the GW detections (e.g. TOBA [177], OLS [189], MAGO-like [199]) but also in the other areas of astrophysics, e.g. in looking for dark matter candidates [16, 296]). Furthermore, the sensitivity of the USOC GW detectors increases proportionally to the square root of their number. Moreover, the setups do not need to be placed in one laboratory since the optical clock community has already performed several observational campaigns with the ad hoc created networks of optical atomic clocks (e.g. [7, 10, 297]).

6. Ultra-stable optical cavities for quantum fluctuations detection

6.1. Theoretical introduction to the spacetime fluctuations

It is expected that both the relativistic theory of gravity and quantum mechanics fail to describe physical phenomena at the Planck scale [298]. The search for a suitable unification of these two forces represents one of the most significant challenges in modern theoretical and experimental physics. There have been many attempts to find an interplay between these two fundamental theories. Many unified theories propose that space-time experiences quantum fluctuations at the smallest feasible distances [298–300]. This inherent fuzziness, sometimes called space-time foam, fundamentally restricts the precision of length measurements, limited to the Planck length l_P [301, 302]. Motivated by the works of Salecker and Wigner [303, 304] and further developed by many others [305–309], I will briefly introduce the concept of integrating quantum mechanics and general relativity into distance measurement analysis. This integration leads to the notion of quantum fluctuations of space-time, manifesting as space-time foam. The analysis will be based on the works of Amelino-Camelia [305, 310], Jack Ng and van Dam [306, 309, 311, 312].

Salecker and Wigner [304] proposed a gedanken experiment to find the fundamental measurement uncertainty of a space-time distance. It involves an idealized clock that emits and receives the reflected light from a mirror at a distance l_{qf}. This distance can be defined by the time of flight of a photon t_{qf}, which moves with the speed of light c, thus $l_{qf} = ct_{qf}/2$. The uncertainty of the distance l_{qf} results from the uncertainties in the positions of both the clock and the mirror. In this analysis, I will focus on the clock and assume a similar effect on the mirror. One should recall the Heisenberg uncertainty principle, which states that the position x and the momentum p_x cannot be known precisely simultaneously

$$\delta x \; \delta p_x \geq \hbar/2, \tag{6.1}$$

where δx, δp_x are the standard uncertainty of the position and momentum, respectively. If the $l_{qf,0}$ is the initial distance, m is a clock mass, the velocity uncertainty is

$$\frac{\delta p}{m} = \delta v \geq \frac{\hbar}{2m\delta l_{qf,0}}. \tag{6.2}$$

Given the clock is not stationary, after time t_{qt}, the distance uncertainty evolves according to

$$\delta l(t) = t_{qf}\delta v = \frac{\hbar t}{2m\delta l_0} = \frac{\hbar}{m\delta l_0}\frac{l}{c}. \tag{6.3}$$

For the observation time $t_{qf} = T_{\text{obs}}$, the total distance uncertainty is the sum of the initial uncertainty δl_0 and the uncertainty that has evolved over T_{obs}

$$\delta l \geq \delta l_0 + T_{obs}\delta v, \tag{6.4}$$

where the minimum of the right-hand side of the equation provides the lower constraint as

$$\delta l \geq \sqrt{\frac{\hbar T_{obs}}{2m}} = \sqrt{\frac{\hbar l}{mc}}. \tag{6.5}$$

Since any object transmitting information must be larger than its Schwarzschild radius (it cannot collapse into a black hole), this condition imposes a second fundamental limitation on the clock. Consequently, the distance uncertainty cannot be determined more precisely than the Schwarzschild radius r_S

$$\delta l > r_S > \frac{Gm}{c^2}. \tag{6.6}$$

By combining both quantum (Eq. 6.5) and relativistic (Eq. 6.6) uncertainties, we derive the final achievable precision of the distance measurements

$$\delta l^3 \geq l\frac{\hbar G}{c^3}, \tag{6.7}$$

$$\delta l \geq (l l_P^2)^{1/3}, \tag{6.8}$$

where $l_P = \sqrt{\hbar G/c^3}$ is the Planck length.

Other analyses made by Amelino-Camelia yield results linking the typical clock size to the Schwarzschild radius, presenting $\delta l \geq \sqrt{l l_P^2/d}$. Regardless of the derivation approach, the uncertainty in space-time measurements can be interpreted as deviations in the space-time metric itself, $\delta l = l^2\delta g$, leading to $\delta g_{\mu\nu} \geq (l_P/l)^{2/3}$, where $g = det(g_{\mu\nu})$. This analysis shows that quantum uncertainty directly affects space-time. As this effect scales with the distance l, the individual length variations accumulate (creating foam), resulting in an amplitude bigger than the Planck scale. The above-presented analysis and length uncertainty dependence show one of the approaches within numerous models. The general view is introduced by the universal form of Eq. 6.8 where 1/3 is replaced by β parameter, allowing numerous models to affect the distance and metric uncertainties [311]

$$\delta l \geq l(l_P/l)^{\alpha}, \tag{6.9}$$

$$\delta g_{\mu\nu} \geq (l/l_P)^{\alpha}. \tag{6.10}$$

The main conclusion from this analysis is that the amplitude of quantum space-time fluctuation should significantly exceed Planck scale unit $l_P \sim 10^{-35}$ m. Moreover, it suggests a power-law behaviour. Numerous proposals for measuring quantum space-time fluctuation by optical interferometers have been made, both by Michelson gravitational-wave interferometers [307, 309] and Fabry-Peròt ultra-stable optical cavities [9, 12]. In this chapter, I will present the improved limits for detecting quantum space-time fluctuation using ultra-stable optical cavities.

6.2. Methods

In the considered quantum-gravity foam-like model, distance uncertainty within space-time is represented as an additional noise source in the measurement system [307]. The fundamental constraints for the space-time fluctuation can be expressed by the root-mean-square deviation of the length x_{RMS}, which is essentially limited by the Planck length $l_P \leq x_{RMS}$. The related power spectral density $S_x(f)$ gives the frequency dependence, which is restricted by the observation time T$_{obs}$ [308]

$$x_{RMS}^2 = \int_{1/T_{obs}}^{f_{max}} S_x(f)df. \tag{6.11}$$

The theory of space-time foam does not impose any intrinsic constraints on the fundamental structure of $S_x(f)$. According to [308], the power spectral density $S_x(f)$ follows the universal power law formula

$$S_x(f) = f^{-2\beta}\mathcal{L}_{\beta}^{3-2\beta}c^{-2\beta-1}, \tag{6.12}$$

where β, $\mathcal{L}_{\beta}$, and c depict the power law parameter, length-unit magnitude of the fluctuation, and speed of light, respectively.

The space-time fluctuation may exhibit a more sophisticated form than the simple power law presented in Eq. 6.12 [308], although there are no alternative models. Thus, assuming a power law, β can take any arbitrary value. Special attention is given to values between $1/2 \leq \beta \leq 1$ [308], where 1/2 represents the model in fuzzy space-time without quantum decoherence, i.e., the loss of information, and $\beta = 1$ [308] represents the simplest stochastic quantum fluctuation modelled as the random-walk model (where $x_{RMS} \sim \sqrt{T_{obs}}$). In addition to 1 and 1/2, 5/6 will be considered into analysis [306, 308, 309]. Apart from the idea of using gravitational interferometers [307, 308] for high-frequency signals (Hz-kHz), the first experiment in the μHz-mHz range was performed by

Schiller et al. [12] and further improved in 2016 [9] using a pair of ultra-stable optical sapphire and ULE resonators. Both studies recorded a beat-note signal between two cavities aligned either parallel [12] or perpendicular [9, 12] to each other. They established limits for f^{-1} and f^{-2} power-law behaviors of the space-time fluctuations.

In this work, I improve their constraint using existing SCS and ULE cavities [3, 4] with a single exponent model, i.e. constraints given separately by the f^{-1}, f^{-2}, and add $f^{-5/3}$ ($\beta = 5/6$). Additionally, a model consisting of the sum of two exponents will be introduced and fitted to the data. Furthermore, I will present original methods for setting space-time fluctuation constraints using optical resonators, including single cavity signals from the cavity-atoms and cavity from the three-cornered hat method (Sec. 2.5).

The analysis presented in this chapter fundamentally assumes that quantum fluctuations between the cavities are uncorrelated. Moreover, we assume that the molecular bonding of the spacer does not compensate for space-time fluctuations of empty space. According to [12], "such a compensation appears unlikely." However, should any compensation effects exist, "experiments with different spacer materials may help set limits to compensation effects" [12], as previous studies using the same materials (ULE [9] and sapphire [12]). This analysis will show signals from SCS and ULE cavities to establish these limits [3, 4].

6.3. Experimental limits of quantum fluctuations

6.3.1. Limits given by single cavity and a pair of cavities

The studies presented in [9, 12] examine PSD for a pair cavities in perpendicular and parallel configurations. In this chapter, I will show the constraints derived from both pairs of cavities and the performance of individual cavities. I use existing data, primarily from [4, 31], to establish more stringent constraints on three possible space-time models. Fig. 6.1 illustrates the PSD of the best up-to-date ultra-stable cavities in the world. Except for ULE [4], which operates at room temperature, the rest are cryogenically cooled SCS [4, 5, 31, 65] (denoted as Si in Fig. 6.1). According to Fig. 6.1, the cavity performance reaches the thermal limit ($S_y \sim f^{-1}$) in the 10^{-3}–1 Hz range, and these data ranges are available in the publications [4, 5, 31, 65]. Having a longer dataset would be beneficial for setting even tighter constraints. All PSD plots presenting the constraints on space-time fluctuation keep a 95% confidence level. Since the data follows an f^{-1} curve, we may safely assume that only a single type of noise (thermal noise) is present in the data. Consequently, we can achieve a 95% confidence level by multiplying the original PSD data by 4, representing the factor for recalculating from 1σ to 2σ (denoted in this work as the 95% confidence level). Because PSD is the ASD squared, the multiplication factor is $4 = 2^2$.

The individual cavity performance reported in [4, 5, 31, 65] is obtained using the

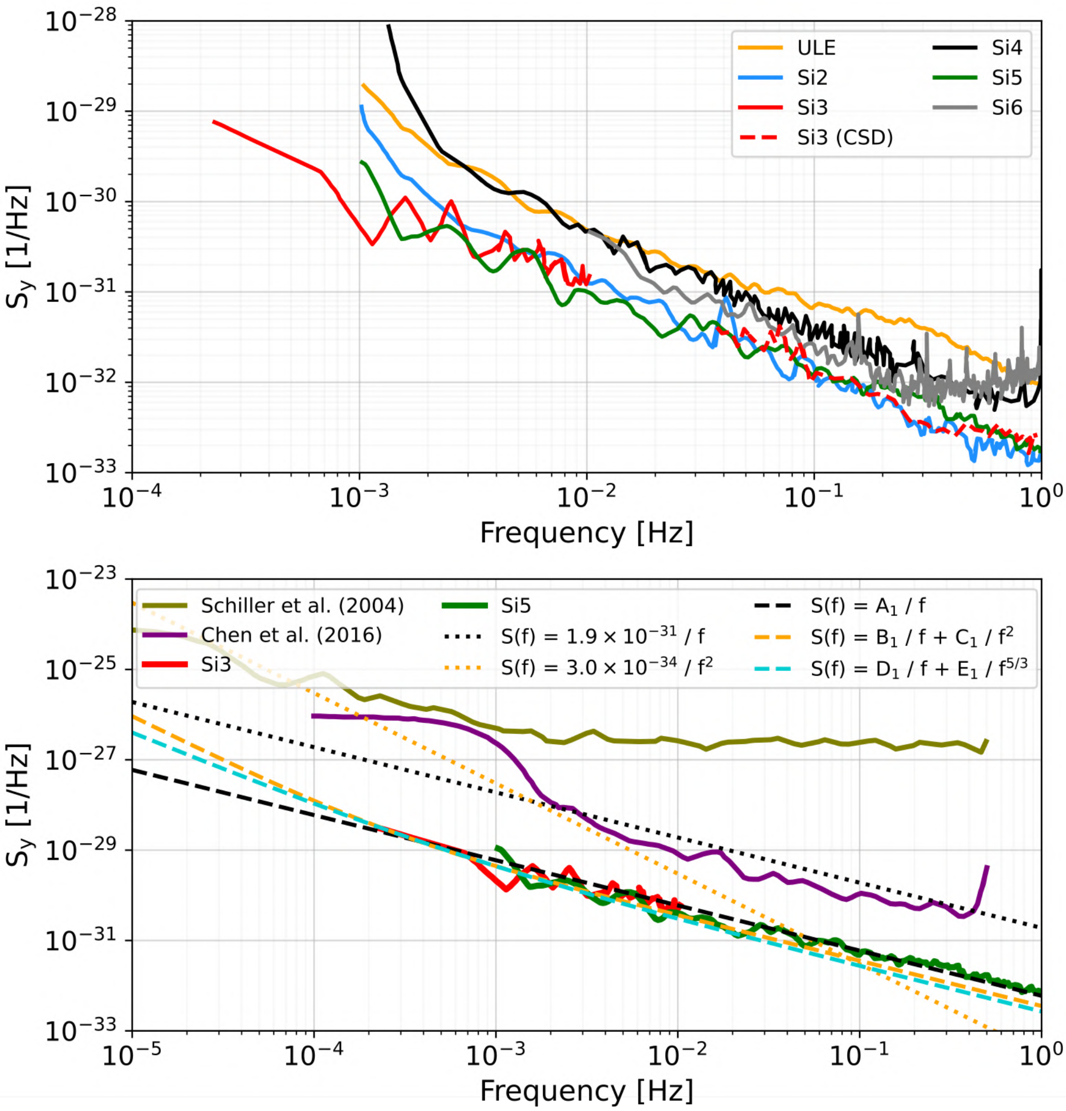

Figure 6.1: (**Top**) Fractional PSD of the state-of-the-art ultra-stable cavities: 48 cm long room temperature horizontal ULE [4], Si2 and Si3 are 21 cm long single-crystal silicon (SCS) placed vertically in 124 K [31]. A dashed red line depicts cross-correlated density (CSD) data [143] of the Si3-Si4 beatnote and 40 cm ULE cavity signal, where Si4 is the 6 cm SCS cavity resing in 4/16 K [65]. Si5 [4] and Si6 [5] are the exact analogues of the Si3 and Si4, but supplied in the crystalline coatings instead of dielectric as in Si2, Si3 and Si4 case. Light blue and green depict the performance of the 21 cm cavities in 124 K with dielectric and crystalline coatings, respectively. **(Bottom)** Fractional PSD with the 95% confidence level (solid red and green lines) for the two most stable cavities [4] from Fig. 6.1 along with the power-law limits of the space-time fluctuations given by them (dashed lines). The olive and purple solid lines and associated constraint represented by dotted lines depict previous studies [9, 12].

three-cornered hat method under the assumption of uncorrelated noises. This assumption is reasonable given that the cavities are located in separate vacuum chambers and mounted on independent anti-vibrational platforms. Additionally, it is presumed that space-time fluctuations are not correlated in direction. Using three cavities aligned orthogonally would be ideal. In the cases presented, two directions are covered (all SCS cavities are vertical, and the ULE cavity is horizontal). Unlike the studies in [9, 12], single cavity performance can constrain quantum space-time fluctuation with this setup since the fundamental distance measurements in the Salecker-Wigner clock are made between two mirrors separated in space-time[304].

Fig. 6.1 illustrates the fractional PSD signal at a 95% confidence level from the two best cavities [4, 31], along with power law limits for space-time fluctuation. The PSD signal from an individual cavity follows an f^{-1} trend, consistent with the thermal noise limit. Space-time fluctuation limit was calculated by fitting the function $S_y(f) = A_1/f$, where $A_1 = 5.97(15) \times 10^{-33}$ for Si3. The previous limit was set at $S_y(f) = 1.9 \times 10^{-31}/f$ [9]. To calculate limits on the f^{-2} and $f^{-5/3}$ models, I performed fits to $S_y(f) = B_1 f^{-1} + C_1 f^{-2}$ and $S_y(f) = D_1 f^{-1} + E_1 f^{-5/3}$, respectively, for the Si3 [31]. This approach differs from methods used in previous studies [12, 26]; therefore, it should not be directly compared. The results of fitting the mentioned functions are as follows: $S_y(f) = 3.55(23) \times 10^{-33}/f + 8.8(8) \times 10^{-37}/f^2$, and for another model, $S_y(f) = 2.7(3) \times 10^{-33}/f + 1.74(15) \times 10^{-35}/f^{5/3}$. If the data from Fig. 6.1 were recorded over a longer time, the constraints derived from the new cavities would be even more stringent.

The final fractional PSD signal from the cavities in Fig. 6.2 (Top) was determined by summing the individual cavity PSDs from the three-cornered hat method. Fig. 6.2 (Bottom) shows the 95% confidence level PSDs for the two best pairs of cavities in parallel Si2 - Si5 $\parallel$ and perpendicular Si5-ULE $\perp$ configurations, and dividing by two to account for the assumption of uncorrelated space-time fluctuations [9]. The limit for space-time fluctuation for the pair of cavities Si2-Si5 was calculated similarly to the individual cavity Si3. The results are $S_y(f) = 7.202(43) \times 10^{-33}/f$ (black dashed line), $S_y(f) = 5.13(51) \times 10^{-33}/f + 6.78(87) \times 10^{-36}/f^2$ (orange dashed line), and $S_y(f) = 2.21(72) \times 10^{-32}/f + 2.54(11) \times 10^{-35}/f^{5/3}$ (dashed cyan line). The constraints from pairs of cavities are generally less stringent than a single cavity across all model laws, mainly due to the lack of a longer common dataset (as in the Si3 case).

Fig. 6.1 and Fig. 6.2 illustrate the performance of the best existing cavities. The Brownian thermal noise floor with $S_y \sim f^{-1}$ behaviour is achieved in the 10^{-3} - 1 Hz frequency range in these figures. Using this assumption, Fig. 6.3 illustrates the theoretical performance limited by the thermal noise floor for two combinations of the temperature, waist, and mirror's coatings material which influence the Brownian noise. Fig. 6.3 shows the performance enhancement (compared to the Si2 and Si5) by increasing the beam spot size on the mirrors (orange solid line) by changing the mirror's curvature from $\mathrm{ROC}_1 = \infty$

and $\mathrm{ROC}_2 = 1$ m to $\mathrm{ROC}_1 = \mathrm{ROC}_2 = 10.2$ m. The loss angle for crystalline mirrors (measured in room temperature) also shows additional noise reduction (pink solid lines). The solid red and cyan lines represent the cavities at 20 mK with $\mathrm{ROC}_1 = \mathrm{ROC}_2 = 10.2$ m and $\mathrm{ROC}_1 = 15$ m, $\mathrm{ROC}_2 = -20$ m, respectively. The cavity spacer length is set to 30 cm. Therefore, the top plots in Fig. 6.3 show the individual cavity thermal noise (left) and the sum of two cavities in the same environmental condition and mirrors. In the bottom left, the 95% confidence level is presented for one cavity. The $5.3 \times 10^{-35} f^{-1}$ constraint of the space-time fluctuation is given by the worst-case scenario, i.e. 30 cm long cavity with $\mathrm{ROC}_1 = \mathrm{ROC}_2 = 10.2$ m in 4 K with dielectric mirror coatings. The bottom right presents the 95% confidence level for the pair of 30 cm long cavities with $\mathrm{ROC}_1 = \mathrm{ROC}_2 = 10.2$ and dielectric mirror coatings, in 4 K. The space-time constraint in this case is $1.1 \times 10^{-34} f^{-1}$.

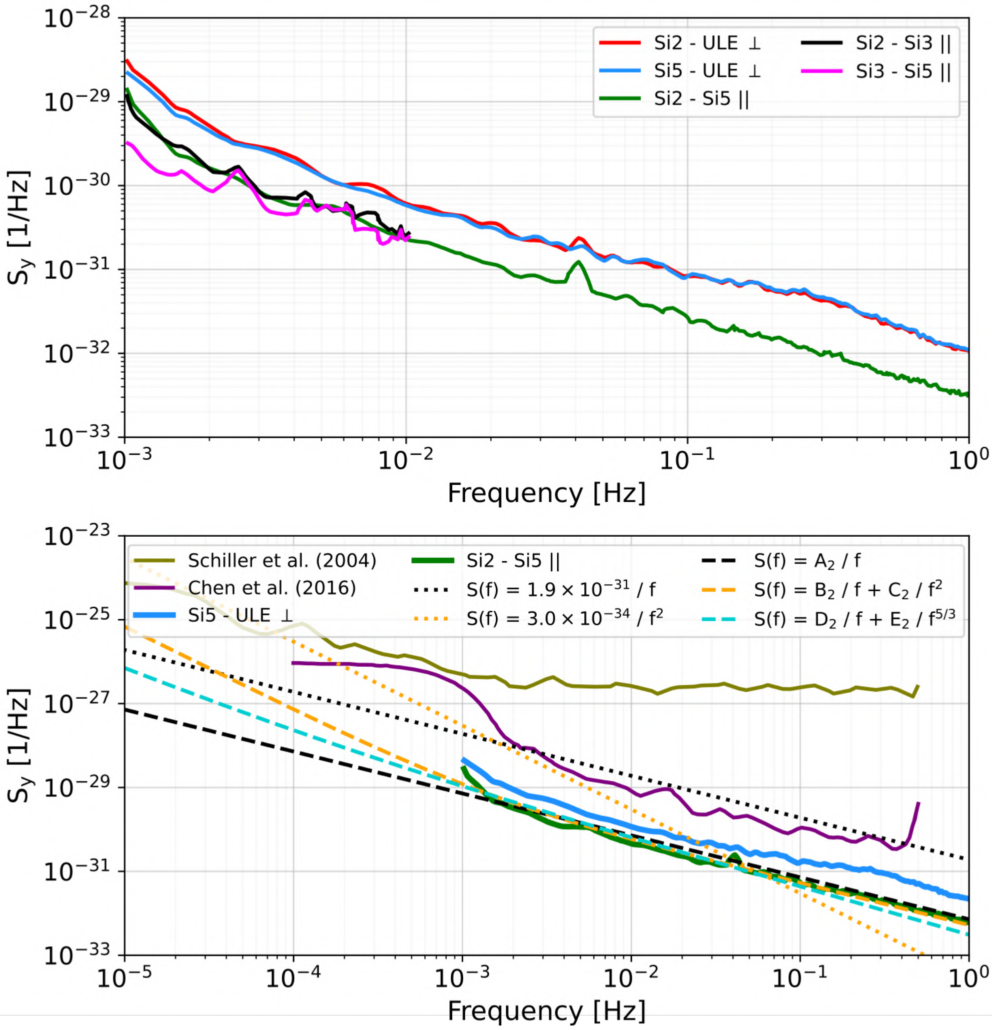

Figure 6.2: **(Top)** The predicted beat note of the chosen pairs of the cavities is a sum of the individual PSDs, assuming the uncorrelated noises. Two cavities' directional alignment was possible, i.e. vertical (Si2 [4], Si3 [31], Si4 [65], Si5 [4], Si6 [5]) and horizontal (ULE) [4] (cavity individual signals are presented in Fig. 6.1). Hence, || and ⊥ depict the beat note between parallel and perpendicular cavities alignment. **(Bottom)** Fractional PSD with the 95% confidence level of the beat note for three pairs of cavities and the power-law limits of the space-time fluctuations (dashed lines). The olive and purple solid lines and associated constraint (represented by dotted lines) depict previous studies [9, 12]. New constraints are presented with dashed lines.

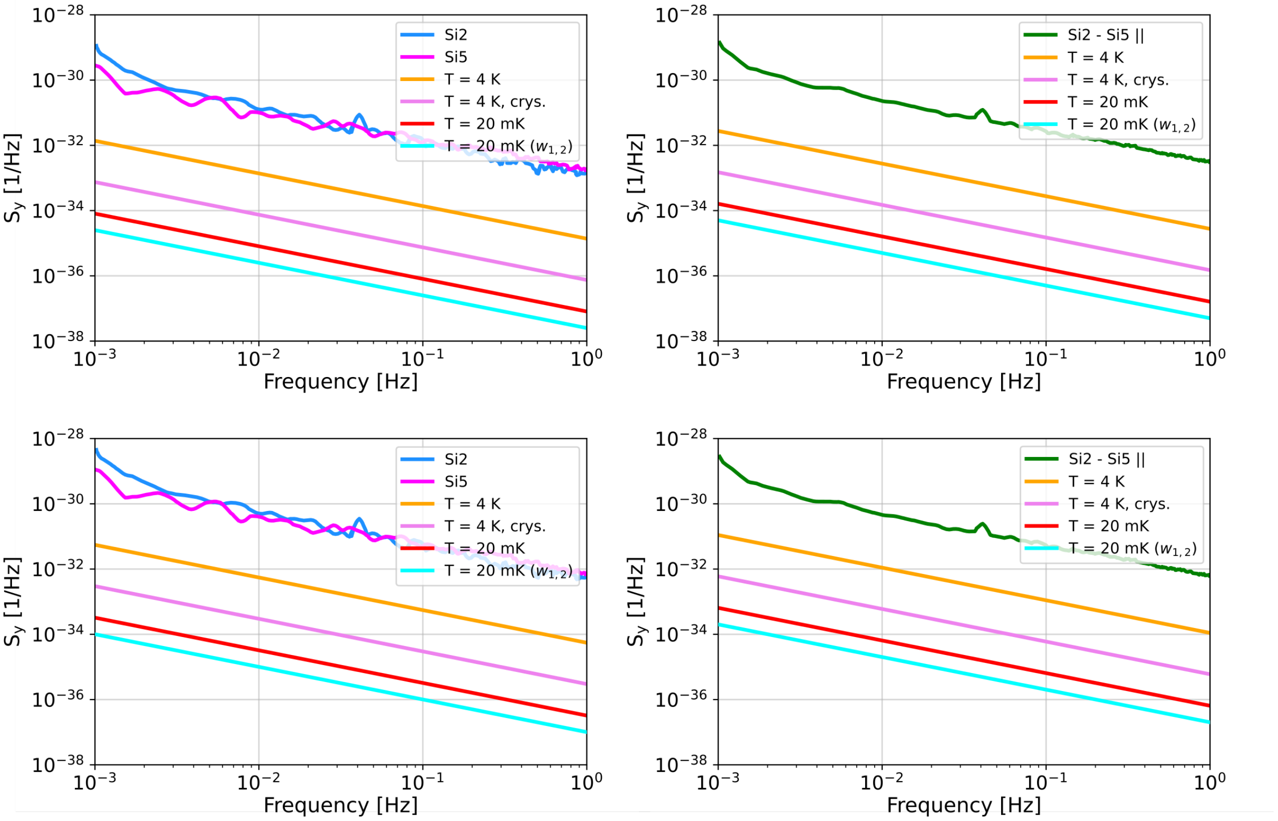

Figure 6.3: Potential thermal sensitivity limits depicted as a fractional PSD for the 30 cm long SCS cavity residing in 4 K and 20 mK. Si2 and Si5 performance are presented for comparison as the best up-to-date ultra-stable optical references. Magenta (Si5) and pink (T = 4 K, crys) solid lines depict the cavity supplied with crystalline coatings. The rest of them are with dielectric coatings. Cyan solid lines show the convex-concave cavity with $\mathrm{ROC}_1 = 15$ m and $\mathrm{ROC}_2 = -20$ m, which results in ~2x bigger beam spot size on the mirrors, compared to the $\mathrm{ROC}_1 = \mathrm{ROC}_2 = 10.2$ m which was assumed for the other calculations. **(Top Left)** The performance of the individual cavity. **(Top Right)** The predicted beat note of the pairs of the same cavities as a sum of the individual PSDs, assuming the uncorrelated noises. Parallel alignment of the || Si2-Si5 beat note is shown for comparison. **(Bottom Left)** Fractional PSD with the 95% confidence level of the cavities from the left top picture. The f^{-1} constraint of the space-time fluctuation given by the worst-case scenario cavity, i.e. $\mathrm{ROC}_1 = \mathrm{ROC}_2 = 10.2$ m in 4 K with dielectric mirror coatings. **(Bottom Right)** Fractional PSD with the 95% confidence level of the beat note for the same pairs of cavities as the top right picture. The f^{-1} constraint of the space-time fluctuation given by the pair of $\mathrm{ROC}_1 = \mathrm{ROC}_2 = 10.2$ in 4 K with dielectric mirror coatings.

6.3.2. Single cavity vs atoms

The frequency stability of the cavity can also be performed by directly comparing the cavity signal and the interrogated atoms' frequency. In this method, no other cavities are needed (as in three-cornered hat), but the atoms with the narrow transition are required. As previously assumed, we consider that quantum fluctuations are uncorrelated between the cavities. Here, we assume that the space-time fluctuations affecting the atomic energy levels and cavity dimensions are uncorrelated.

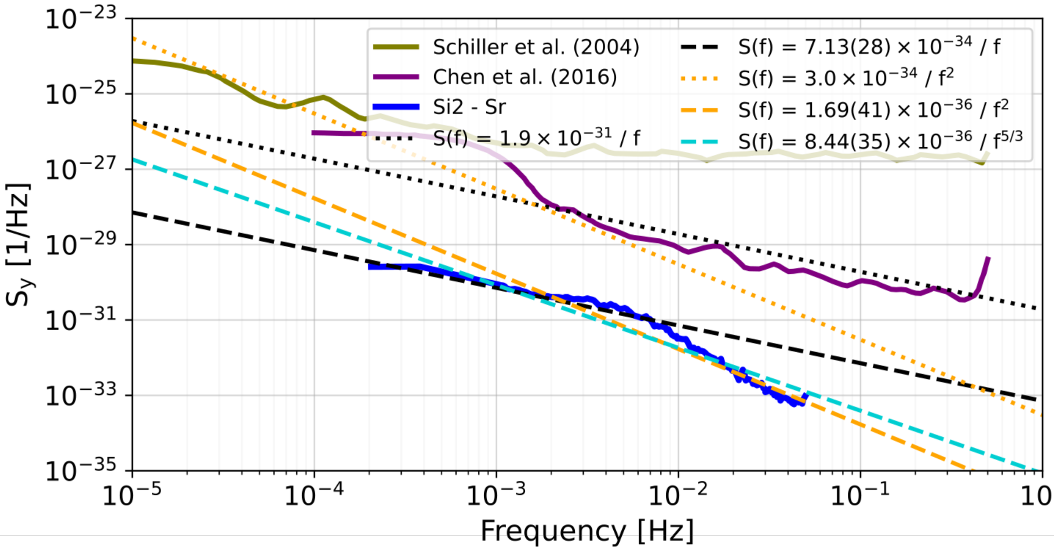

Figure 6.4: Fractional PSD of Si2 measured in reference to the $^1S_0 - ^3P_0$ Strontium clock transition with a 95% confidence level. The Si2 - Sr measurements were performed and analyzed at Physikalisch-Technische Bundesanstalt. The best 10-hour data interval is plotted with the cavity drift removed. I derived the space-time fluctuation constraints (dashed lines) based on the received data, compared to previous studies (dotted lines) [9, 12]. The established constraints are even more stringent than those from individual cavities (using the three-cornered hat method) and pairs of cavities.

Fig. 6.4 illustrates the instability of the SCS cavity measured in reference to the $^1S_0 - ^3P_0$ strontium clock transition, with a 95% confidence level. The data was recorded and analyzed at Physikalisch-Technische Bundesanstalt by Uwe Sterr and Sofia Herbers. In the case of cavity-atoms data, there is no clear f^{-1} behaviour (as observed in cavities, see Fig. 6.1 and Fig.6.2) across the recorded frequencies. Therefore, constraints were obtained by fitting the models $A_{ca}f^{-1}$, $B_{ca}f^{-5/3}$, and $C_{ca}f^{-2}$ to the data points. The constraints on space-time fluctuations set by this method are even more stringent than the best results achieved using only cavities (discussed in the previous section) for the f^{-1} model, achieving $7.13(28) \times 10^{-34}/f$ compared to $5.97(15) \times 10^{-33}/f$. This represents a constraint that is three orders of magnitude better than the previously published $1.9 \times 10^{-31}/f$ [9]. Moreover, results from the f^{-2} model in this work, $1.69(41) \times 10^{-36}/f^2$, are two orders of magnitude more stringent than the previously obtained $3.0 \times 10^{-34}/f^2$ [12]. Results between experimental data from [9, 12], and the values obtained in this work for a single exponent model are compared in Tab. 6.1.

Table 6.1: Comparison between the constraints on the low-frequency quantum space-time given by the ultra-stable optical resonators. Previous constraint, obtained from a comparison of two cavities (cav-cav), is presented in the first row [9, 12]. Results obtained in this work, i.e., "Current" and "Future" are the limits given by individual cavity (cav) from the three-cornered hat method, cavity atom comparison (cav - atom), and calculation of the Brownian noise presented in Fig. 6.3, respectively. All results are presented only for the amplitude of a single exponent model.

Model \Constraint	f^{-1}	$f^{-5/3}$	f^{-2}
Previous cav - cav	1.9×10^{-31}	-	3.0×10^{-34}
Current cav - cav ‖	$7.202(43) \times 10^{-33}$	-	-
Current cav	$5.97(15) \times 10^{-33}$	-	-
Current cav - atom	$7.13(28) \times 10^{-34}$	$8.44(35) \times 10^{-36}$	$1.69(41) \times 10^{-36}$
Future cav - cav	1.1×10^{-34}	-	-
Future cav	5.3×10^{-35}	-	-

7. Conclusions

This thesis introduces the design of an ultra-stable, room-temperature ULE cavity equipped with crystalline mirror coatings. Switching from dielectric to crystalline coatings is expected to lower the theoretical thermal noise floor from $\sqrt{S_y} = 8.82 \times 10^{-17}$ Hz$^{-1/2}$ to $\sqrt{S_y} = 4.11 \times 10^{-17}$ Hz$^{-1/2}$ at 1 Hz. The predominant noise across the frequency range from 30 mHz to 20 Hz is produced by the substrate thermoelastic effect, driven by a high FS coefficient of thermal expansion at room temperature. The Brownian noise originating from crystalline coatings, characterized by a loss angle $\phi = 2.5 \times 10^{-5}$ (compared to $\phi = 4 \times 10^{-4}$ for dielectric coatings), is calculated at a level of $\sqrt{S_y} = 1.97 \times 10^{-17}$ Hz$^{-1/2}$ at 1 Hz. The support points of the cylindrical cavity have been designed using finite element method simulations to minimize acceleration sensitivity, which allows to reach the calculated thermal noise floor.

Thermal noise currently limits the performance of both room-temperature and cryogenic resonators. We propose using a convex-concave mirror configuration to reduce thermal noises, which depend on the laser beam spot size on the mirror w. For Brownian noise in coatings and substrates, the noise scales as $S^{Br}_{x,ct} \sim w^{-2}$ and $S^{Br}_{x,sb} \sim w^{-1}$, respectively. The thermo-optic noise in coatings behaves as $S^{TO}_{x,ct} \sim w^{-2}$ in the adiabatic limit and $S^{TO}_{x,ct} \sim w^{-1}$ in the non-adiabatic limit, while the substrate thermoelastic noise behaves as $S^{TE}_{x,sb} \sim w^{-3}$ in the adiabatic regime. Consequently, increasing the laser beam spot size reduces thermal noise. Therefore, mirror radii of curvature ranging from -25 m to 20 m were investigated. A configuration with $\mathrm{ROC}_1 = 20$ m, $\mathrm{ROC}_2 = -25$ m and the 30 cm spacer length is expected to show an order of magnitude improvement in coatings' Brownian noise and a factor of three improvements in substrates' noise. To achieve comparable levels of thermal noise reduction for 30 cm long spacer with a plano-concave mirror, the concave mirror should have a $\mathrm{ROC}_2 = 50$ m. However, the plano-concave configuration results in slightly better optical stability $g_1 g_2 = 0.9940$, compared to $g_1 g_2 = 0.9947$ for convex-concave mirrors. Further studies on the feasibility of the near-unstable convex-concave configuration are planned.

The long-term stability of an optical resonator is critical for metrology and precise measurements. A new ceramic material, NEXCERA 117 B, shows promising characteristics with better long-term drift than ULE, positioning it as a potential replacement for spacers in room-temperature ultra-stable cavities. However, its loss angle is similar to ULE's;

NEXCERA's higher Young's modulus results in even lower Brownian thermal noise than widely used ULE. This work proposes replacing the ULE substrate in NEXCERA cavities with FS, resulting in lower thermal noise. Such a scenario is designed to improve the thermal noise floor from $\sqrt{S_y} = 1.25 \times 10^{-16}$ Hz$^{-1/2}$ to $\sqrt{S_y} = 3.89 \times 10^{-17}$ Hz$^{-1/2}$ at 1 Hz in a plano-concave configuration with ROC$_2$ = 1 m for a 30 cm cavity and crystalline mirror coatings.

In the second part of this thesis, the use of ultra-stable cavities for fundamental physics tests is proposed. First, we propose an ultra-stable cavity as a resonant gravitational wave detector. Using the mechanical resonance of the spacer cavity may allow for the detection of gravitational waves whose frequency matches the resonant frequency of the spacer. The shift of the resonant peak is achieved by changing the spacer's size and material. The strain sensitivity is enhanced by increasing the spacer mass, lowering the temperature, and expanding the beam spot size on the mirror using convex-concave mirrors to improve sensitivity to gravitational wave radiation. This method allows the using an existing cavity as a gravitational wave detector, offering strain sensitivity from 10^{-19} for cavities at room temperature to 10^{-22} for cryogenic single-crystal silicon cavities within the kHz to tens of kHz frequency range. The ultra-stable cavity detector is mainly designed to observe frequencies beyond the current range of existing interferometers, such as LIGO, Virgo and KAGRA. This also is the range beyond the classical gravitational radiation sources but allows the observation of non-classical objects, such as black holes with masses less than 1 $M_\odot$, often called primordial black holes. Moreover, a positive observation in the high frequencies could prove the existence of sources beyond standard models, such as axions and axion-like particles. Furthermore, long-term observation by an ultra-stable cavity detector may also provide limits for the gravitational background signal at high frequencies above 10 kHz.

The second application of ultra-stable cavities for fundamental physics enhance the constraints on space-time fluctuations in the so-called space-time "foam" model. This work proposes improving existing limits using a set of two cavities aligned both perpendicularly and parallelly, which has improved the previous constraints by at least an order of magnitude. Moreover, the novel approach includes two methods of using a single cavity to limit space-time fluctuations. The first data set is obtained from the three-cornered hat method, which gives two orders of magnitude improvement for f^{-1} and f^{-2} theoretical models. The second approach, which involves data from a single cavity compared with strontium atoms, sets limits that are an order of magnitude more stringent than those achieved using the single cavity with the three-cornered hat method.

Bibliography

[1] Theodor W. Hänsch. “Nobel Lecture: Passion for precision”. In: *Rev. Mod. Phys.* 78 (4 Nov. 2006), pp. 1297–1309. DOI: `10.1103/RevModPhys.78.1297`. URL: `https://link.aps.org/doi/10.1103/RevModPhys.78.1297` (cit. on p. 5).

[2] Eric D. Black. “An introduction to Pound–Drever–Hall laser frequency stabilization”. In: *American Journal of Physics* 69.1 (Jan. 2001), pp. 79–87. ISSN: 0002-9505. DOI: `10.1119/1.1286663`. eprint: `https://pubs.aip.org/aapt/ajp/article-pdf/69/1/79/10115998/79\_1\_online.pdf`. URL: `https://doi.org/10.1119/1.1286663` (cit. on pp. 5, 16, 17, 41, 89).

[3] D. G. Matei et al. “1.5 μm Lasers with Sub-10 mHz Linewidth”. In: *Phys. Rev. Lett.* 118 (26 June 2017), p. 263202. DOI: `10.1103/PhysRevLett.118.263202`. URL: `https://link.aps.org/doi/10.1103/PhysRevLett.118.263202` (cit. on pp. 5, 16, 22, 31, 42, 55, 92, 94, 95, 108, 113).

[4] Jialiang Yu et al. “Excess Noise and Photoinduced Effects in Highly Reflective Crystalline Mirror Coatings”. In: *Phys. Rev. X* 13 (4 Oct. 2023), p. 041002. DOI: `10.1103/PhysRevX.13.041002`. URL: `https://link.aps.org/doi/10.1103/PhysRevX.13.041002` (cit. on pp. 5, 6, 13, 22, 42, 107, 113–115, 117).

[5] Dhruv Kedar et al. “Frequency stability of cryogenic silicon cavities with semiconductor crystalline coatings”. In: *Optica* 10.4 (Apr. 2023), pp. 464–470. DOI: `10.1364/OPTICA.479462`. URL: `https://opg.optica.org/optica/abstract.cfm?URI=optica-10-4-464` (cit. on pp. 5, 6, 22, 94, 95, 113, 114, 117).

[6] A. Derevianko and M. Pospelov. “Hunting for topological dark matter with atomic clocks”. In: *Nature Physics* 10.12 (Dec. 2014), pp. 933–936. ISSN: 1745-2481. DOI: `10.1038/nphys3137`. URL: `https://doi.org/10.1038/nphys3137` (cit. on p. 5).

[7] P. Wcisło et al. “New bounds on dark matter coupling from a global network of optical atomic clocks”. In: *Science Advances* 4.12 (2018), eaau4869. DOI: `10.1126/sciadv.aau4869`. eprint: `https://www.science.org/doi/pdf/10.1126/sciadv.aau4869`. URL: `https://www.science.org/doi/abs/10.1126/sciadv.aau4869` (cit. on pp. 5, 109).

[8] Holger Müller et al. “Modern Michelson-Morley Experiment using Cryogenic Optical Resonators”. In: *Phys. Rev. Lett.* 91 (2 July 2003), p. 020401. DOI: `10.1103/PhysRevLett.91.020401`. URL: `https://link.aps.org/doi/10.1103/PhysRevLett.91.020401` (cit. on pp. 5, 22, 39, 94).

[9] Q. Chen, E. Magoulakis, and S. Schiller. “High-sensitivity crossed-resonator laser apparatus for improved tests of Lorentz invariance and of space-time fluctuations”. In: *Phys. Rev. D* 93 (2 Jan. 2016), p. 022003. DOI: `10.1103/PhysRevD.93.022003`. URL: `https://link.aps.org/doi/10.1103/PhysRevD.93.022003` (cit. on pp. 5, 112–115, 117, 119, 120).

[10] P. Delva et al. “Test of Special Relativity Using a Fiber Network of Optical Clocks”. In: *Phys. Rev. Lett.* 118 (22 June 2017), p. 221102. DOI: `10.1103/PhysRevLett.118.221102`. URL: `https://link.aps.org/doi/10.1103/PhysRevLett.118.221102` (cit. on pp. 5, 109).

[11] Norman Gürlebeck et al. “BOOST: A satellite mission to test Lorentz invariance using high-performance optical frequency references”. In: *Phys. Rev. D* 97 (12 June 2018), p. 124051. DOI: `10.1103/PhysRevD.97.124051`. URL: `https://link.aps.org/doi/10.1103/PhysRevD.97.124051` (cit. on p. 5).

[12] S. Schiller et al. “Experimental limits for low-frequency space-time fluctuations from ultrastable optical resonators”. In: *Phys. Rev. D* 69 (2 Jan. 2004), p. 027504. DOI: `10.1103/PhysRevD.69.027504`. URL: `https://link.aps.org/doi/10.1103/PhysRevD.69.027504` (cit. on pp. 5, 42, 112–115, 117, 119, 120).

[13] B.P. Abbott et al. “Observation of Gravitational Waves from a Binary Black Hole Merger”. In: *Phys. Rev. Lett.* 116 (6 Feb. 2016), p. 061102. DOI: `10.1103/PhysRevLett.116.061102`. URL: `https://link.aps.org/doi/10.1103/PhysRevLett.116.061102` (cit. on pp. 5, 82, 85, 86).

[14] S. Kolkowitz et al. “Gravitational wave detection with optical lattice atomic clocks”. In: *Phys. Rev. D* 94 (12 Dec. 2016), p. 124043. DOI: `10.1103/PhysRevD.94.124043`. URL: `https://link.aps.org/doi/10.1103/PhysRevD.94.124043` (cit. on pp. 5, 84, 86, 100).

[15] M. Narożnik, M. Bober, and M. Zawada. “Ultra-stable optical clock cavities as resonant mass gravitational wave detectors in search for new physics”. In: *Physics Letters B* 846 (2023), p. 138260. ISSN: 0370-2693. DOI: `https://doi.org/10.1016/j.physletb.2023.138260`. URL: `https://www.sciencedirect.com/science/article/pii/S0370269323005944` (cit. on pp. 5, 88, 89).

[16] Andrew A. Geraci et al. “Searching for Ultralight Dark Matter with Optical Cavities”. In: *Phys. Rev. Lett.* 123 (3 July 2019), p. 031304. DOI: `10.1103/PhysRevLett.123.031304`. URL: `https://link.aps.org/doi/10.1103/PhysRevLett.123.031304` (cit. on pp. 5, 109).

[17] Koki Ono et al. “Observation of Nonlinearity of Generalized King Plot in the Search for New Boson”. In: *Phys. Rev. X* 12 (2 May 2022), p. 021033. DOI: `10.1103/PhysRevX.12.021033`. URL: `https://link.aps.org/doi/10.1103/PhysRevX.12.021033` (cit. on p. 5).

[18] Krehlik, P. et al. “Fibre-optic delivery of time and frequency to VLBI station”. In: *A&A* 603 (2017), A48. DOI: `10.1051/0004-6361/201730615`. URL: `https://doi.org/10.1051/0004-6361/201730615` (cit. on p. 5).

[19] Johann Riemensberger et al. “Massively parallel coherent laser ranging using a soliton microcomb”. In: *Nature* 581.7807 (May 2020), pp. 164–170. ISSN: 1476-4687. DOI: `10.1038/s41586-020-2239-3`. URL: `https://doi.org/10.1038/s41586-020-2239-3` (cit. on p. 5).

[20] E. A. Burt et al. “Demonstration of a trapped-ion atomic clock in space”. In: *Nature* 595.7865 (July 2021), pp. 43–47. ISSN: 1476-4687. DOI: `10.1038/s41586-021-03571-7`. URL: `https://doi.org/10.1038/s41586-021-03571-7` (cit. on p. 5).

[21] Jérôme Lodewyck. “On a definition of the SI second with a set of optical clock transitions”. In: *Metrologia* 56.5 (Sept. 2019), p. 055009. DOI: `10.1088/1681-7575/ab3a82`. URL: `https://dx.doi.org/10.1088/1681-7575/ab3a82` (cit. on p. 5).

[22] W. F. McGrew et al. “Towards the optical second: verifying optical clocks at the SI limit”. In: *Optica* 6.4 (Apr. 2019), pp. 448–454. DOI: `10.1364/OPTICA.6.000448`. URL: `https://opg.optica.org/optica/abstract.cfm?URI=optica-6-4-448` (cit. on p. 5).

[23] William R. Milner et al. “Demonstration of a Timescale Based on a Stable Optical Carrier”. In: *Phys. Rev. Lett.* 123 (17 Oct. 2019), p. 173201. DOI: `10.1103/PhysRevLett.123.173201`. URL: `https://link.aps.org/doi/10.1103/PhysRevLett.123.173201` (cit. on p. 5).

[24] N Dimarcq et al. “Roadmap towards the redefinition of the second”. In: *Metrologia* 61.1 (Jan. 2024), p. 012001. DOI: `10.1088/1681-7575/ad17d2`. URL: `https://dx.doi.org/10.1088/1681-7575/ad17d2` (cit. on p. 5).

[25] T. Nazarova, F. Riehle, and U. Sterr. “Vibration-insensitive reference cavity for an ultra-narrow-linewidth laser”. In: *Applied Physics B* 83.4 (June 2006), pp. 531–536. ISSN: 1432-0649. DOI: `10.1007/s00340-006-2225-y`. URL: `https://doi.org/10.1007/s00340-006-2225-y` (cit. on pp. 5, 24, 56).

[26] Lisheng Chen et al. “Vibration-induced elastic deformation of Fabry-Perot cavities”. In: *Phys. Rev. A* 74 (5 Nov. 2006), p. 053801. DOI: `10.1103/PhysRevA.74.053801`. URL: `https://link.aps.org/doi/10.1103/PhysRevA.74.053801` (cit. on pp. 5, 56, 115).

[27] Thomas Legero, Thomas Kessler, and Uwe Sterr. “Tuning the thermal expansion properties of optical reference cavities with fused silica mirrors”. In: *J. Opt. Soc. Am. B* 27.5 (May 2010), pp. 914–919. DOI: `10.1364/JOSAB.27.000914`. URL: `https://opg.optica.org/josab/abstract.cfm?URI=josab-27-5-914` (cit. on pp. 5, 24, 51).

[28] T. Kessler et al. “A sub-40-mHz-linewidth laser based on a silicon single-crystal optical cavity”. In: *Nature Photonics* 6.10 (Oct. 2012), pp. 687–692. DOI: `10.1038/nphoton.2012.217`. arXiv: `1112.3854 [physics.optics]` (cit. on pp. 5, 22).

[29] Sebastian Häfner et al. “8×10^{-17} fractional laser frequency instability with a long room-temperature cavity”. In: *Optics Letters* 40.9 (May 2015), p. 2112. DOI: `10.1364/OL.40.002112`. arXiv: `1502.02608 [physics.optics]` (cit. on pp. 5, 22, 50, 55, 56, 94).

[30] W. Zhang et al. “Ultrastable Silicon Cavity in a Continuously Operating Closed-Cycle Cryostat at 4 K”. In: *Phys. Rev. Lett.* 119 (24 Dec. 2017), p. 243601. DOI: `10.1103/PhysRevLett.119.243601`. URL: `https://link.aps.org/doi/10.1103/PhysRevLett.119.243601` (cit. on pp. 5, 6, 22, 39, 42, 94, 107).

[31] John M. Robinson et al. “Thermal noise and mechanical loss of SiO2/Ta2O5 optical coatings at cryogenic temperatures”. In: *Opt. Lett.* 46.3 (Feb. 2021), pp. 592–595. DOI: `10.1364/OL.413758`. URL: `https://opg.optica.org/ol/abstract.cfm?URI=ol-46-3-592` (cit. on pp. 5, 22, 31, 32, 41, 113–115, 117).

[32] Gregory M Harry et al. “Titania-doped tantala/silica coatings for gravitational-wave detection”. In: *Classical and Quantum Gravity* 24.2 (Dec. 2006), p. 405. DOI: `10.1088/0264-9381/24/2/008`. URL: `https://dx.doi.org/10.1088/0264-9381/24/2/008` (cit. on p. 5).

[33] Steven D Penn et al. “Mechanical loss in tantala/silica dielectric mirror coatings”. In: *Classical and Quantum Gravity* 20.13 (June 2003), p. 2917. DOI: `10.1088/0264-9381/20/13/334`. URL: `https://dx.doi.org/10.1088/0264-9381/20/13/334` (cit. on pp. 5, 39).

[34] I W Martin et al. “Effect of heat treatment on mechanical dissipation in Ta2O5 coatings”. In: *Classical and Quantum Gravity* 27.22 (Oct. 2010), p. 225020. DOI: `10.1088/0264-9381/27/22/225020`. URL: `https://dx.doi.org/10.1088/0264-9381/27/22/225020` (cit. on pp. 5, 39–41).

[35] I Martin et al. “Measurements of a low-temperature mechanical dissipation peak in a single layer of Ta2O5 doped with TiO2”. In: *Classical and Quantum Gravity* 25.5 (Feb. 2008), p. 055005. DOI: `10.1088/0264-9381/25/5/055005`. URL: `https://dx.doi.org/10.1088/0264-9381/25/5/055005` (cit. on pp. 5, 41).

[36] D R M Crooks et al. “Experimental measurements of mechanical dissipation associated with dielectric coatings formed using SiO2, Ta2O5 and Al2O3”. In: *Classical and Quantum Gravity* 23.15 (July 2006), p. 4953. DOI: `10.1088/0264-9381/23/15/014`. URL: `https://dx.doi.org/10.1088/0264-9381/23/15/014` (cit. on pp. 5, 32, 33, 39, 41).

[37] Gabriele Vajente et al. “Low Mechanical Loss $TiO_2 : GeO_2$ Coatings for Reduced Thermal Noise in Gravitational Wave Interferometers”. In: *Phys. Rev. Lett.* 127 (7 Aug. 2021), p. 071101. DOI: `10.1103/PhysRevLett.127.071101`. URL: `https://link.aps.org/doi/10.1103/PhysRevLett.127.071101` (cit. on p. 5).

[38] Garrett Cole et al. “Tenfold reduction of Brownian noise in high-reflectivity optical coatings”. In: *Nature Photonics* 7 (July 2013), pp. 644–650. DOI: `10.1038/nphoton.2013.174` (cit. on pp. 5, 29–33, 39).

[39] Johannes Dickmann and Stefanie Kroker. “Highly reflective low-noise etalon-based metamirror”. In: *Phys. Rev. D* 98 (8 Oct. 2018), p. 082003. DOI: `10.1103/PhysRevD.98.082003`. URL: `https://link.aps.org/doi/10.1103/PhysRevD.98.082003` (cit. on pp. 6, 22, 30, 31, 39).

[40] J. Dickmann et al. “Influence of polarization and material on Brownian thermal noise of binary grating reflectors”. In: *Physics Letters A* 382.33 (2018). Special Issue in memory of Professor V.B. Braginsky, pp. 2275–2281. ISSN: 0375-9601. DOI: `https://doi.org/10.1016/j.physleta.2017.07.006`. URL: `https://www.sciencedirect.com/science/article/pii/S0375960117304243` (cit. on pp. 6, 22).

[41] Johannes Dickmann et al. “Experimental realization of a 12,000-finesse laser cavity based on a low-noise microstructured mirror”. In: *Communications Physics* 6.1 (Jan. 2023), p. 16. ISSN: 2399-3650. DOI: `10.1038/s42005-023-01131-1`. URL: `https://doi.org/10.1038/s42005-023-01131-1` (cit. on pp. 6, 30, 31).

[42] Adcanced Optics SCHOTT AG. *ZERODUR*. 2023. URL: `https://www.schott.com/en-us/products/zerodur-p1000269/downloads` (cit. on pp. 6, 29, 53).

[43] Corning Advanced Optics. *Corning ULE 7973 Low Expansion Glass*. 2015. URL: `https://www.corning.com/media/worldwide/csm/documents/7973%20Product%20Brochure_0919.pdf` (cit. on pp. 6, 26, 29, 51, 53).

[44] Eugen Wiens et al. “Silicon single-crystal cryogenic optical resonator”. In: *Opt. Lett.* 39.11 (June 2014), pp. 3242–3245. DOI: `10.1364/OL.39.003242`. URL: `https://opg.optica.org/ol/abstract.cfm?URI=ol-39-11-3242` (cit. on pp. 6, 25).

[45] Ronny Nawrodt et al. “Mirror thermal noise calculation for ET ET-027-09 Thermal noise calculation for ET”. In: (Mar. 2023) (cit. on pp. 6, 26).

[46] Leilei He et al. “Ultra-stable cryogenic sapphire cavity laser with an instability reaching 2 $\times 10^{-16}$ based on a low vibration level cryostat”. In: *Opt. Lett.* 48.10 (May 2023), pp. 2519–2522. DOI: `10.1364/OL.488195`. URL: `https://opg.optica.org/ol/abstract.cfm?URI=ol-48-10-2519` (cit. on p. 6).

[47] Eugen Wiens et al. “Optical frequency reference based on a cryogenic silicon resonator”. In: *Opt. Express* 31.25 (Dec. 2023), pp. 42059–42076. DOI: `10.1364/OE.497365`. URL: `https://opg.optica.org/oe/abstract.cfm?URI=oe-31-25-42059` (cit. on p. 6).

[48] NEXTLASERS. *C20FUN08 NEXT-LASERS*. 2023. URL: `https://www.euramet.org/research-innovation/search-research-projects/details?tx_eurametctcp_project%5Bproject%5D=1740&cHash=f95f8edd28067dbbd484ceba04703bef` (cit. on pp. 6, 95, 109).

[49] A. Perot and Charles Fabry. “On the Application of Interference Phenomena to the Solution of Various Problems of Spectroscopy and Metrology”. In: ApJ 9 (Feb. 1899), p. 87. DOI: `10.1086/140557` (cit. on p. 8).

[50] Fritz Riehle. *Frequency Standards*. John Wiley & Sons, Ltd, 2003 (cit. on pp. 8, 11, 20, 21, 24).

[51] Wolfgang Demtröder. *Laser Spectroscopy 1: Basic Principles*. 2014. DOI: `10.1007/978-3-642-53859-9` (cit. on pp. 8, 11).

[52] Eugene Hecht. *Optics 4th edition*. 2001 (cit. on pp. 8, 11).

[53] Anthony E. Siegman. *Lasers.* University Science Books, 1986 (cit. on pp. 9, 11, 13, 16).

[54] Nur Ismail et al. “Fabry-Pérot resonator: spectral line shapes, generic and related Airy distributions, linewidths, finesses, and performance at low or frequency-dependent reflectivity”. In: *Opt. Express* 24.15 (July 2016), pp. 16366–16389. DOI: `10.1364/OE.24.016366`. URL: `https://opg.optica.org/oe/abstract.cfm?URI=oe-24-15-16366` (cit. on p. 11).

[55] H. Kogelnik and T. Li. “Laser Beams and Resonators”. In: *Appl. Opt.* 5.10 (Oct. 1966), pp. 1550–1567. DOI: `10.1364/AO.5.001550`. URL: `https://opg.optica.org/ao/abstract.cfm?URI=ao-5-10-1550` (cit. on p. 12).

[56] Sebastian Hafner. “Ultra-stabile Lasersysteme fur Weltraum- und Bodenanwendungen”. PhD thesis. 2015 (cit. on pp. 12, 13, 42).

[57] Christian Hagemann. “Ultra-stable Laser Based on A Cryogenic Single-crystal Silicon Cavity”. PhD thesis. 2013 (cit. on pp. 12, 13).

[58] Dhruv Kedar. “A Fully Crystalline Cryogenic Reference Cavity”. PhD thesis. 2023 (cit. on pp. 12, 55).

[59] The LIGO Scientific Collaboration et al. “Advanced LIGO”. In: *Classical and Quantum Gravity* 32.7 (Mar. 2015), p. 074001. DOI: `10.1088/0264-9381/32/7/074001`. URL: `https://dx.doi.org/10.1088/0264-9381/32/7/074001` (cit. on pp. 12, 13).

[60] F Acernese et al. “Advanced Virgo: a second-generation interferometric gravitational wave detector”. In: *Classical and Quantum Gravity* 32.2 (Dec. 2014), p. 024001. DOI: `10.1088/0264-9381/32/2/024001`. URL: `https://dx.doi.org/10.1088/0264-9381/32/2/024001` (cit. on pp. 12, 13).

[61] Yoichi Aso et al. “Interferometer design of the KAGRA gravitational wave detector”. In: *Phys. Rev. D* 88 (4 Aug. 2013), p. 043007. DOI: `10.1103/PhysRevD.88.043007`. URL: `https://link.aps.org/doi/10.1103/PhysRevD.88.043007` (cit. on pp. 12, 13).

[62] Samuel Rowlinson et al. “Feasibility study of beam-expanding telescopes in the interferometer arms for the Einstein Telescope”. In: *Phys. Rev. D* 103 (2 Jan. 2021), p. 023004. DOI: `10.1103/PhysRevD.103.023004`. URL: `https://link.aps.org/doi/10.1103/PhysRevD.103.023004` (cit. on pp. 12, 13).

[63] B. E. A. Saleh and M. C. Teich. *Fundamentals of Photonics.* John Wiley & Sons, Ltd, 1991 (cit. on pp. 13, 15).

[64] Simin Feng and Herbert G. Winful. “Physical origin of the Gouy phase shift”. In: *Opt. Lett.* 26.8 (Apr. 2001), pp. 485–487. DOI: `10.1364/OL.26.000485`. URL: `https://opg.optica.org/ol/abstract.cfm?URI=ol-26-8-485` (cit. on p. 15).

[65] John M. Robinson et al. “Crystalline optical cavity at 4  K with thermal-noise-limited instability and ultralow drift”. In: *Optica* 6.2 (Feb. 2019), pp. 240–243. DOI: `10.1364/OPTICA.6.000240`. URL: `https://opg.optica.org/optica/abstract.cfm?URI=optica-6-2-240` (cit. on pp. 16, 113, 114, 117).

[66] R. W. P. Drever et al. “Laser phase and frequency stabilization using an optical resonator”. In: *Applied Physics B: Lasers and Optics* 31.2 (June 1983), pp. 97–105. DOI: `10.1007/BF00702605` (cit. on p. 16).

[67] Alexander Franzen. *ComponentLibrary (a vector graphics library for illustrations of optics experiments).* 2023. URL: `https://www.gwoptics.org/ComponentLibrary/` (cit. on p. 17).

[68] Max Mäusezahl, Fabian Munkes, and Robert Löw. “Tutorial on laser locking techniques and the manufacturing of vapor cells for spectroscopy”. In: *arXiv e-prints*, arXiv:2401.16068 (Jan. 2024), arXiv:2401.16068. DOI: `10.48550/arXiv.2401.16068`. arXiv: `2401.16068 [physics.atom-ph]` (cit. on p. 17).

[69] William Riley and David Howe. *Handbook of Frequency Stability Analysis.* en. July 2008. URL: `https://tsapps.nist.gov/publication/get_pdf.cfm?pub_id=50505` (cit. on pp. 19, 21).

[70] D.W. Allan. “Statistics of atomic frequency standards”. In: *Proceedings of the IEEE* 54.2 (1966), pp. 221–230. DOI: `10.1109/PROC.1966.4634` (cit. on p. 19).

[71] David W. Allan and James A. Barnes. “A Modified "Allan Variance" with Increased Oscillator Characterization Ability”. In: 1981. URL: `https://api.semanticscholar.org/CorpusID:17740484` (cit. on p. 20).

[72] J. Rutman and F.L. Walls. “Characterization of frequency stability in precision frequency sources”. In: *Proceedings of the IEEE* 79.7 (1991), pp. 952–960. DOI: `10.1109/5.84972` (cit. on pp. 20, 21).

[73] Samuel T. Dawkins, John J. McFerran, and Andre N. Luiten. “Considerations on the Measurement of the Stability of Oscillators with Frequency Counters”. In: *2007 IEEE International Frequency Control Symposium Joint with the 21st European Frequency and Time Forum.* 2007, pp. 759–764. DOI: `10.1109/FREQ.2007.4319178` (cit. on p. 21).

[74] Enrico Rubiola. *Phase Noise and Frequency Stability in Oscillators.* The Cambridge RF and Microwave Engineering Series. Cambridge University Press, 2008 (cit. on p. 21).

[75] J. Rutman. “Characterization of phase and frequency instabilities in precision frequency sources: Fifteen years of progress”. In: *Proceedings of the IEEE* 66.9 (1978), pp. 1048–1075. DOI: `10.1109/PROC.1978.11080` (cit. on p. 21).

[76] Enrico Rubiola and François Vernotte. “The Companion of Enrico’s Chart for Phase Noise and Two-Sample Variances”. In: *IEEE Transactions on Microwave Theory and Techniques* 71.7 (2023), pp. 2996–3025. DOI: `10.1109/TMTT.2023.3238267` (cit. on p. 21).

[77] N. M. Sampas, E. K. Gustafson, and R. L. Byer. “Long-term stability of two diode-laser-pumped nonplanar ring lasers independently stabilized to two Fabry–Perot interferometers”. In: *Opt. Lett.* 18.12 (June 1993), pp. 947–949. DOI: `10.1364/OL.18.000947`. URL: `https://opg.optica.org/ol/abstract.cfm?URI=ol-18-12-947` (cit. on p. 22).

[78] G Ruoso et al. “Nd:YAG laser frequency stabilization to a supercavity at the 0.1 Hz level”. In: *Optics Communications* 133.1 (1997), pp. 259–262. ISSN: 0030-4018. DOI: `https://doi.org/10.1016/S0030-4018(96)00444-0`. URL: `https://www.sciencedirect.com/science/article/pii/S0030401896004440` (cit. on p. 22).

[79] H. Stoehr et al. “Diode laser with 1 Hz linewidth”. In: *Opt. Lett.* 31.6 (Mar. 2006), pp. 736–738. DOI: `10.1364/OL.31.000736`. URL: `https://opg.optica.org/ol/abstract.cfm?URI=ol-31-6-736` (cit. on p. 22).

[80] J.E. Gray and D.W. Allan. “A Method for Estimating the Frequency Stability of an Individual Oscillator”. In: *28th Annual Symposium on Frequency Control.* 1974, pp. 243–246. DOI: `10.1109/FREQ.1974.200027` (cit. on p. 22).

[81] J. Groslambert et al. “Characterization of Frequency Fluctuations by Crosscorrelations and by Using Three or More Oscillators”. In: *Thirty Fifth Annual Frequency Control Symposium.* 1981, pp. 458–463. DOI: `10.1109/FREQ.1981.200512` (cit. on p. 23).

[82] A. Premoli and P. Tavella. “A revisited three-cornered hat method for estimating frequency standard instability”. In: *IEEE Transactions on Instrumentation and Measurement* 42.1 (1993), pp. 7–13. DOI: `10.1109/19.206671` (cit. on p. 23).

[83] François Vernotte, Claudio Eligio Calosso, and Enrico Rubiola. “Three-cornered hat versus allan covariance”. In: *2016 IEEE International Frequency Control Symposium (IFCS).* 2016, pp. 1–6. DOI: `10.1109/FCS.2016.7546784` (cit. on p. 23).

[84] M. Tse et al. “Quantum-Enhanced Advanced LIGO Detectors in the Era of Gravitational-Wave Astronomy”. In: *Phys. Rev. Lett.* 123 (23 Dec. 2019), p. 231107. DOI: `10.1103/PhysRevLett.123.231107`. URL: `https://link.aps.org/doi/10.1103/PhysRevLett.123.231107` (cit. on p. 24).

[85] Erika D’Ambrosio. “Nonspherical mirrors to reduce thermoelastic noise in advanced gravitational wave interferometers”. In: *Phys. Rev. D* 67 (10 May 2003), p. 102004. DOI: `10.1103/PhysRevD.67.102004`. URL: `https://link.aps.org/doi/10.1103/PhysRevD.67.102004` (cit. on p. 24).

[86] Mihai Bondarescu and Kip S. Thorne. “New family of light beams and mirror shapes for future LIGO interferometers”. In: *Phys. Rev. D* 74 (8 Oct. 2006), p. 082003. DOI: `10.1103/PhysRevD.74.082003`. URL: `https://link.aps.org/doi/10.1103/PhysRevD.74.082003` (cit. on p. 24).

[87] Jean-Yves Vinet. “On Special Optical Modes and Thermal Issues in Advanced Gravitational Wave Interferometric Detectors”. In: *Living Reviews in Relativity* 12.1 (Dec. 2009), p. 5. ISSN: 1433-8351. DOI: `10.12942/lrr-2009-5`. URL: `https://doi.org/10.12942/lrr-2009-5` (cit. on p. 24).

[88] S. Braccini et al. "Measurement of the seismic attenuation performance of the VIRGO Superattenuator". In: *Astroparticle Physics* 23.6 (2005), pp. 557–565. ISSN: 0927-6505. DOI: `https://doi.org/10.1016/j.astropartphys.2005.04.002`. URL: `https://www.sciencedirect.com/science/article/pii/S092765050500068X` (cit. on pp. 24, 55).

[89] K. G. Lyon et al. "Linear thermal expansion measurements on silicon from 6 to 340 K". In: *Journal of Applied Physics* 48.3 (Mar. 1977), pp. 865–868. ISSN: 0021-8979. DOI: `10.1063/1.323747`. eprint: `https://pubs.aip.org/aip/jap/article-pdf/48/3/865/18376098/865\_1\_online.pdf`. URL: `https://doi.org/10.1063/1.323747` (cit. on p. 25).

[90] Thomas Middelmann et al. "Thermal expansion coefficient of single-crystal silicon from 7 K to 293 K". In: *Phys. Rev. B* 92 (17 Nov. 2015), p. 174113. DOI: `10.1103/PhysRevB.92.174113`. URL: `https://link.aps.org/doi/10.1103/PhysRevB.92.174113` (cit. on pp. 25, 26).

[91] S. J. Collocott and G. K. White. "Heat capacity and thermal expansion of Zerodur and Zerodur M at low temperatures". In: *Cryogenics* 31.2 (Jan. 1991), pp. 102–104. DOI: `10.1016/0011-2275(91)90254-T` (cit. on p. 26).

[92] Stéphane Roose and Stan Heltzel. "High-precision measurements of thermal expansion at cryogenic temperature on stable materials". In: 2013. DOI: `10.7795/810.20130822T` (cit. on p. 26).

[93] R. Jedamzik and T. Westerhoff. "ZERODUR TAILORED for cryogenic application". In: Proc. SPIE. Vol. 9151. Society of Photo-Optical Instrumentation Engineers (SPIE) Conference Series. 2014, 91512P, 91512P. DOI: `10.1117/12.2055086` (cit. on p. 26).

[94] Jonathan Crass et al. "The iLocater cryostat: design and thermal control strategy for precision radial velocity measurements". In: *Ground-based and Airborne Instrumentation for Astronomy VI.* Ed. by Christopher J. Evans, Luc Simard, and Hideki Takami. Vol. 9908. International Society for Optics and Photonics. SPIE, 2016, p. 990873. DOI: `10.1117/12.2233617`. URL: `https://doi.org/10.1117/12.2233617` (cit. on p. 26).

[95] Isao Ito et al. "Stable CW laser based on low thermal expansion ceramic cavity with 4.9 mHz/s frequency drift". In: *Opt. Express* 25.21 (Oct. 2017), pp. 26020–26028. DOI: `10.1364/OE.25.026020`. URL: `https://opg.optica.org/oe/abstract.cfm?URI=oe-25-21-26020` (cit. on pp. 26, 47, 48).

[96] Krosaki Harima Corporation, Ceramics Division. *NEXCERA ultra low thermal expansion ceramics.* 2023. URL: `https://krosaki-fc.com/en/ceramics/nexcera.html` (cit. on pp. 26, 47, 50, 51, 53).

[97] Peter R. Saulson. "Thermal noise in mechanical experiments". In: *Phys. Rev. D* 42 (8 Oct. 1990), pp. 2437–2445. DOI: `10.1103/PhysRevD.42.2437`. URL: `https://link.aps.org/doi/10.1103/PhysRevD.42.2437` (cit. on pp. 27, 28, 31).

[98] Herbert B. Callen and Theodore A. Welton. “Irreversibility and Generalized Noise”. In: *Phys. Rev.* 83 (1 July 1951), pp. 34–40. DOI: `10.1103/PhysRev.83.34`. URL: `https://link.aps.org/doi/10.1103/PhysRev.83.34` (cit. on p. 28).

[99] Herbert B. Callen and Richard F. Greene. “On a Theorem of Irreversible Thermodynamics”. In: *Phys. Rev.* 86 (5 June 1952), pp. 702–710. DOI: `10.1103/PhysRev.86.702`. URL: `https://link.aps.org/doi/10.1103/PhysRev.86.702` (cit. on p. 28).

[100] Kenji Numata, Amy Kemery, and Jordan Camp. “Thermal-Noise Limit in the Frequency Stabilization of Lasers with Rigid Cavities”. In: *Phys. Rev. Lett.* 93 (25 Dec. 2004), p. 250602. DOI: `10.1103/PhysRevLett.93.250602`. URL: `https://link.aps.org/doi/10.1103/PhysRevLett.93.250602` (cit. on pp. 29, 33, 34).

[101] V. B. Braginsky and S. P. Vyatchanin. “Thermodynamical fluctuations in optical mirror coatings”. In: *Physics Letters A* 312.3-4 (June 2003), pp. 244–255. DOI: `10.1016/S0375-9601(03)00473-0`. arXiv: `cond-mat/0302617 [cond-mat.stat-mech]` (cit. on p. 29).

[102] T. Uchiyama et al. “Mechanical quality factor of a cryogenic sapphire test mass for gravitational wave detectors”. In: *Physics Letters A* 261.1 (1999), pp. 5–11. ISSN: 0375-9601. DOI: `https://doi.org/10.1016/S0375-9601(99)00563-0`. URL: `https://www.sciencedirect.com/science/article/pii/S0375960199005630` (cit. on pp. 29, 40).

[103] Matthew A. Hopcroft, William D. Nix, and Thomas W. Kenny. “What is the Young’s Modulus of Silicon?” In: *Journal of Microelectromechanical Systems* 19.2 (2010), pp. 229–238. DOI: `10.1109/JMEMS.2009.2039697` (cit. on pp. 29, 33).

[104] Ronny Nawrodt et al. “High mechanical Q-factor measurements on silicon bulk samples”. In: *Journal of Physics: Conference Series* 122 (July 2008), p. 012008. DOI: `10.1088/1742-6596/122/1/012008` (cit. on pp. 29, 33, 40).

[105] Thomas Kessler, Thomas Legero, and Uwe Sterr. “Thermal noise in optical cavities revisited”. In: *Journal of the Optical Society of America B Optical Physics* 29.1 (Jan. 2012), p. 178. DOI: `10.1364/JOSAB.29.000178`. arXiv: `1111.4950 [physics.optics]` (cit. on p. 29).

[106] A. Gillespie and F. Raab. “Thermally excited vibrations of the mirrors of laser interferometer gravitational-wave detectors”. In: *Phys. Rev. D* 52 (2 July 1995), pp. 577–585. DOI: `10.1103/PhysRevD.52.577`. URL: `https://link.aps.org/doi/10.1103/PhysRevD.52.577` (cit. on p. 31).

[107] Aaron Gillespie. “Thermal Noise in the Initial LIGO Interferometers”. PhD dissertation. California Institute of Technology, 1995 (cit. on p. 31).

[108] N. Nakagawa et al. “Estimation of thermal noise in the mirrors of laser interferometric gravitational wave detectors: Two point correlation function”. In: *Review of Scientific Instruments* 68.9 (Sept. 1997), pp. 3553–3556. ISSN: 0034-6748. DOI: `10.1063/1.1148321`. eprint: `https://pubs.aip.org/aip/rsi/article-pdf/68/9/3553/8812097/3553\_1\_online.pdf`. URL: `https://doi.org/10.1063/1.1148321` (cit. on pp. 31, 32).

[109] Yu. Levin. “Internal thermal noise in the LIGO test masses: A direct approach”. In: *Phys. Rev. D* 57 (2 Jan. 1998), pp. 659–663. DOI: `10.1103/PhysRevD.57.659`. URL: `https://link.aps.org/doi/10.1103/PhysRevD.57.659` (cit. on pp. 31, 32, 34, 35).

[110] François Bondu, Patrice Hello, and Jean-Yves Vinet. “Thermal noise in mirrors of interferometric gravitational wave antennas”. In: *Physics Letters A* 246.3 (1998), pp. 227–236. ISSN: 0375-9601. DOI: `https://doi.org/10.1016/S0375-9601(98)00450-2`. URL: `https://www.sciencedirect.com/science/article/pii/S0375960198004502` (cit. on pp. 31, 32).

[111] N. Nakagawa et al. “Estimating the off resonance thermal noise in mirrors, Fabry-Perot interferometers, and delay lines: The half infinite mirror with uniform loss”. In: *Phys. Rev. D* 65 (8 Mar. 2002), p. 082002. DOI: `10.1103/PhysRevD.65.082002`. URL: `https://link.aps.org/doi/10.1103/PhysRevD.65.082002` (cit. on pp. 31, 32).

[112] N. Nakagawa et al. “Thermal noise in half-infinite mirrors with nonuniform loss: A slab of excess loss in a half-infinite mirror”. In: *Phys. Rev. D* 65 (10 Apr. 2002), p. 102001. DOI: `10.1103/PhysRevD.65.102001`. URL: `https://link.aps.org/doi/10.1103/PhysRevD.65.102001` (cit. on pp. 31, 32).

[113] Jolien D. E. Creighton and Warren G. Anderson. *Gravitational-Wave Physics and Astronomy. An Introduction to Theory, Experiment and Data Analysis.* Wiley, 2011 (cit. on pp. 31, 80–82, 84, 89, 90, 101, 103).

[114] Gregory M Harry et al. “Thermal noise in interferometric gravitational wave detectors due to dielectric optical coatings”. In: *Classical and Quantum Gravity* 19.5 (Feb. 2002), p. 897. DOI: `10.1088/0264-9381/19/5/305`. URL: `https://dx.doi.org/10.1088/0264-9381/19/5/305` (cit. on pp. 31, 32).

[115] Craig Cahillane and Georgia Mansell. “Review of the Advanced LIGO Gravitational Wave Observatories Leading to Observing Run Four”. In: *Galaxies* 10.1 (Feb. 2022), p. 36. ISSN: 2075-4434. DOI: `10.3390/galaxies10010036`. URL: `http://dx.doi.org/10.3390/galaxies10010036` (cit. on p. 32).

[116] Tara Chalermsongsak et al. “Coherent cancellation of photothermal noise in GaAs/Al0.92Ga0.08As Bragg mirrors”. In: *Metrologia* 53.2 (Mar. 2016), p. 860. DOI: `10.1088/0026-1394/53/2/860`. URL: `https://dx.doi.org/10.1088/0026-1394/53/2/860` (cit. on pp. 32, 35–37).

[117] Anja Schroeter et al. “On the mechanical quality factors of cryogenic test masses from fused silica and crystalline quartz”. In: (Oct. 2007) (cit. on pp. 33, 40).

[118] R Schnabel et al. “Building blocks for future detectors: Silicon test masses and 1550 nm laser light”. In: *Journal of Physics: Conference Series* 228.1 (May 2010), p. 012029. DOI: `10.1088/1742-6596/228/1/012029`. URL: `https://dx.doi.org/10.1088/1742-6596/228/1/012029` (cit. on p. 33).

[119] Garrett Cole et al. “Supplementary information. Tenfold reduction of Brownian noise in high-reflectivity optical coatings”. In: *Nature Photonics* 7 (July 2013), pp. 644–650. DOI: `10.1038/nphoton.2013.174` (cit. on p. 33).

[120] Corning Advanced Optics. *Corning HPFS 7979, 7980, 8655 Fused Silica.* 2023. URL: `https://www.corning.com/media/worldwide/csm/documents/HPFS_Product_Brochure_All_Grades_2015_07_21.pdf` (cit. on p. 33).

[121] E.M Lifshitz L.D. Landau. *Statistical Physics.* Pergamon Press, New York, 1984 (cit. on p. 34).

[122] V.B. Braginsky, M.L. Gorodetsky, and S.P. Vyatchanin. “Thermodynamical fluctuations and photo-thermal shot noise in gravitational wave antennae”. In: *Physics Letters A* 264.1 (1999), pp. 1–10. ISSN: 0375-9601. DOI: `https://doi.org/10.1016/S0375-9601(99)00785-9`. URL: `https://www.sciencedirect.com/science/article/pii/S0375960199007859` (cit. on p. 34).

[123] Kenji Numata et al. “Wide-Band Direct Measurement of Thermal Fluctuations in an Interferometer”. In: *Phys. Rev. Lett.* 91 (26 Dec. 2003), p. 260602. DOI: `10.1103/PhysRevLett.91.260602`. URL: `https://link.aps.org/doi/10.1103/PhysRevLett.91.260602` (cit. on p. 35).

[124] V.B. Braginsky, M.L. Gorodetsky, and S.P. Vyatchanin. “Thermo-refractive noise in gravitational wave antennae”. In: *Physics Letters A* 271.5 (2000), pp. 303–307. ISSN: 0375-9601. DOI: `https://doi.org/10.1016/S0375-9601(00)00389-3`. URL: `https://www.sciencedirect.com/science/article/pii/S0375960100003893` (cit. on p. 35).

[125] H. J. Kimble, Benjamin L. Lev, and Jun Ye. “Optical Interferometers with Reduced Sensitivity to Thermal Noise”. In: *Phys. Rev. Lett.* 101 (26 Dec. 2008), p. 260602. DOI: `10.1103/PhysRevLett.101.260602`. URL: `https://link.aps.org/doi/10.1103/PhysRevLett.101.260602` (cit. on p. 35).

[126] Michael L. Gorodetsky. “Thermal noises and noise compensation in high-reflection multilayer coating”. In: *Physics Letters A* 372.46 (2008), pp. 6813–6822. ISSN: 0375-9601. DOI: `https://doi.org/10.1016/j.physleta.2008.09.056`. URL: `https://www.sciencedirect.com/science/article/pii/S0375960108014692` (cit. on pp. 35, 37).

[127] M. Evans et al. “Thermo-optic noise in coated mirrors for high-precision optical measurements”. In: *Phys. Rev. D* 78 (10 Nov. 2008), p. 102003. DOI: `10.1103/PhysRevD.78.102003`. URL: `https://link.aps.org/doi/10.1103/PhysRevD.78.102003` (cit. on pp. 35, 36).

[128] Yuk Tung Liu and Kip Thorne. “Thermoelastic Noise and Homogeneous Thermal Noise in Finite Sized Gravitational-Wave Test Masses”. In: *Physical Review D* 62 (Feb. 2000). DOI: `10.1103/PhysRevD.62.122002` (cit. on p. 37).

[129] M. Cerdonio et al. “Thermoelastic effects at low temperatures and quantum limits in displacement measurements”. In: *Physical Review D* (2001). DOI: `10.1103/physrevd.63.082003` (cit. on p. 37).

[130] Kazuhiro Yamamoto et al. “Measurement of the mechanical loss of a cooled reflective coating for gravitational wave detection”. In: Phys. Rev. D 74.2, 022002 (July 2006), p. 022002. DOI: `10.1103/PhysRevD.74.022002`. arXiv: `gr-qc/0601031 [gr-qc]` (cit. on p. 40).

[131] D. F. McGuigan et al. “Measurements of the mechanical Q of single-crystal silicon at low temperatures”. In: *Journal of Low Temperature Physics* 30.5-6 (Mar. 1978), pp. 621–629. DOI: `10.1007/BF00116202` (cit. on p. 40).

[132] Ronny Nawrodt et al. “High mechanical Q-factor measurements on calcium fluoride at cryogenic temperatures”. In: *http://dx.doi.org/10.1051/epjap:2007040* 38 (Apr. 2007). DOI: `10.1051/epjap:2007040` (cit. on p. 40).

[133] R. Nawrodt et al. “A new apparatus for mechanical Q-factor measurements between 5 and 300K”. In: *Cryogenics* 46.10 (2006), pp. 718–723. ISSN: 0011-2275. DOI: `https://doi.org/10.1016/j.cryogenics.2006.06.001`. URL: `https://www.sciencedirect.com/science/article/pii/S0011227506000993` (cit. on p. 40).

[134] Henning Vahlbruch et al. “Detection of 15 dB Squeezed States of Light and their Application for the Absolute Calibration of Photoelectric Quantum Efficiency”. In: *Phys. Rev. Lett.* 117 (11 Sept. 2016), p. 110801. DOI: `10.1103/PhysRevLett.117.110801`. URL: `https://link.aps.org/doi/10.1103/PhysRevLett.117.110801` (cit. on p. 41).

[135] D. Ganapathy et al. “Broadband Quantum Enhancement of the LIGO Detectors with Frequency-Dependent Squeezing”. In: *Phys. Rev. X* 13 (4 Oct. 2023), p. 041021. DOI: `10.1103/PhysRevX.13.041021`. URL: `https://link.aps.org/doi/10.1103/PhysRevX.13.041021` (cit. on p. 41).

[136] Kenji Numata. “Direct measurements of coating thermal noise”. In: *Optical Coatings and Thermal Noise in Precision Measurement.* Ed. by Gregory Harry, Timothy P. Bodiya, and RiccardoEditors DeSalvo. Cambridge University Press, 2012, pp. 55–72. DOI: `10.1017/CBO9780511762314.007` (cit. on p. 41).

[137] Haoyu Wang et al. “Feasibility of near-unstable cavities for future gravitational wave detectors”. In: *Phys. Rev. D* 97 (2 Jan. 2018), p. 022001. DOI: `10.1103/PhysRevD.97.022001`. URL: `https://link.aps.org/doi/10.1103/PhysRevD.97.022001` (cit. on p. 43).

[138] Krosaki Harima Corporation, Ceramics Division. *NEXCERA ultra-low thermal expansion ceramics.* 2023. URL: `https://www.yange-plus.com/spec/7%20NEXCERA%20Ceramics.pdf` (cit. on p. 47).

[139] J. Keupp et al. “A high-resolution Ramsey-Bordé spectrometer for optical clocks based on cold Mg atoms”. In: *The European Physical Journal D - Atomic, Molecular, Optical and Plasma Physics* 36.3 (Dec. 2005), pp. 289–294. ISSN: 1434-6079. DOI: `10.1140/epjd/e2005-00302-7`. URL: `https://doi.org/10.1140/epjd/e2005-00302-7` (cit. on pp. 47, 48).

[140] Akira Takahashi. “Long-term dimensional stability and longitudinal uniformity of line scales made of glass ceramics”. In: *Measurement Science and Technology* 21.10 (Aug. 2010), p. 105301. DOI: `10.1088/0957-0233/21/10/105301`. URL: `https://dx.doi.org/10.1088/0957-0233/21/10/105301` (cit. on p. 47).

[141] J. Alnis et al. “Subhertz linewidth diode lasers by stabilization to vibrationally and thermally compensated ultralow-expansion glass Fabry-Pérot cavities”. In: *Phys. Rev. A* 77 (5 May 2008), p. 053809. DOI: `10.1103/PhysRevA.77.053809`. URL: `https://link.aps.org/doi/10.1103/PhysRevA.77.053809` (cit. on p. 47).

[142] Chang Jian Kwong et al. “Characterization of the long-term dimensional stability of a NEXCERA block using the optical resonator technique”. In: *Measurement Science and Technology* 29.7 (June 2018), p. 075011. DOI: `10.1088/1361-6501/aac3b0`. URL: `https://dx.doi.org/10.1088/1361-6501/aac3b0` (cit. on pp. 47, 48).

[143] E. Oelker et al. “Demonstration of 4.8 × 10-17 stability at 1 s for two independent optical clocks”. In: *Nature Photonics* 13.10 (Oct. 2019), pp. 714–719. ISSN: 1749-4893. DOI: `10.1038/s41566-019-0493-4`. URL: `https://doi.org/10.1038/s41566-019-0493-4` (cit. on pp. 47, 48, 114).

[144] Eugen Wiens et al. “A simplified cryogenic optical resonator apparatus providing ultralow frequency drift”. In: *Review of Scientific Instruments* 91.4 (Apr. 2020), p. 045112. ISSN: 0034-6748. DOI: `10.1063/1.5140321`. eprint: `https://pubs.aip.org/aip/rsi/article-pdf/doi/10.1063/1.5140321/14735723/045112\_1\_online.pdf`. URL: `https://doi.org/10.1063/1.5140321` (cit. on pp. 47, 48, 108).

[145] E. Wiens, A. Yu. Nevsky, and S. Schiller. “Resonator with Ultrahigh Length Stability as a Probe for Equivalence-Principle-Violating Physics”. In: *Phys. Rev. Lett.* 117 (27 Dec. 2016), p. 271102. DOI: `10.1103/PhysRevLett.117.271102`. URL: `https://link.aps.org/doi/10.1103/PhysRevLett.117.271102` (cit. on p. 47).

[146] P. Dubé et al. “A narrow linewidth and frequency-stable probe laser source for the 88Sr+ single ion optical frequency standard”. In: *Applied Physics B* 95.1 (Apr. 2009), pp. 43–54. ISSN: 1432-0649. DOI: `10.1007/s00340-009-3390-6`. URL: `https://doi.org/10.1007/s00340-009-3390-6` (cit. on p. 48).

[147] J C Phillips. “Stretched exponential relaxation in molecular and electronic glasses”. In: *Reports on Progress in Physics* 59.9 (Sept. 1996), p. 1133. DOI: `10.1088/0034-4885/59/9/003`. URL: `https://dx.doi.org/10.1088/0034-4885/59/9/003` (cit. on p. 48).

[148] E. Cesarini et al. “A “gentle” nodal suspension for measurements of the acoustic attenuation in materials”. In: *Review of Scientific Instruments* 80.5 (May 2009), p. 053904. ISSN: 0034-6748. DOI: `10.1063/1.3124800`. eprint: `https://pubs.aip.org/aip/rsi/article-pdf/doi/10.1063/1.3124800/14845568/053904\_1\_online.pdf`. URL: `https://doi.org/10.1063/1.3124800` (cit. on p. 48).

[149] Kazumoto Hosaka et al. “A Fabry–Pérot Etalon with an Ultralow Expansion Ceramic Spacer”. In: *Japanese Journal of Applied Physics* 52.3R (Feb. 2013), p. 032402. DOI: `10.7567/JJAP.52.032402`. URL: `https://dx.doi.org/10.7567/JJAP.52.032402` (cit. on p. 48).

[150] Thomas Legero, Thomas Kessler, and Uwe Sterr. “Tuning the thermal expansion properties of optical reference cavities with fused silica mirrors”. In: *Journal of the Optical Society of America B Optical Physics* 27.5 (Apr. 2010), p. 914. DOI: `10.1364/JOSAB.27.000914`. arXiv: `1002.2070 [physics.optics]` (cit. on p. 49).

[151] Corning Advanced Optics. *Corning ULE 7972 Low Expansion Glass.* 2016. URL: `https://www.corning.com/media/worldwide/csm/documents/7972%20ULE%20Product%20Information%20Jan%202016.pdf` (cit. on pp. 50, 53).

[152] Eng K. Wong et al. “Temperature-compensated cryogenic Fabry–Perot cavity”. In: *Appl. Opt.* 36.33 (Nov. 1997), pp. 8563–8566. DOI: `10.1364/AO.36.008563`. URL: `https://opg.optica.org/ao/abstract.cfm?URI=ao-36-33-8563` (cit. on p. 50).

[153] Mateusz Narożnik, Michal Zawada, and Marcin Bober. “The design of an ultra-stable cavity with crystalline mirror coatings for atomic optical clock”. In: *2022 Joint Conference of the European Frequency and Time Forum and IEEE International Frequency Control Symposium (EFTF/IFCS).* 2022, pp. 1–2. DOI: `10.1109/EFTF/IFCS54560.2022.9946296` (cit. on pp. 50, 55, 94, 95).

[154] Megan L. Kelleher et al. “Compact, portable, thermal-noise-limited optical cavity with low acceleration sensitivity”. In: *Opt. Express* 31.7 (Mar. 2023), pp. 11954–11965. DOI: `10.1364/OE.486087`. URL: `https://opg.optica.org/oe/abstract.cfm?URI=oe-31-7-11954` (cit. on pp. 50, 95).

[155] Garrett D. Cole et al. “Towards space-deployable laser stabilization systems based on vibration-insensitive cubic cavities with crystalline coatings”. In: *Opt. Express* 32.4 (Feb. 2024), pp. 5380–5396. DOI: `10.1364/OE.506833`. URL: `https://opg.optica.org/oe/abstract.cfm?URI=oe-32-4-5380` (cit. on p. 50).

[156] Richard W. Fox. “Temperature analysis of low-expansion Fabry-Perot cavities”. In: *Opt. Express* 17.17 (Aug. 2009), pp. 15023–15031. DOI: `10.1364/OE.17.015023`. URL: `https://opg.optica.org/oe/abstract.cfm?URI=oe-17-17-15023` (cit. on p. 51).

[157] M. Simpson, P. Krok, G. Thomas, M. Lessing. *Menlo Systems‘ ORS Ultrastable Laser System: A portable solution for state-of-the-art performance in high-precision measurements.* 2023. URL: `https://www.menlosystems.com/assets/white-paper/Menlo-Systems-ORS-White-Paper_230908_3w.pdf` (cit. on pp. 55, 56).

[158] Stable Lasers Systems. *Fabry-Pérot cavities.* 2024. URL: `https://stablelasers.com/fabry-perot-cavities/` (cit. on pp. 55, 56).

[159] Jon R. Peterson. *Observations and modeling of seismic background noise.* English. Tech. rep. Report. 1993. DOI: `10.3133/ofr93322`. URL: `https://doi.org/10.3133/ofr93322` (cit. on pp. 55, 67).

[160] J. Keller et al. “Simple vibration-insensitive cavity for laser stabilization at the 10-16 level”. In: *Applied Physics B* 116.1 (July 2014), pp. 203–210. ISSN: 1432-0649. DOI: `10.1007/s00340-013-5676-y`. URL: `https://doi.org/10.1007/s00340-013-5676-y` (cit. on pp. 56, 107).

[161] Andreas Melcher. *THE Room Mode Calculator*. 2023. URL: `https://amcoustics.com/` (cit. on p. 63).

[162] K P Birch and M J Downs. “An Updated Edlén Equation for the Refractive Index of Air”. In: *Metrologia* 30.3 (Jan. 1993), p. 155. DOI: `10.1088/0026-1394/30/3/004`. URL: `https://dx.doi.org/10.1088/0026-1394/30/3/004` (cit. on p. 74).

[163] K. P. Birch and M. J. Downs. “LETTER TO THE EDITOR: Correction to the Updated Edlén Equation for the Refractive Index of Air”. In: *Metrologia* 31.4 (Jan. 1994), pp. 315–316. DOI: `10.1088/0026-1394/31/4/006` (cit. on p. 74).

[164] Jack Ekin. *Experimental Techniques for Low-Temperature Measurements: Cryostat Design, Material Properties and Superconductor Critical-Current Testing*. Oxford University Press, Oct. 2006. ISBN: 9780198570547. DOI: `10.1093/acprof:oso/9780198570547.001.0001`. URL: `https://doi.org/10.1093/acprof:oso/9780198570547.001.0001` (cit. on p. 76).

[165] Moustafa Abdel-Hafiz et al. *Guidelines for developing optical clocks with* 10^{-18} *fractional frequency uncertainty*. 2019. arXiv: `1906.11495 [physics.atom-ph]` (cit. on pp. 76, 107).

[166] Piotr Ablewski, Marcin Bober, and Michał Zawada. “Emissivities of vacuum compatible materials: towards minimising blackbody radiation shift uncertainty in optical atomic clocks at room temperatures”. In: *Metrologia* 57.3 (May 2020), p. 035004. DOI: `10.1088/1681-7575/ab63ae`. URL: `https://dx.doi.org/10.1088/1681-7575/ab63ae` (cit. on p. 76).

[167] A. Einstein. “Die Grundlage der allgemeinen Relativitätstheorie”. In: *Annalen der Physik* 354.7 (Jan. 1916), pp. 769–822. DOI: `10.1002/andp.19163540702` (cit. on p. 80).

[168] Albert Einstein. “Näherungsweise Integration der Feldgleichungen der Gravitation”. In: *Sitzungsberichte der Königlich Preußischen Akademie der Wissenschaften (Berlin), Seite 688-696.* (1916) (cit. on p. 80).

[169] H. Rizwana Kausar, Lionel Philippoz, and Philippe Jetzer. “Gravitational wave polarization modes in $f(R)$ theories”. In: *Phys. Rev. D* 93 (12 June 2016), p. 124071. DOI: `10.1103/PhysRevD.93.124071`. URL: `https://link.aps.org/doi/10.1103/PhysRevD.93.124071` (cit. on p. 81).

[170] Thomas Callister et al. “Polarization-Based Tests of Gravity with the Stochastic Gravitational-Wave Background”. In: *Phys. Rev. X* 7 (4 Dec. 2017), p. 041058. DOI: `10.1103/PhysRevX.7.041058`. URL: `https://link.aps.org/doi/10.1103/PhysRevX.7.041058` (cit. on p. 81).

[171] Srashti Goyal et al. “Testing the nature of gravitational-wave polarizations using strongly lensed signals”. In: *Phys. Rev. D* 103 (2 Jan. 2021), p. 024038. DOI: `10.1103/PhysRevD.103.024038`. URL: `https://link.aps.org/doi/10.1103/PhysRevD.103.024038` (cit. on p. 81).

[172] Yudai Suwa et al. “On the minimum mass of neutron stars”. In: *Monthly Notices of the Royal Astronomical Society* 481.3 (Sept. 2018), pp. 3305–3312. ISSN: 0035-8711. DOI: `10.1093/mnras/sty2460`. eprint: `https://academic.oup.com/mnras/article-pdf/481/3/3305/25834769/sty2460.pdf`. URL: `https://doi.org/10.1093/mnras/sty2460` (cit. on p. 82).

[173] Peter Kafka. “Physics and astrophysics of gravitational waves.” In: *ESA Special Publication.* Ed. by W. R. Burke. Vol. 283. ESA Special Publication. May 1988, pp. 121–130 (cit. on p. 82).

[174] R. Abbott et al. “GWTC-2: Compact Binary Coalescences Observed by LIGO and Virgo during the First Half of the Third Observing Run”. In: *Phys. Rev. X* 11 (2 June 2021), p. 021053. DOI: `10.1103/PhysRevX.11.021053`. URL: `https://link.aps.org/doi/10.1103/PhysRevX.11.021053` (cit. on pp. 82, 86, 106).

[175] The LIGO Scientific Collaboration, the Virgo Collaboration, and the KAGRA Collaboration. “GWTC-3: Compact Binary Coalescences Observed by LIGO and Virgo During the Second Part of the Third Observing Run”. In: *arXiv e-prints*, arXiv:2111.03606 (Nov. 2021), arXiv:2111.03606. DOI: `10.48550/arXiv.2111.03606`. arXiv: `2111.03606 [gr-qc]` (cit. on pp. 82, 86).

[176] Alex Nitz et al. *gwastro/pycbc: v2.3.2 release of PyCBC.* Version v2.3.2. Nov. 2023. DOI: `10.5281/zenodo.10137381`. URL: `https://doi.org/10.5281/zenodo.10137381` (cit. on p. 83).

[177] Masaki Ando et al. “Torsion-Bar Antenna for Low-Frequency Gravitational-Wave Observations”. In: *Phys. Rev. Lett.* 105 (16 Oct. 2010), p. 161101. DOI: `10.1103/PhysRevLett.105.161101`. URL: `https://link.aps.org/doi/10.1103/PhysRevLett.105.161101` (cit. on pp. 84, 86, 100, 109).

[178] Jan Harms et al. “Lunar Gravitational-wave Antenna”. In: *The Astrophysical Journal* 910.1 (Mar. 2021), p. 1. DOI: `10.3847/1538-4357/abe5a7`. URL: `https://dx.doi.org/10.3847/1538-4357/abe5a7` (cit. on pp. 84, 86, 88).

[179] Michael Coughlin and Jan Harms. “Constraining the gravitational wave energy density of the Universe using Earth’s ring”. In: *Phys. Rev. D* 90 (4 Aug. 2014), p. 042005. DOI: `10.1103/PhysRevD.90.042005`. URL: `https://link.aps.org/doi/10.1103/PhysRevD.90.042005` (cit. on pp. 84, 86, 88).

[180] Shohei Aoyama, Rina Tazai, and Kiyotomo Ichiki. “Upper limit on the amplitude of gravitational waves around 0.1 Hz from the Global Positioning System”. In: *Phys. Rev. D* 89 (6 Mar. 2014), p. 067101. DOI: `10.1103/PhysRevD.89.067101`. URL: `https://link.aps.org/doi/10.1103/PhysRevD.89.067101` (cit. on pp. 84, 86).

[181] Deniz Soyuer et al. "Searching for gravitational waves via Doppler tracking by future missions to Uranus and Neptune". In: *Monthly Notices of the Royal Astronomical Society: Letters* 503.1 (Mar. 2021), pp. L73–L79. ISSN: 1745-3925. DOI: `10.1093/mnrasl/slab025`. eprint: `https://academic.oup.com/mnrasl/article-pdf/503/1/L73/36685971/slab025.pdf`. URL: `https://doi.org/10.1093/mnrasl/slab025` (cit. on pp. 84, 86, 100, 106).

[182] Travis Robson, Neil J Cornish, and Chang Liu. "The construction and use of LISA sensitivity curves". In: *Classical and Quantum Gravity* 36.10 (Apr. 2019), p. 105011. DOI: `10.1088/1361-6382/ab1101`. URL: `https://dx.doi.org/10.1088/1361-6382/ab1101` (cit. on pp. 84, 86, 106).

[183] Diego Blas and Alexander C. Jenkins. "Bridging the μHz Gap in the Gravitational-Wave Landscape with Binary Resonances". In: *Phys. Rev. Lett.* 128 (10 Mar. 2022), p. 101103. DOI: `10.1103/PhysRevLett.128.101103`. URL: `https://link.aps.org/doi/10.1103/PhysRevLett.128.101103` (cit. on pp. 84, 86, 106).

[184] Gemma Janssen et al. "Gravitational Wave Astronomy with the SKA". In: *PoS* AASKA14 (2015), p. 037. DOI: `10.22323/1.215.0037` (cit. on pp. 84, 86).

[185] Z. Arzoumanian et al. "The NANOGrav 11 Year Data Set: Pulsar-timing Constraints on the Stochastic Gravitational-wave Background". In: ApJ 859.1, 47 (May 2018), p. 47. DOI: `10.3847/1538-4357/aabd3b`. arXiv: `1801.02617 [astro-ph.HE]` (cit. on p. 84).

[186] Shuichi Sato et al. "The status of DECIGO". In: *Journal of Physics: Conference Series* 840.1 (May 2017), p. 012010. DOI: `10.1088/1742-6596/840/1/012010`. URL: `https://dx.doi.org/10.1088/1742-6596/840/1/012010` (cit. on pp. 84, 86, 100).

[187] B Canuel et al. "ELGAR—a European Laboratory for Gravitation and Atom-interferometric Research". In: *Classical and Quantum Gravity* 37.22 (Oct. 2020), p. 225017. DOI: `10.1088/1361-6382/aba80e`. URL: `https://dx.doi.org/10.1088/1361-6382/aba80e` (cit. on pp. 84, 86, 100).

[188] K. Ackley et al. "Neutron Star Extreme Matter Observatory: A kilohertz-band gravitational-wave detector in the global network". In: *Publications of the Astronomical Society of Australia* 37 (2020), e047. DOI: `10.1017/pasa.2020.39` (cit. on pp. 84, 87, 100, 109).

[189] Nancy Aggarwal et al. "Searching for New Physics with a Levitated-Sensor-Based Gravitational-Wave Detector". In: *Phys. Rev. Lett.* 128 (11 Mar. 2022), p. 111101. DOI: `10.1103/PhysRevLett.128.111101`. URL: `https://link.aps.org/doi/10.1103/PhysRevLett.128.111101` (cit. on pp. 84, 87, 100, 101, 105, 109).

[190] Michele Maggiore et al. "Science Case for the Einstein Telescope". In: *JCAP* 03 (2020), p. 050. DOI: `10.1088/1475-7516/2020/03/050`. arXiv: `1912.02622 [astro-ph.CO]` (cit. on pp. 84, 87, 100, 109).

[191] R. Abbott et al. "GWTC-2: Compact Binary Coalescences Observed by LIGO and Virgo during the First Half of the Third Observing Run". In: *Phys. Rev. X* 11 (2 June 2021), p. 021053. DOI: `10.1103/PhysRevX.11.021053`. URL: `https://link.aps.org/doi/10.1103/PhysRevX.11.021053` (cit. on pp. 84, 100).

[192] The LIGO Scientific Collaboration et al. "First joint observation by the underground gravitational-wave detector KAGRA with GEO 600". In: *Progress of Theoretical and Experimental Physics* 2022.6 (Apr. 2022), 063F01. ISSN: 2050-3911. DOI: `10.1093/ptep/ptac073`. eprint: `https://academic.oup.com/ptep/article-pdf/2022/6/063F01/43989382/ptac073.pdf`. URL: `https://doi.org/10.1093/ptep/ptac073` (cit. on p. 84).

[193] Antonio Branca et al. "Search for an Ultralight Scalar Dark Matter Candidate with the AURIGA Detector". In: *Phys. Rev. Lett.* 118 (2 Jan. 2017), p. 021302. DOI: `10.1103/PhysRevLett.118.021302`. URL: `https://link.aps.org/doi/10.1103/PhysRevLett.118.021302` (cit. on pp. 84, 88, 100).

[194] Odylio Denys Aguiar. "Past, present and future of the Resonant-Mass gravitational wave detectors". In: *Research in Astronomy and Astrophysics* 11.1 (Jan. 2011), pp. 1–42. DOI: `10.1088/1674-4527/11/1/001`. arXiv: `1009.1138 [astro-ph.IM]` (cit. on pp. 84, 88).

[195] V. Liccardo et al. "The design strain sensitivity of the schenberg spherical resonant antenna for gravitational waves". In: *Scientific Reports* 13.1 (Oct. 2023), p. 17706. ISSN: 2045-2322. DOI: `10.1038/s41598-023-43808-1`. URL: `https://doi.org/10.1038/s41598-023-43808-1` (cit. on pp. 84, 88, 100).

[196] Antonio Branca et al. "Search for an Ultralight Scalar Dark Matter Candidate with the AURIGA Detector". In: *Phys. Rev. Lett.* 118 (2 Jan. 2017), p. 021302. DOI: `10.1103/PhysRevLett.118.021302`. URL: `https://link.aps.org/doi/10.1103/PhysRevLett.118.021302` (cit. on pp. 84, 88, 100).

[197] William M. Campbell, Maxim Goryachev, and Michael E. Tobar. "The multi-mode acoustic gravitational wave experiment: MAGE". In: *Scientific Reports* 13.1 (June 2023), p. 10638. ISSN: 2045-2322. DOI: `10.1038/s41598-023-35670-y`. URL: `https://doi.org/10.1038/s41598-023-35670-y` (cit. on pp. 84, 87, 88).

[198] Aaron S. Chou et al. "MHz gravitational wave constraints with decameter Michelson interferometers". In: *Phys. Rev. D* 95 (6 Mar. 2017), p. 063002. DOI: `10.1103/PhysRevD.95.063002`. URL: `https://link.aps.org/doi/10.1103/PhysRevD.95.063002` (cit. on pp. 84, 87).

[199] Asher Berlin et al. "Electromagnetic cavities as mechanical bars for gravitational waves". In: *Phys. Rev. D* 108 (8 Oct. 2023), p. 084058. DOI: `10.1103/PhysRevD.108.084058`. URL: `https://link.aps.org/doi/10.1103/PhysRevD.108.084058` (cit. on pp. 84, 100, 101, 109).

[200] Teng Zhang et al. “Gravitational-Wave Detector for Postmerger Neutron Stars: Beyond the Quantum Loss Limit of the Fabry-Perot-Michelson Interferometer”. In: *Phys. Rev. X* 13 (2 May 2023), p. 021019. DOI: `10.1103/PhysRevX.13.021019`. URL: `https://link.aps.org/doi/10.1103/PhysRevX.13.021019` (cit. on pp. 84, 87, 100).

[201] Varun Srivastava et al. “Science-driven Tunable Design of Cosmic Explorer Detectors”. In: *The Astrophysical Journal* 931.1 (May 2022), p. 22. DOI: `10.3847/1538-4357/ac5f04`. URL: `https://dx.doi.org/10.3847/1538-4357/ac5f04` (cit. on pp. 84, 87, 100, 106, 109).

[202] C J Moore, R H Cole, and C P L Berry. “Gravitational-wave sensitivity curves”. In: *Classical and Quantum Gravity* 32.1 (Dec. 2014), p. 015014. DOI: `10.1088/0264-9381/32/1/015014`. URL: `https://dx.doi.org/10.1088/0264-9381/32/1/015014` (cit. on pp. 83, 84, 87, 88).

[203] Pau Amaro-Seoane et al. “Intermediate and extreme mass-ratio inspirals—astrophysics, science applications and detection using LISA”. In: *Classical and Quantum Gravity* 24.17 (Aug. 2007), R113. DOI: `10.1088/0264-9381/24/17/R01`. URL: `https://dx.doi.org/10.1088/0264-9381/24/17/R01` (cit. on pp. 83, 84).

[204] Wen-Biao Han et al. “Very-Extreme-mass-ratio gravitational wave bursts in the Galaxy and neighbors for space-borne detectors”. In: *Mon. Not. Roy. Astron. Soc.* 498.1 (2020), pp. L61–L65. DOI: `10.1093/mnrasl/slaa115`. arXiv: `2004.04016 [gr-qc]` (cit. on pp. 83, 84).

[205] Pau Amaro-Seoane et al. “eLISA: Astrophysics and cosmology in the millihertz regime”. In: *GW Notes* 6 (May 2013), pp. 4–110. arXiv: `1201.3621 [astro-ph.CO]` (cit. on pp. 83, 84).

[206] Giacomo Fragione et al. “Gravitational-wave Captures by Intermediate-mass Black Holes in Galactic Nuclei”. In: ApJ 897.1, 46 (July 2020), p. 46. DOI: `10.3847/1538-4357/ab94b2`. arXiv: `2002.02975 [astro-ph.GA]` (cit. on pp. 84, 85).

[207] Pablo Cerdá-Durán et al. “GRAVITATIONAL WAVE SIGNATURES IN BLACK HOLE FORMING CORE COLLAPSE”. In: *The Astrophysical Journal Letters* 779.2 (Dec. 2013), p. L18. DOI: `10.1088/2041-8205/779/2/L18`. URL: `https://dx.doi.org/10.1088/2041-8205/779/2/L18` (cit. on pp. 84, 101, 102).

[208] Takumu Kawamura et al. “Binary neutron star mergers and short gamma-ray bursts: Effects of magnetic field orientation, equation of state, and mass ratio”. In: *Phys. Rev. D* 94 (6 Sept. 2016), p. 064012. DOI: `10.1103/PhysRevD.94.064012`. URL: `https://link.aps.org/doi/10.1103/PhysRevD.94.064012` (cit. on pp. 84, 101, 102).

[209] Maximiliano Isi et al. “Directed searches for gravitational waves from ultralight bosons”. In: *Phys. Rev. D* 99 (8 Apr. 2019), p. 084042. DOI: `10.1103/PhysRevD.99.084042`. URL: `https://link.aps.org/doi/10.1103/PhysRevD.99.084042` (cit. on pp. 84, 104, 105).

[210] A. Sesana. “Systematic investigation of the expected gravitational wave signal from supermassive black hole binaries in the pulsar timing band”. In: *Monthly Notices of the Royal Astronomical Society: Letters* 433.1 (May 2013), pp. L1–L5. ISSN: 1745-3925. DOI: `10.1093/mnrasl/slt034`. eprint: `https://academic.oup.com/mnrasl/article-pdf/433/1/L1/2801328/slt034.pdf`. URL: `https://doi.org/10.1093/mnrasl/slt034` (cit. on p. 83).

[211] G. Nelemans, L. R. Yungelson, and S. F. Portegies Zwart. “Short-period AM CVn systems as optical, X-ray and gravitational-wave sources”. In: *Monthly Notices of the Royal Astronomical Society* 349.1 (Mar. 2004), pp. 181–192. ISSN: 0035-8711. DOI: `10.1111/j.1365-2966.2004.07479.x`. eprint: `https://academic.oup.com/mnras/article-pdf/349/1/181/11180320/349-1-181.pdf`. URL: `https://doi.org/10.1111/j.1365-2966.2004.07479.x` (cit. on p. 83).

[212] David Merritt et al. “Stellar dynamics of extreme-mass-ratio inspirals”. In: *Phys. Rev. D* 84 (4 Aug. 2011), p. 044024. DOI: `10.1103/PhysRevD.84.044024`. URL: `https://link.aps.org/doi/10.1103/PhysRevD.84.044024` (cit. on p. 83).

[213] Mar Mezcua. “Observational evidence for intermediate-mass black holes”. In: *International Journal of Modern Physics D* 26.11 (2017), p. 1730021. DOI: `10.1142/S021827181730021X`. eprint: `https://doi.org/10.1142/S021827181730021X`. URL: `https://doi.org/10.1142/S021827181730021` (cit. on p. 83).

[214] R. de Vita et al. “Prospects for detection of intermediate-mass black holes in globular clusters using integrated-light spectroscopy”. In: MNRAS 467.4 (June 2017), pp. 4057–4066. DOI: `10.1093/mnras/stx325`. arXiv: `1702.01741 [astro-ph.GA]` (cit. on p. 83).

[215] B.P. Abbott et al. “GW190521: A Binary Black Hole Merger with a Total Mass of 150 $M_{\odot}$”. In: *Phys. Rev. Lett.* 125 (10 Sept. 2020), p. 101102. DOI: `10.1103/PhysRevLett.125.101102`. URL: `https://link.aps.org/doi/10.1103/PhysRevLett.125.101102` (cit. on p. 85).

[216] Michele Maggiore. *Gravitational Waves. Vol. 2: Astrophysics and Cosmology.* Oxford University Press, 2018. ISBN: 9780198570899. URL: `https://global.oup.com/academic/product/gravitational-waves-9780198570899?cc=de&lang=en&#` (cit. on p. 85).

[217] B. P. Abbott et al. “GW190425: Observation of a Compact Binary Coalescence with Total Mass $\sim 3.4\ \mathrm{M}_{\odot}$”. In: *The Astrophysical Journal Letters* 892.1 (Mar. 2020), p. L3. DOI: `10.3847/2041-8213/ab75f5`. URL: `https://dx.doi.org/10.3847/2041-8213/ab75f5` (cit. on pp. 85, 103).

[218] Sarah Shandera, Donghui Jeong, and Henry S. Grasshorn Gebhardt. “Gravitational Waves from Binary Mergers of Subsolar Mass Dark Black Holes”. In: *Phys. Rev. Lett.* 120 (24 June 2018), p. 241102. DOI: `10.1103/PhysRevLett.120.241102`. URL: `https://link.aps.org/doi/10.1103/PhysRevLett.120.241102` (cit. on pp. 85, 104).

[219] Basudeb Dasgupta, Ranjan Laha, and Anupam Ray. "Low Mass Black Holes from Dark Core Collapse". In: *Phys. Rev. Lett.* 126 (14 Apr. 2021), p. 141105. DOI: `10.1103/PhysRevLett.126.141105`. URL: `https://link.aps.org/doi/10.1103/PhysRevLett.126.141105` (cit. on pp. 85, 104).

[220] Asimina Arvanitaki et al. "String axiverse". In: *Phys. Rev. D* 81 (12 June 2010), p. 123530. DOI: `10.1103/PhysRevD.81.123530`. URL: `https://link.aps.org/doi/10.1103/PhysRevD.81.123530` (cit. on pp. 85, 105).

[221] Asimina Arvanitaki and Sergei Dubovsky. "Exploring the string axiverse with precision black hole physics". In: *Phys. Rev. D* 83 (4 Feb. 2011), p. 044026. DOI: `10.1103/PhysRevD.83.044026`. URL: `https://link.aps.org/doi/10.1103/PhysRevD.83.044026` (cit. on pp. 85, 105).

[222] H. Bondi, F. A. E. Pirani, and I. Robinson. "Gravitational Waves in General Relativity. III. Exact Plane Waves". In: *Proceedings of the Royal Society of London. Series A, Mathematical and Physical Sciences* 251.1267 (1959), pp. 519–533. ISSN: 00804630. URL: `http://www.jstor.org/stable/100727` (cit. on p. 85).

[223] Ivor Robinson and A. Trautman. "Spherical Gravitational Waves". In: *Phys. Rev. Lett.* 4.8 (Apr. 1960), pp. 431–432. DOI: `10.1103/PhysRevLett.4.431` (cit. on p. 85).

[224] J. Weber. "Detection and Generation of Gravitational Waves". In: *Phys. Rev.* 117 (1 Jan. 1960), pp. 306–313. DOI: `10.1103/PhysRev.117.306`. URL: `https://link.aps.org/doi/10.1103/PhysRev.117.306` (cit. on pp. 85, 86, 88).

[225] J. Weber. "Evidence for Discovery of Gravitational Radiation". In: *Phys. Rev. Lett.* 22 (24 June 1969), pp. 1320–1324. DOI: `10.1103/PhysRevLett.22.1320`. URL: `https://link.aps.org/doi/10.1103/PhysRevLett.22.1320` (cit. on pp. 85, 88).

[226] Joel M. Weisberg, Joseph H. Taylor, and Lee A. Fowler. "Gravitational Waves From an Orbiting Pulsar". In: *Scientific American - SCI AMER* 245 (Oct. 1981), pp. 74–82. DOI: `10.1038/scientificamerican1081-74` (cit. on p. 85).

[227] J. M. Weisberg and Y. Huang. "RELATIVISTIC MEASUREMENTS FROM TIMING THE BINARY PULSAR PSR B1913+16". In: *The Astrophysical Journal* 829.1 (Sept. 2016), p. 55. DOI: `10.3847/0004-637X/829/1/55`. URL: `https://dx.doi.org/10.3847/0004-637X/829/1/55` (cit. on p. 85).

[228] M. E. Gertsenshtein and V. I. Pustovoit. "On the Detection of Low Frequency Gravitational Waves". In: *Sov. Phys. JETP* 16 (1962), p. 433 (cit. on p. 85).

[229] Rainer Weiss. "Electromagnetically coupled broadband gravitational antenna". In: *K.S. Thorne, "Gravitational radiation", 300 Years of Gravitation, S W Hawking and W Israel, pp 330–458*. University Press, 1972 (cit. on p. 85).

[230] Paul Linsay, Peter Saulson, and Rainer Weiss Stan Whitcomband. *A Study of a Long Baseline Gravitational Wave Antenna System.* Oct. 1983. URL: `https://dcc.ligo.org/public/0028/T830001/000/NSF_bluebook_1983.pdf` (cit. on p. 86).

[231] Rochus E. Vogt et al. *The Construction, Operation, and Supporting Research and Development od a Laser Interferometer Gravitational-Wave Observatory (LIGO). VOLUME 1: LIGO Sience and Concepts.* Dec. 1989. URL: `https://dcc.ligo.org/public/0065/M890001/003/M890001-02%5C%20edited.pdf` (cit. on p. 86).

[232] Rosa Poggiani. "Results from the O3 observing run of the LIGO/VIRGO collaboration". In: *PoS* HEASA2021 (2021), p. 060. DOI: `10.22323/1.401.0060` (cit. on p. 86).

[233] R. Abbott et al. "Properties and Astrophysical Implications of the 150 $M_\odot$ Binary Black Hole Merger GW190521". In: *The Astrophysical Journal Letters* 900.1 (Sept. 2020), p. L13. DOI: `10.3847/2041-8213/aba493`. URL: `https://dx.doi.org/10.3847/2041-8213/aba493` (cit. on p. 86).

[234] H Abe et al. "Noise subtraction from KAGRA O3GK data using Independent Component Analysis". In: *Classical and Quantum Gravity* 40.8 (Mar. 2023), p. 085015. DOI: `10.1088/1361-6382/acc0cb`. URL: `https://dx.doi.org/10.1088/1361-6382/acc0cb` (cit. on p. 86).

[235] Gabriella Agazie et al. "The NANOGrav 15 yr Data Set: Evidence for a Gravitational-wave Background". In: *The Astrophysical Journal Letters* 951.1 (June 2023), p. L8. DOI: `10.3847/2041-8213/acdac6`. URL: `https://dx.doi.org/10.3847/2041-8213/acdac6` (cit. on p. 86).

[236] Paul D. Lasky et al. "Gravitational-Wave Cosmology across 29 Decades in Frequency". In: *Phys. Rev. X* 6 (1 Mar. 2016), p. 011035. DOI: `10.1103/PhysRevX.6.011035`. URL: `https://link.aps.org/doi/10.1103/PhysRevX.6.011035` (cit. on pp. 87, 105, 106).

[237] A. Ejlli et al. "Upper limits on the amplitude of ultra-high-frequency gravitational waves from graviton to photon conversion". In: *The European Physical Journal C* 79.12 (Dec. 2019), p. 1032. ISSN: 1434-6052. DOI: `10.1140/epjc/s10052-019-7542-5`. URL: `https://doi.org/10.1140/epjc/s10052-019-7542-5` (cit. on p. 87).

[238] A M Cruise. "An electromagnetic detector for very-high-frequency gravitational waves". In: *Classical and Quantum Gravity* 17.13 (July 2000), p. 2525. DOI: `10.1088/0264-9381/17/13/305`. URL: `https://dx.doi.org/10.1088/0264-9381/17/13/305` (cit. on p. 87).

[239] Asuka Ito et al. "Probing GHz gravitational waves with graviton–magnon resonance". In: *The European Physical Journal C* 80.3 (Feb. 2020), p. 179. ISSN: 1434-6052. DOI: `10.1140/epjc/s10052-020-7735-y`. URL: `https://doi.org/10.1140/epjc/s10052-020-7735-y` (cit. on p. 87).

[240] Fangyu Li et al. "Signal photon flux and background noise in a coupling electromagnetic detecting system for high-frequency gravitational waves". In: *Phys. Rev. D* 80 (6 Sept. 2009), p. 064013. DOI: `10.1103/PhysRevD.80.064013`. URL: `https://link.aps.org/doi/10.1103/PhysRevD.80.064013` (cit. on p. 87).

[241] Bruce Allen and Joseph D. Romano. “Detecting a stochastic background of gravitational radiation: Signal processing strategies and sensitivities”. In: *Phys. Rev. D* 59 (10 Mar. 1999), p. 102001. DOI: `10.1103/PhysRevD.59.102001`. URL: `https://link.aps.org/doi/10.1103/PhysRevD.59.102001` (cit. on p. 87).

[242] N. Aghanim et al. “Planck 2018 results. VI. Cosmological parameters”. In: *Astronomy & Astrophysics* (Apr. 2020). ISSN: 1432-0746. DOI: `10.1051/0004-6361/201833910`. URL: `http://dx.doi.org/10.1051/0004-6361/201833910` (cit. on p. 87).

[243] Adam G. Riess et al. “Large Magellanic Cloud Cepheid Standards Provide a 1% Foundation for the Determination of the Hubble Constant and Stronger Evidence for Physics beyond ΛCDM”. In: *The Astrophysical Journal* 876.1 (May 2019), p. 85. DOI: `10.3847/1538-4357/ab1422`. URL: `https://doi.org/10.3847%5C%2F1538-4357%5C%2Fab1422` (cit. on p. 87).

[244] Maxim Goryachev et al. “Rare Events Detected with a Bulk Acoustic Wave High Frequency Gravitational Wave Antenna”. In: *Phys. Rev. Lett.* 127 (7 Aug. 2021), p. 071102. DOI: `10.1103/PhysRevLett.127.071102`. URL: `https://link.aps.org/doi/10.1103/PhysRevLett.127.071102` (cit. on p. 88).

[245] Paul D. Lasky and Eric Thrane. “Did Goryachev et al. detect megahertz gravitational waves?” In: *Phys. Rev. D* 104 (10 Nov. 2021), p. 103017. DOI: `10.1103/PhysRevD.104.103017`. URL: `https://link.aps.org/doi/10.1103/PhysRevD.104.103017` (cit. on p. 88).

[246] Guillem Domènech. “Were recently reported MHz events planet mass primordial black hole mergers?” In: *The European Physical Journal C* 81.11 (Nov. 2021), p. 1042. ISSN: 1434-6052. DOI: `10.1140/epjc/s10052-021-09853-8`. URL: `https://doi.org/10.1140/epjc/s10052-021-09853-8` (cit. on p. 88).

[247] Andrew D. Ludlow et al. “Optical atomic clocks”. In: *Rev. Mod. Phys.* 87 (2 June 2015), pp. 637–701. DOI: `10.1103/RevModPhys.87.637`. URL: `https://link.aps.org/doi/10.1103/RevModPhys.87.637` (cit. on pp. 88, 107).

[248] M Cerdonio et al. “The ultracryogenic gravitational-wave detector AURIGA”. In: *Classical and Quantum Gravity* 14.6 (June 1997), p. 1491. DOI: `10.1088/0264-9381/14/6/016`. URL: `https://dx.doi.org/10.1088/0264-9381/14/6/016` (cit. on p. 94).

[249] Stefan Seel et al. “Cryogenic Optical Resonators: A New Tool for Laser Frequency Stabilization at the 1 Hz Level”. In: *Phys. Rev. Lett.* 78 (25 June 1997), pp. 4741–4744. DOI: `10.1103/PhysRevLett.78.4741`. URL: `https://link.aps.org/doi/10.1103/PhysRevLett.78.4741` (cit. on p. 94).

[250] Michele Maggiore. *Gravitational Waves. Theory and Experiments.* Oxford University Press, 2008 (cit. on p. 101).

[251] Evan O'Connor and Christian D. Ott. "BLACK HOLE FORMATION IN FAILING CORE-COLLAPSE SUPERNOVAE". In: *The Astrophysical Journal* 730.2 (Mar. 2011), p. 70. DOI: `10.1088/0004-637X/730/2/70`. URL: `https://dx.doi.org/10.1088/0004-637X/730/2/70` (cit. on p. 101).

[252] Nicolas de Brye et al. "General Relativistic Simulations of the Collapsar Scenario". In: *Progress in Mathematical Relativity, Gravitation and Cosmology.* Ed. by Alfonso García-Parrado et al. Berlin, Heidelberg: Springer Berlin Heidelberg, 2014, pp. 231–235. ISBN: 978-3-642-40157-2 (cit. on p. 101).

[253] David Vartanyan et al. "Gravitational-wave signature of core-collapse supernovae". In: *Phys. Rev. D* 107 (10 May 2023), p. 103015. DOI: `10.1103/PhysRevD.107.103015`. URL: `https://link.aps.org/doi/10.1103/PhysRevD.107.103015` (cit. on p. 101).

[254] Anthony Mezzacappa et al. "Core collapse supernova gravitational wave emission for progenitors of 9.6, 15, and 25 $M_\odot$". In: Phys. Rev. D 107.4, 043008 (Feb. 2023), p. 043008. DOI: `10.1103/PhysRevD.107.043008`. arXiv: `2208.10643 [astro-ph.SR]` (cit. on pp. 101, 102).

[255] A. Heger et al. "How Massive Single Stars End Their Life". In: *The Astrophysical Journal* 591.1 (July 2003), p. 288. DOI: `10.1086/375341`. URL: `https://dx.doi.org/10.1086/375341` (cit. on p. 101).

[256] Oliver Eggenberger Andersen et al. "Equation-of-state Dependence of Gravitational Waves in Core-collapse Supernovae". In: *The Astrophysical Journal* 923.2 (Dec. 2021), p. 201. DOI: `10.3847/1538-4357/ac294c`. URL: `https://dx.doi.org/10.3847/1538-4357/ac294c` (cit. on pp. 101, 102).

[257] N. K. Glendenning and S. A. Moszkowski. "Reconciliation of neutron-star masses and binding of the Λ in hypernuclei". In: *Phys. Rev. Lett.* 67 (18 Oct. 1991), pp. 2414–2417. DOI: `10.1103/PhysRevLett.67.2414`. URL: `https://link.aps.org/doi/10.1103/PhysRevLett.67.2414` (cit. on p. 101).

[258] Jocelyn S. Read et al. "Constraints on a phenomenologically parametrized neutron-star equation of state". In: *Phys. Rev. D* 79 (12 June 2009), p. 124032. DOI: `10.1103/PhysRevD.79.124032`. URL: `https://link.aps.org/doi/10.1103/PhysRevD.79.124032` (cit. on p. 101).

[259] Masaru Shibata and Keisuke Taniguchi. "Merger of binary neutron stars to a black hole: Disk mass, short gamma-ray bursts, and quasinormal mode ringing". In: *Phys. Rev. D* 73 (6 Mar. 2006), p. 064027. DOI: `10.1103/PhysRevD.73.064027`. URL: `https://link.aps.org/doi/10.1103/PhysRevD.73.064027` (cit. on p. 103).

[260] Luca Baiotti, Bruno Giacomazzo, and Luciano Rezzolla. "Accurate evolutions of inspiralling neutron-star binaries: Prompt and delayed collapse to a black hole". In: *Phys. Rev. D* 78 (8 Oct. 2008), p. 084033. DOI: `10.1103/PhysRevD.78.084033`. URL: `https://link.aps.org/doi/10.1103/PhysRevD.78.084033` (cit. on p. 103).

[261] Ben Margalit and Brian D. Metzger. "The Multi-messenger Matrix: The Future of Neutron Star Merger Constraints on the Nuclear Equation of State". In: *The Astrophysical Journal Letters* 880.1 (July 2019), p. L15. DOI: `10.3847/2041-8213/ab2ae2`. URL: `https://dx.doi.org/10.3847/2041-8213/ab2ae2` (cit. on p. 103).

[262] B.P. Abbott, LIGO Scientific Collaboration, Virgo Collaboration, et al. "GW170817: Observation of Gravitational Waves from a Binary Neutron Star Inspiral". In: Phys. Rev. Lett. 119.16, 161101 (Oct. 2017), p. 161101. DOI: `10.1103/PhysRevLett.119.161101`. arXiv: `1710.05832 [gr-qc]` (cit. on p. 103).

[263] B. P. Abbott, LIGO Scientific and Virgo Collaboration, et al. "Search for Gravitational Waves from a Long-lived Remnant of the Binary Neutron Star Merger GW170817". In: *The Astrophysical Journal* 875.2 (Apr. 2019), p. 160. DOI: `10.3847/1538-4357/ab0f3d`. URL: `https://dx.doi.org/10.3847/1538-4357/ab0f3d` (cit. on p. 103).

[264] Luciano Rezzolla, Elias R. Most, and Lukas R. Weih. "Using Gravitational-wave Observations and Quasi-universal Relations to Constrain the Maximum Mass of Neutron Stars". In: *The Astrophysical Journal Letters* 852.2 (Jan. 2018), p. L25. DOI: `10.3847/2041-8213/aaa401`. URL: `https://dx.doi.org/10.3847/2041-8213/aaa401` (cit. on p. 103).

[265] David Pooley et al. "GW170817 Most Likely Made a Black Hole". In: ApJ 859.2, L23 (June 2018), p. L23. DOI: `10.3847/2041-8213/aac3d6`. arXiv: `1712.03240 [astro-ph.HE]` (cit. on p. 103).

[266] Ya. B. Zel'dovich and I. D. Novikov. "The Hypothesis of Cores Retarded during Expansion and the Hot Cosmological Model". In: Soviet Ast. 10 (Feb. 1967), p. 602 (cit. on p. 104).

[267] Stephen Hawking. "Gravitationally Collapsed Objects of Very Low Mass". In: *Monthly Notices of the Royal Astronomical Society* 152.1 (Apr. 1971), pp. 75–78. ISSN: 0035-8711. DOI: `10.1093/mnras/152.1.75`. eprint: `https://academic.oup.com/mnras/article-pdf/152/1/75/9360899/mnras152-0075.pdf`. URL: `https://doi.org/10.1093/mnras/152.1.75` (cit. on p. 104).

[268] Paolo Pani and Abraham Loeb. "Tidal capture of a primordial black hole by a neutron star: implications for constraints on dark matter". In: *Journal of Cosmology and Astroparticle Physics* 2014.06 (June 2014), p. 026. DOI: `10.1088/1475-7516/2014/06/026`. URL: `https://dx.doi.org/10.1088/1475-7516/2014/06/026` (cit. on p. 104).

[269] Divya Singh et al. "Gravitational-wave limit on the Chandrasekhar mass of dark matter". In: *Phys. Rev. D* 104 (4 Aug. 2021), p. 044015. DOI: `10.1103/PhysRevD.104.044015`. URL: `https://link.aps.org/doi/10.1103/PhysRevD.104.044015` (cit. on p. 104).

[270] Maximiliano Isi et al. "Erratum: Directed searches for gravitational waves from ultralight bosons [Phys. Rev. D 99, 084042 (2019)]". In: *Phys. Rev. D* 102 (4 Aug. 2020), p. 049901. DOI: `10.1103/PhysRevD.102.049901`. URL: `https://link.aps.org/doi/10.1103/PhysRevD.102.049901` (cit. on pp. 104, 105).

[271] T. Damour, N. Deruelle, and R. Ruffini. "On quantum resonances in stationary geometries". In: *Lettere al Nuovo Cimento (1971-1985)* 15.8 (Feb. 1976), pp. 257–262. ISSN: 1827-613X. DOI: `10.1007/BF02725534`. URL: `https://doi.org/10.1007/BF02725534` (cit. on p. 104).

[272] I. M. Ternov et al. "Finite motion of massive particles in the Kerr and Schwarzschild fields". In: *Soviet Physics Journal* 21.9 (Sept. 1978), pp. 1200–1204. ISSN: 1573-9228. DOI: `10.1007/BF00894575`. URL: `https://doi.org/10.1007/BF00894575` (cit. on p. 104).

[273] Theodoros J.M Zouros and Douglas M Eardley. "Instabilities of massive scalar perturbations of a rotating black hole". In: *Annals of Physics* 118.1 (1979), pp. 139–155. ISSN: 0003-4916. DOI: `https://doi.org/10.1016/0003-4916(79)90237-9`. URL: `https://www.sciencedirect.com/science/article/pii/0003491679902379` (cit. on p. 104).

[274] Steven Detweiler. "Klein-Gordon equation and rotating black holes". In: *Phys. Rev. D* 22 (10 Nov. 1980), pp. 2323–2326. DOI: `10.1103/PhysRevD.22.2323`. URL: `https://link.aps.org/doi/10.1103/PhysRevD.22.2323` (cit. on p. 104).

[275] Richard Brito, Vitor Cardoso, and Paolo Pani. *Superradiance*. Springer International Publishing, 2020. DOI: `10.1007/978-3-030-46622-0`. URL: `https://doi.org/10.1007/978-3-030-46622-0` (cit. on p. 105).

[276] Hirotaka Yoshino and Hideo Kodama. "Gravitational radiation from an axion cloud around a black hole: Superradiant phase". In: *Progress of Theoretical and Experimental Physics* 2014.4 (Apr. 2014). 043E02. ISSN: 2050-3911. DOI: `10.1093/ptep/ptu029`. eprint: `https://academic.oup.com/ptep/article-pdf/2014/4/043E02/19300525/ptu029.pdf`. URL: `https://doi.org/10.1093/ptep/ptu029` (cit. on p. 105).

[277] Asimina Arvanitaki, Masha Baryakhtar, and Xinlu Huang. "Discovering the QCD axion with black holes and gravitational waves". In: *Phys. Rev. D* 91 (8 Apr. 2015), p. 084011. DOI: `10.1103/PhysRevD.91.084011`. URL: `https://link.aps.org/doi/10.1103/PhysRevD.91.084011` (cit. on p. 105).

[278] Richard Brito, Vitor Cardoso, and Paolo Pani. "Black holes as particle detectors: evolution of superradiant instabilities". In: *Classical and Quantum Gravity* 32.13 (June 2015), p. 134001. DOI: `10.1088/0264-9381/32/13/134001`. URL: `https://dx.doi.org/10.1088/0264-9381/32/13/134001` (cit. on p. 105).

[279] Asimina Arvanitaki et al. "Black hole mergers and the QCD axion at Advanced LIGO". In: *Phys. Rev. D* 95 (4 Feb. 2017), p. 043001. DOI: `10.1103/PhysRevD.95.043001`. URL: `https://link.aps.org/doi/10.1103/PhysRevD.95.043001` (cit. on p. 105).

[280] Richard Brito et al. "Stochastic and Resolvable Gravitational Waves from Ultralight Bosons". In: *Phys. Rev. Lett.* 119 (13 Sept. 2017), p. 131101. DOI: `10.1103/PhysRevLett.119.131101`. URL: `https://link.aps.org/doi/10.1103/PhysRevLett.119.131101` (cit. on p. 105).

[281] Richard Brito et al. “Gravitational wave searches for ultralight bosons with LIGO and LISA”. In: *Phys. Rev. D* 96 (6 Sept. 2017), p. 064050. DOI: `10.1103/PhysRevD.96.064050`. URL: `https://link.aps.org/doi/10.1103/PhysRevD.96.064050` (cit. on p. 105).

[282] Daniel Baumann, Horng Sheng Chia, and Rafael A. Porto. “Probing ultralight bosons with binary black holes”. In: *Phys. Rev. D* 99 (4 Feb. 2019), p. 044001. DOI: `10.1103/PhysRevD.99.044001`. URL: `https://link.aps.org/doi/10.1103/PhysRevD.99.044001` (cit. on p. 105).

[283] Ken K. Y. Ng et al. “Searching for ultralight bosons within spin measurements of a population of binary black hole mergers”. In: *Phys. Rev. D* 103 (6 Mar. 2021), p. 063010. DOI: `10.1103/PhysRevD.103.063010`. URL: `https://link.aps.org/doi/10.1103/PhysRevD.103.063010` (cit. on p. 105).

[284] Michele Maggiore. “Gravitational wave experiments and early universe cosmology”. In: *Physics Reports* 331.6 (2000), pp. 283–367. ISSN: 0370-1573. DOI: `https://doi.org/10.1016/S0370-1573(99)00102-7`. URL: `http://www.sciencedirect.com/science/article/pii/S0370157399001027` (cit. on p. 105).

[285] Xiao-Jin Liu et al. “Detecting relic gravitational waves by pulsar timing arrays: Effects of cosmic phase transitions and relativistic free-streaming gases”. In: *Phys. Rev. D* 93 (2 Jan. 2016), p. 024031. DOI: `10.1103/PhysRevD.93.024031`. URL: `https://link.aps.org/doi/10.1103/PhysRevD.93.024031` (cit. on p. 105).

[286] Eric Thrane and Joseph D. Romano. “Sensitivity curves for searches for gravitational-wave backgrounds”. In: *Phys. Rev. D* 88 (12 Dec. 2013), p. 124032. DOI: `10.1103/PhysRevD.88.124032`. URL: `https://link.aps.org/doi/10.1103/PhysRevD.88.124032` (cit. on p. 105).

[287] Marina Cortês, Andrew R. Liddle, and David Parkinson. “Tensors, BICEP2 results, prior dependence, and dust”. In: *Phys. Rev. D* 92 (6 Sept. 2015), p. 063511. DOI: `10.1103/PhysRevD.92.063511`. URL: `https://link.aps.org/doi/10.1103/PhysRevD.92.063511` (cit. on p. 105).

[288] Nicola Bartolo et al. “Science with the space-based interferometer LISA. IV: probing inflation with gravitational waves”. In: *Journal of Cosmology and Astroparticle Physics* 2016.12 (Dec. 2016), pp. 026–026. DOI: `10.1088/1475-7516/2016/12/026`. URL: `https://doi.org/10.1088%5C%2F1475-7516%5C%2F2016%5C%2F12%5C%2F026` (cit. on p. 105).

[289] Edward A. Whittaker, Manfred Gehrtz, and Gary C. Bjorklund. “Residual amplitude modulation in laser electro-optic phase modulation”. In: *J. Opt. Soc. Am. B* 2.8 (Aug. 1985), pp. 1320–1326. DOI: `10.1364/JOSAB.2.001320`. URL: `http://josab.osa.org/abstract.cfm?URI=josab-2-8-1320` (cit. on p. 107).

[290] Mark Notcutt et al. “Simple and compact 1-Hz laser system via an improved mounting configuration of a reference cavity”. In: *Opt. Lett.* 30.14 (July 2005), pp. 1815–1817. DOI: `10.1364/OL.30.001815`. URL: `http://ol.osa.org/abstract.cfm?URI=ol-30-14-1815` (cit. on p. 107).

[291] S. A. Webster et al. "Thermal-noise-limited optical cavity". In: Phys. Rev. A 77.3, 033847 (Mar. 2008), p. 033847. DOI: `10.1103/PhysRevA.77.033847` (cit. on p. 107).

[292] J. Millo et al. "Ultrastable lasers based on vibration insensitive cavities". In: *Phys. Rev. A* 79 (5 May 2009), p. 053829. DOI: `10.1103/PhysRevA.79.053829`. URL: `https://link.aps.org/doi/10.1103/PhysRevA.79.053829` (cit. on p. 107).

[293] Garrett D. Cole et al. "High-performance near- and mid-infrared crystalline coatings". In: *Optica* 3.6 (June 2016), pp. 647–656. DOI: `10.1364/OPTICA.3.000647`. URL: `https://opg.optica.org/optica/abstract.cfm?URI=optica-3-6-647` (cit. on p. 108).

[294] T. Hata et al. "Development and Comparison of Two Types of Cryogen-Free Dilution Refrigerator". In: *Journal of Low Temperature Physics* 175.1 (Apr. 2014), pp. 471–479. ISSN: 1573-7357. DOI: `10.1007/s10909-013-0986-3`. URL: `https://doi.org/10.1007/s10909-013-0986-3` (cit. on p. 109).

[295] National Science Foundation. *LIGO Factsheet.* 2012. URL: `https://www.nsf.gov/news/special_reports/ligoevent/pdfs/LIGO_factsheet_2017_v01.pdf` (cit. on p. 109).

[296] P. Wcisło et al. "Experimental constraint on dark matter detection with optical atomic clocks". In: *Nature Astronomy* 1.1 (Dec. 2016), p. 0009. ISSN: 2397-3366. DOI: `10.1038/s41550-016-0009`. URL: `https://doi.org/10.1038/s41550-016-0009` (cit. on p. 109).

[297] C. Lisdat et al. "A clock network for geodesy and fundamental science". In: *Nature Communications* 7.1 (Aug. 2016), p. 12443. ISSN: 2041-1723. DOI: `10.1038/ncomms12443`. URL: `https://doi.org/10.1038/ncomms12443` (cit. on p. 109).

[298] Claus Kiefer. *Quantum Gravity.* Oxford University Press UK, 2004 (cit. on p. 110).

[299] Gianluca Calcagni and Michele Ronco. "Dimensional flow and fuzziness in quantum gravity: Emergence of stochastic spacetime". In: *Nuclear Physics B* 923 (2017), pp. 144–167. ISSN: 0550-3213. DOI: `https://doi.org/10.1016/j.nuclphysb.2017.07.016`. URL: `https://www.sciencedirect.com/science/article/pii/S055032131730247X` (cit. on p. 110).

[300] Houri Ziaeepour. "Comparing Quantum Gravity Models: String Theory, Loop Quantum Gravity, and Entanglement Gravity versus SU(∞)-QGR". In: *Symmetry* 14.1 (2022). ISSN: 2073-8994. DOI: `10.3390/sym14010058`. URL: `https://www.mdpi.com/2073-8994/14/1/58` (cit. on p. 110).

[301] John Archibald Wheeler. "From relativity to mutability". In: *Revista Mexicana de Física* 23.1y2 (Jan. 1974), pp. 1–57. URL: `https://rmf.smf.mx/ojs/index.php/rmf/article/view/1041` (cit. on p. 110).

[302] S. W. Hawking. "Space-Time Foam". In: *Nucl. Phys. B* 144 (1978), pp. 349–362. DOI: `10.1016/0550-3213(78)90375-9` (cit. on p. 110).

[303] EugSene P. Wigner. "Relativistic Invariance and Quantum Phenomena". In: *Rev. Mod. Phys.* 29 (3 July 1957), pp. 255–268. DOI: `10.1103/RevModPhys.29.255`. URL: `https://link.aps.org/doi/10.1103/RevModPhys.29.255` (cit. on p. 110).

[304] H. Salecker and E. P. Wigner. “Quantum Limitations of the Measurement of Space-Time Distances”. In: *Phys. Rev.* 109 (2 Jan. 1958), pp. 571–577. DOI: `10.1103/PhysRev.109.571`. URL: `https://link.aps.org/doi/10.1103/PhysRev.109.571` (cit. on pp. 110, 115).

[305] Giovanni Amelino-Camelia. “Limits on the measurability of space-time distances in (the semiclassical approximation of) quantum gravity”. In: *Modern Physics Letters A* 09.37 (1994), pp. 3415–3422. DOI: `10.1142/S0217732394003245`. URL: `https://doi.org/10.1142/S0217732394003245` (cit. on p. 110).

[306] Y. Ng and Hendrik van Dam. “LIMIT TO SPACE-TIME MEASUREMENT”. In: *Modern Physics Letters A* 09 (1994), pp. 335–340. URL: `https://api.semanticscholar.org/CorpusID:122137188` (cit. on pp. 110, 112).

[307] Giovanni Amelino-Camelia. “Gravity-wave interferometers as quantum-gravity detectors”. In: *Nature* 398.6724 (Mar. 1999), pp. 216–218. ISSN: 1476-4687. DOI: `10.1038/18377`. URL: `https://doi.org/10.1038/18377` (cit. on pp. 110, 112).

[308] Giovanni Amelino-Camelia. “Gravity-wave interferometers as probes of a low-energy effective quantum gravity”. In: *Phys. Rev. D* 62 (2 June 2000), p. 024015. DOI: `10.1103/PhysRevD.62.024015`. URL: `https://link.aps.org/doi/10.1103/PhysRevD.62.024015` (cit. on pp. 110, 112).

[309] Y. Jack Ng and H. van Dam. “Measuring the Foaminess of Space-Time with Gravity-Wave Interferometers”. In: *Foundations of Physics* 30.5 (May 2000), pp. 795–805. ISSN: 1572-9516. DOI: `10.1023/A:1003745212871`. URL: `https://doi.org/10.1023/A:1003745212871` (cit. on pp. 110, 112).

[310] Giovanni Amelino-Camelia. “On the Salecker-Wigner limit and the use of interferometers in space-time-foam studies”. In: *Physics Letters B* 477.4 (2000), pp. 436–450. ISSN: 0370-2693. DOI: `https://doi.org/10.1016/S0370-2693(00)00231-8`. URL: `https://www.sciencedirect.com/science/article/pii/S0370269300002318` (cit. on p. 110).

[311] Y. JACK NG. “SELECTED TOPICS IN PLANCK-SCALE PHYSICS”. In: *Modern Physics Letters A* 18.16 (2003), pp. 1073–1097. DOI: `10.1142/S0217732303010934`. eprint: `https://doi.org/10.1142/S0217732303010934`. URL: `https://doi.org/10.1142/S0217732303010934` (cit. on pp. 110, 111).

[312] Y.Jack Ng and H. van Dam. “On Wigner’s clock and the detectability of spacetime foam with gravitational-wave interferometers”. In: *Physics Letters B* 477.4 (2000), pp. 429–435. ISSN: 0370-2693. DOI: `https://doi.org/10.1016/S0370-2693(00)00232-X`. URL: `https://www.sciencedirect.com/science/article/pii/S037026930000232X` (cit. on p. 110).